ISSN: 2150-4091 Volume 2, Number 7, July 2010

Scientific Research

Natural Science

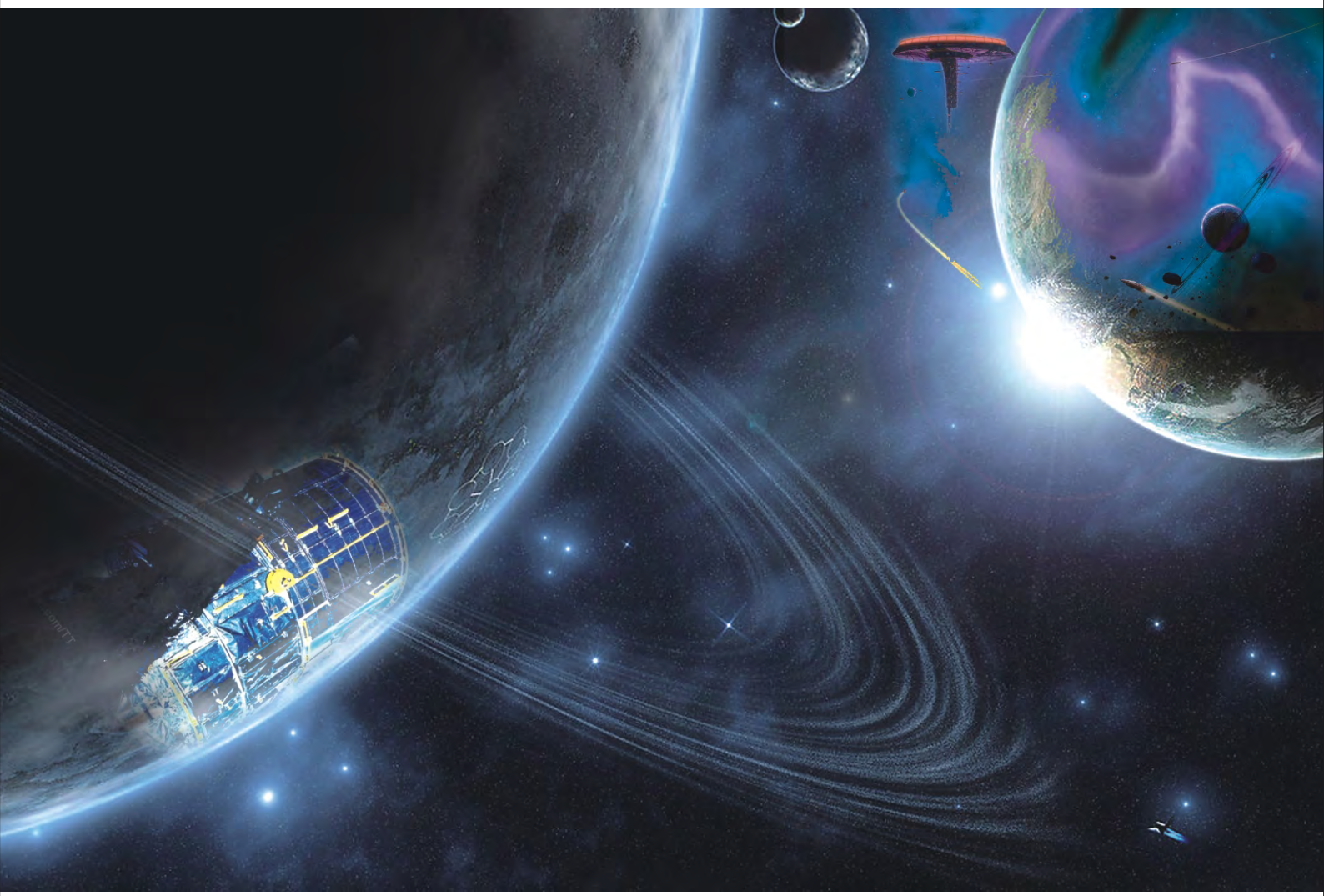

ISSN: 2150-4091

www.scirp.org/journal/ns/

Journal Editorial Board

ISSN: 2150-4091 (Print) ISSN: 2150-4105 (Online)
http://www.scirp.org/journal/ns/

TABLE OF CONTENTS

Volume 2, Number 7, July 2010

Natural Science

Journal Information

SUBSCRIPTIONS

The *Natural Science* (Online at Scientific Research Publishing, www.SciRP.org) is published monthly by Scientific Research Publishing, Inc., USA.

Subscription rates:

Print: $50 per copy.
To subscribe, please contact Journals Subscriptions Department, E-mail: sub@scirp.org

SERVICES

Advertisements
Advertisement Sales Department, E-mail: service@scirp.org

Reprints (minimum quantity 100 copies)
Reprints Co-ordinator, Scientific Research Publishing, Inc., USA.
E-mail: sub@scirp.org

COPYRIGHT

PRODUCTION INFORMATION

For manuscripts that have been accepted for publication, please contact:
E-mail: ns@scirp.org

Vol.2, No.7, 667-680 (2010)
doi:10.4236/ns.2010.27083

Natural Science

Development of extensional stresses in the compressional setting of the Himalayan thrust wedge: inference from numerical modelling

Ganesh Raj Joshi*, Daigoro Hayashi

Simulation Tectonics Laboratory, University of the Ryukyus, Okinawa, Japan; *Corresponding Author: ganeshr_joshi@hotmail.com

Received 16 March 2010; revised 10 May 2010; accepted 15 May 2010.

ABSTRACT

The estimation of contemporary tectonic stress field and deformation in active fold-and-thrust belts are imperative in identifying active geodynamics and resulting faulting phenomenon. In this paper, we focus on contemporary extensional tectonics in the overall compressive setting of the Himalayan orogen. Here we examine the regional tectonic stress field and upper crustal deformation in the Himalayan thrust wedge using a 2D finite element technique, incorporating elastic rheology under plain strain condition. The elastic models demonstrate that the extensional tectonic stress and related normal faulting is extensively developed in the southern front of the Himalaya at shallow crustal level (< 10 km in depth). Our modelling shows a good consistency with the geological field evidences of active faulting, focal mechanism solutions of medium size earthquakes in the several sectors of the Himalaya. Results based on numerical simulation, tectonic analysis and taking geological and geophysical data into account, we interpret that the present-day extensional tectonic activity is not restricted in the southern Tibet but distributed in the different sectors of the Himalayan fold-and-thrust belt co-exist with compressional structures. Modelling results also indicate that the nature, distribution and orientation of the maximum compressive stress (σ_1) of the Himalaya are mainly controlled by the intra crustal Main Himalayan décollement (MHT). The significant amount of shear stress/strain concentration along the MHT in the western Nepal predict that the region is prone to moderate and great future earthquakes.

Keywords: Extensional Stress Field; Convergent Displacement; Finite Element Modelling; Himalayan Wedge

1. INTRODUCTION

The existence of syn-orogenic extension is relatively new discovery, which was described only since the eighties and has received quite a lot of attention in the past two decades. Understanding the mechanisms that produce extensional deformation in contractional orogenic belts is a major issue in the study of the plate continental structure and its dynamics. During the past few decades, extensional deformation structures have been mapped in several contractional orogen such as the eastern Alps [1], Andean Cordillera [2], Southern Apennines [3], Scandinavian Caledonides [4], North American Cordillera [5], and the Himalayan orogen [6-8]. Generally, the normal faults appear to be late stage or post-orogenic structures, while documented cases of syn-orogenic normal faulting are less common, which does not fit readily into the paradigm of plate tectonics [9].

The Himalayan continental collision is formed as a result of collision between Indian and Eurasian landmasses ca 65-40 Ma ago [10]. The dominant structures of the Himalayan chain show a stack of large south-vergent thrust sheets emplaced successively from north to south [11] and bounded by major intra-crustal thrusts. These intra-continental tectonic features, general seismic phenomenon, major folds and other deformation structures indicate the predominantly compressional tectonic regime of the Himalaya. However, lately, a variety of extensional expressions and normal faults have been recognized in the southern Tibet [6,12,13]. Although it is believed that these extensional structures are generally restricted only in the southern Tibet [6,12]; however, recent research has shown that normal faults and other extensional features are not restricted only within southern Tibet but distributed in the several sectors of the Himalaya [14-19]. These extensional features, however, are

not obviously consistent with the dominant seismicity and southward thrusting of the Himalaya. Moreover, the mechanism and the kinematics leading to the formation of orogen-parallel extensional structures are still little understood. Therefore, it is important to understand the cause of ongoing paradoxical extensional tectonic activities in the overall compressive setting of the Himalaya.

Compared to other techniques, numerical modelling is a fast, more economical and powerful tool which allows for various geological structures and deformation phenomenon to be modeled in the full scale. Stress and strain values can be computed over long time periods using various constitutive laws [20]. Thus, numerical models have long been used to develop our understanding of the mechanics of crustal deformation [7,21-24] but most of these studies have been focus on the northern part of the Himalaya and no one describes about the extensional tectonic activities in the Himalayan front.

In this paper, we primarily focus on present-day ongoing extensional tectonics evidences in the southern part of the Himalayan fold-and-thrust belt applying a 2D finite element model (FEM). The final goal of this kind of work is to understand the possible mechanism that responsible for the development of the extensional stress and normal faulting in the overall compressive setting of the Himalaya thrust wedge.

2. TECTONIC SETTING

The Himalayas, one of the most seismo-tectonically active regions of the world, are generally defined as a 2500 km-long arc of mountains stretching between Namche Barwa in the east and Nanga Parbat in the west. The Himalaya can be subdivided into western, central and eastern sectors on the basis of variations in regional geomorphology. This study focuses on the central sector of the Himalayan fold-and-thrust belt, between 76°E and 91°E (**Figure 1**). From the south of the STDS the geological structure and tectonic setting of the fold-and-thrust belt of the Himalayas are mainly characterized by several prominent south-vergent thrust structures. These intra-continental structural features are the Main Central thrust (MCT), Main Boundary thrust (MBT) and the Himalayan Frontal thrust (HFT) from north to south, respectively. These north-dipping thrust faults have a southward transport direction, and are inferred to branch from the décollement thrust known as the Main Himalayan Thrust (MHT), which marks the underthrusting of the Indian lithosphere beneath the Himalaya and Tibet [25]. Several geological cross-sections across the Himalaya as well as seismic and other geophysical data suggest that a crustal ramp is present on the MHT [26,27]. Numerous studies indicating lateral variations in the geometry of the MHT décollement from east to west in the Himalaya [25,28,29]. This lateral disparity of MHT ramp geometry is the main cause for the abrupt change in topographic relief, variation of elastic strain/stress and intense seismic activities of the Himalaya [28,30].

The STDS is an east striking, north dipping system of the normal faults that extends at least 700 km and probably through the entire length of the northern front of the Himalaya orogen, initiated during the Miocene and contemporaneous with the MCT [5,13,21,22]. The MCT is the large-scale high strain zone that commonly occurs along the base of ductile shear zone and inverted metamorphism sequence, which places Tertiary metamorphic rocks of the Great Himalayan sequence over weakly metamorphosed the Precambrain-Paleozoic rocks

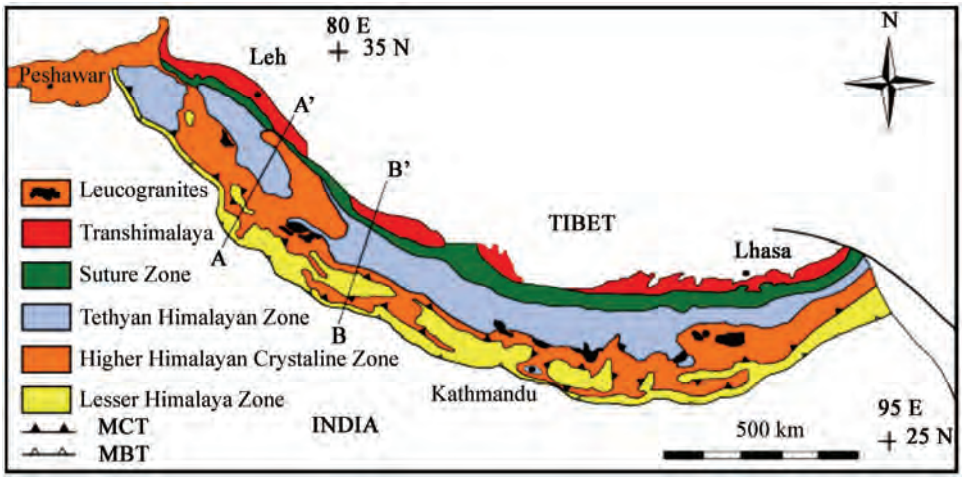

Figure 1. Geological map of the Himalaya showing major structural elements (MBT-Main Boundary Thrust, MCT- Main Central Thrust) (adopted from Lefort, 1988) and tentative locations of regional geological cross-sections lines A-A' and B-B'.

of the Lesser Himalaya [31]. The MBT, a regional-scale sinuous, steeply north-dipping active thrust zone, separates folded and faulted Miocene and younger molasse sediments of the Sub-Himalaya from Precambrian rocks of the Lesser Himalaya [27]. Deformation of the MBT began before 10 Ma [32]. However, several active fault systems are commonly associated with the MBT system, implying significant reactivation along many of its segments [15,33,34]. The MBT shows a down-to-the-north displacement in the central and western sector of the Himalaya [14,15]. The HFT is the southernmost, youngest, non-continuous, NW-SE striking and recently the most active imbricate thrust system in the Himalaya [14,29]. The HFT is a series of thrust faults that separate the Tertiary assemblage of the Sub-Himalaya from Quaternary sediments of the Ganga foreland basin.

3. EVIDENCE FOR AN EXTENSIONAL REGIME AND NORMAL FAULTING

3.1. Geometry and Pattern of Active Normal Faulting

In the overall compressional tectonic regime of the Himalaya, numerous contradictory orogen parallel and perpendicular microscopic to mesoscopic evidences of normal faults are well distributed. There are two main types of normal faults that developed in the Himalayan orogen; the first are the east-west striking, shallowly north-dipping, normal faults of the STDS and Zanskar shear zone which developed during the Early Miocene [8], while the second are relatively active and younger age normal faults which mainly restricted south of the MCT and associated with the mega thrust systems in the Himalayan [14,15,19,33]. In this section, we focus particularly on the evidence for syn-orogenic normal faulting and extensional tectonic structures and their significance are discussed in order to explain ongoing extensional tectonic activity at the overall compressive setting of the Himalaya.

Several normal faults on mesoscopic scale are observed in the Panjal Thrust Zone in the Dalhousie area of western Himachal [16]. Similarly, on the basis of field mapping and shear sense criteria Thakur *et al.* (1995) found that the boundary between the southern margin of the Higher Himalaya Crystalline (HHC) of Zanskar and the Chamba syncline sequence is a normal fault. The NW-SE and NNW-SSE oriented Karcham normal fault (KNF) (**Figure 2**) and the regional scale, steeply south-dipping Bhadarwas normal fault are found in the central Hi machal. Regional scale normal faults are also observed in the Pinjor Thrust Zone in the Lesser Himalaya [16]. In the Kala Amb area, the NE-SW to E-W trending

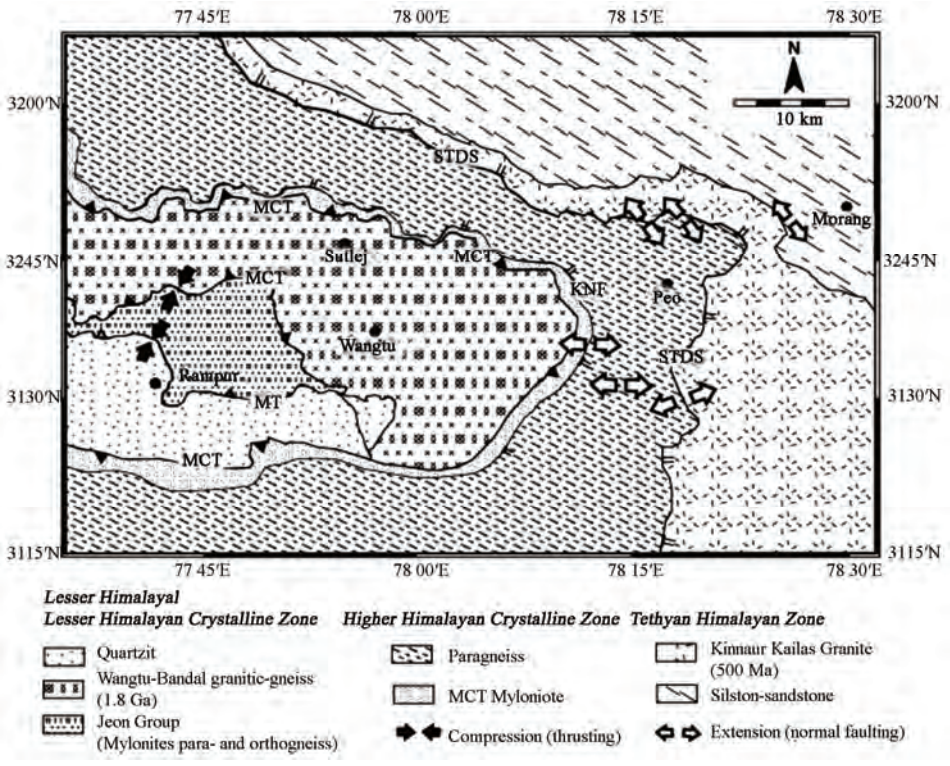

Figure 2. Geological map of the NW-Himalaya showing main faulting regime deduced from the fault-slip analysis adopted from the Vanney *et al.*, 2004.

Singhauli Active fault (SAF) shows normal faulting [35]. Near the southern termination of the SAF, another set of WNW-ESE trending south-side-up normal faults that dip steeply toward the northeast with well-defined fault scarps are observed [19]. In the Garhwal Himalaya, up to 40 km long, E-W to NW-SE trending, northward dipping Donga and Asan normal faults are well developed parallel to the MBT, while the NE-SW trending Kalsi normal fault is perpendicular to the MBT [33]. Similarly, the Surkhet-Ghorahi fault emerges as a single, continuous, steeply-dipping normal fault extends about 90 km long parallel to the MBT system in western Nepal, [15] (**Figure 3**).

3.2. Geomorphologic Features

Geomorphic and morphotectonic analysis of the landform further provide insights into style and pattern of ongoing tectonic deformation. The Himalayan fold-and-thrust belt is characterized by several landforms produced by active tectonics along the mega thrust systems. The field observations in the different parts of centre Himalaya reveal that advancement of large scale lineaments, tilting and shifting of river and piedmont, subsidence of land and older rock sequences, uplift of river terraces and overriding of younger (Holocene) sediments by active thrusts and normal faults noticeably indicate the co-existence of compressional as well as extensional regimes in the Himalaya [19,36,37]. Moreover, the number of places just adjacent to the MBT and HFT, which defines the zone of convergent between Himalaya and Indo-gangetic plains, evidence of active normal faulting occurs [36]. These faulting have produced several topographic and geomorphic features such as active fault traces, lateral offsets of streams, offset of quaternary terraces, linear valleys running along faults and narrow, deep gorges in the Himalayan front [19,36,37], and suggest that the overall compressive setting of the Himalaya front contradictory exhibit extensional tectonic activities in the several parts.

4. FINITE ELEMENT MODELLING

In this paper, a 2D finite element (FE) technique has been used to simulate the present-day tectonic stress field and deformation of the Himalayan orogenic wedge using a software package developed by Hayashi [38]. The important part of the mathematical formulations about the software is provided and successfully applied in previous studies [12,38-40].

4.1. Fault Analysis

It is well-known fact that elastic deformations, even if small, govern the initiation of fault in nature [21]. Faulting observed in nature is in very good agreement with the simulated stress distribution for elastic models [41]. Therefore, elastic models have been considered in studying the development of extensional deformation in the overall compressive setting of the Himalaya. The models assume elastic rheology for the brittle upper crust of the Himalaya. Brittle failure is determined by the Mohr-Coulomb failure criterion, which is based on a linear relation between the shear stress (τ) and the normal stress (σ_n) which can be express by following equation.

$$\tau_{failure} = c + \sigma_n \tan\varphi \quad (1)$$

where, c is the cohesive strength and ϕ is the angle of internal friction. Failure occurs when the Mohr circle first touches the failure envelope. This occurs when the radius of the Mohr circle, $(\sigma_1 - \sigma_3)/2$, is equal to the perpendicular distance from the center of the circle at $(\sigma_1 + \sigma_3)/2$ to the failure envelope which is given by

$$\left(\frac{\sigma_1 - \sigma_3}{2}\right)_{failure} = c\cos\phi + \left(\frac{\sigma_1 + \sigma_3}{2}\right)\sin\phi \quad (2)$$

According to Melosh and William (1998), the prox-

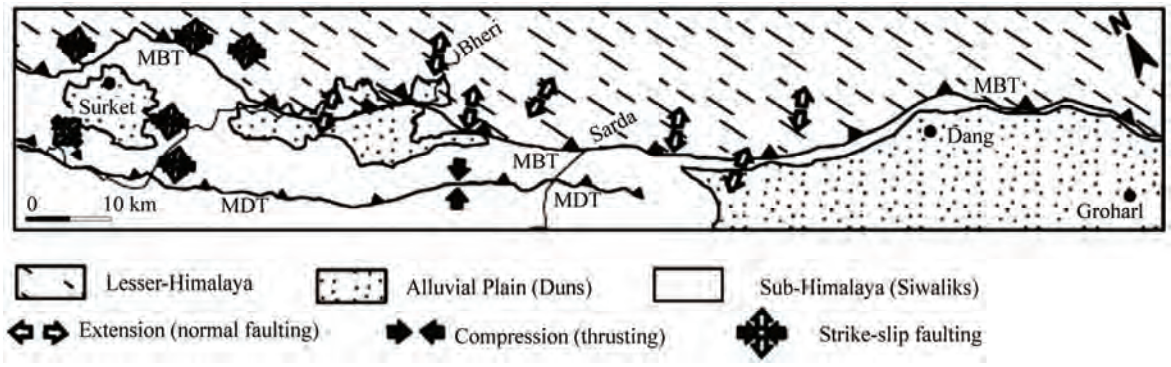

Figure 3. Geological map of the Surkhet-Goarahi fault in the western Nepal Himalaya showing main faulting regime deduced from slickenside analysis adopted from Mugnier *et al.*, 2004.

imity to failure (P_f) is the ratio between the calculated-stress and failure stress can be express by

$$P_f = \left[\frac{\left(\frac{\sigma_1 - \sigma_3}{2} \right)}{\left(\frac{\sigma_1 - \sigma_3}{2} \right)_{failure}} \right] \quad (3)$$

When the ratio reaches $P_f = 1$, failure occurs, but when $P_f < 1$ stress is within the failure envelope rocks does not fail. The proximity to failure reveals which part of the model is close to failure or already failed by generating faults.

4.2. Model Set-Up and Assumptions

We adopted two N-S regional structural cross-sections through the Himachal Himalaya and western Nepal Himalaya for modelling. The NW-Himalaya model extends up to 200 km in length, with a maximum thickness of 40 km in the north, and the western Nepal model is 272 km in length and up to 40 km thick in the northern part (**Figure 4**). The major tectonic units and the approximate locations of the profiles are reported in **Figure 1**. Each cross-section is divided into different layers that represent major structural and lithological units according to their regional setting in the Himalaya. The convergence displacement has been applied, instead of stress and forces because the relative velocity of the Indian plate with respect to Eurasian plate for the central Himalaya is well constrained. The basement fault (MHT) is introduced with a prescribed geometry (**Figure 4**). Studies of the focal mechanism of the large earthquakes in the Himalaya [43] suggest that the MHT dips gently 4° to 9° from south to north [30], which is consistent with the INDEPTH profile [25] and topographic studies of the Himalaya [44]. For simplicity, we adopted dip angles 7°, 5° and 30° for the northern flat, southern flat and the MHT ramp, respectively [30]. Here, only the brittle portion of the MHT is prescribed. In our model, the crust up to 40 km is assumed to behave as an elastic material because of intense seismicity and generate several faults suggest the brittle characteristics of upper crust in the Himalaya.

4.3. Boundary Conditions

The Indian plates moves at N20°E with constant rate of the convergence displacement relative to Eurasia [45], and subducts along a shallow dipping detachment known as the MHT beneath the Himalaya, and it is still continuing [25]. This continuous horizontal displacement caused by convergence of Indian plate has been considered as a prime driving force for the overriding crustal deformation of the Himalayan orogen. Therefore, simulation of the observed tectonic features of the Himalaya using appropriate boundary condition could be modeled by applying a horizontal convergence displacement from the southern face of the model with present-day shorting rate of the central Himalaya. Since the rate of displace-

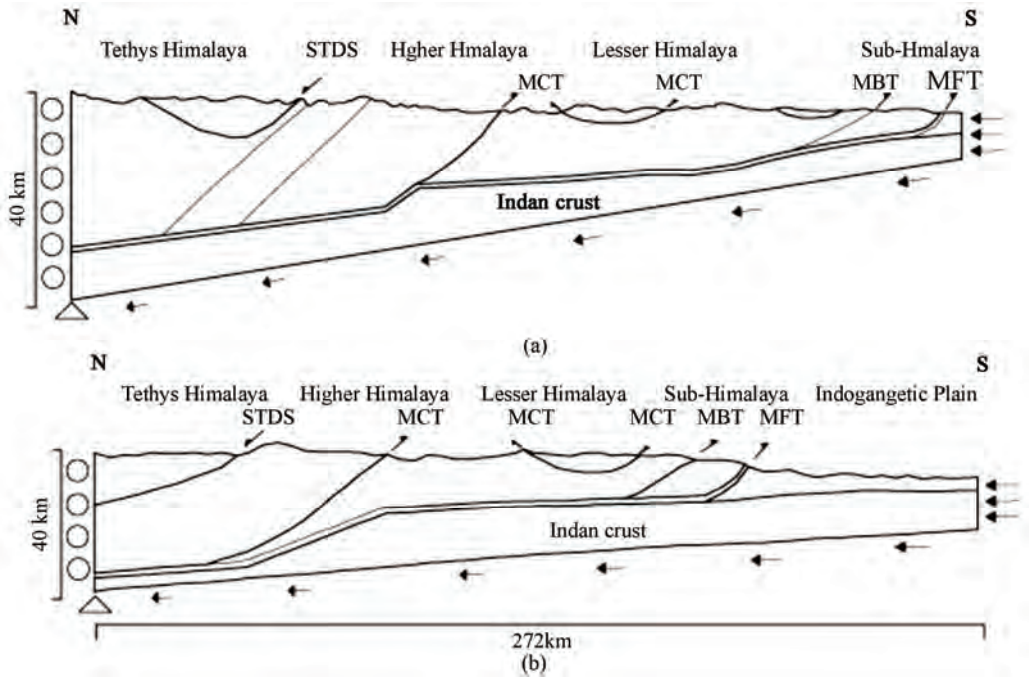

Figure 4. Simplified geological cross-sections and applied boundary conditions adopted for the modeling. (a) NW-Himalaya cross-section along A-A' and (b) western Nepal cross-section along B-B' in **Figure 1**.

ment is varied in the different part of the Himalaya [44,46] the uniform horizontal displacement rate of 17 mm/yr for the NW-Himalaya and 20 mm/yr for the western Nepal have been adopted. These convergence rates are well consistent with GPS measurements [44,46] and long-term geological observations [47,48] along the Himalayan front. **Figure 4** shows the geometry and applied boundary conditions of our FE models based on present-day tectonic setting and kinematics of the Himalayan thrust wedge. The upper part of the entire model represents surface topography which is free to deform in all directions. The northern side of the model only can move vertically. The lowermost nodal point marked by a triangle is fixed. Since the lower boundary of the model is inclined, the convergence displacement is resolved into both x and y directions (**Figure 4**). The model is loaded with gravitational body force (g = 9.8 m/s).

4.4. Model Parameters

The model consists of eight layers, which represent distinct litho-tectonic sequences of the Himalayan wedge. Each rock sequence has been assigned with distinct rock layer properties on the basis of predominant rock types as shown in **Figure 5**. The crustal density was obtained from published gravity-seismic model [47]. Since the density of the rock layers of the individual tectonic blocks are known, we obtained seismic P-wave (V_p) and S-wave (V_s) velocities for the each rock layer from the velocity models [28,50]. In order to solve elastic equations, we need to know the independent elastic constants Young's modulus of elasticity (E) and Poisson's ratio (υ) where Poisson's ratio is assumed to be constant at 0.25 for individual tectonic blocks. E can be calculated by [37,49]:

$$E = \rho V_p^2 \frac{(1+v)(1-2v)}{(1-v)} \quad (4)$$

Other input parameters required for modelling include the angle of internal friction (ϕ) and the cohesive strength (c) which obtained from the handbook of physical constants [53].

5. MODELLING RESULTS

The series of numerical experiments were conducted for the two representative structural cross-sections of the Himalaya. Here, we present new evidence for extensional stresses and normal faulting in the several sectors of the Himalayan shallow crust. The results presented herein are based on: 1) the distribution, orientation and the magnitude of the principal stresses, 2) proximity of failure and 3) the magnitude of the shear stress and strain.

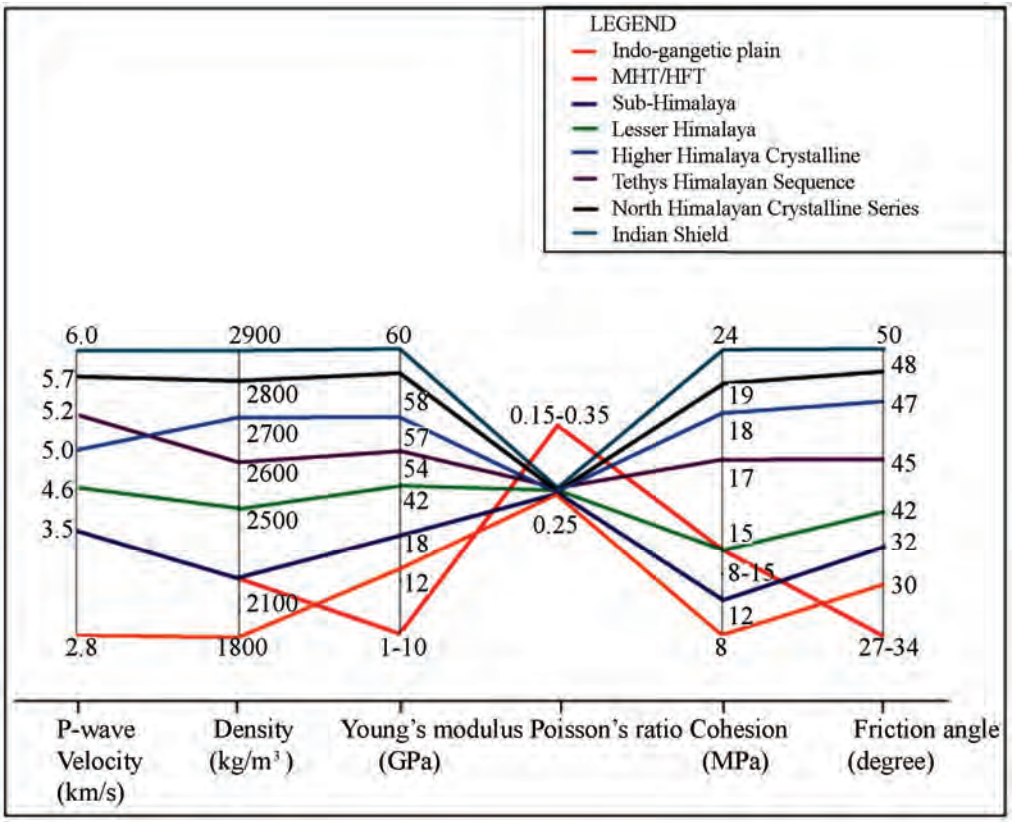

Figure 5. Physical parameters and material properties of the different rock units used for modelling.

5.1. Stress Distribution

Figures 6 and **7** show the spatial distribution of the simulated stress field developed for the different horizontal convergent displacement conditions in both NW-Himalaya and western Nepal models. The principal axis of maximum compressive stress (σ_1) and and minimum compressive stress (σ_3) are aligned in the horizontal and vertical lines, respectively. Notice that if σ_1 aligned in the horizontal and σ_3 aligned vertically represent compressional stress regime, while the orientation of σ_1 is vertical and σ_3 is horizontal together with the tensional component (red bar) implying extensional tectonic state of stress. The overall simulated stress pattern shows two distinct types of the characteristic stress field developed in the Himalayan crustal wedge. The most compressive stress regime found in the northern part, while an extensional stress develops in the southern front of the Himalaya at shallow (< 10 in km) crustal level. However, when increase the convergent displacement up to 500 m the principal axis of stress are considerably tilted and finally rotated from the original coordinate axis and the deformation front shifts progressively toward the southern front of the Himalaya (**Figures 6(c)** and **7(c)**).

It is noteworthy that the change in stress field and progression of deformation shows the thrust faults have migrated from hinterland to foreland and the stress field changes from extensional to a compressional regime. In general, the predicted stress field on the Himalayan upper crust shows almost similar and uniform pattern in both models, while some discrepancy also observed in the northern part of Himalaya. In the NW-Himalaya model (**Figure 6**), the extensional stress field is restricted more northern part of the Himalaya whereas in the western Nepal model (**Figure 7**), extensional stress regime only developed south from the MCT. The stress is uniformly distributed throughout the Indian crust. Nevertheless, magnitudes of the principal stresses have increases with depth because of topographic loading.

5.2. Maximum Shear Stress Distribution

Figure 8 shows the distribution of maximum shear stress predicted from our modelling within the Himalayan upper crustal wedge.

The computed maximum shear stress (τ_{max}) revealed

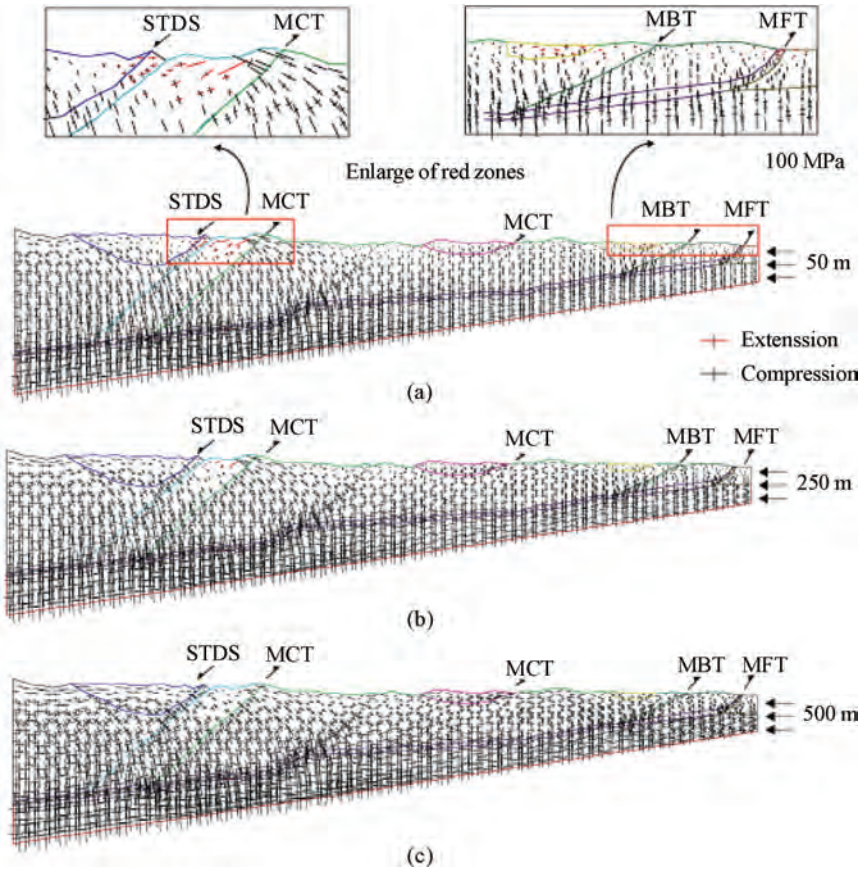

Figure 6. Predicted stress distribution in the NW-Himalaya model applying uniform convergence displacements: (a) at 50 m; (b) at 250 m; (c) at 500 m.

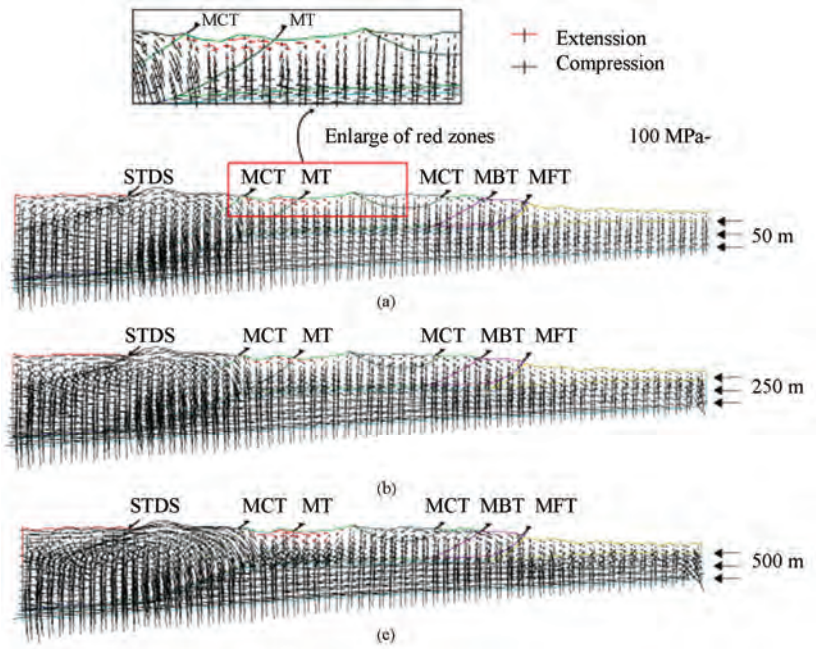

Figure 7. Predicted stress distribution in the western Nepal model applying uniform convergence displacements: (a) at 50 m; (b) at 250 m; (c) at 500 m.

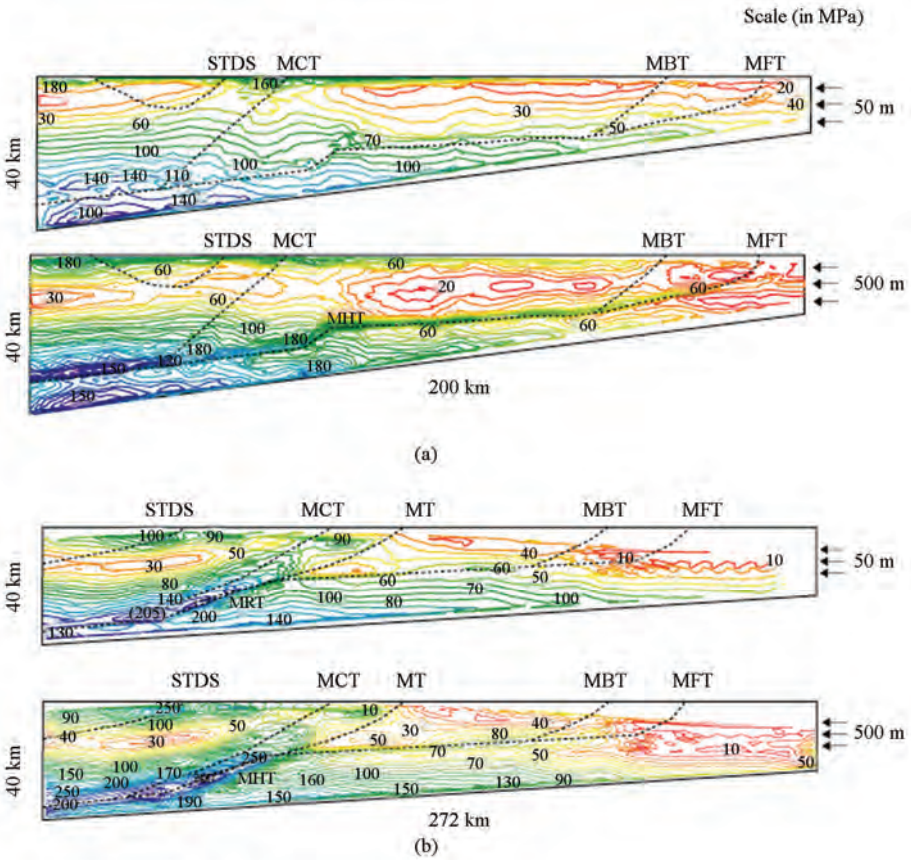

Figure 8. Predicted maximum shear stress (in MPa) distribution for (a) NW-Himalaya model and (b) western Nepal model, at 50 m and 500 m convergent displacement conditions, respectively.

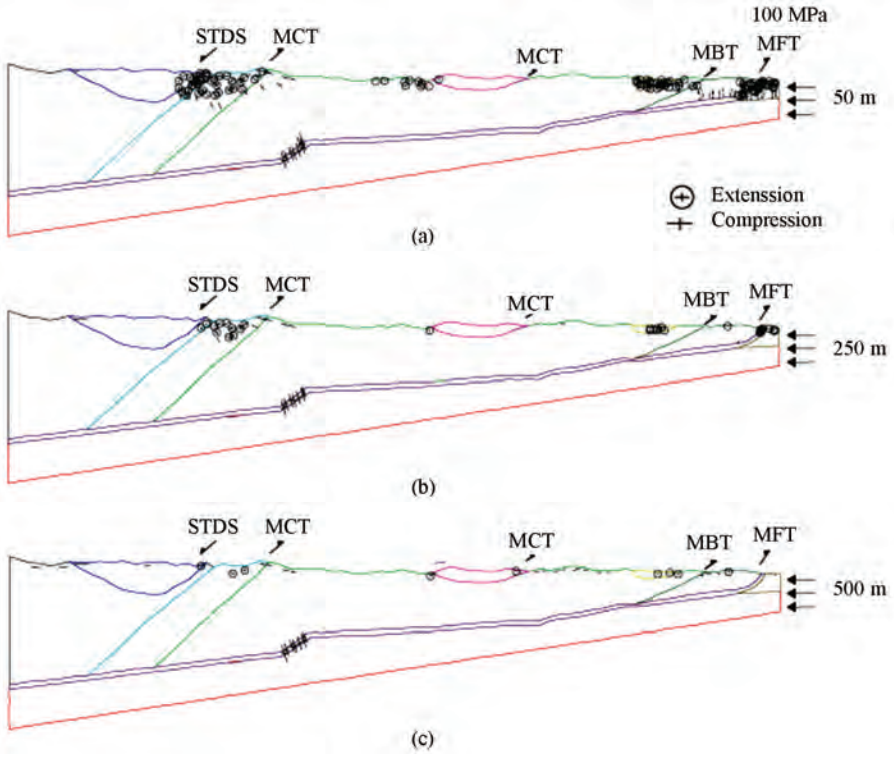

Figure 9. Predicted faulting elements in the NW-Himalaya model by imposing. (a) at 50 m; (b) at 250 m and (c) at 500 m convergent displacements.

that the major concentration of τ_{max} along the Himalayan basal décollement (MHT) zone. The trajectories of (τ_{max}) along the MHT increases from the southernmost part and reach a maximum to the northern flat of the MHT ramp in both models. Our model shows that the maximum shear stress (τ_{max}) levels of 250 MPa and 300 MPa from NW-Himalaya model and western Nepal model, respectively (**Figure 8**). This result suggests that the Himalaya has continually built up significant amounts of stress along the MHT décollement.

5.3. Faulting Patterns

We also examined the faulting pattern in the Himalayan brittle upper crust based on the proximity of failure. The Mohr-Coulomb failure criterion is used to determine the faulting conditions. Because in the faulting regimes σ_1 and σ_2 are nearly vertical and horizontal, the types of faulting can be easily determined using the method of Anderson [54]. **Figures 9** and **10** illustrate the predicted faulting pattern for both the NW-Himalaya and western Nepal models. In general, both models demonstrate similar patterns of fault development under different horizontal convergence displacement conditions. Normally, our models clearly show two distinct types of faulting patterns in the Himalayan wedge where thrust faults are primarily concentrated in the north part (hinterland) and normal faults are extensively developed at the southern front (foreland) of the Himalaya. **Figure 9** shows failure pattern in the NW-Himalaya models from 50 to 500 m convergence displacement conditions. At 50 m horizontal convergent displacement, the modelling results show that normal faults have predicted within the Higher Himalaya, central and southernmost Lesser Himalaya and Siwalik front, while thrust faults are primarily predicted north of the MCT and in and around the MHT ramp in the Higher Himalaya. Small open circle indicates normal and pair of perpendicular lines represents thrust faults, respectively. Nonetheless, when the applied displacement gradually increases up to 500 m, normal faults reduces considerably and thrust faults were developed in such region and progressively migrated towards the foreland. **Figure 10** illustrates the distribution of predicted failure elements in the western Nepal model. This model shows noticeably more failure elements compared with the NW-Himalaya model. In this model, normal faults are mostly developed in the northern part of the Lesser Himalaya and the Siwalik area, where the juxtaposition of normal and thrust faulting along the ramp part of the MHT décollement is well developed at low convergent displacement (**Figure 10(a)**).

6. DISCUSSION

Previous studies illustrate that using an elastic models are appropriate to obtain the tectonic stress field and deformation of the brittle upper crust [7,21]. Although several models have been proposed to explain the extensional state of stress and formation of the normal faults in the southern Tibet and Himalaya [7,21,22,41], but none of them explain the development of extensional stress regime and normal faults in the Himalayan front. Here, we have presented a series of experiments using 2D finite element elastic models to examine the present-day tectonic state of stress and deformation in the Himalayan upper crustal wedge. For better understanding the basic mechanism of the extensional tectonics of the overall compressive tectonic setting of the Himalayan thrust wedge we have kept the models relatively simple, and limited the model. We prescribed convergence displacement boundary conditions consistent with the contemporary plate kinematics of the central Himalaya region. We further assumed that the Himalayan upper crust behaves elastic in order to model faulting pattern of the region. Some factors are not incorporated in the current models are potentially important in the convergent tectonic belts. For example, we did not consider the effect of erosion at the surface of the Himalayan thrust wedge. However, most of syn-orogenic erosion process controls the dynamics of the orogenic wedge [55]. Despite the simplicity of the model our results may provide useful insight into extensional tectonics in the overall contractional setting of the Himalaya.

6.1. Present-Day Stress Distribution in the Central Himalaya

The distribution of the present-day stress field can provide a significant explanation for the ongoing geodynamics and tectonic forces acting in the India-Asia collision zone. Since the convergence rate of Indian plate has been decreasing ca 40 Ma [56], the Himalayan stress field would show consequence changes in overall compressive regime of the Himalaya. Nakata *et al.* [57], argue that the direction of the horizontal compressive stress axis has changed due to changes in the direction of the relative plate motion between the Indian plate and tectonic sliver. Our modelling results also support this idea and show two types of stresses developed in the Himalayan upper crustal wedge. The compressional stresses regime predicted in the northern part while extension stress regime predicted in the southern front. These stresses further retained at all convergence displacement conditions (**Figures 6** and **7**). Although predicted extensional stresses developed in the Himalayan front are obviously not consistent with major seismic events and dominant southward thrusting of the overall compressive setting of the Himalaya, but well corresponding with the field observations of active faulting in the several sector of Himalayan thrust wedge [14-16, 19,34], neotectonic model of Nakata [57], and focal mechanism of solutions of medium size earthquakes (**Figure 11**). Taking advantage from predicted extensional stress regime from our models, it can be inferred that the recent changes in compressional tectonic regime locally in the several part of the Himalayan front. Although we strongly believed that the entire orogen is still in overall compression, the predicted extensional stress regime and observed normal faults in the Himalayan frontal part are mainly due to local adjustment of tectonics regime due to the taper angle readjustment and weak Himalayan décollement. The computed stress fields

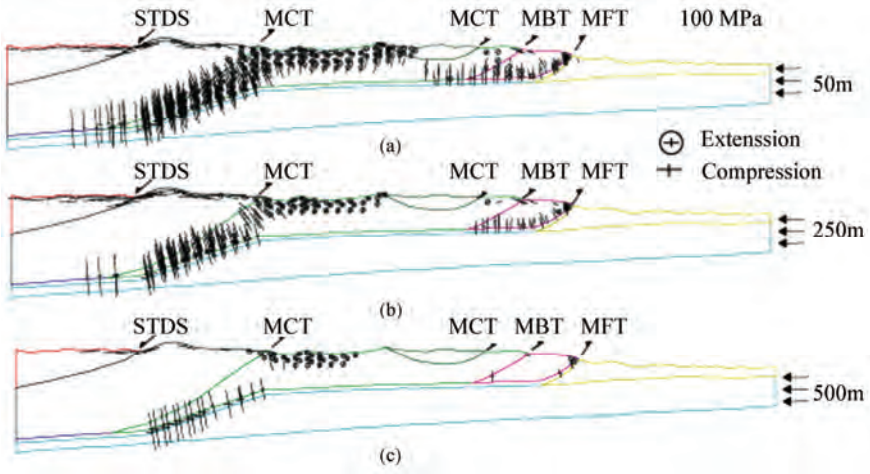

Figure 10. Predicted faulting elements in the western Nepal model by imposing different convergent displace- ment conditions for (a) at 50 m; (b) at 250 m; (c) at 500 m convergent displacements.

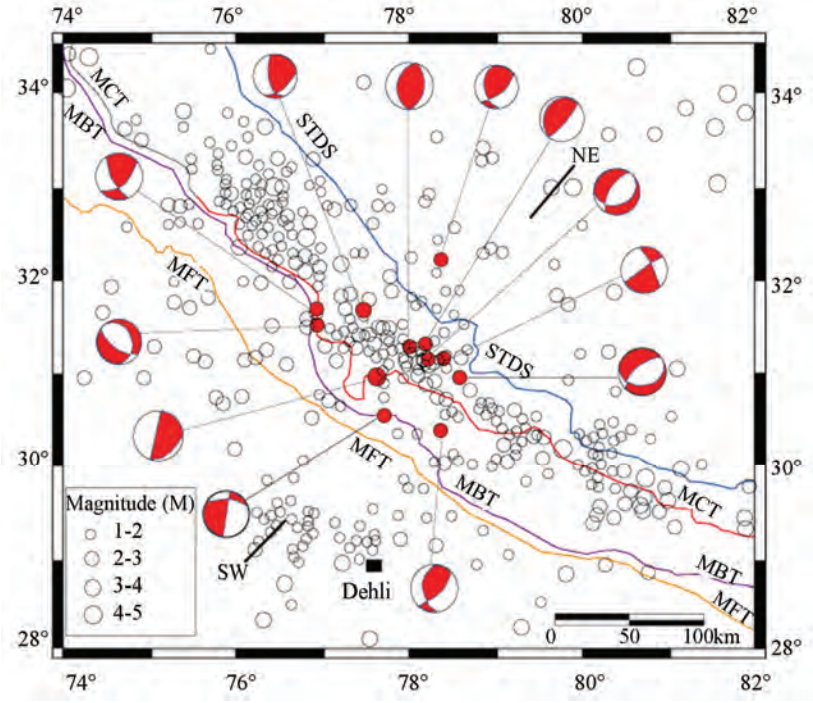

Figure 11. Focal mechanism of solutions of medium size earthquakes in NW-Himalaya adopted after Yadav *et al.* (2009).

show significant deflection and rotation of the maximum compressive stress (σ_1) from their original horizontal position to vertical when increase the compressive displacement (**Figure 7**). The predicated rotation of the stress trajectories might be the effect of ramp geometry of the MHT décollement, and consistent with the seismic study of Pandey *et al*. [28]. In which they demonstrated that the MHT ramp acts as a geometrical barrier to changes in the orientation of the maximum principal stress in the Himalaya, causing the significant change in the stress field of the Himalaya. Nonetheless, Mugnier *et al*. [15] argued that if the principal stress axis deviates significantly from the horizontal, and when this deviation exceeds the dip of the vectors normal to back-tilting thrusts, the normal component of displacement may act along these faults; therefore, steep north-dipping segments of the MBT show a normal component of displacement. The rotation of the stress trajectories would facilitate the formation of imbricated thrust in the moving thrust sheet. In both models, thrusts are propagated towards the foreland of the Himalayan wedge as we increase the convergent displacement (**Figures 6** and **7**). This is characteristic feature of thrust propagation in fold-and-thrust belts, and consistence with fold-bend-fault model of Yeats and Thakur (1998) [51].

6.2. Magnitude of the Stresses in Central Himalaya

Our models predicate the horizontal stress level of 300-500 MPa at the depth of 40 km of the Indian lithosphere which is consistent with other studies [58,59]. The region with high maximum shear stress (τ_{max}) induced will be more active [60]. If we compare both of our models; the western Nepal model shows considerable amount of maximum shear stress (300 MPa) accumulated along the MHT décollement suggests that possible major earthquake in the region due to the reactivation of the basal décollement of this part of the Himalaya. This prediction is further supported by the concentration of microseismic clusters in and around ramping part of the MHT [28], consistent with the numerical simulations [30] and GPS measurements [46].

6.3. Development of Faulting Pattern in the Central Himalaya

The computed results from our model predicted two types of characteristic faulting patterns developed in the Himalayan thrust wedge. In general, thrust faults are predicted in the northern Himalaya (north of MCT) while normal faults are predominantly predicted in the southern front of Himalaya for all 50 m to 500 m convergent displacements (**Figures 9** and **10**). According to Mugnier *et al*. [15] normal faults that are associated with the Himalayan major thrust structures in the frontal part of Himalaya (e.g., normal fault along the MBT) is due to a very poor strength contrast between the basal décollement and rock in wedge body and high pore fluid pres-

sure ratios (up to 1). They further argued that the outer Himalaya extends over the width of several tens of kilometers in the central sector of Himalaya, and are presumably displaced along a décollement located in pelitic formations. There is therefore a small contrast of strength between rocks in the décollement levels and displaced sheets, a condition that favors normal faulting in the region [15]. However, Nakata *et al*. [57] argued that the Lesser Himalayan block is subsiding, causing normal faulting due to a change in tectonic regime of the Himalaya. From computer simulation Shankar *et al.* [22] proposed that the presence of a weak MHT décollement below south Tibet is the main cause of extension in the Himalaya. Our modelling results shows that the Himalayan décollement thrust (MHT) have significant role to the development of extensional state of stress and normal faulting in the Himalayan front. We believed that the formation of ramp geometry on the MHT décollement is the major causes of the development of extensional stress and normal faulting in the various part of the Himalaya fold-and-thrust belt. Moreover, we suggest that the local adjustment of the tectonic activities influenced by taper angle adjustment further influences to the formation of the extensional tectonic activities and normal faulting in the overall contractional setting of the Himalaya.

6.4. Comparison with Field Observations

Since our models were constrained by present-day structural sections of the Himalaya, the predicted stress regime and faulting pattern from our models can be directly compared with field observations. The simulated faulting pattern appropriately corresponds to the natural situation of the Himalaya and several faults are computed at analogous locations, which show good agreement with the position of normal faults and the extensional regime across the Himalayan thrust wedge. The stress fields and faulting pattern predicted from our model is well consistent with field observations of previous studies [13-19,22,26,37]. Our modelling results further support the formation of extension stress field and normal faulting mainly dominated in the frontal part of the Himalayan thrust wedge.

In addition, if we compare out numerical experiment results with the observations of the microseismicity and medium size earthquake focal mechanism solutions of the Himalayan front our result shows good consistency (**Figure 11**).

7. CONCLUSIONS

In this paper, the 2D finite element modelling was used to simulate the present-day extensional tectonic state of stresses and deformation in the overall compressional setting of the Himalayan brittle upper crust incorporated an elastic rheology under plain strain condition. Based on our modelling results, compared with geological field observations, records of active normal faults and the in situ stress regime, we conclude that the extensional tectonic regime and normal faulting of the Himalaya is not only restricted within the southern Tibet but distributed throughout the Himalayan thrust wedge as observed in field. Modelling results further indicate that the extensional tectonic deformation in the brittle upper crust of the Himalayan thrust wedge is still active; although the overall tectonic setting of the Himalaya is in compression. Our results show that the MHT décollement plays a pivotal role in changing the tectonic stress field and faulting regime in the Himalayan thrust wedge, and accumulating significant amount of stress/strain along the ramp part. This continuous process of the stress/strain accumulation along the MHT décollement triggers intense microseismic activities, and increases the risk of the future great earthquake in the central Himalayan region.

8. ACKNOWLEDGEMENTS

The Ministry of Education, Culture, Science and Technology (Monbukagakusho) of Japan is acknowledged for the financial support of the first author. The authors are thankful to Prof. Laurent Godin, Dawn Kellett and P. Mandal for their valuable comments and suggestions, which greatly helped to improve the earlier version of the manuscript.

REFERENCES

[1] Ratschbacher, L., Frisch, W., Neubauer, F., Schmid, S.M. and Neugebauer, J. (1989) Extension in compressional orogenic belt: The eastern Alps, *Geology*, **17(5)**, 404-407.

[2] Corredor, F. (2003) Eastward extend of the late eocene-early oligocene onset of deformation across the northern Andes: constraints from the northern portion of the Eastern Cordillera fold belt, Colombia. *Journal of South American Earth Sciences*, **16(6)**, 445-457.

[3] Caiazzo, C., Ascione, A. and Cinque, A. (2006) Late tertiary-quaternary tectonics of the southern-apennines (Italy): New evidences from the Tyrrhenian slop. T*ectonophysics*, **421(1-2)**, 23-51.

[4] Norton, M. (1986) Late Caladonian extension in western Norway: A response to extreme crustal thickening. *Tectonics*, **5(2)**, 192-204.

[5] Hodges, K.V. and Walker, J.D. (1992) Extension in the cretaceous Sevier Oroben, North American Cordillera. *Geology*, **104(5)**, 560-569.

[6] Burg, J.P., Brunel, M., Gapais, D., Chen, G.M. and Liu, G.H. (1984) Deformation of leucogranites of the crystalline main central thrust sheet in southern Tibet (China). *Journal of Structural Geology*, **6**, 219-223.

[7] Royden, L.H. and Burchfiel, B.C. (1987) Thin skinned N-S extension within the convergence Himalayan region; Gravitational collapse of a Miocene topographic front. In: *Continental Extensional Tectonics*, Croward, M.P., Dewey, J.F. and Hanback, P.L., Eds., *Geological Society London*, **26(5-6)**, 611-619.

[8] Hodges, K.V., Parrish, R., Housh, T., Lux, D., Burchfiel, B.C., Royden, L. and Chan, Z. (1992) Simultaneous Miocene extension and shortening in the Himalayan origin. *Science*, **258(5087)**, 1466-1470.

[9] Gansser, A. (1964) Geology of the Himalayas. Wiley Inter-Science, New York, 289.

[10] Molnar, P. and Lyon-Caen, H. (1988) Some simple physical aspects of the support, structure, and evolution of mountain belts. In: Clark, S., Burchfiel, B.C. and Suppe, J., Eds., *Processes in Continental Lithospheric Deformation, Geological Society of America Special Paper*, **218**, 179-207.

[11] Le Fort, P. (1975) Himalayas, the collided range: Present knowledge of the continental arc. *American Journal of Science*, **275(A)**, 1-44.

[12] Joshi G.R. and Hayashi, D. (2008b). Numerical modelling of neotectonic movements and state of stresses in the central Seismic Gap region, Garhwal Himalaya. *Journal of Mountain Science*, **5(4)**, 279-298.

[13] Hodges, K., Bowring, S., Davidek, K., David Hawkins, D. and Krol, M. (1998) Evidence for rapid displacement on Himalayan normal faults and the importance of tectonic denudation in the evolution of mountain ranges. *Geology*, **26(6)**, 483-486.

[14] Nakata, T. (1989) Active faults of Himalaya of India and Nepal. *Geological Society of America*, **332(1)**, 243-264.

[15] Mugnier, J.-L., Huyghe, P., Chalaron, E. and Mascle, G. (1994) Recent movements along the main boundary thrust of the Himalayas: Normal faulting in an over-critical thrust wedge? *Tectonophysics*, **238(1-4)**, 199-215.

[16] Thakur, V.C., Rautela, P. and Jafaruddin, M. (1995) Normal faults in pinjor thrust zone in Lesser Himalaya and between the higher Himalaya Crystallines and Chamba sequence in Kashmir Himalaya, India. *Earth Planetary Science*, **104(3)**, 499-508.

[17] Vanney, J., Grasemann, B., Rahn, M., Frank, W., Carter, A., Baudraz, V. and Cosca, M. (2004) Miocene to Holocene exhumation of metamorphic crustal wedges in the NW Himalaya: Evidence for tectonic extrusion coupled to fluvial erosion. *Tectonics*, **23(1)**, 1-24.

[18] Vanney, J. and Grasemann, B. (2001) Himalayan inverted metamorphism and syn-convergence extension as a consequence of a general shear extrusion. *Geological Magazine*, **138(3)**, 253-276.

[19] Philips, G. and Virdi, N.S. (2006) Co-existing compressional and extensional regiems along the Himalayan front vis-à-vis active fault near Singhauli, Haryana, India; Active faults and neotectonic activity in the Panjour Dun, Northwestern Frontal Himalaya. *Current Science*, **90(9)**, 1267-1271.

[20] Vanbrabant, Y, Jongmans, D., Hassani, R. and Bellono, D. (1999) An application of two-dimensitional finite-element modelling for studying the deformation of the Vriscan fold-and-thrust belt (Belgium). *Tectonophysics*, **309(1-4)**, 141-159.

[21] Yin, A. (1993) Mechanics of wedge shaped fault blocks an elstic solution for compressional wedge. *Journal of Geophysical Research*, **98(B8)**, 14245-14256.

[22] Shankar, D., Kapur, N. and Singh, B. (2002) Thrust-wedge mechanics and coeval development of normal and reverse faults in the Himalayas. *Journal of Geological Society*, **137(1)**, 1-34.

[23] Beaumont, C., Jamieson, R.A., Nguyen, M.H. and Lee, B. (2001) Himalayan tectonics explained by extrusion of a low-viscosity crustal channel coupled to focus surface denudation. *Nature*, **414(6865)**, 738-742.

[24] Jamieson, R.A., Beaumont, C., Medvedev, S. and Nguyen, M.H. (2004) Crustal channel flows: Numerical models with implications for metamorphism in the Himalayan-Tibetan Orogen. *Journal of Geophysical Research*, **109(B06407)**, 1-24.

[25] Zhao, W., Nelson, K.D. and Team, P.I. (1993) Deep seismic reflection evidence for continental underthrusting beneath southern Tibet. *Nature*, **366(6455)**, 557-559.

[26] Schelling, D. and Arita, K. (1991) Thrust tectonics, crustal shortening and the structure of the far eastern Nepal Himalaya. *Tectonics*, **10(5)**, 851-862.

[27] Srivastava, P. and Mitra, G. (1994) Thrust geometries and deep structure of the outer and inner Lesser Himalaya, Kumaun and Garhwal (India): Implications for evolution of the Himalayan fold-and-thrust belt. *Tectonics*, **13(1)**, 89-109.

[28] Pandey, M.R., Tandukar, R.P., Avouac, J.P., Leve, J. and Massot, P. (1995) Interseismic stress accumulation on the Himalayan crustal ramp (Nepal). *Geophysical Research Letter*, **22(16)**, 751-754.

[29] Yeats, R.S., Nakata, T., Farah, A., Fort, M., Miza, M.A., Pandey, M.R. and Stein, R.S. (1992) The Himalayan frontal fault system. *Annales Tectonicas*, **6(Suppl.)**, 85-98.

[30] Berger, A., Jouanne, F., Hassani, R.D. and Mugnier, J.L. (2004) Modelling the spatial distribution of the present-day deformation in Nepal: How cylindrical is the main Himalayan thrust in Nepal? *Geophysical Journal International*, **156(1)**, 94-114.

[31] Searle, M.P., Law, R.D., Godin, L., Larson, K.P., Streule, M.J., Cottle, J.M. and Jessup, M.J. (2008) Defining the Himalayan main central thrust in Nepal. *Journal of the Geological Society*, **165(2)**, 523-534.

[32] Meigs, A.J., Douglas, W., Burbank, B. and Beck, A.B. (1995) Middle-late Miocene (> 10 Ma) formation of the main boundary thrust in the western Himalaya. *Geology*, **23(5)**, 423-426.

[33] Valdiya, K.S. (2001) Reactivation of terrene-defining boundary thrusts in central sector of the Himalaya: Implications. *Current Science*, **81(11)**, 1418-1431.

[34] Malik, J.N. and Nakata, T. (2003) Active faults and related late quaternary deformation along the Northwestern Himalayan Frontal zone, India. *Analysis of Geophysics*, **46(5)**, 917-936.

[35] Kumar, S., Wesnousky, W.S., Rockwell, T.K., Ragona, D., Thakur, V.C. and Seitz, G. (2001) Earthquake recurrence and rupture dynamics of the Himalayan Frontal thrust, India. *Science*, **294(5550)**, 2328-2331.

[36] Philip, G. and Sah, M.P. (1999) Geomorphic Signatures for active tectonics in the Trans Yamuna segment of the western Doon Valley, NW Himalaya. *International Journal of Applied Earth Observation and Geoinforma-*

tion, **1(1)**, 54-63.
[37] Malik, J.N. and Mohanty, C. (2007) Active tectonic influence on the evolution of drainage and landscape: Geomorphic signatures from frontal and hinterland areas along the Northern Himalaya, India. *Journal of Asian Earth Sciences*, **29(5-6)**, 604-618.
[38] Hayashi, D. (2008) Theoretical basis of FE simulation software package. *Bulletin Faculty of Science University of the Ryukyus*, **85(3)**, 81-95.
[39] Joshi G.R. and Hayashi D. (2008) Neotectonic deformation and shortening along the Himalayan front in the Garhwal region by finite element modelling. *Bullettino di Geofisica Teorica ed Applicacate*, **49(Suppl.2)**, 228-233.
[40] Joshi G.R. and Hayashi, D. (2010). Finite element modelling of the pull-apart formation: Implication for tectonics of Bengo Co pull-apart basin, Southern Tibet. *Natural Science*, **2(6)**, 654-666.
[41] Wang, K., He, J. and Devis, E.E. (1997) Transform puss, oblique subduction resistance, and intraplate stress of the Juan de Fuca plate. *Journal of Geophysical Research*, **102(B1)**, 661-674.
[42] Melosh, F.J. and Williams, C.A. (1989) Mechanics of graben formation in crustal rocks: A Finite element analysis. *Journal of Geophysical Research*, **94(B10)**, 13961-13973.
[43] Ni, J. and Barazangi, M. (1984) Seismotectonics of the Himalayan collision zone; Geometry of the underthrusting Indian plate beneath the Himalaya. *Journal of Geophysical Research*, **89(B8)**, 1147-1163.
[44] Bilham, R., Larson, K., Freymueller, J., *et al.* (1997) GPS measurements of present-day convergence across the Nepal Himalaya. *Nature*, **386(6620)**, 61-64.
[45] DeMets, C., Gordon, R.G., Argus, D.F. and Stein, S. (1994) Effect of recent revisions to the geomagnetic reversal time scale on estimates of current plate motions. *Geophysical Research Letter*, **21(20)**, 2191-2194.
[46] Banerjee, P. and Bürgmann, R. (2002) Convergence across the northwestern Himalaya from GPS measurements. *Geophysical Research Letters*, **29(20)**, 30-34.
[47] Wesnousky G.S., Kumar, S., Mohindra, R. and Thakur, V.C. (1999) Uplift and convergence along the Himalayan frontal thrust of India. *Tectonics*, **18(6)**, 967-976.
[48] Lave, J. and Avouac, J.P. (2000) Active folding of fluvial terraces across the Siwalik Hills, Himalayas of Central Nepal. *Journal of Geophysical Research*, **105(B3)**, 5735-5770.
[49] Hetényi, G., Cattin, R., Brunet, F., Bollinger, L., VergenJone, J., Nábělek, L. and Diament, M. (2007) Density distribution of the India plate beneath the Tibetan plateau: Geophysical and petrological constraints on the kinetics of lower-crustal eclogitization. *Earth and Planetary Science Letter*, **264(1-2)**, 226-244.
[50] Cotton, F., Compillo, M., Deschamps, A. and Rastogi, B. K. (1996) Rupture history and seismotectonics of the 1991 Uttarkashi, Himalaya earthquake. *Tectonophysics*, **258(1-4)**, 35-51.
[51] Yeats, R. and Thakur, V.C. (1998) Reassessment of earthquake hazard based on a fault-bend-fold model of the Himalayan plate-boundary fault. *Current Science*, **74(3)**, 230-233.
[52] Timoshenko, S.P. and Goodier, J.N. (1970) *Theory of Elasticity*, McGraw-Hill Book Company, 3rd Edition, London, 567-588.
[53] Clark, S.P., Jr., Ed. (1966) *Handbook of Physical Constants*, *Geological Society America*, Memoir, **97**, 587.
[54] Anderson, E.M. (1951) The dynamics of faulting and dike formation with application to Britain. *Oliver and Boyd*, 2nd Edition, Edinburgh, 133-147.
[55] Dahlen, F.A. and Suppe, J. (1988) Mechanics, growth and erosion of mountain belts. *Processes in Continental Lithospheric Deformation, Geological Society of America*, **218(1-2)**, 161-178.
[56] Patrait, M.R. and Achache, J. (1984) India-Eurasia collision chronology and its implications for crustal shortening and driving mechanisms of the plates. *Nature*, **311(18)**, 615-621.
[57] Nakata, T., Otsuki, K. and Khan, S.H. (1990) Active faults, stress field and plate motion along the Indo-Eurasian plate boundary. *Tectonophysics*, **181(1-4)**, 83-95.
[58] Wills, S. and Buck, W.R. (1997) Stress field rotation and rooted detachment faults: A coulomb failure analysis. *Journal of Geophysical Research*, **102(B9)**, 20503-20514.

Vol.2, No.7, 681-687 (2010)
doi:10.4236/ns.2010.27084

Natural Science

Impacts of oasis on the atmospheric hydrological cycle over the nearby desert

Qiang Zhang[1,2,3*], Yuhe Nan[2], Sheng Wang[1,3]

[1]Key Laboratory of Arid Climatic Changes and Disaster Reduction of Gansu Province, Institute of Arid Meteorology, China Meteorological Administration, Lan Zhou, China; *Corresponding Author: qzhang@ns.lzb.ac.cn
[2]College of Atmospheric Science, Lan Zhou University, Lan Zhou, China
[3]Meteorological Bureau of Gansu Province, Lan Zhou, China

Received 22 February 2010; revised 23 April 2010; accepted 28 April 2010.

ABSTRACT

Using the data of "A field experiment on land-atmosphere interaction over arid region in Northwest China" carried out in Dunhuang of Gansu Province from May to June 2000; Characteristics of the atmospheric humidity over desert and Gobi near oasis in the Northwest China Arid Region are analyzed. According to the difference of the characteristics in different wind directions, the impacts of oasis on atmospheric hydrological cycle over desert and Gobi near it are revealed. The relation of atmosphere inverse humidity and negative water vapor flux to wind direction and atmospheric stability is studied. It shows that distribution of the atmosphere inverse humidity is inconsistent with that of the negative water vapor flux; sometimes 1-hour-average value demonstrates the characteristic of counter-gradient transfer. And the diurnal variation of distribution of the counter-gradient transfer and the effect of atmospheric stability on the counter-gradient transfer are also given.

Keywords: Desert or Gobi; Hydrologic Cycle; Atmospheric Inverse Humidity; Negative Water Vapor Flux; Counter-Gradient Transfer

1. INTRODUCTION

Oasis is one of the underlying heterogeneous factors. It directly affects the pattern of the atmospheric energy and hydrology transfer over grid points in the region in a model [1-3]. The interaction of the oasis system and the desert system is relative to the maintenance and degeneration processes of oasis ecology system. The special microclimate characteristics and the hydrological cycle mechanism formed under the condition of the interaction are two of the important natural factors (except the factor of water resource) which maintain the oasis system [4-6].

Some special interaction processes between oasis and desert have been found in some experiments and studies carried out in the Northwest China Arid Region [4-12]. However, how the oasis impacts on the water vapor and energy transfer over desert or Gobi near it is still unknown. Most of the former field experiments were carried out in the arid climate region where annual precipitation is about 150 mm, but experiments in arider climate regions where annual precipitation is blow 50 mm, such as Dunhuang, are scarce.

Through analysis and study the data of "The Dunhuang Experiment", the special physical rule of the land-surface under the interaction between oasis and desert near it as well as the ecological maintenance mechanism of oasis will be discussed in the following passages.

2. OBSERVATION DATA AND ANALYTICAL METHOD

The data analyzed in this paper is from a 20-day intensive observation experiment in Dunhuang Gobi micrometeorological central station from May 25 to June 17, 2000 (briefly, "The Dunhuang Experiment"), which is a part of "Land-atmosphere Interactive Field Experiment over Arid Region of Northwest China". The station is located at 40°10′ N, 94°31′ E. Its surface elevation is 1150 meters above sea level. It lies in the flat Shuangdunzi Gobi west to Dunhuang oasis, about 7 km to the edge of the oasis. Annual precipitation is about 40 mm and annual potential evaporation is about 3400 mm. Its main wind direction is east, generally occurring with the frequency of more than 50 percent, so the oasis strongly affects the atmosphere over the observation field. The data include the gradients of wind, temperature and hu-

midity on a tower, soil heat fluxes, the fluctuations of wind, temperature, humidity and wind observed by using a tethered balloon within hundreds of meters high. The sensors of wind, temperature and humidity on the tower are installed at 18, 8, 4 and 2 m high respectively. The sensor of wind direction is installed at 10 m high. The sensors of supersonic fluctuation instrument were installed at 2.9 m with a data processing system that can give the hourly-average momentum flux, sensible heat flux, and latent heat fluxes averaged. The details about the data and the station in Dunhuang experiment have been described in the paper [5,9]. The accuracy of the instruments refers to the correlated references [13-14].

During the Dunhuang experiment, there are 445 valid sets of data which are hourly averaged and 10-day's data to show full diurnal variation. So the amount of samples of hourly data is 445 and that of diurnal variation is 10. Among the ten days, one day is affected evidently by the precipitation. In order to make the results universal, the data which is evidently affected by the precipitation is picked out. The turbulent sensible and latent heat flux is computed by the supersonic fluctuation data.

3. ATMOSPHERIC INVERSE HUMIDITY STRUCTURE AND WATER VAPOR FLUX

In **Figure 1**, the characteristics of 9-day average daily variation of atmospheric specific humidity at four levels (a) and latent heat flux at 2.9 m high (b) are given in May-June over Dunhuang Gobi. As seen in **Figure 1**, because of the influence of the oasis, the atmospheric specific humidity over Gobi is inverse humidity from 0:00 to 6:00. In the daytime, although the specific humidity mainly decreases with height, the inverse humidity appears at 2-8 m high after 14:00 in the afternoon. **Figure 1(b)** shows the negative water vapor flux dominates at night and the water vapor transfers up in the daytime. From its overall characteristics, the diurnal variation of the specific humidity can be divided into four stages that are respectively called the wet stage, the losing-water stage, the dry stage and the attainting-water stage [15].

The daily integration of latent heat flux is 0.117 MJ/m^2 and that of sensible heat flux is 8.692 MJ/m^2. Difference between them is in two orders of magnitude. The climatic Bowen ratio reachs 74.5 which is an extreme arid climate index.

In fact, the impact of the oasis on desert near it is dynamic, which is quite different under different types of synoptic situation. Especially, the wind direction is essential to the impact. The representative data on two full days are selected to analyze. One is 16 June on which

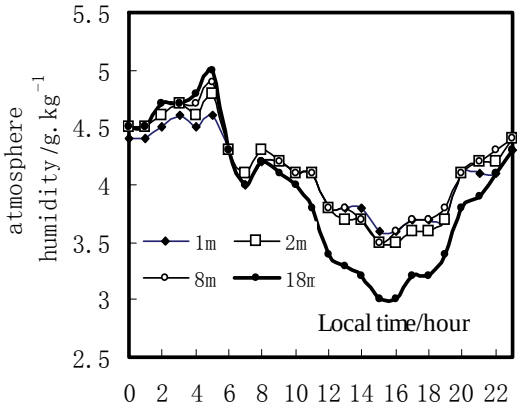

(a)

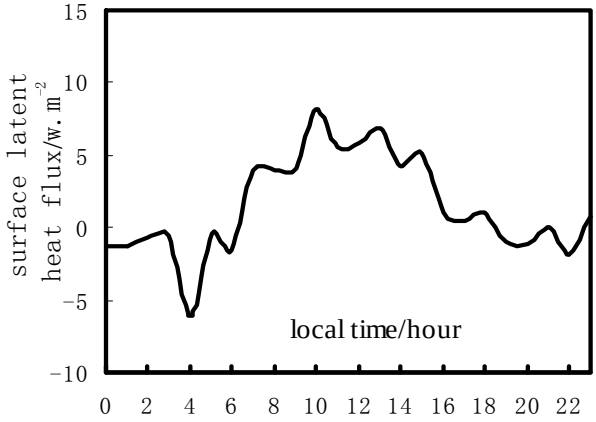

(b)

Figure 1. Daily variation of atmospheric specific humidity at four levels. (a) and latent heat flux at 2.9 m; (b) average data from May 27 to June 15 over Dunhuang Gobi.

wind is from the oasis (named oasis wind), another is 14 June on which wind is from desert (named desert wind) expect 4:00 and 5:00 in which wind direction can not be clearly distinguished into oasis wind and desert wind. **Figure 2** shows the four stages of the wet stage (a), the losing-water stage (b), the dry stage (c) and the attainting-water stage (d) in daily variation of the specific humidity profile in the wind from oasis. It indicates that the specific humidity profile is mainly inverse humidity all day. In the wet stage, inverse humidity appears below 18 m high. In the losing-water stage Inverse humidity appears at about 2 m high and in 8-18 m and the humidity diminishes obviously with time. In the dry stage, inverse humidity appears only below 2 m, and inverse humidity disappears in few stronger heating hours. In the water-gaining stage, inverse humidity strengthens gradually and moves up, at last, all is inverse humidity below 18m and humidity increases obviously.

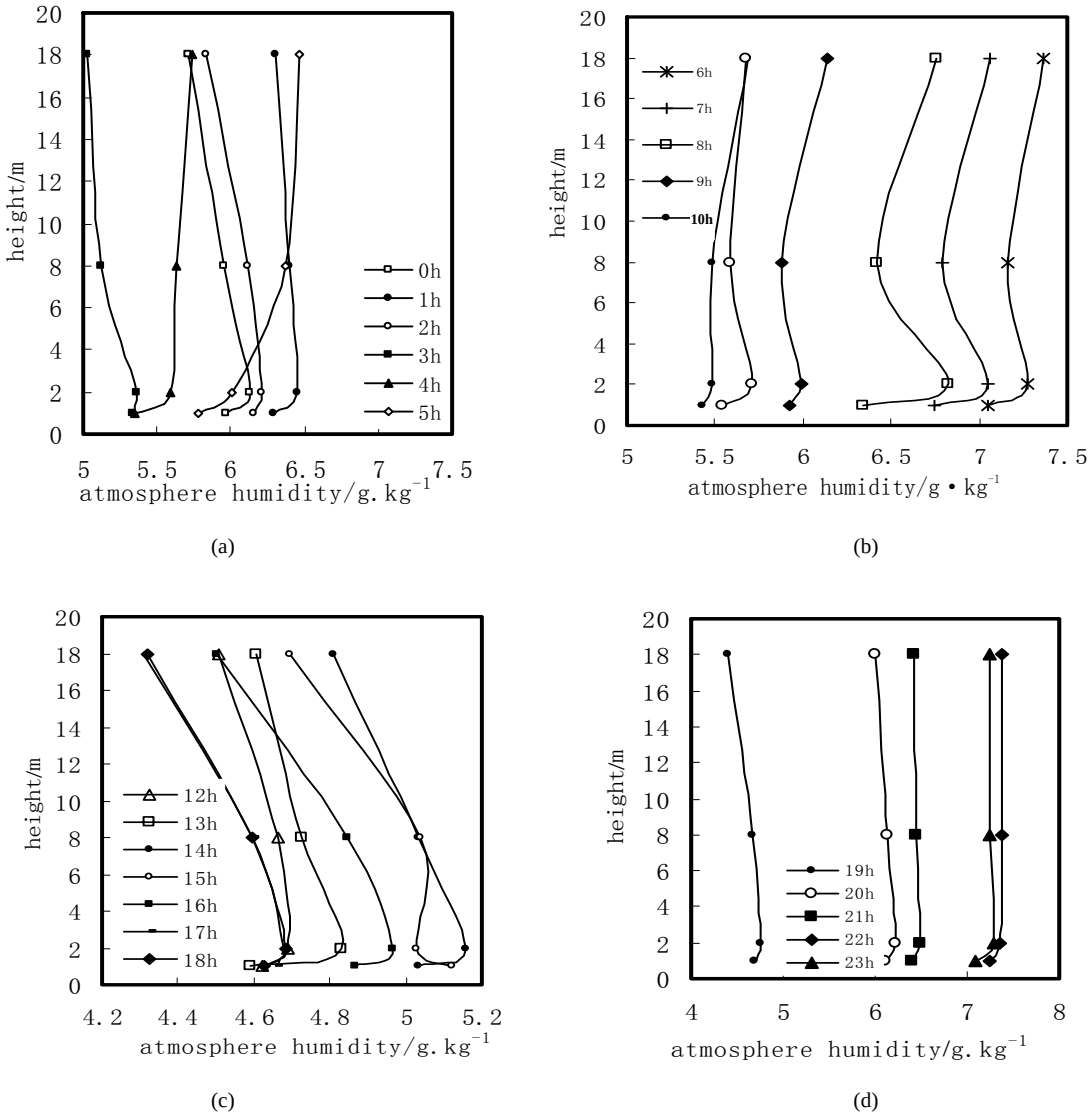

Figure 2. The four stages of the wet stage. (a) the losing-water stage; (b) and the dry stage; (c) the attainting-water stage; (d) in daily variation of the specific humidity profile in the wind from oasis.

Compared with **Figure 2**, the daily variation of the specific humidity profile over desert near oasis in the four stages in the wind from desert (given in **Figure 3**) is quite different. It shows the specific humidity decreases progressively with height all day. In the wet stage, weak inverse humidity appears mainly in 2 m in general, but in all layer in transient wind direction. In the losing-water stage, inverse humidity below 2 m diminishes gradually and disappears or moves up to 2-8 m. In the dry stage, inverse humidity in 2-8 m and air becomes moist obviously. In the attainting-water stage, the profiles of specific humidity decreases up and changes gradually into constant humidity with time. Except 4:00 and 5:00, there is no water vapor advection from oasis to Gobi, but the weak inverse humidity still maintains in long time in dry stage. The reasons are worthy to be discussed.

Figure 4 is the daily variation of the latent heat flux at 2.9 m over Gobi near the oasis in the wind from the oasis (a) and from Gobi or desert (b). In the wind from the oasis, positive latent heat flux is much smaller than that in the wind from the desert ,and further, negative water vapor flux appears mainly in the evening, which are own to the effect of atmospheric inverse humidity. But in the wind from the desert, not only is the latent heat flux bigger, but also the water vapor still transfers generally up in the evening.

The daily integration of the latent heat flux is –0.051 MJ/m^2 in the wind from oasis and is 0.443 MJ/m^2 in the wind from desert. The contributions of the latent heat flux to the surface heat balance in different kind of wind

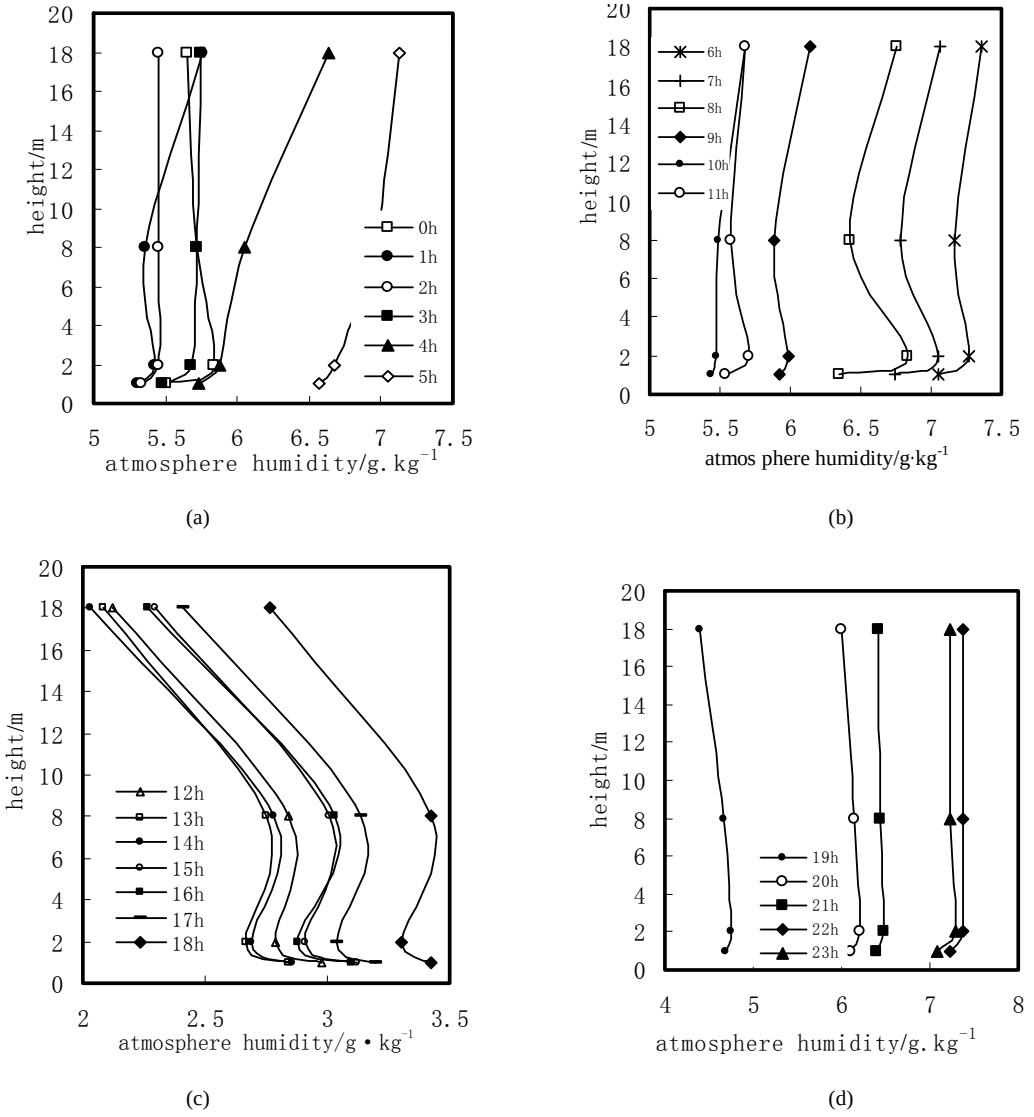

Figure 3. The four stages of the wet stage. (a) the losing-water stage; (b) the dry stage; (c) the attainting-water stage; (d) in daily variation of the specific humidity profile in the wind from desert.

directions are completely different. When the latent heat flux is converted to the water vapor flux, its daily integration is –0.0155 mm in the wind from the oasis and is 0.1355 mm in the wind from desert. In the common synoptic background annual evaporation over desert and Gobi is bigger than the climatic mean value without the infect of the oasis. This result means that it is the effect of the oasis makes the climatic state and the vegtation ecological type better in the desert region near the oasis than that in dersert or Gobi. It can be called the clmatic effect of inverse humidity. Dunhuang Oasis is smaller, so maybe its climatic effect isn't more evidient than that of bigger or more prosperous oasis. The point isn't found in former relative studies on arid region.

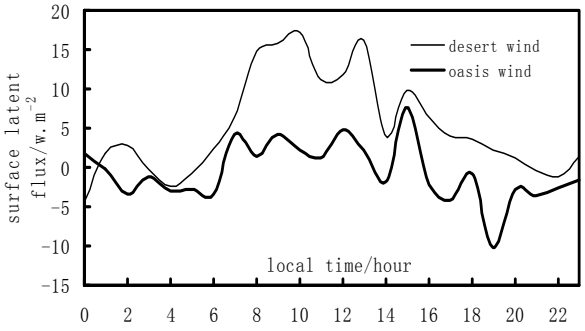

Figure 4. (a) Characteristics of daily variation of the latent heat flux at 2.9 m over Gobi in the wind from oasis; (b) and from Gobi or desert.

4. DISTRIBUTION OF ATMOSPHERIC INVERSE HUMIDITY AND NEGATIVE WATER VAPOR FLUX AS WELL AS COUNTER-GRADIENT TRANSFER

Figure 5 is a comparison of distribution of the wind from the oasis and inverse humidity as well as negative water vapor within 1-2 m over Gobi in Dunhuang. It indicates that frequency of oasis wind keeps at about 50 percent all day, frequency of the atmosphere inverse humidity is bigger at night than that in the daytime. Frequency of inverse humidity is bigger than that of oasis wind at night, but smaller at noon and in the afternoon. There are two main reasons for this feature. On the one hand, the turbulent mixing is very strong and demolishes the inverse humidity structure in the daytime. Thus the inverse humidity structure is hard to maintain. On the other hand, surface evaporation in the daytime can partly counteract the effect of the water vapor advection. Therefore, if the water vapor advection isn't strong enough the inverse humidity will not appear in the daytime. But at night the turbulent mixing is weaker, evaporation is less and atmosphere is of generalized conservation (It means atmospheric motion and exchange is inactive), and inertia of the atmosphere inverse humidity is strong. Thus, the inverse humidity can still keep for a long time, even if there isn't the water vapor advection from the oasis. These conclusions haven't been drawn from the observations in desert near Zhangye-Linze prosperous oasis in Heihe region [2]. There are two main reasons about it. On the one hand, the wind direction is more irregular in the observation of Heihe region which is affected by Qilian Mountain. On the other hand, perhaps the water vapor transfer of Dunhuang oasis isn't as strong as Zhangye-Linze oasis's.

Generally the direction of the water vapor flux is controlled by the specific humidity gradient. For example, if the specific humidity decreases with height the water vapor flux will be positive, namely upwards, vice versa.

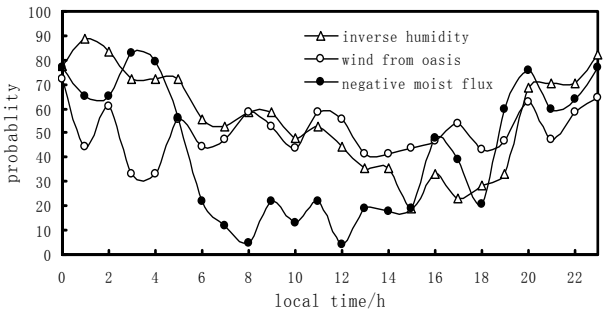

Figure 5. A comparison of distribution of the wind from the oasis, inverse humidity and negative water vapor within 1-2 m over Gobi in Dunhuang.

Figure 5 shows that, the distribution of the negative water vapor flux is consistent with that of the inverse specific humidity at night, but is quite inconsistent with it in the daytime. Frequency of the negative water vapor flux is under 20 percent and less than that of the inverse specific humidity in the daytime. It means that, the latent heat bulk transfer coefficients must be positive, namely counter-gradient transfer appears most times. It also appears over desert near oasis in Heihe region, but is omitted as error in the former studies. The counter-gradient transfer is partly related to the observational error because both the humidity and latent heat flux are too small. But its distribution shows such good rule which makes us to look for other reasons. Some studies show that the counter-gradient transfer can result from the horizontal heterogeneity which is caused by the motion of convective eddy, complicated underlying and cumulus convection [6,7]. The strong horizontal heterogeneity of water vapor caused by distribution of oases in arid region is a typical mesoscale process. Based on Taylor hypothesis, temporal averaged values can respond to the effect of the spatial heterogeneity, and it results in opposite symbol between the hourly averaged gradient and the turbulent flux.

Figure 6 is a comparison of the characteristics of daily variation of distribution of counter-gradient transfer (a) and the bulk Richardson number (b). **Figure 6(a)** indicates that the frequency of the counter-gradient transfer over desert and Gobi near oasis in the daytime is bigger than that at night. Its maximum is over 60 percent at 9:00 o' and the minimum is about 20 percent at 18:00. It basically maintains about 40 percent in a longer time.

The daily variation of the counter-gradient transfer may be related to the atmospheric stability. Comparing **Figure 6(a)** with **Figure 6(b)**, the daily variation of the distribution of counter-gradient transfers and is mainly correlative to that of the Richardson number. The bigger the frequency of counter-gradient transfer is, the stronger the atmospheric instability is, vice versa.

The atmospheric stability indirectly affects the counter-gradient transfer through its influence on the oasis effect. Generally, the stronger the heterogeneity is, the counter-gradient transfer caused by the temporal averaging [16] is more obvious. At night the atmosphere over oasis is stable, inactive and its impact on desert near it is smaller, so the frequency of the counter-gradient transfer is less. But in the daytime the great instability makes the atmosphere over oasis active, and the influence of atmosphere over the oasis on the atmosphere over desert near oasis is greater, so the frequency of the counter-gradient transfer is bigger. After the surface atmosphere exchanges strongly between oasis and desert during a period in the daytime, horizontal distribution of atmos

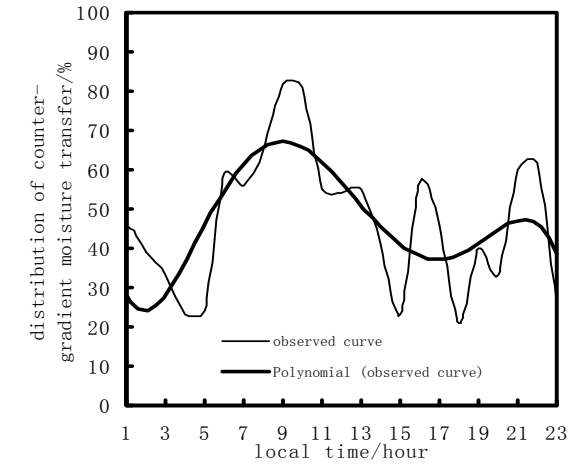

(a)

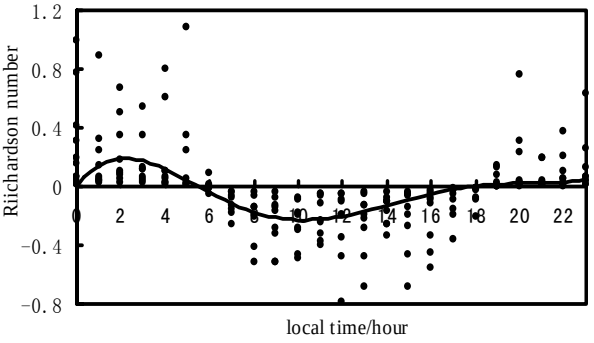

(b)

Figure 6. (a) A comparison of the characteristics of daily variation of distribution of counter-gradient transfer; (b) and the bulk Richard-son number.

pheric humidity tends to even and the impact of the oasis on desert become weaker. So the counter-gradient transfer of water vapor appears at 9:00, not at noon or in the afternoon.

5. CONCLUSIONS AND DISCUSSIONS

The daily variation of the specific humidity over desert near oasis can be divided into four stages which are the wet stage, the losing-water stage, the dry stage and the attaining-water stage. This is similar to the general Gobi or desert. Differences caused by the oasis wind are given in the following content. Firstly, the atmosphere specific humidity over Gobi near oasis is basically in inverse humidity and the water vapor flux is negative at night. Secondly, the specific humidity decreases progressively with height and the water vapor flux is positive in the daytime. Thirdly, the difference between the daily integrated values of the latent and sensible heat flux are in two orders of magnitude.

The structure of humidity profiles and the water vapor transfer in desert wind are very different from those in oasis wind. In the wind from desert, the specific humidity decreases with height all day and the water vapor basically transfers up. However, in the wind from oasis, the inverse humidity is dominant and the water vapor flux is negative all day except few hours. The daily integrated value of water vapor flux in the wind from oasis is significantly different from that in the wind from desert. Such effect of the oasis indicates that less annual precipitation can support the climatic state or the vegtation ecological type with greater annual evaporation over desert region near the oasis. Namly, the effect of the oasis makes the climatic state and the vegtation ecological type better in the dersert region near the oasis than that in the desert or Gobi.

The atmosphere over oasis is conservative at night and active in the daytime. So the frequence of inverse humidity is bigger than that of the oasis wind at night, while is smaller in the daytime. Because of the influence of horizontal spatial heterogeneity of water vapor caused by distribution of oasis, sometimes the direction of water vapor transfer is inconsistent with specific humidity gradient, namely the counter-gradient transfer of water vapor appears in a longer time.

The frequency of the counter-gradient transfer in the daytime is bigger than that at night and it is much relative to the atmospheric stability. These features are relative to the counteraction of the turbulent mixing on the horizontal heterogeneity of water vapor over oasis.

The effects of thermal circulation between oasis and desert near it, which were found in the former studies [12] on the Northwest China Arid Region, doesn't appear in the Dunhuang experiment. The flowing are the possible reasons. Firstly, Dunhuang oasis is smaller. Secondly, the thermal circulation is weaker. At last, its influence on atmospheic humidity over gobi or desert may be offset by the strong turbulent mixing resulting from extreme arid environment.

6. ACKNOWLEDGEMENTS

We thank Mr. Zeyong Hu, Xuhong Hou, Ping Hou and Yanjiang Nei *et al.* for their assistance in the observation and data procession. We also thank for the comments of the reviewer. This work was supported by the National Natural Science Foundation of China (Grant No. 40830957) and the National Key Program for Basic Sciences – Research on Formation Mechanism and Prediction Theory of Heavy Climatic Disasters in China (Grant No.G1999040904-2).

REFERENCES

[1] Zhang, Q. and Huang, R.H. (2004) Water vapor exchange

between soil and atmosphere over a gobi surface near an oasis in summer. *Journal of Applied Meteorology*, **43(12)**, 1917-1928.

[2] Zhang, Q. and Huang, R.H. (2004) Parameters of land surface processes on Gobi in northwest China. *Boundary-Layer Meterology*, **110(3)**, 471-478.

[3] Zeng, X. and Pielke, R.A. (1995) Landscape-induced atmospheric flow and its parameterization in large-scale numerical models. *Journal of Climate*, **8(5)**, 1156-1177.

[4] Zhang, Q., Hu, Y.Q., Cao, X.Y. and Liu, W.M. (2000) About some problems of arid climate system of Northwest China. *Journal of Desert Research* (*in Chinese*), **20(4)**, 357-362.

[5] Zhang, Q. and Cao, X.Y. (2003) A study of surface heat and radiation budget energy in Dunhuang region. *Chinese Journal of Atmospheric Sciences*, **27(2)**, 165-176.

[6] Zhang, Q., Wang, S. and Sun, Z.X. (2009) A study of Atmospheric Boundary layer structure during a clear day in the Arid Region of Northwest China. *ACTA Meteor Sinica*, **23(3)**, 327-337.

[7] Zhang, Q. and Hu, Y.Q. (1992) Characteristics of micrometeorology over the farmland in Oasis Heihe region. *Plateau Meteorite* (*in Chinese*), **11(4)**, 361-370.

[8] Zhang, Q. and Zhao, M. (1999) Field experiment and numerical simulation of inverse humidity of atmosphere over desert near oasis. *ACTA Meteor Sinica* (*in Chinese*), **57(6)**, 729-740.

[9] Zhang, Q., Song, L.C. and Wei, G.A. (2003) Characteristics of hydrologic transfer between soil and Atmosphere over Gobi near oasis at the end of summer. *Advance in Atmospheric Science*, **20(3)**, 442-452.

[10] Zhang, Q., Wang, S., Michael, B., Tian, W.S. and Huang, R.H. (2010) The characteristics of sensible heat and momentum transfer coefficients over the Gobi in the northwest China. *International Journal of Climatology*, **2**, 586-589.

[11] Wang, J.M. and Mitsuta, Y. (1991) Turbulence structure and transfer characteristics in the surface layer of the HEIFE Gobi area. *Journal of the Meteorology Society of Japan*, **69(5)**, 587-593.

[12] Hu, Y.Q., Yang, X.L., Zhang, Q. and Zuo, H.C. (1992) The characters of energy budget on the Gobi and desert surface in Hexi region. *ACTA Meteor Sinica*, **6(1)**, 82-91.

[13] Zhang, Q. and Hu, Y.Q. (1992) The instrumental accuracy and observational error about micrometeorological mast of Chinese side in "HEIFE". *Plateau Meteorite* (*in Chinese*), **11(4)**, 460-469.

[14] Wang, J.M., *et al.* (1992) A real-time, low cost turbulence data acquisition and processing system. *Plateau Meteorite* (*in Chinese*), **11(4)**, 451-490.

[15] Zhang, Q., Wei, G.A. and Huang, R.H. (2002) The bulk transfer coefficients of the atmospheric momentum and sensible heat over desert and Gobi in arid climate region of Northwest China. *Science in China* (*Series D*), **45(5)**, 468-480.

[16] Deardorf, J.W. (1972) Theoretical expression for the counter gradient vertical heat flux. *Journal of Geophysical Research*, **77(30)**, 5900-5904.

Vol.2, No.7, 688-693 (2010)
doi:10.4236/ns.2010.27085

Natural Science

Synthesis, structural characterization and formation mechanism of giant-dielectric $CaCu_3Ti_4O_{12}$ nanotubes

Nirupam Banerjee, Saluru Baba Krupanidhi*

Materials Research Center, Indian Institute of Science, Bangalore, India; nirupam@mrc.iisc.ernet.in; nirupam1986@gmail.com;
*Corresponding Author: sbk@mrc.iisc.ernet.in

Received 5 March 2010; revised 10 April 2010; accepted 18 April 2010.

ABSTRACT

A capillary-enforced template-based method has been applied to fabricate calcium copper titanate ($CaCu_3Ti_4O_{12}$, CCTO) nanotubes (diameter ~200 nm) by filling sol-gel CCTO precursor solution into the nanochannels of porous anodic aluminum oxide (AAO) templates, subsequent heating for phase formation and finally the removal of nano-channel templates by applying basic solution. X-ray diffraction (XRD), field emission scanning electron microscopy (FE-SEM) and transmission electron microscopy (TEM) equipped with Energy-dispersive X-ray spectroscopy (EDX) have been employed to characterize the morphology, structure, and composition of as-prepared nanotubes. XRD and selected-area electron diffraction (SAED) investigations demonstrated that postannealed (750°C for 1 h) CCTO nanotubes were polycrystalline with a cubic pseudo-perovskite crystal structure. The FE-SEM and TEM results showed that CCTO nanotubes were of uniform diameter (~200 nm) throughout their length. High resolution TEM (HRTEM) analysis confirmed that the obtained CCTO nanotubes are made of randomly aligned nano-particles 5-10 nm in size. EDX analysis demonstrated that stoichiometric $CaCu_3Ti_4O_{12}$ was formed. The possible formation mechanism of CCTO nanotubes in the AAO template is discussed.

Keywords: Nano-Tubes; Sol-Gel; Templated Growth; High-K-Dielectrics

1. INTRODUCTION

Subsequent to the discovery of carbon nanotubes [1] by Iijima *et al.* many research groups around the globe have become involved in the development of one-dimensional nano-structures such as nano-tubes, nano-rods, nanowires etc. of various functional materials due to their important role in mesoscopic physics and nanoscale device fabrication, as they can be utilized as both nanoscale device elements and interconnections while retaining unique properties due to size confinement in the radial direction [2-6]. Recently efforts have been made to synthesize and understand the growth of different nanostructures of the functional materials such as complex dielectric and ferroelectric oxides because of their promising applications for pyroelectric detectors, piezoelectric actuators and transducers, nonvolatile memory, ultrasonic devices, piezoelectric ink-jet printers etc. [7-11]. Nanotubes of various materials have been synthesized through various methods, among which sol-gel template technology provides a versatile technique for synthesizing highly ordered and controlled with the same structure and properties at large-scale production of one dimensional nanostructures, which is the basic building block of nanodevices. The nanochannel of template can be viewed as a reactor, in which one-dimensional nanostructure of the desired material can be synthesized in which the shape and size of the nanostructures depend only on the dimension of the pores present in the template.

High dielectric constant materials are immensely useful for miniaturization of electronic devices which is a recent goal of our technological progress. In this scenario ferroelectric materials are on demand due to their high dielectric constant values. Hernandez *et al.* have fabricated $BaTiO_3$ (BT) and $PbTiO_3$ (PT) nanotubes using template approach [12]. Using the same synthetic approach Zhang *et al.* have fabricated highly ordered $Pb(Zr_{0.53}Ti_{0.47})O_3$ (PZT) nanowires which were found to exhibit a significant piezoresponse and proposed for potential device applications [13]. Recently, Singh *et al.* reported the fabrication of $Ba_{0.6}Sr_{0.4}TiO_3$ (BST) nanotubes [14]. But one serious drawback in these well known ferroelectric materials possessing higher dielectric constant values is these are Pb or Ba containing materials which are severely toxic to human bodies and

therefore are non-environment friendly materials. One more important point is that the dielectric constant (ε) for most of these ferroelectric ceramics has strong temperature dependence and shows rapid change near ferroelectric transition temperature which makes them inefficient to act as a good ceramic capacitor material. In the first of this millennium Subramanian *et al*. [15] have discovered a new pseudo-perovskite $CaCu_3Ti_4O_{12}$ (CC TO) possessing a very high value of dielectric constant (~10,000 for bulk and ~10^5 for single crystals) and moderately lower dielectric loss (~0.1). The dielectric constant remains reasonably invariant over a wide temperature range from 100 to 400 K below 1 MHz. Hence the material is capable of potential industrial application for miniaturizing electronic devices. To a surprise the material is non-ferroic and shows a centrosymmetric structure down to 35 K [16]. Both intrinsic and extrinsic mechanisms were employed to explain this unusual phenomenon. Most of the studies have taken the help of Internal Barrier Layer Capacitor (IBLC) model consisting of semiconducting grains and insulating grain boundaries to explain this enormously large dielectric const [17-18]. whereas Lunkenheimer *et al.* believe it is arising from the electrode polarization effects [19]. Although there are few reports on the synthesis of nano-particles of this giant dielectric material [20], fabrication of its nanostructures is rare in literature. In this article we are reporting the synthesis of gaint dielectric CCTO nanotubes of about 200 nm diameter by means of a sol-gel method utilizing nano-porous anodic aluminum oxide (AAO) templates, structural characterization of the nano-tubes and high resolution electron microscopic (HRTEM) studies on the nano-tube walls to reveal the crystalline structures.

2. EXPERIMENTAL DETAILS

$CaCu_3Ti_4O_{12}$ precursor-solution was prepared through conventional sol-gel route whreby metallic-acetates namely copper-acetate monohydrate ($Cu(CH_3COO)_2.H_2O$ > 99%, Aldrich) and calcium acetate monohydrate ($Ca(CH_3COO)_2.H_2O$ > 99%, Aldrich) were used as metal-ion precursors. Appropriate amount of these metallic-acetates, corresponding to 1:3 ratios of Ca:Cu metal ions were dissolved in glacial acetic acid which was used as solvent. Titanium isopropoxide (TIP) ($Ti\text{-}\{OCH(CH_3)_2\}_4$ > 99.9%, Aldrich) was used as Ti-source and was dropwise added in appropriate amount (*i.e.*, amount corresponding 1:3:4 stoichiometric ratios of Ca:Cu:Ti metal ions) to glacial acetic acid with a gas-tight syringe while stirring the solution continuously with the help of a magnetic stirrer. It is a well known phenomenon that transition metallic alkoxides are unstable due to the presence of extremely reactive alkoxide groups and are prone to hydrolysis. Hence acetylacetone ($CH_2(CH_3CO)_2$, Merck) was added to the solution for stabilization of TIP. Next these two solutions were mixed together to form the final precursor solution which was adjusted to a concentration 0.1 M (in terms of CCTO) and was subsequently refluxed for one hour at 160°C for homogeneity. The final precursor solution was transparent, dark blue in color and was stable for long time without any precipitation.

Nanopourous Anodic Aluminum Oxide (AAO) membranes (pore diameter: ~200 nm, and 60 μm thickness) were purchase from Whatman®, were used as the templates for synthesis of CCTO nanotubes. Before using, templates were cleaned for 20 min in an ultrasonic bath using solvents of different polarity such as double distilled water, acetone, hexane, toluene and were annealed at 200°C for 2 h in vacuum to make free of any existent impurities. Next the AAO templates were immersed in the precursor solution for 2 h and were dried at 150°C for 1 h. These templates containing the precursor were heated in air at 750°C for 1 h with the help of a thermal annealing furnace for the desired phase to form. CCTO nanotubes were isolated on removal of the AAO templates by immersing them in 6 M NaOH solution at room temperature for 24 h. To obtain higher amount of nanotubes, the base solution was diluted in several steps with distilled water and finally with ethanol. The isolated nanotubes were collected by centrifugation. The structural studies on the as prepared CCTO nanotubes were carried out using X-ray powder diffraction (XRD) using a Philips PW3710 diffractometer (Cu-K radiation, 30 kV and 20 mA, λ = 1.5406 Å).The morphology of the CCTO nanotubes was studied by scanning electron microscope (SEM) (Quanta 200). To reduce the charging effects on insulating AAO templates and CCTO nanotubes during SEM studies, a very thin layer of gold was sputtered for conductivity enhancement. The X-ray structural data were corroborated by the transmission electron microscopic (TEM, Tecnai F30) studies, operating at an acceleration voltage of 200 kV.

3. RESULTS AND DISCUSSIONS

Since the size and uniformity of the product nanotubes solely depend on the used nanoporous AAO template, its features namely the uniformity of size of the pores in the template were studied by SEM. **Figure 1(a)** and **Figure 1(b)** show typical scanning electron micrographs of top-view and lateral-views of an empty AAO template respectively. It can be noticed that the pores size (diameter) in the AAO template were in the range of 190-220 nm and pores are well-uniformly distributed over

the template matrix in an approximately hexagonal-shaped "honey-comb" like structure. **Figure 1(c)** shows SEM image of CCTO nano-tubes after almost 90% removal of the AAO template with NaOH solution. **Figure 1(d)** features a side view of some of the prepared nano-tubes. The micrographs clearly show that as synthesized CCTO nanotubes were hollow, roughly parallel to each other, and vertically oriented on the AAO template to form an array. The average diameter of the nano-tubes are in the range of 160-180 nm, little smaller than the expected value of 200 nm. This contraction of nano-tubes from the original dimension of the pores is probably due to the shrinkage experienced by CCTO nano-tubes on densification and dehydration associated with thermal treatment. The diameter is quite uniform for most of the nano-tubes indicating the superiority of this method for large scale homogeneous nanotube synthesis.

To examine crystallinity and phase-purity of as-prepared nano-tubes obtained after annealing at 700°C, X-ray diffraction studies were carried out. **Figure 2** shows the X-ray diffraction pattern of template free CCTO nano-tubes, which were collected and gathered as centrifuge residue after removal of NaOH solution and subsequent washing with different solvent mediums for several times. The XRD pattern clearly indicates the crystallinity of the nano-tubes. All the peaks in the diffractogram can be well-indexed according to the pseudo-perovskite phase of CCTO (JCPDS card No. 75-2188). Absence of any impurity peaks proves the phase-purity. The orientations and the intensity ratios of the CCTO nanotubes matched well with the cubic pseudo-perovs-

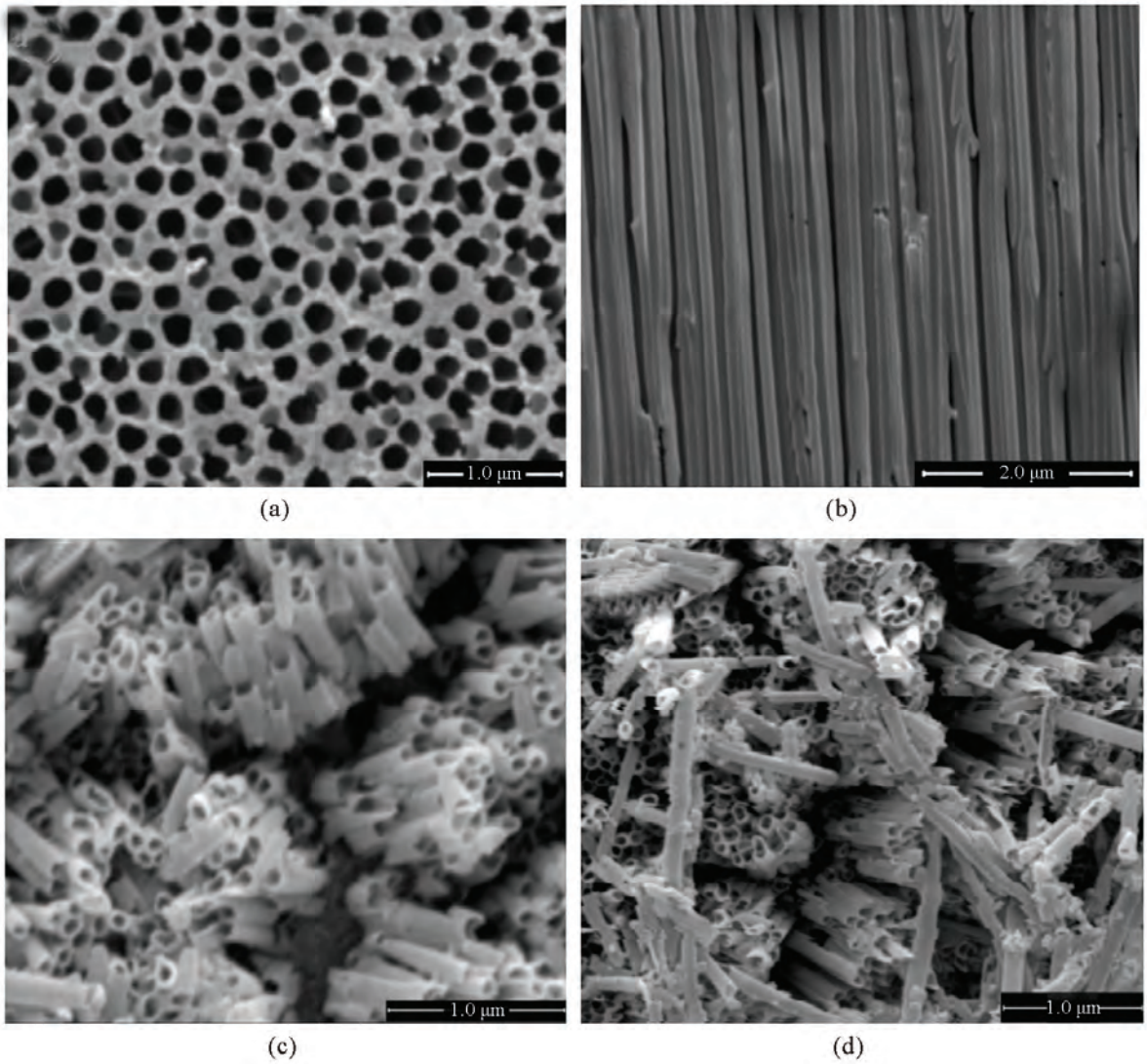

Figure 1. SEM images. (a) top-view of AAO template; (b) lateral-view of AAO template; (c) CCTO nanotubes after > 90% removal of AAO templates with the help of NAOH solution; (d) lateral view of some of the CCTO nano-tubes.

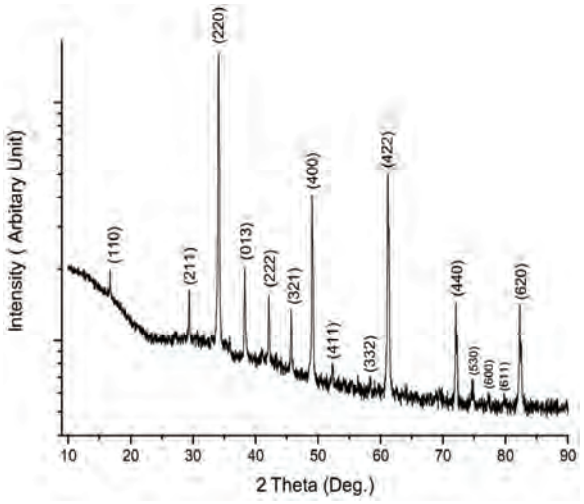

Figure 2. X-Ray Diffraction pattern of prepared CCTO nano-tubes annealed at 700°C after removal of AAO templates.

kite phase of bulk CCTO.

Figure 3(a) shows TEM image of a CCTO nano-tube after complete removal of AAO template by dissolution in 6 M NaOH solution. The difference in contrast between the middle and the edges of the tube in **Figure 3(a)** clearly indicates its hollow structure. Enhanced scattering at edges of the tube makes it darker than the middle portion in the TEM picture. The diameter of the nano- tube is almost uniform throughout its length which is approximately equal (slightly smaller) to channel diameter of the applied template. The length of these nano- tubes was found to be shorter than the thickness (60 μm) of the AAO templates. The possible reason may be the inefficient filling upto the pore-depth in the template and also breakage of some tubes to shorter ones during intense ultra-sonic dispersion treatment. **Figure 3(b)** re- presents corresponding SAED pattern which clearly proves the polycrystalline nature of the nano-tubes. The rings in the SEAD pattern corresponds to (422), (400), (013), (220) and (200) crystal planes of cubic pseudo- perovskite phase of CCTO. The d-spacings were calculated from the diameter of the bright circular rings observed in the electron diffraction pattern which were found to be in good agreement with that calculated from the XRD data (JCPDS card No. 75-2188) and the data available in the literature.

The micro-structure of the CCTO nano-tubes were further investigated with the help of High Resolution Transmission Electron Microscope (HRTEM) studies to get a clear insight of the features. **Figure 3(c)** shows a typical HRTEM image of the wall of a CCTO nano-tube prepared with the help of AAO templates. The HRTEM image clearly shows that the nano-tube is made up with a number of CCTO well-resolved nano-particles that are randomly oriented in the wall. The nano-particles comprising the walls of nano-tubes of other oxide materials have been previously observed and reported in the literature [14,21]. The size of the constituent particles is in the range of 5-10 nm which is in good agreement with the previously reported data of these functionally complex oxide nano-structures [14]. The observation of few unresolved spaces in the HRTEM image suggests the presence of few pores in the wall of CCTO nano-tubes. The lattice spacing values (d220, d400) as obtained from the HRTEM image closely resembles to that calculated on the basis of XRD and SEAD results.

Energy dispersive X-ray (EDX) spectrum of the CCTO nano-tubes after complete removal of AAO template is shown in the **Figure 3(d)**. No emission peaks from Al, and other elements from the etching NaOH solution, reagent, and template appeared in this spectrum. The absence of any impurity peaks in the EDS spectrum and the close resemblance of the atomic ratios of Ca, Cu and Ti to the nominal composition in $CaCu_3Ti_4O_{12}$ prove the elemental and phase purity of prepared CCTO nanotubes.

CCTO nanotubes were grown by sol-filling in the AAO template with the help of capillary force. The sol was drawn up into and filled the pores of the AAO template. Air in the pores and vapor from the sol were evaporated from the top surface of the AAO template. The possible formation mechanism of CCTO nanotubes inside the pores of AAO template is proposed here. Schematics of the possible formation mechanism of CCTO nanotube inside the pores of AAO template is shown in **Figure 4** (growth process of CCTO nanotube). Initially, the template was put on the CCTO precursor solution as shown in **Figure 4** because the solution is easier to fill into the pores of the template due to the capillary force. As the solvent evaporates from the surface and the concentration is enriched at the top of the pores, precipitation or gelation occurs first at the top of the pores on the AAO template surface exposed to the air and subsequently proceeds downward along the entire wall of the pores. The precursor solution consists of sol nanoparticles or nanoclusters homogeneously dispersed in the solvent. Such nanoclusters, which develop surface charges and form a double layer, can respond to an externally applied electric field or other nanoclusters [22]. When the surface of the AAO template is brought into contact with a sol, a surface charge and a double layer are formed on the surface of the AAO template. Therefore, when sols are drawn into the pore channels of the AAO template, if the surface charges of nanoclusters in a sol and the surface of the AAO template are opposite, there will be an electrostatic attraction force, and the

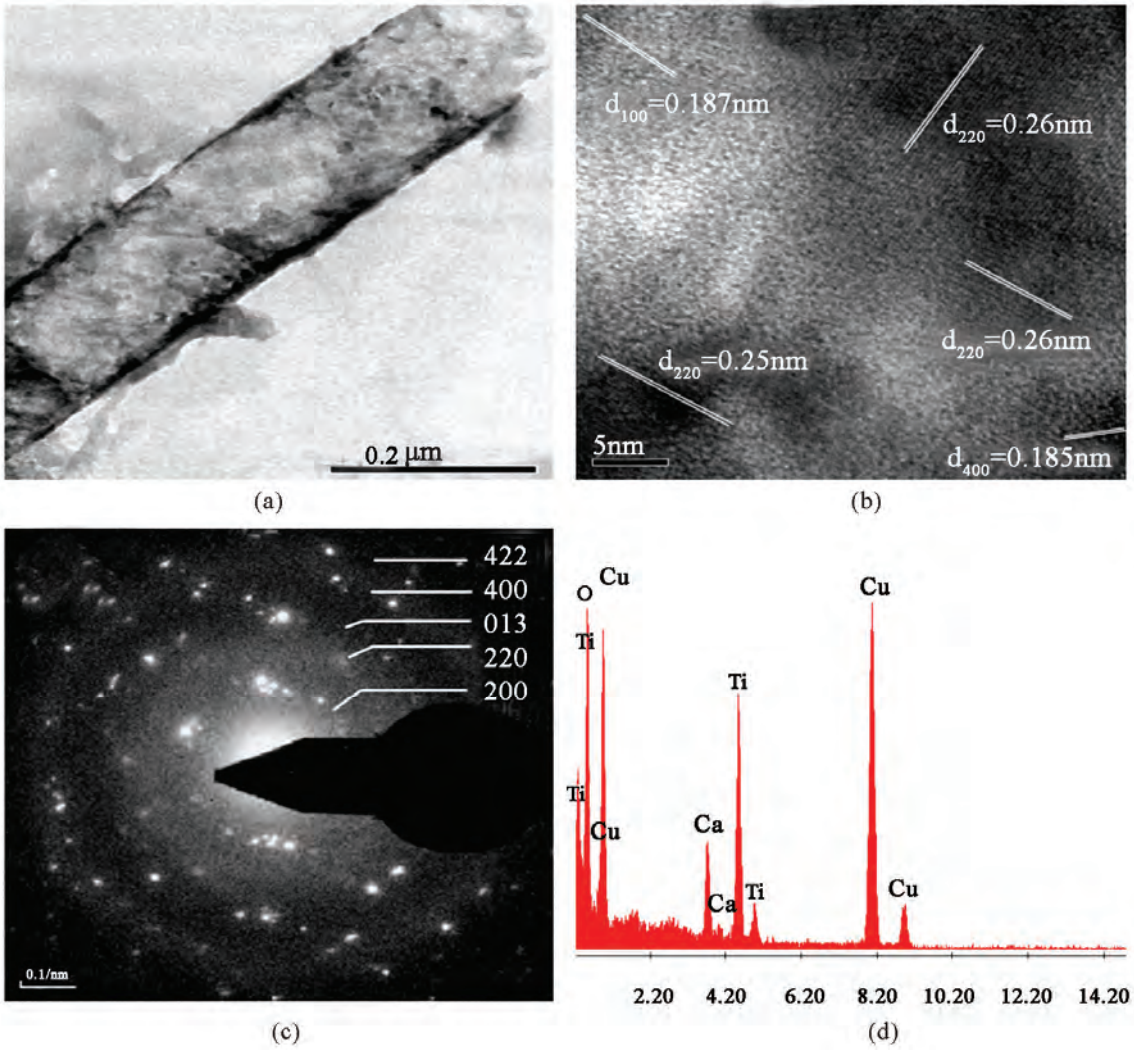

Figure 3. TEM image of (a) a CCTO nano-tube after complete removal of AAO template; (b) HRTEM image of a single nano-tube surface revealing that it is comprised of a number of randomly oriented particles; (c) corresponding SEAD pattern and (d) EDS spectrum of CCTO Nano-tubes.

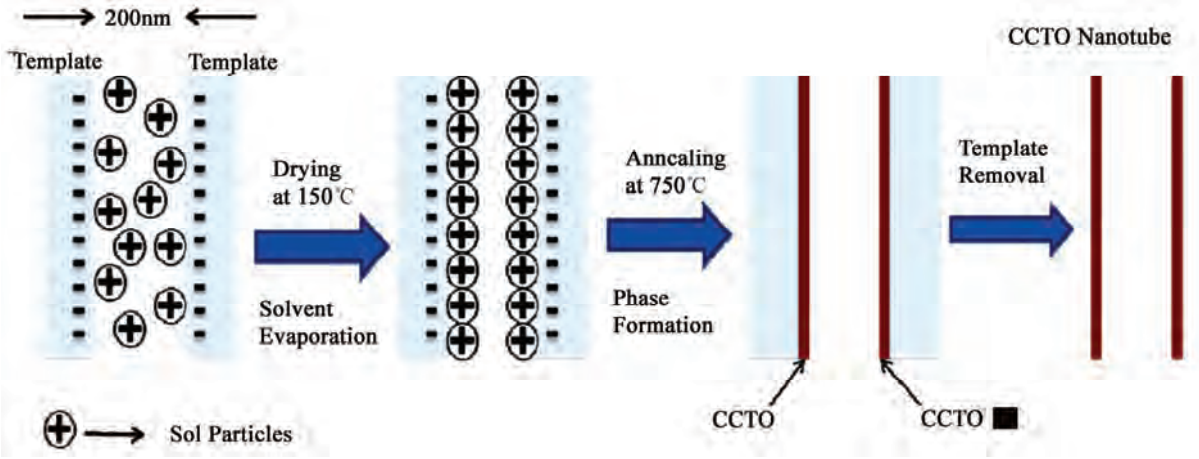

Figure 4. A schematic diagram of the possible growth mechanism of CCTO nanotubes in the AAO template.

nanoclusters will preferentially deposit on the surface of the pore channel, resulting in the formation of nanotubes.

4. CONCLUSIONS

In summary, CCTO nanotubes have been prepared successfully by sol-gel method using the closely packed porous nanochannel alumina templates. The crystallinity and phase purity of the CCTO nanotubes were confirmed via XRD and SAED analysis. EDX analysis corroborated the stoichiometric $CaCu_3Ti_4O_{12}$ formation. The walls of the nanotubes were found to be made up of nanoparticles as confirmed by the HRTEM studies. The nanoparticles embedded in the wall were found in the range of 5-10 nm. This facile method of preparing the $CaCu_3Ti_4O_{12}$ nanotubes at a large scale might be important for many applications in nanodevices.

5. ACKNOWLEDGEMENTS

N. B. thanks to Int. PH.D program, Indian Institute of Science for financial assistances and Institute Nano-Science Initiative for microscopic facilities.

REFERENCES

[1] Iijima, S. (1991) Helical microtubules of graphitic carbon. *Nature*, **354(6348)**, 56-58.

[2] Hu, J., Odom, T.W. and Lieber, C.M. (1999) Chemistry and physics in one dimension: Synthesis and properties of nanowires and nanotubes. *Accounts of Chemical Research*, **32(5)**, 435-445.

[3] Atzke, G.R.P., Rumeich, F.K. and Nesper, R. (2002) Based on oxide nanotubes and nanorods − anisotropic building blocks for future nanotechnology. *Angewandte Chemie*, **114(14)**, 2554-2571.

[4] Goldberger, J., He, R., Zhang, Y., Lee, S., Yan, H., Choi, H. and Yang, P. (2003) Single-crystal gallium nitride nanotubes, *Nature*, **422(6932)**, 599-602.

[5] Lee, S.B., Mitchell, D.T., Rofin, L.T., Ne vanen, T.K., Sçderlund, H. and Martin, C.R. (2002) Antibody-based bio-nanotube membranes for enantiomeric drug separations. *Science*, **296(5576)**, 2198-2200.

[6] Sha, J., Niu, J., Ma, X., Xu, J., Zhang, X., Yang, Q. and Yang, D. (2002) Silicon nanotubes. *Advanced Materials*, **14(17)**, 1219-1224.

[7] Junquera, J. and Ghosez, P. (2003) Critical thickness for ferroelectricity in perovskite ultrathin films. *Nature*, **422(6931)**, 534-539.

[8] Wang, Y. and Santiago-Aviles, J.J. (2004) Synthesis of lead zirconate titanate nanofibres and the Fourier-transform infrared characterization of their metallo-organic decomposition process. *Nanotechnology*, **15**, 32.

[9] Luo, Y., Szafraniak, I., Zakharo, N.D., Nagarajan, V., Steinhart, M., Ehrspohn, R.B.W., Endorff, J.H.W., Ramesh, R. and Alexe, M. (2003) Nanoshell tubes of ferroelectric lead zirconate titanate and barium titanate. *Applied Physics Letters*, **83(5377)**, 440-442.

[10] Chu, M.W., Szafraniak, I., Scholz, R., Harnagea, C., Hesse, D., Alexe, M. and Gosele, U. (2004) Impact of misfit dislocations on the polarization instability of epitaxial nanostructured ferroelectric perovskites. *Nature Materials*, **3(2)**, 87-90.

[11] Roelofs, A., Schneller, I., Szot, K. and Waser, R. (2002) Piezoresponse force microscopy of lead titanate nanograins possibly reaching the limit of ferroelectricity. *Applied Physics Letters*, **81(27)**, 5231-5233.

[12] Hernandez, B.A., Chang, K.S., Fisher, E.R. and Dorhout, P.K. (2002) Sol-Gel template synthesis and characterization of batio3 and pbtio3 nanotubes. *Chemistry of Materials*, **4**, 480.

[13] Zhang, X.Y., Zhao, X., Lai, C.W., Wang, J., Tang, X.G. and Dai, J.Y. (2004) Synthesis and piezoresponse of highly ordered $Pb(Zr_{0.53}Ti_{0.47})O_3$ nanowire arrays. *Applied Physics Letters*, **85(18)**, 4190-4192.

[14] Singh, S. and Krupanidhi, S.B. (2007) Synthesis and structural characterization of Ba0.6Sr0.4TiO3 nanotubes. *Physics Letter A*, **367(4-5)**, 356-359.

[15] Subramanian, M.A., Li, D., Duan, N., Reisner, B.A. and Sleight, A.W. (2000) High dielectric constant in $ACu_3Ti_4O_{12}$ and $ACu_3Ti_3FeO_{12}$ phase. *Journal of Solid State Chemistry*, **151(2)**, 323-325.

[16] Liu, J. J., Sui, Y.C., Duan, C.-G., Mei, W.-N., Smith, R.W., and Hardy, J.R. (2006) $CaCu_3Ti_4O_{12}$: Low-temperature synthesis by pyrolysis of an organic solution. *Chemistry Materials*, **18(16)**, 3878-3882.

[17] Sinclair, D.C., Adams, T.B., Morrison, F.D. and West, A.R. (2002) $CaCu_3Ti_4O_{12}$: One-step internal barrier layer capacitor. *Applied Physics Letters*, **80(12)**, 2153-2155.

[18] Liu, J., Duan, C., Yin, W., Mei, W.N., Smith, R.W. and Hardy, J.R. (2004) Large dielectric constant and maxwell-wagner relaxation in $Bi_{23}Cu_3Ti_4O_{12}$. *Physics Review B*, **70**, 144106.

[19] Lunkenheimer, P., Bobnar, V., Pronin, A.V., Ritus, A.I., Volkov, A.A. and Loidl, A. (2002) Origin of apparent colossal dielectric constants. *Physics Review B*, **66**, 052105.

[20] Thomas, P., Dwarakanath, K., Varma, K.B.R. and Kutty, T.R.N. (2008) Nanoparticles of the giant dielectric material, $CaCu_3Ti_4O_{12}$ from a precursor route. *Journal of Physics and Chemistry of Solids*, **69(10)**, 2594-2604.

[21] Zhang, X.Y., Lai, C.W., Zhao, X., Wang, D.Y. and Dai, J.Y. (2005) Synthesis and ferroelectric properties of multiferroic $BiFeO_3$ nanotube arrays. *Applied Physics Letters*, **87**, 143102.

[22] Wang, Y. and Cao, G. (2007) Synthesis and electrochemical properties of InVO4 nanotube arrays. *Journal of Materials Chemistry*, **17(2298)**, 894-899.

Vol.2, No.7, 694-706 (2010)
doi:10.4236/ns.2010.27086

Natural Science

Formation characterization and rheological properties of zirconia and ceria-stabilized zirconia

Arvind K. Nikumbh*, Parag V. Adhyapak

Department of Chemistry, University of Pune, Ganeshkhind, India; *Corresponding Author: aknik@chem.unipune.ernet.in

Received 17 February 2010; revised 3 May 2010; accepted 8 May 2010.

ABSTRACT

Zirconia and ceria-stabilized zirconia (12Ce-TZP) were synthesized by the dicarboxylate coprecipitation technique such as fumarate, succinate, tartarate and adipate. The formation of these dicarboxylate precursors was studied by elemental analysis, thermal analysis and infrared spectroscopy. The precursors were further decomposed at 650°C for 2 hours to form respective zirconia and ceria-stabilized zirconia. The composition of these oxides was checked by Atomic absorption spectrometer and Energy dispersive X-ray analysis. The structural and morphological characterization of these oxides was done by using X-ray diffraction analysis, surface area, scanning electron micrographs and particle size distribution analysis. These properties were found depending to great extent on the nature of the precursors. The zirconia and ceria-stabilized zirconia obtained from adipate precursor were found to be good for slip-casting. The slips (*i.e.*, suspensions) of these oxides with different solid contents were prepared at different pH with distilled water and ethanol as dispersing agents, with and without deflocculant. The suspension rheological flow (*i.e.*, variation of shear stress and viscosity with shear rate) was determined. The minimum viscosities were observed at pH = 10.16 for ZrO_2-water and pH = 10.26 for 12Ce–TZP-water system. The slip, green and sedimentation bulk density were measured.

Keywords: Oxides; Ceramics; Chemical Synthesis; Surface Properties

1. INTRODUCTION

Zirconia and zirconia-base ceramics are of both scientific and technological interest as structural and functional materials due to their superior properties [1]. These powders have attracted much interest recently due to their specific optical and electrical properties [2-5] and potential applications [6-11]. Zirconia has three polymorphs: monoclinic, tetragonal and cubic [1]. The former is the thermodynamically stable and the other two are metastable polymorphs.

The addition of 'stabilizing' oxides, like CaO, MgO, CeO_2, Y_2O_3 to pure zirconia allows to generate multiphase materials known as partially stabilized zirconia, whose microstructure at room temperature generally consists of cubic zirconia as the major phase, with monoclinic and tetragonal zirconia precipitated as the minor phase [12]. The improvement in the mechanical strength and toughness due to phase transformation in partially stabilized zirconia was first reported by Garvie *et al.* [13].

During the last decades an active research has been undertaken in different laboratories, in order to obtain zirconia and stabilized-zirconia powders with the required characteristics of size, purity, uniformity, crystallinity etc. A variety of methods have recently been described for the preparation of ZrO_2 and CeO_2-ZrO_2 for potential applications. These methods includes conventional methods like co-precipitation [14-20], citrate process [17], polymerized complex process [18-21], sol-gel [22], gel-combustion process [23,24], spray pyrolysis [25], hydrothermal [26], surfactant templating [27,28], ultrasound [29] and sonochemical [30] methods etc.

A strong effort has been directed to increase the overall efficiency of CeO_2-ZrO_2 in various applications. One of the keys to this success is the selection of appropriate preparation methods and composition (*i.e.*, Ce/Zr ratio), which in turn determine homogeneity at a molecular level and morphological properties. Considerable interest is being shown in tetragonal zirconia polycrystalline ceramics. Coyle *et al.* [31] were among the first researchers to study tetragonal zirconia produced using the ZrO_2-CeO_2 system. The presence of tetragonal phase is an essential condition for zirconia toughening besides

hindering or interrupting crack propagation [32].

In all the above technological applications, the control of rheology is of paramount importance for zirconia and partially stabilized zirconia [33-35], especially when stabilization and milling processes are used [33,35,36]. The rheological characteristics of aqueous suspensions depends on several experimental parameters such as particle size and particle size distributions, solids volume fraction, pH of suspending media, type and amount of added dispersing agents [37-40]. Despite the good knowledge of stabilization mechanism [41,42] and the methods to make a well dispersed and stable slip, there is no general process applicable for ceria stabilized ZrO_2 powders.

In this work we have prepared zirconia and ceria-stabilized zirconia by dicarboxylate precursor method. This method offers several advantages for processing ceramic powders such as direct and precise control of stoichiometry, uniform mixing of multicomponents on a molecular scale, and homogeneity. This method is also applied to synthesize ceria-stabilized zirconia showing to be effective to prepare zirconia with a tetragonal structure. In addition, the rheology of zirconia and ceria-stabilized zirconia is investigated in order to find out a suitable stabilization method. Several critical factors related to the slip rheology are studied, such as the influence of the amount of dispersant, and pH on viscosity of concentrated aqueous and nonaqueous slips. Finally, the density of green cast samples is studied and related to the degree of slip dispersion.

2. EXPERIMENTAL PROCEDURE

2.1. Synthesis of Zirconyl Dicarboxylate Precursors

(a) Zirconyl fumarate dihydrate, $ZrO(C_4H_2O_4)\cdot 2H_2O$ was prepared by the precipitation method by taking high purity $ZrO(NO_3)_2\cdot nH_2O$ (9.989 gm) in deionized water (100 ml) in a beaker. The pH of the medium was adjusted to a low enough value ($pH \leq 6$), so that hydroxide precipitate does not form. The solution was stirred vigorously with a magnetic stirrer. To this fumaric acid (0.15 M) solution was then added slowly with stirring till a permanent precipitate occurred (precaution: don't add excess dicarboxylate). Acetone was added in equal amounts to metal salts to get more homogenous, stoichiometric, fine grained powders. The resultant precipitate of $ZrO(C_4H_2O_4)\cdot 2H_2O$ was white in colour. The solution was filtered after stirring it for 30 minutes. The filtrate was checked for Zr^{4+} whose absence ensured complete precipitation. The precipitate was washed several times with cold distilled water and then with acetone to speed up the drying. It was air dried at the ambient temperature.

The similar experimental conditions were used for the preparation of other dicarboxylates such as (b) succinate, $(ZrO(C_4H_4O_4)\cdot 2H_2O)$; (c) tartarate, $(ZrO(C_4H_4O_6)\cdot 2H_2O)$; and (d) adipate, $(ZrO(C_6H_8O_4)\cdot 2H_2O)$.

2.2. Synthesis of Ceria Doped Zirconyl Dicarboxylate Precursors

(a) Ceria doped zirconyl fumarate one and half hydrate, $Ce_{0.12}Zr_{0.88}O(C_4H_2O_4)\cdot 1.5H_2O$ was prepared according to the similar procedure described in above Subsection 2.1. by taking $Ce(NO_3)_3\cdot 6H_2O$ (3.076 gm), $ZrO(NO_3)_2\cdot nH_2O$ (12.012 gm) in deionized water (100 ml).

Other dicarboxylates such as (b) succinate, $(Ce_{0.12}Zr_{0.88}O(C_4H_4O_4)\cdot H_2O)$; (c) tartarate, $(Ce_{0.12}Zr_{0.88}O(C_4H_4O_6)\cdot 2H_2O)$; and (d) adipate, $(Ce_{0.12}Zr_{0.88}O(C_6H_8O_4)\cdot H_2O)$ were prepared by following the procedure given above.

2.3. Synthesis of Zirconia and Ceria-Stabilized Zirconia

For the synthesis of zirconia and ceria-stabilized zirconia, the above dicarboxylate precipitates were decomposed and calcined slowly at 650°C for about 2 h in a platinum crucible under static air atmosphere and then slowly cooled (3°C/min) down to the room temperature. Thus the heat treatment is sufficient for achieving a complete decomposition of dicarboxylates. The powder obtained was polycrystalline. This sample was then reground and recalcined at the same temperature for another 2 h. The furnace was turned off and sample was removed at room temperature. The obtained samples of zirconia and ceria-stabilized zirconia were stored in a desiccator.

2.4. Sample Characterization

The elemental analysis of carbon and hydrogen were done by microanalytical technique. The metal analysis of the samples was carried out by Atomic absorption spectrometer (AAS) and Energy dispersive X-ray analysis (EDAX). The infrared spectra of precursor were recorded in the region 4000-450 cm^{-1} on the Perkin-Elmer – 1600 series FTIR spectrophotometer using KBr pellets. The TGA, DTG and DTA were recorded on Mettler Toledo 850 instrument.

The X-ray powder diffraction patterns were determined on Rigaku Miniflex Diffractometer using CuK_α radiation (λ = 1.5405 Å; nickel filter). The BET surface area was determined from N_2 adsorption isotherms using a Coulter (Omnisorp 100 CX) instrument. Morphological studies were carried out using scanning electron microscope (SEM) Philips 30XL model. The particle size distribution analysis was done using a dynamic light scattering method (Ultrafine Particle Analyzer (UPA) from Leeds and Northrup instrument).

2.5. Slip Preparation and Characterization

For studying suspension rheological flow characteristics of oxide powders, several suspensions were prepared at conditions where they could be cast. Rheological tests permit to identify the conditions where the suspensions are better dispersed. For these tests, zirconia and ceria-stabilized zirconia suspensions were prepared in water and ethanol with different solid loading, by using two different deflocculants such as Darvan (*i.e.* polymethcrylic acid) and M2OC (*i.e.* ammonium polyacrylate), by varying their concentrations and by varying the pH of the suspension.

The suspensions were placed in a polyethylene bottle with alumina balls and milled for 24 h to achieve good homogenous dispersion. After dispersing, the suspensions were degassed for several minutes under a rotary vacuum pump. Elico pH-meter with a glass combination electrode was used to measure the pH in all suspension (*i.e.* slip). Hydrochloric acid (HCl) and tetramethyl ammonium hydroxide ($C_4H_{13}NO$) solutions were used to adjust the suspension pH. Suspension rheological flow characteristics (*i.e.* variation of shear stress and viscosity with shear rate) were determined with Brookfield viscometer model RVT with small sample adaptor accessory SC4 – 14/6R.

The degree of dispersion stability in the ceramic slurries was determined by measuring slip and sedimentation bulk density. For measuring the slip density, the suspension was poured in 5 ml specific gravity bottle and suspension weight was measured. Sedimentation bulk density was determined by pouring the suspension *i.e.* slip (of known weight) into 5 ml measuring cylinder. The measuring cylinder was covered with flexible film (to prevent solvent evaporation) and the particles in suspension were allowed to settle until the sediment height no longer changed with time. The sedimentation bulk volume was determined directly from sedimentation height in the measuring cylinder. The weight of ZrO_2 or ceria-stabilized ZrO_2 in the sedimentation volume was determined by multiplying the known weight of suspension in the cylinder times the known weight percentage of ZrO_2 or ceria-stabilized ZrO_2 in the suspension.

The suspension was then cast in a 20 mm × 20 mm × 10 mm acrylate mould placed on a plaster of Paris bricks. After 2 h, the cast solid (*i.e.* green body) was removed from the mould. The obtained green bodies were dried at room temperature for one day, and then at 110°C for one day.

For measuring the percent shrinkage, the dimension of the green bodies dried at room temperature was measured using the Vernier caliper. The green bodies were then dried at 110°C for one day in electric oven. After drying again the dimension of the green bodies was measured. The green density of the samples was measured using Archimedes method. Before determination of the weight in water, the green bodies were immersed in paraffin to close the pores.

3. RESULTS AND DISCUSSION

3.1. Dicarboxylate Coprecipitation

During synthesis, several parameters which may influence the amount of zirconyl dicarboxylate precipitates at 25°C. In order to reach required stoichiometry in dicarboxylate precipitates, the control pH and concentration of metal salt solution is very important.

1) Effect of zirconium concentration

A series of experiments has been made to determine the most appropriate zirconium concentration values for a maximum precipitation of dicarboxylates. Several dicarboxylates such as fumarate, succinate, tartarate and adipate have been prepared with the zirconium concentration ranging from 0.05 to 0.4 M. The maximum amount of zirconyl dicarboxylate precipitates (~90%) are obtained for the zirconium content equals to 0.25 M.

2) Effect of dicarboxylate concentration

A second series of trials has been made to determine the most appropriate concentrations of dicarboxylic acids such as fumaric, succinic, tartaric and adipic acid. It is observed that in all cases the maximum (~92%) precipitation yield is obtained when dicarboxylic acid concentration is equals to 0.15 M. For more dicarboxylic acid concentration, it shows a decrease of zirconyl precipitation. Therefore to balance this concentration and to satisfy practical considerations, we use optimal concentration, *i.e.*, 0.15 M dicarboxylic acid is used for precipitation.

In case of zirconyl dicarboxylates, the effect of pH could not studied, since for pH adjustment, precipitation occur immediately by addition of 10% NH_4OH. So the pH and dicarboxylic acid concentration have been chosen so that the solubility of zirconyl dicarboxylates is as low as possible. It is difficult to give an exact figure for new solubility values for dicarboxylate precipitate. The best range of pH ≈ 4.5 to 6.0 is used for the synthesis of zirconyl dicarboxylate (*i.e.* precursor).

3.2. Characterization of Dicarboxylate Precursors

The composition of precursor is characterized at first stage by elemental analysis and Atomic absorption spectrometry (AAS). The elemental analysis of dicarboxylate precursors were made in wt.%: for fumarate, ZrO ($C_4H_2O_4$)·$2H_2O$ (C, 18.83 (18.67); H, 2.22 (2.33); Zr, 35.86 (35.45)) and $Ce_{0.12}Zr_{0.88}O(C_4H_2O_4)\cdot 1.5H_2O$ (C, 18.32 (18.90); H, 2.06 (1.96); Zr, 31.60 (31.57); Ce, 6.51 (6.61)). For succinate, $ZrO(C_4H_4O_4)\cdot 2H_2O$ (C, 18.67 (18.52); H,

2.54 (3.08); Zr, 35.19 (35.18)) and $Ce_{0.12}Zr_{0.88}O(C_4H_4O_4)\cdot H_2O$ (C, 19.53 (19.43); H, 2.65 (2.42); Zr, 32.55 (32.47); Ce, 6.93 (6.80)). For tartarate, $ZrO(C_4H_4O_6)\cdot 2H_2O$ (C, 16.65 (16.49); H, 2.84 (2.74); Zr, 31.18 (31. 31)) and $Ce_{0.12}Zr_{0.88}O(C_4H_4O_6)\cdot 2H_2O$ (C, 16.45 (16.17); H, 3.01 (2.69); Zr, 27.16 (27.00); Ce, 5.73 (5.65)). For adipate, $ZrO(C_6H_8O_4)\cdot 2H_2O$ (C, 24.81 (25.07); H, 3.71 (4.17); Zr, 31.95 (31.74)) and $Ce_{0.12}Zr_{0.88}O(C_6H_8O_4)\cdot H_2O$ (C, 26.24 (26.16); H, 3.12 (3.63); Zr, 29.18 (29.15); Ce, 6.07 (6.11)). The values in the parenthesis are calculated ones. The observed values are found to be ± 0.5% of the nominated values.

The energy dispersive X-ray analysis (EDAX) further confirms all the cations were present in a perfect cationic ratio in the precursor. The peaks pertaining to all the cations were present in the EDAX spectrum. The elemental composition analysis at several spots was uniform, which is indicative of a highly homogeneous material. This is due to the fact that all the cations are uniformly mixed.

The presence of water of crystallization for these precursors was confirmed on the basis of the thermal analysis curves under static air atmosphere. These results are further supplemented by infrared spectroscopic measurements. The bidentate linkage of dicarboxylate group with metal was confirmed on the basis of the difference between the antisymmetric and symmetric stretching frequencies. A chain like polymeric octahedral structure has been assigned by infrared spectra for these precursors.

Thermal analysis (TGA, DTG and DTA) of the precursors shows that all the complexes dehydrate and decompose in the temperature range 30-600°C. It is observed that the weight loss in TGA corresponds to the formation of respective zirconia or ceria-stabilized zirconia.

3.3. Characterization of Zirconia and Ceria-stabilized Zirconia

After characterizing the above precursor was decomposed slowly at 650°C to form respective oxides. The X-ray diffraction (XRD) patterns of zirconia obtained from all precursors shows the tetragonal phase. The experimentally observed d-spacing values and relative intensities are compared with those reported in the literature [43]. The lattice parameters for each compound are calculated and are listed in **Table 1**.

Similarly the addition of 3, 6, 9, 12 mol.% of ceria to the system, allows stabilization of zirconia matrix in tetragonal phase. It is observed that for 3 to 9 mol.% ceria in ZrO_2, the diffraction peak to XRD spectra reveal that the material crystallizes in face centered cubic fluorite type structure. However, for 12 mol.% ceria in ZrO_2 powder, the diffraction lines are matched to the tetragonal phase, on the other hand above 12 mol.% ceria the tetragonal phase is collapse. Thus 12 mol.% ceria stabilized ZrO_2 retained tetragonal phase at room temperature. The experimentally observed d-spacing values and relative intensities are compared with those reported in the literature [43]. The lattice parameter for 12 mol.% ceria stabilized zirconia prepared from different dicarboxylate are then calculated and shown in **Table 1**.

The morphology of ceria-stabilized ZrO_2 powders was also analyzed by scanning electron micrographs (SEM), which revealed agglomerates with irregular shape and variable packing density of their primary particles (**Figure 1**). According to literature [44], these agglomerates can be classified as 'soft' or 'hard', the hard agglomerates consisting of close-packed particles with high densities. As can be seen from **Figures 1(a)** and **(b)**, the 3 and 6 mol% ceria stabilized zirconia shows agglomerated structures, while 9 mol% ceria content zirconia show fused agglomerates (**Figure 1(c)**). However, for 12 mol% ceria content zirconia, the SEM show less dense agglomerates, suggesting soft agglomerates with particles connected by Van der Waals forces. Thus increasing ceria content, the concentration of intra-aggregate pore are decreased meaning a reduction of the aggregates content, up to the disappearance for powder containing12 mol.% CeO_2.

The common notation used in tetragonal zirconia

Table 1. X-ray Powder diffraction and particulate properties data of zirconia and ceria-stabilized zirconia powders.

Compound	Lattice Parameters (nm) a_0	c_0	Mean Grain size $<D>_{Xray}$ nm ± 10 %	Surface Area m^2/g	Average particle size (by SEM) nm
			(a) zirconia		
Fumarate	0.511	0.518	21.03	4.87	900
Succinate	0.510	0.519	22.37	1.00	427
Tartarate	0.510	0.519	22.11	1.83	569
Adipate	0.511	0.518	16.77	7.26	222
			(b) ceria-stabilized zirconia		
Fumarate	0.509	0.513	18.03	10.33	178
Succinate	0.507	0.511	19.24	12.88	357
Tartarate	0.510	0.513	14.35	11.26	476
Adipate	0.507	0.512	13.46	10.55	264

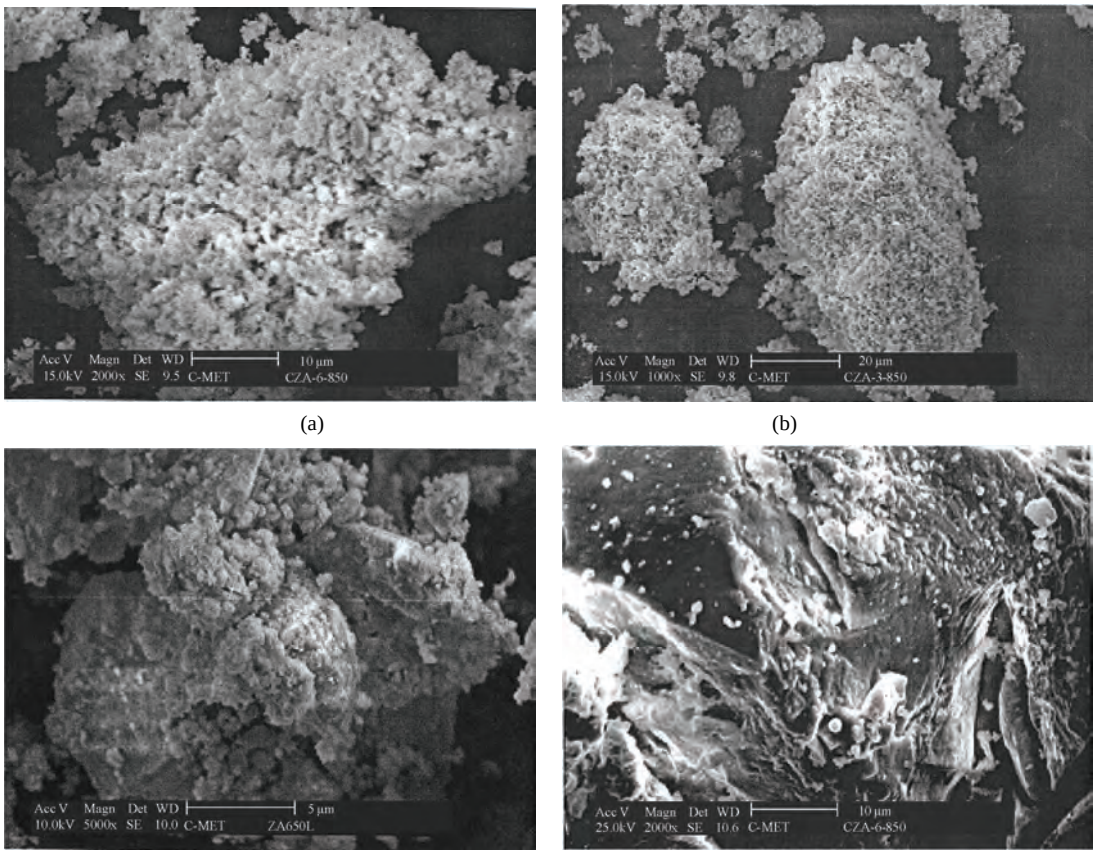

Figure 1. Scanning electron micrographs (SEM) of zirconia powders containing: (a) 3 mol.% ceria; (b) 6 mol.% ceria; (c) 9 mol.% ceria and (d) 12 mol.% ceria.

polycrystal (TZP), literature [45] involves placing the cation symbol of the stabilizing oxide before the TZP abbreviation. In some cases the molarity of the stabilizing oxide will be indicated by a number before the cation symbol e.g.

$$ZrO_2 - 12 \text{ mol.\% } CeO_2 = 12 \text{ Ce} - \text{TZP}.$$

The mean grain sizes of ZrO_2 and 12Ce–TZP are also calculated from Debye-Scherrer equation [46]. The observed mean grain size $\langle D \rangle_{X\text{-ray}}$ for ZrO_2 and 12Ce–TZP compounds are respectively in the range of 16.77 to 22.36 nm, and 13.46 to 19.24 nm (**Table 1**). The BET specific surface areas are also listed in **Table 1**. Under the experimental conditions, the CeO_2 content affected both grain size and surface area of the powders. As observed in **Table 1**, the grain size decreases with the increase of CeO_2 content, *i.e.*, grain growth of zirconia is inhibited by the ceria doping in zirconia. It is interesting to observe here that, surface areas increased with a increase of CeO_2 content because of the crystallite coarsening. This suggests that increasing ceria content reduces the surface free energy of zirconia particles and so increases the surface area, which is accompanied by more effective tetragonal phase stabilization.

Figure 2 shows scanning electron micrographs (SEM) of ZrO_2 and 12Ce–TZP powders obtained from fumarate, succinate, tartarate and adipate precursors at 650°C. The ZrO_2 powder obtained from fumarate precursor shows higher degree of agglomerations, whereas ZrO_2 obtained from tartarate shows apparent agglomeration of very fine particles (**Figure 2(a)**). Highly irregular shaped large particles are observed in case of ZrO_2 obtained from succinate. Moderate sized particles with less agglomeration are observed in ZrO_2 obtained from adipate. The average particle size for all ZrO_2 powders is in the range of 222 to 900 nm.

All 12Ce–TZP powders show less agglomerated structures as compared to ZrO_2 powders (**Figure 2(b)**). Among these powders the 12Ce–TZP obtained from adipate precursor shows moderate size less agglomerated particles than 12Ce–TZP obtained from fumarate, succinate and tartarate precursor. The average particle sizes of 12Ce–TZP powders obtained from different dicarboxylates are in the range of 178 to 476 nm.

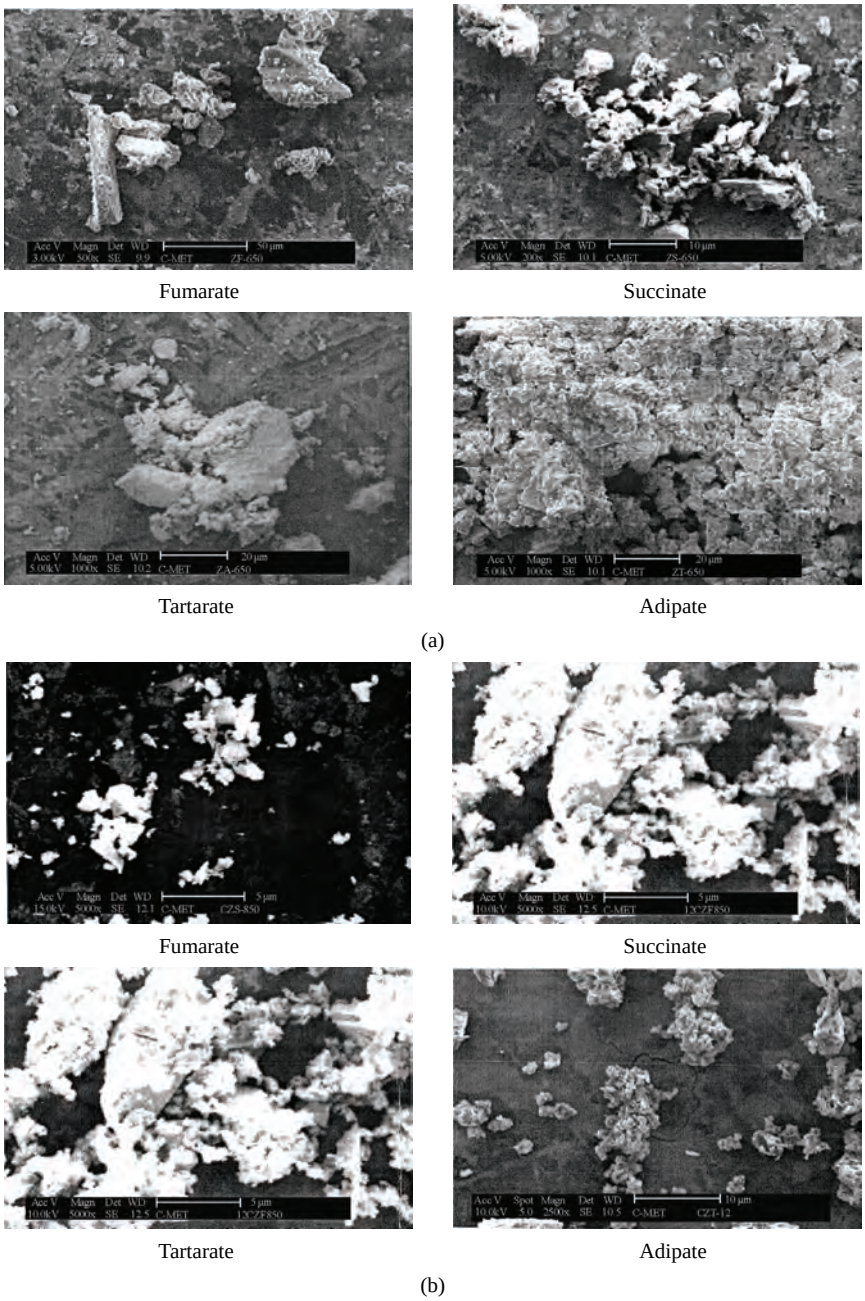

Figure 2. Scanning electron micrographs (SEM) of (a) zirconia (ZrO_2) (b) ceria-stabiized zirconia (12 Ce–TZP) powders obtained from different dicarboxylate precursors.

3.4. Rheological Studies

3.4.1. Powder Characteristics

Particle size distribution was measured using laser based particle size analyzer. The preliminary experiments indicated that distilled water and ethanol could be used to disperse the powder. **Figure 3** displays the particle size distribution of ZrO_2 and 12Ce–TZP powders obtained from different dicarboxylates. From the particle size distribution measurements occurred that the powder exhibits a wide size distribution and 90% powder being below 2.5 μm for ZrO_2 and 0.9 μm for 12Ce–TZP (**Figures 3(a)** and **(b)**). The particle size distribution of ZrO_2 obtained from adipate precursor show 30 to 40% particles below 1.6 μm and remaining particle have above 1.6 μm. While, 12Ce–TZP powders shows 30 to 40% particles of 0.4 μm range and remaining have above 0.4 μm. Thus bimodal type of particle distribution is observed in both the oxides obtained from adipate precursor. The

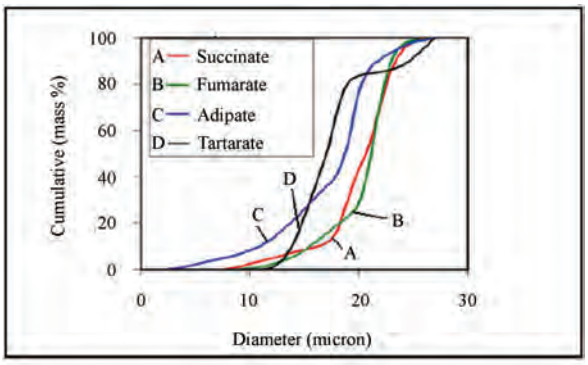

(a)

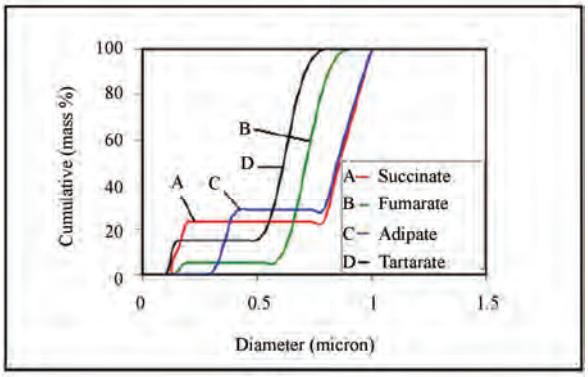

(b)

Figure 3. Particle size distribution analysis of (a) zirconia ZrO_2 and (b) ceria stabilized zirconia 12 Ce-TZP powders obtained from different dicarboxylate precursors.

particle packing is based on the concept of filling the voids in a bed of large spheres with smaller sized spheres. The remaining pores between the smaller spheres are then filled with still smaller spheres, etc. to give good particle packing [47]. The particle size distribution of ZrO_2 and 12Ce–TZP powders obtained from fumarate, succinate and tartarate shows either smaller or larger particles (**Figure 3**). Thus ZrO_2 and 12Ce–TZP obtained from adipate are considered to be good for slip-casting and hence we prepared in large quantity (~ 200 gm).

3.4.2. Optimization of Rheological Properties of Slurries

The state of particulate dispersion is affected mainly by particle size and particle size distribution, specific surface area of powder and on chemistry of solid/liquid interface [48], dispersion mechanism [49], and so on. The viscosity of the suspensions increases drastically and abruptly, when the weight percent of solid in the suspension is increased beyond a critical value.

1) Effects of solid loading

The present study shows the viscosity versus shear rate (**Figure 4**) for aqueous (distilled water) and non-aqueous (ethanol), ZrO_2 and 12Ce–TZP (obtained from adipate precursor) suspensions prepared with various solid loadings (solid/liquid ratios of 75/25, 80/20 and 70/30 by weight and 1.0 wt.% M20C deflocculant). It can be seen that the aqueous and non-aqueous suspensions with 80 wt.% maximum loading can be achieved a low viscosity for ZrO_2 powder, while 75 wt.% maximum solid loading can be seen the suspension exhibit low viscosity for 12Ce–TZP powder. Above these weight percent, the suspension has a high viscosity and pseudoplastic behavior.

2) Effect of dispersant concentration

In the present study, Darvan and M20C are used as a dispersants (sometimes called deflocculants). The viscosity versus shear rate curves of the suspensions with constant solid loading (80 wt.% ZrO_2 and 75 wt.% 12Ce–TZP) in the presence of different added amounts of Darvan and M20C dispersants are presented in **Figures 5** and **6** respectively. From the plots, an optimum Darvan concentration with 1 wt% for ZrO_2-water and ethanol system and 0.8 wt% for 12Ce–TZP-water and ethanol system could be determined to be minimum viscosity (**Fig-**

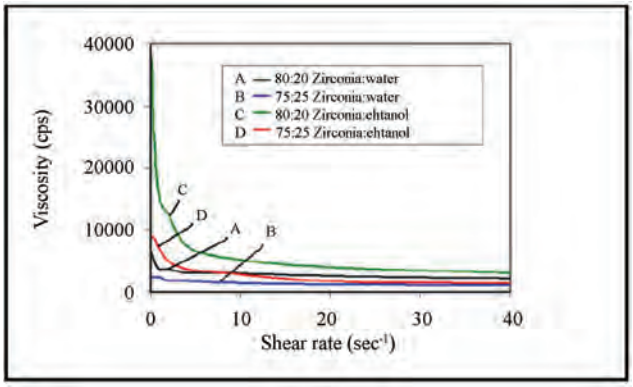

(a)

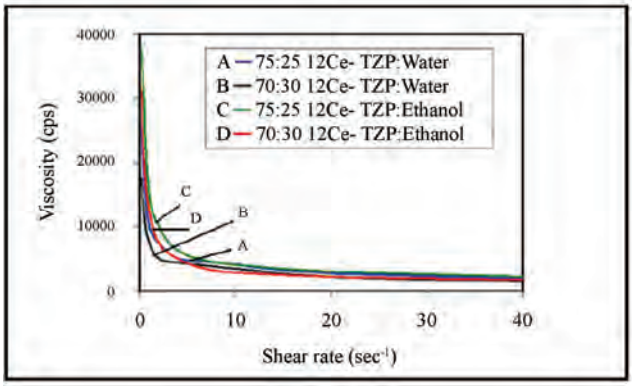

(b)

Figure 4. Plots of viscosity against shear rate with different percentage solid loading. (a) zirconia and (b) 12 Ce–TZP powders in water and ethanol system.

ure 5). Similarly, in the presence of M20C dispersant, the optimum concentration with 1.2 wt% for ZrO_2-water and ethanol system and 1.0 wt% for 12Ce–TZP-water and ethanol, the suspension exhibits nearly constant viscosity and could be fitted to Newtonian flow behavior (**Figure 6**). With further increasing the amount of dispersant, the suspensions show pseudoplastic behavior and the viscosity level also increases. It is interesting to observe that the M20C is the best dispersant, which show minimum value of viscosity than Darvan dispersant. Similarly, slurries prepared in distilled water along with M20C dispersant show low viscosity than slurries prepared in ethanol medium. Thus, distilled water and M20C dispersant are used for rheological studies for ZrO_2 and 12Ce–TZP powders.

In above two cases, with low solid loading, the mag-nitude of the average Van der Waals forces could be small due to the relatively large distance between suspended particles, so a small addition of dispersant could lead to repulsion forces with enough magnitude to counterbalance Van der Waals forces [50], and the frequency of the collisions between separated particles is lower.

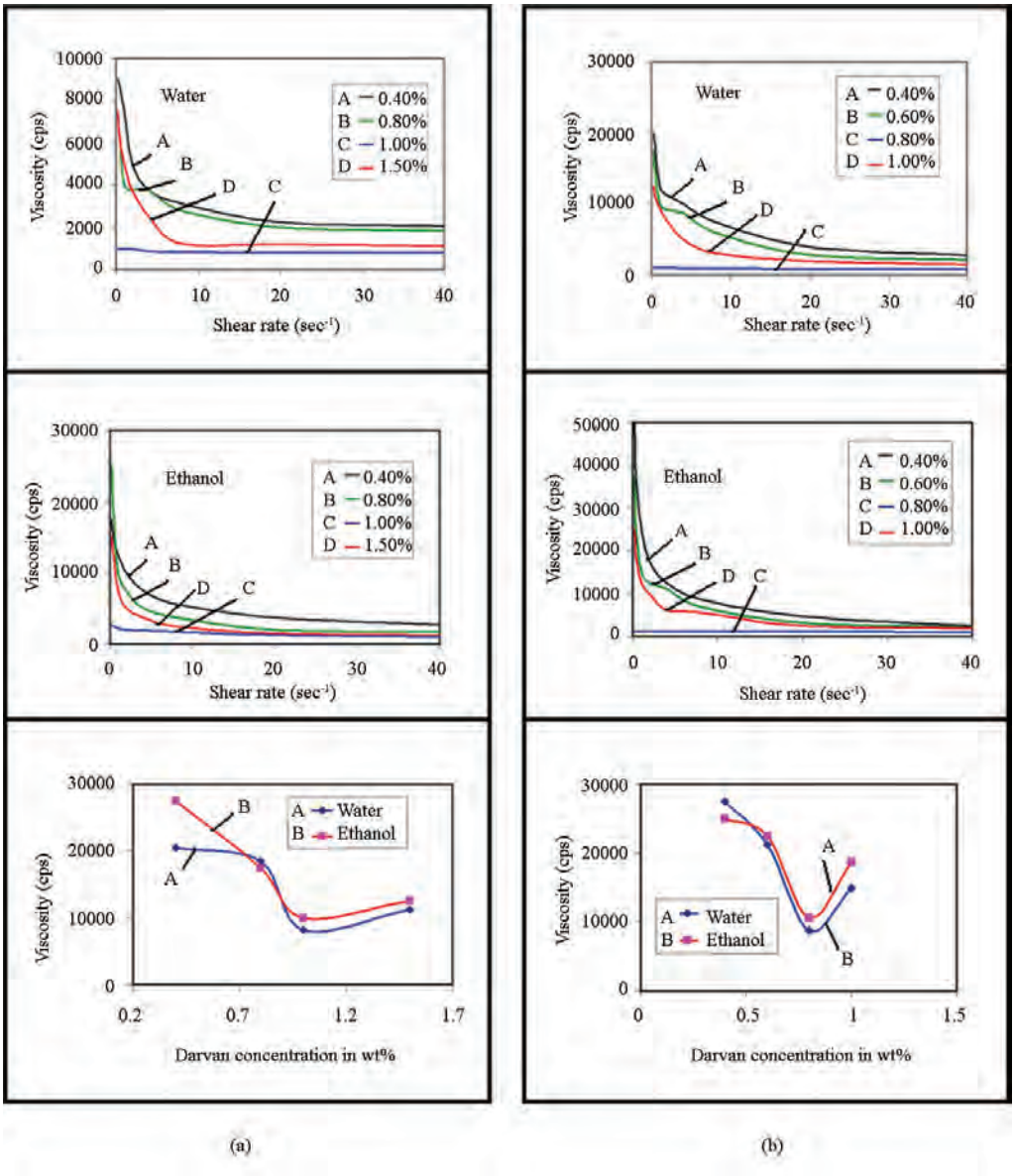

Figure 5. Plots of viscosity against shear rate for different concentration of Darvan deflocculant (dispersant) in water and ethanol system and plots of viscosity against Darvan concentration (at constant shear rate of 40 sec^{-1}). (a) ZrO_2; (b) 12 Ce–TZP powders.

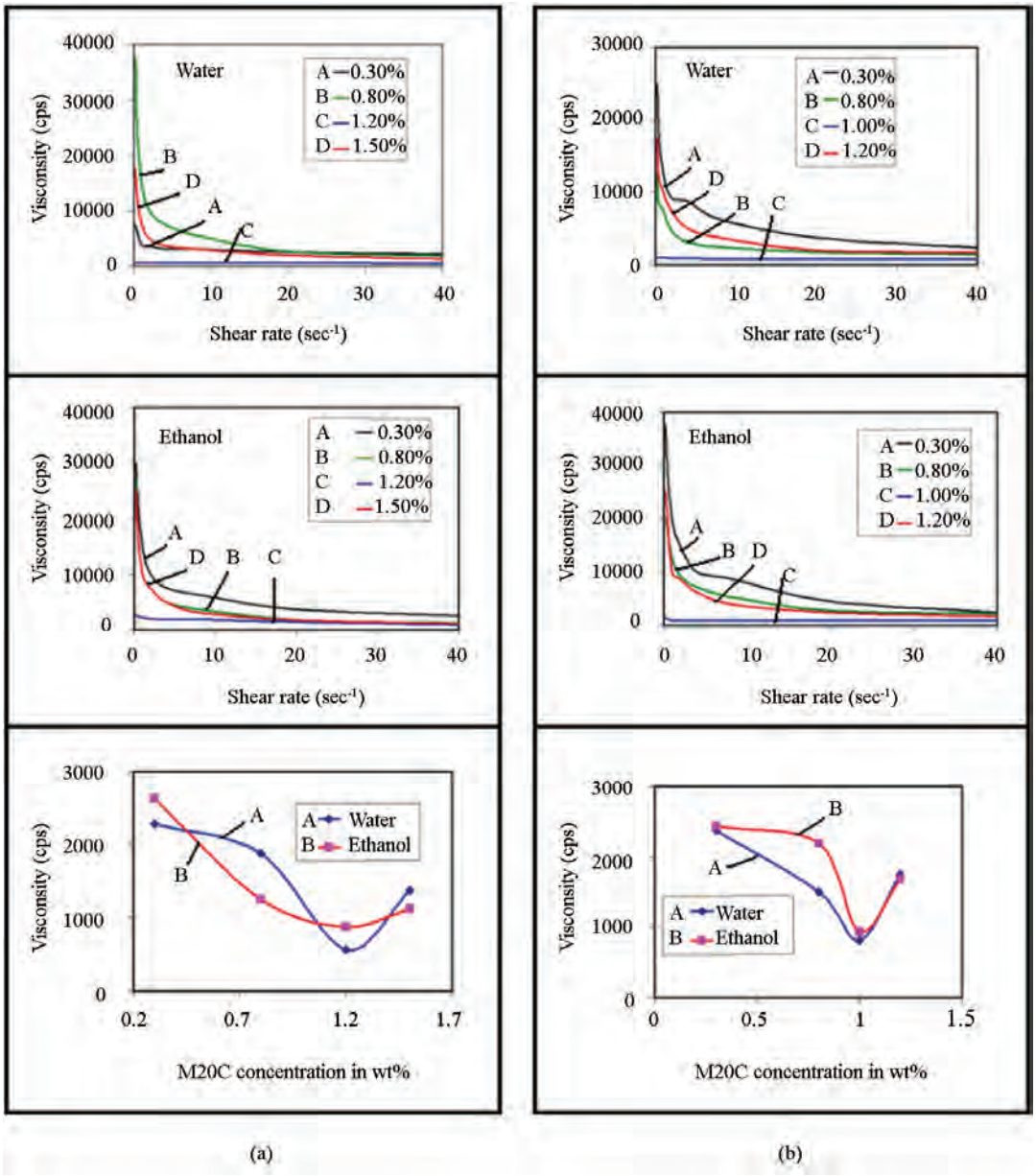

Figure 6. Plots of viscosity against shear rate for different concentration of M20C deflocculant (dispersant) in water and ethanol system and plots of viscosity against M20C concentration (at constant shear rate of 40 sec^{-1}). (a) ZrO_2 (b) 12 Ce–TZP powders.

This explains why the rheological properties of the suspensions are almost unaffected by the amount of dispersant at low solids loading. However, it should also be pointed out that due to insufficient surface coverage at lower dispersant additions, the balance between Van der Waals forces and steric forces is not completely stable, and agglomerates would easily form through the uncovered surface sites due to Brownian motion. With increasing solid loading, the importance of Van der Waals forces also increases due to the shorter distances between suspended particles. Therefore, agglomerates will readily form if insufficient amount of dispersant is added, under which conditions Van der Waals forces will dominate the interaction between suspended particles, and significant shear thinning will be observed due to the breakdown of agglomerates because of the applied shear [51].

3.4.3. Rheology of Slips

One of the widely practiced methods to stabilize the slips is electrostatic stabilization, achieved by the repulsion of equally charged particles. The repulsive interac-

tion results from the development of an electric double layer around the particles up on dispersing a powder into a aqueous (polar) media and is a function of pH, the concentration of specifically adsorbed ions and the ionic strength of the suspension [52]. The repulsive force decreases with increasing separation between the particles. The possibility of electrostatic stabilization can be evaluated by measuring viscosity-shear rate as a function of pH.

To study the rheological properties, the slips were prepared in the following way:

1) 80 wt% ZrO_2 and 20 wt% distilled water along with 1.2 wt% M20C dispersant.

2) 75 wt% 12Ce–TZP and 25 wt% distilled water along with 1.0 wt% M20C dispersant.

After homogeneous mixing of slips, the pH was adjusted to various levels by adding HCl or tetramethyl ammonium hydroxide. In slip-casting processing, the amount and rate of dissolution of ions is important [53]. The dissolution of Zr is lower than that of Si and is slightly reduced with increasing mixing time, *i.e.*, above 110 h [42]. In other report [54], cerium dissolution rate of Ce-ZrO_2 powder under slightly acidic conditions (pH = 3 to 5.5), only small amounts (1-2 mg L^{-1} after 10 h stirring) of cerium were dissolved. No dissolution of cerium or zirconium was found under basic conditions. According to these literatures, in the present case the slurries were prepared by mechanical stirring at room temperature for 4 h before the viscosity measurements. Thus, the dissolution of Zr and Ce are totally negligible in our samples (ZrO_2 and 12Ce–TZP powders). The slurry stability was also evaluated by measuring the settling of powder (sedimentation height as a percentage of the total suspension height) for different pH of the slips. The viscosity behavior and sedimentation density are given in **Table 2**.

Figures 7(a) and **(b)** show the rheological behavior (*i.e.* viscosity-shear rate) at several pH values for ZrO_2-water and 12Ce-TZP-water systems, with M20C dispersant (*i.e.* deflocculant). The viscosity dependence of various pH values at constant shear rate (D = 40 sec^{-1}) are also shown in **Figure 7**. It is seen that, at neutral pH the viscosity shows a maximum value, while for acidic or basic range of pH, the viscosity shows a minimum value. At these minimum viscosity values, the rheological behavior is Newtonian, *i.e.*, viscosity is independent of shear rate. At this pH range, the particles are well dispersed and show high slip and sedimentation density. These results are also presented in **Table 2**. At remaining pH values, viscosity is high and slip has pseudoplastic behavior. Thus, the high sedimentation density and low viscosity values tend to form good green bodies. Usually, basic slips are preferred to prevent the rapid formation of strong bond between the contracted particulate suspension and mould during casting process [53]. On the other hand a high concentration of acid slips is corrosive and attacks the mould used for casting, which can cause contamination by dissolution of gypsum.

3.4.4. Slip Casting

The packing ability of the dispersed particles on the slip casting is a good index of the dispersion degree achieved in the suspensions, and was evaluated by pouring the required amounts of the slips into a plaster mould. The ZrO_2 and 12Ce–TZP slips obtained at different pH are then de-aired under a mild vaccum for 15 min. These slips are then poured into a square plaster mould (20 mm × 20 mm × 10 mm). The liquid is draw into pores by capillary action. After 2 h the rectangular green bodies were removed from the mould and dried at room temperature for 24 h and then put in an oven at 110°C for another 24 h period. The percent shrinkage was calcu-

Table 2. Rheological properties of ZrO_2 and 12Ce–TZP slips at several pH values

pH	Viscosity Behaviour	Slip density (gm cm^{-3})	Bulk sedimentation density (gm cm^{-3})	% Shrinkage	Green density (% Theorotical)
		(a) 80 wt% ZrO_2 + 20 wt% water + 1.2 wt% M20C			
1.26	Pseudoplastic	2.86	2.47	0.62	59.99
3.11	Newtonian	2.86	2.58	0.08	71.98
5.76	Pseudoplastic	2.86	2.47	1.03	45.06
8.58	Near Newtonian	2.87	2.54	1.40	72.99
10.16	Newtonian	2.86	2.66	0.16	77.94
13.34	Pseudoplastic	2.86	2.44	0.13	50.27
		(b) 75 wt% 12Ce–TZP + 25 wt% water + 1.0 wt% M20C			
2.11	Pseudoplastic	2.93	2.58	0.21	47.51
3.41	Near Newtonian	2.90	2.61	0.18	60.14
6.06	Pseudoplastic	2.92	2.52	1.28	42.12
8.16	Near Newtonian	2.89	2.69	1.01	72.19
10.26	Newtonian	2.90	2.71	0.98	75.86
13.04	Pseudoplastic	2.92	2.57	1.52	45.70

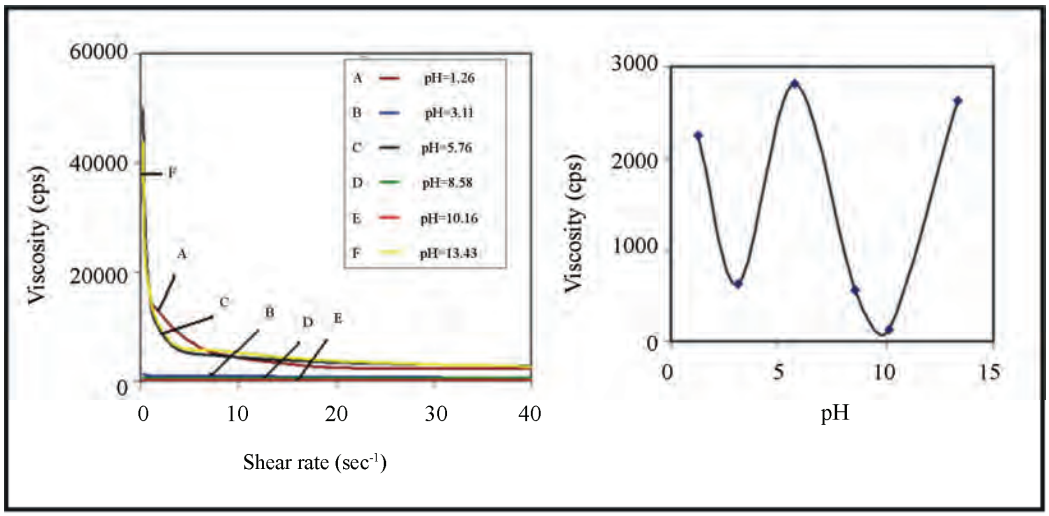

(a)

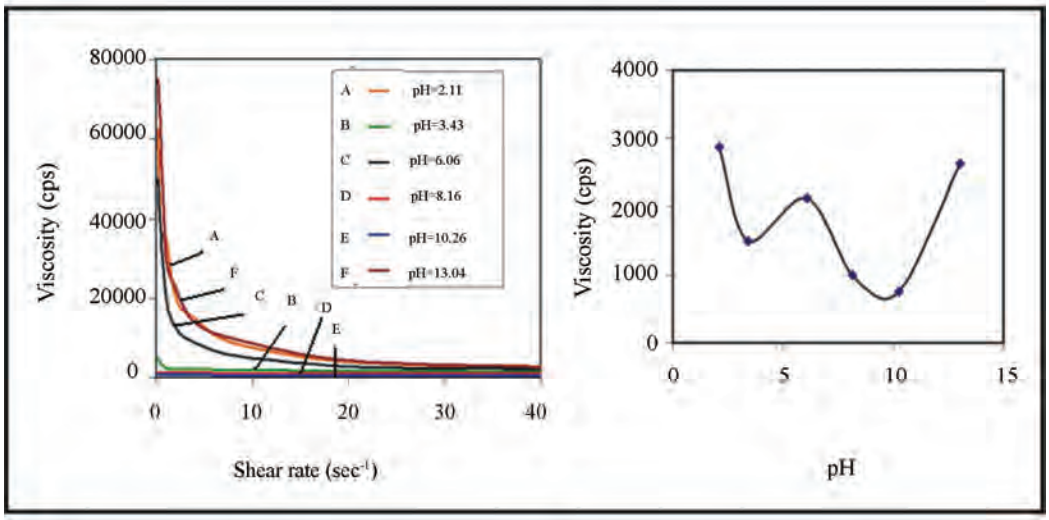

(b)

Figure 7. Plots of viscosity against shear rate for suspensions with pH values indicated and plots of viscosity against several pH values (at constant shear rate of 40 sec^{-1}). (a) 80 wt.% zirconia–20 wt.% water–M20C deflocculant; (b) 75 wt.% 12 Ce–TZP –25 wt.% water–M20C deflocculant.

lated. The density of green bodies was also measured according to the Archimedes method. These results are also summarized in **Table 2**. For both the systems, the highest green density and low percent shrinkage corresponds to minimum viscosity of Newtonian behavior are observed. In these systems, the highest theoretical green density was 77% for ZrO_2 and 75% for 12Ce–TZP. The acidic slips of ZrO_2 and 12Ce–TZP (both in water-M20C system) are found to be minute pits on the mould surface after casting. Basic slips however have a general roughening of the surface rather than pitting. The solid casting obtained from ZrO_2 is white, good in nature and higher strength than the solid-cast obtained from 12Ce–TZP and it has pale yellow in colour.

4. CONCLUSIONS

The results presented in this work enable us to draw the following conclusions:

1) Zirconia (ZrO_2) and ceria-stabilized zirconia (12 mol% ceria in ZrO_2) powders are synthesized by different dicarboxylates such as fumarate, succinate, tartarate and adipate precursor method.

2) Based on the results obtained from X-ray diffrac-

tometry, particle size distribution, scanning electron microscopy and BET surface area measurements, ZrO_2 and ceria-stabilized ZrO_2 (12Ce–TZP) powders obtained from adipate precursor are found to be good for slip casting. Both powders have tetragonal structure. The ceria addition is affected the powder characteristics. The grain size decreases with ceria content, which is accompanied by more effective tetragonal phase stabilization in this powder.

3) The intensity of shear during slip preparation, as controlled by the solid volume fraction, has a great influence on the dispersion efficiency, which, in turn, is reflected in the rheological characteristics of the suspensions and their packing ability on slip-casting. Preliminary test on the rheological behavior shows 80 wt% ZrO_2 and 75 wt% 12Ce–TZP powders in distilled water and M20C dispersant gives minimum viscosity and Newtonian flow behavior.

4) Rheological properties show minimum viscosity for the system ZrO_2-water-M20C at pH = 10.16 and 12Ce–TZP-water-M20C at pH = 10.26. At these pH range, the particles are well dispersed and show high slip, green and sedimentation density. The green density seems even more reliable in the evaluation of the dispersing degree.

5) The solid casting obtained from ZrO_2 powder is white, good in nature and higher strength than 12Ce–TZP powder and it has pale yellow colour.

5. ACKNOWLEDGEMENTS

The authors thank Dr Grathwhol from Universitat Bremen, Germany, for suggestions and helpful discussions. They also thank the Executive Director, Centre for Materials for Electronics Technology (C-MET) and Dr. C. V. Rode, National Chemical Laboratory (NCL), Pashan Road, Pune-411008, India, for the facilities given for part of the work.

REFERENCES

[1] Hannink, R.H.J., Kelly, P.M. and Muddle, B.C. (2000) Transformation toughening in zirconia-containing ceramics. *Journal of the American Ceramic Society*, **83(3)**, 461-487.

[2] Marray, E.P., Tsai, T. and Barnett, S.A. (1999) A direct-methane fuel cell with a ceria-based anode. *Nature*, **400(6745)**, 649-651.

[3] Haase, F. and Sauer, F. (1998) The surface structure of sulfated zirconia: Periodic ab initio study of sulfuric acid adsorbed on ZrO_2(101) and ZrO_2(001). *Journal of the American Chemical Society*, **120(51)**, 13503-13512.

[4] Chandwick, A.V. (2000) Nanotechnology: Solid progress in ion conduction. *Nature*, **408(6815)**, 925-926.

[5] Steele, B.C.H. and Heinzel, A. (2001) Materials for fuel-cell technologies. *Nature*, **414(6861)**, 345-352.

[6] Wu, N.L., Wang, S.Y. and Rusakova, I.A. (1999) Inhibition of crystallite growth in the sol-gel synthesis of nanocrystalline metal oxides. *Science*, **285(5432)**, 1375-1377.

[7] Maczka, M., Lutz, E.T.G., Verbeck, H.J., Oskam, K., Meijerink, A., Hanuza, J. and Stuivinga, M. (1999) Spectroscopic studies of dynamically compacted monoclinic ZrO_2. *Journal of Physics and Chemistry Solids*, **60(12)**, 1909-1914.

[8] Park, S., Vohs, J.M. and Gorte, R.J. (2000) Direct oxidation of hydrocarbons in a solid-oxide fuel cell. *Nature* **404(6775)**, 265-267.

[9] Cheung, T.K. and Gates, B.C. (1997) Activation of ethane in the presence of solid acids: Sulfated zirconia, iron- and manganese-promoted sulfated zirconia, and zeolites. *Journal of Catalysis*, **168(2)**, 522-531.

[10] Sayama, K. and Arakawa, H. (1993) Photocatalytic decomposition of water and photocatalytic reduction of carbon dioxide over zirconia catalyst. *Journal of Physical Chemistry*, **97(3)**, 531-533.

[11] Shi, J.L. (1999) Relation between coarsening and densification in solid-state sintering of ceramics: Experimental test on superfine zirconia powder compacts. *Journal of Materials Research*, **14(4)**, 1389-1397.

[12] Subbarao, E.C. (1981) Advances in ceramics. *Science and Technology of Zirconia*, Heuer, A.H. and Hobbs, L.W., Eds., Elsevier, Amsterdam, **3**, 1-24.

[13] Garvie, R.C., Hannink R.H. and Pascoe, R.T. (1975) Ceramic steel. *Nature*, **258(5537)**, 703-704.

[14] Yashima, M., Morimoto, K., Ishizawa, N. and Yoshimura, M. (1993) Zirconia–ceria solid solution synthesis and the temperature–time–transformation diagram for the 1:1 composition. *Journal of the American Ceramic Society*, **76(7)**, 1745-1750.

[15] Murugave, P., Kalaiselvam, M., Raju, A.R. and Rao, C.N.R. (1997) Sub-micrometre spherical particles of TiO_2, ZrO_2 and PZT by nebulized spray pyrolysis of metal–organic precursors. *Journal of Materials Chemistry*, **7(8)**, 1433-1438.

[16] Li, M., Feng, Z., Xiong, G., Ying, P., Xin, Q. and Li, C. (2001) Phase transformation in the surface region of zirconia detected by uv raman spectroscopy. *Journal of Physical Chemistry B*, **105(34),** 8107-8111.

[17] Yashma, M., Kakihana, M., Ishii, K., Ikuma Y. and Yoshimura, M. (1996) Synthesis of metastable tetragonal (t′) zirconia-calcia solid solution by pyrolysis of organic precursors and coprecipitation route. *Journal of Materials Research*, **11(6)**, 1410-1420.

[18] Duh, J.G., Dai, H.T. and Hsu, W.Y. (1988) Synthesis and sintering behaviour in CeO_2–ZrO_2 ceramics. *Journal of Materials Science*, **23(6)**, 2786-2791.

[19] Sato, T., Dosaka, K., Yoshika, T., Okuwaka, A., Yorii, K. and Onodera, Y. (1992) Sintering of ceria-doped tetragonal zirconia crystallized in organic solvents, water, and air. *Journal of the American Ceramic Society*, **75(3)**, 552-556.

[20] Maschio, S., Baxhiorrini A. and Lucchini, E. (1998) Sintering behaviour of mechanically alloyed and coprecipitated 12Ce–PSZ powders. *Journal of Materials Science*, **33(13)**, 3437-3441.

[21] Yashima, M., Ohtake, K., Kakihana, M. and Yoshimura, M. (1994) Synthesis of metastable tetragonal (t') zirconia–ceria solid solutions by the polymerized complex method. *Journal of the American Ceramic Society*, **77(10)**, 2773-2776.

[22] Caruso, R., Benavidez, E., de Sanctis, O., Caracoche, M.C., Ravas, P.C., Cervera, M., Caneiro, A. and Serquis, A. (1997) Phase structure and thermal evolution in coating films and powders obtained by the sol-gel process: Part II. ZrO_2-2.5 mol% Y_2O_3. *Journal of Materials Research*, **12(10)**, 2594-2601.

[23] Lumas, D.G., Lascalea G.E. and Walsoe de Reca, N.E. (1998) Synthesis and characterization of nanocrystalline powders for partially stabilized zirconia ceramics. *Journal of the European Ceramic Society*, **18(9)**, 1217-1221.

[24] Venkatachari, K.R., Huang, D., Ostrander, S.P., Shulze W.A. and Stangle, G.C. (1995) Preparation of nanocrystalline yttria-stabilized zirconia. *Journal of Materials Research*, **10(3)**, 756-761.

[25] Xiaming, D., Qingfeng, L. and Yuying, T. (1993) Study of phase formation in spray pyrolysis of ZrO_2 and ZrO_2−Y_2O_3 powders. *Journal of the American Ceramic Society*, **76(3)**, 760-762.

[26] Srinivasan, R., DeAngeles, R. and Davis, B.H. (1986) Factors influencing the stability of the tetragonal form of zirconia. *Journal of Materials Research*, **1(4)**, 583-588.

[27] Kresge, C.T., Leonowicz, M.E., Roth, W.J., Vartuli, J.C., and Beck, J.S. (1992) Ordered mesoporous molecular sieves synthesized by a liquid-crystal template mechanism. *Nature*, **359(6397)**, 710-712.

[28] Huo, Q., Margolese, D.I., Ciesla, U., Feng, P., Gier, T.E., Sieger, P., Leon, R., Petroff, P.M., Schuth, B. and Stucky, G.D. (1994) Generalized synthesis of periodic surfactant/inorganic composite materials. *Nature*, **368(6469)**, 317-321.

[29] Wang Y., Yin, L., Palhcik, O., Hacohen, Y.R., Koltypin, Y. and Gedanken, A. (2001) Sonochemical synthesis of layered and hexagonal yttrium−zirconium oxides. *Chemistry of Materials*, **13(4)**, 1248-1251.

[30] Liang, J., Jiang, X., Liu, G., Deng, Z., Zhuang, J., Li, F. and Li, Y. (2003) Characterization and synthesis of pure ZrO_2 nanopowders via sonochemical method. *Materials Research Bulletin*, **38(1)**, 161-168.

[31] Coyle, T.W., Coblenz, W.S. and Bender, B.A. (1983) Toughness, strength, and microstructures of sintered CeO_2-doped ZrO_2 alloys. *American Ceramic Society Bulletin*, **62(12)**, 966-967.

[32] Heathote, R. (1993) Sustainable humanosphere: Bulletin of research institute for sustainable humanosphere. *American Ceramic Society Bulletin*, **72(6)**, 123-128.

[33] Taguchi, H., Takahashi, Y. and Miyamoto, H. (1985) Slip casting of partially stabilized zirconia. *American Ceramic Society Bulletin*, **64(2)**, 325-329.

[34] Lange, F.F. (1989) Powder processing science and technology for increased reliability. *Journal of the American Ceramic Society*, **72(1)**, 3-15.

[35] Raedy, M.J. (1993) Optimized processing ceramics. *International Journal of Applied Ceramic Technology*, 47-53.

[36] Taguchi, H., Takahashiand Y. and Miyamoto, H. (1985) Effect of milling on slip casting of partially stabilized zirconia. *Journal of the American Ceramic Society*, **68(10)**, C264-C265.

[37] Leong, Y.K., Katiforis, N., Harding, D.B.O.C., Healy T.W. and Boger, D.V. (1993) Polymeric stabilization of colloidal dispersions. *Journal of Materials Proceedings on Manufacturing Science*, **1**, 445-453.

[38] Leong, Y.K., Boger, D.V. and Parris, D. (1991) Surface chemistry and rheological properties of zirconia suspensions. *Journal of Rheology*, **35(1)**, 149-165.

[39] Hashiba, M., Okamoto, H., Nurishi, Y. and Hiramatsu, K. (1989) Dispersion of ZrO_2 particles in aqueous suspensions by ammonium polyacrylate. *Journal of Materials Science*, **24(3)**, 873-876.

[40] Nikumbh, A.K., Schmidt, H., Martin, K. and Porz, F. (1991) Slip casting of partially stabilized zirconia. *Journal of Materials Science*, **26(13)**, 3649-3656.

[41] Suarez, G., Albano, M.P., Garrido, L.B. and Aglietti, E.F. (2007) Dispersion of concentrated aqueous yttria-stabilized zirconia with ammonium polyacrylate. *Ceramics International*, **33(6)**, 925-929

[42] Shojai, F., Pettersson, A.B.A., Mantyla, T. and Rosenholm, J.B. (2000) Electrostatic and electrosteric stabilization of aqueous slips of 3Y-ZrO_2 powder. *Journal of the European Ceramic Society*, **20(3)**, 277-283.

[43] Joint Committee on Powder Diffraction Standards, PDF No. 17-923.

[44] Dodd, A.C. and McCornick, P.G. (1999) Synthesis and processing of ultrafine Mg-PSZ powder. *Journal of Metastable and Nanocrystalline Materials*, **312-314**, 221-228.

[45] Nettleship, I. and Stevens, R. (1987) Tetragonal zirconia polycrystal (TZP)—a review, *International Journal of High Technology Ceramics*, **3(1)**, 1-32.

[46] Klug, H.P. and Alexander, L.E. (1954) X-Ray diffraction procedure. Wiley-Interscience, New York, Ch.9.

[47] MacGeary, R.K. (1961) Mechanical packing of spherical particles. *Journal of the American Ceramic Society*, **44(10)**, 513-522.

[48] Laarz, E., Zhmud, B.V. and Bergstroem, L. (2000) Dissolution and deagglomeration of silicon nitride in aqueous medium. *Journal of the American Ceramic Society*, **83(10)**, 2394-2400.

[49] Tari, G., Ferreira, J.M.F. and Lyckfeldt, O.L. (1998) Influence of the stabilising mechanism and solid loading on slip casting of alumina. *Journal of the European Ceramic Society*, **18(5)**, 479-486.

[50] Sigmund, W.M., Bell, N.S. and Bergstrom, L. (2000) Novel powder-processing methods for advanced ceramics. *Journal of the American Ceramic Society*, **83(7)**, 1557-1574.

[51] Bergstrom, L. (1998) Shear thinning and shear thickening of concentrated ceramic suspensions. *Colloids and Surfaces A*: *Physicochemical and Engineering Aspects*, **133(1-2)**, 151-155.

[52] Moreno, R. (1992) The role of slip additives in tape-casting technology. Part I: Solvents and dispersants. *American Ceramic Society Bulletin*, **71(10)**, 1521-1531.

[53] Smart, S.T.C.R. and Nowotny, J. (1998) Ceramic interface—properties and applications. IOM Communications Ltd., London, 433-460.

[54] Greenwood, R. and Bergstrom, L. (1997) Electroacoustic and rheological properties of aqueous Ce-ZrO_2 (Ce-TZP) suspensions. *Journal of the European Ceramic Society*, **17(4)**, 537-548.

Vol.2, No.7, 707-712 (2010)
doi:10.4236/ns.2010.27087

Natural Science

Synthesis and characterization of an amphiphilic chitosan bearing octyl and methoxy polyethylene glycol groups

Guanghua Liu, Jianqun Gan, Aimin Chen, Qian Liu, Xusheng Zhao*

Guangzhou Institute of Chemistry, Chinese Academy of Sciences, Guangzhou, China;
*Corresponding Author: zhao7503@yahoo.com

Received 14 April 2010; revised 18 May 2010; accepted 25 May 2010.

ABSTRACT

An amphiphilic N-octyl-O-methoxy poly (ethylene glycol) chitosan was successfully prepared by grafting successively octyl groups onto amino groups at chitosan's C-2 position as hydrophobic moieties and methoxy polyethylene glycol (MPEG) groups onto hydroxyl groups at C-6, C-3 as hydrophilic ones. A certain amount of -NH_2 was retained in the structure of chitosan derivatives through protection by phthalic anhydride. The chemical structures and degree of N-and O-substitution of chitosan derivatives were characterized by FTIR, ^{1}H NMR, GPC and elemental analysis, respectively. The amphiphilic property for convenient self-assembly and the preserved -NH_2 groups for progressive chemical cross-linking make the resultant N-ocyl-O-MPEG chitosan soluble in water and potentially applicable in preparing stable chitosan hollow microspheres, a demanding drug-carrier in medical and pharmaceutical sciences.

Keywords: Amphiphilic Groups; Chitosan Derivatives; Protection; Hollow Microsperes

1. INTRODUCTION

In recent years, micelles and hollow microspheres prepared from self-assemblies of amphiphilic polymers have attracted great attention due to a variety of applications in DNA, antigens, delivery carriers for drugs and protection proteins or/and enzymes, especially for controlled or sustained drug-delivery systems [1]. The unique core-shell architecture is composed of hydrophobic segment, which acted as internal core, and hydrophilic segment which acted as surrounding corona in aqueous medium [2]. The hydrophobic core provides a loading space for water-insoluble drugs and stabilizes them, whereas the hydrophilic shell protects encapsulated drugs [3]. Additionally, the modification of hydrophilic shell affects pharmacokinetic behavior, such as prolonged circulation time, target release [4] and controlled drug release by using stimuli-sensitive copolymers [5].

In comparison with common polymers, chitosan, the second most abundant natural biopolymer only to cellulose [6] and known as its excellent property in non-toxicity, biodegradability, good biocompatibility, etc. [7], would exhibit special advantages in drug delivery system. The active hydroxyl and amino groups within chitosan could be easily modified to endow it with new or improved properties, and at the same time, keeping its original physiochemical and biochemical properties [6]. As a result, various amphiphilic chitosan derivatives and hollow microspheres prepared from them have been extensively published [6]. For examples, highly N-methylated modified chitosan possessing hydrophobic -N$(CH_3)_2$, -NH(CH_3) and hydrophilic -$N^+(CH_3)_3$ groups was reported by Sieval *et al.* which is soluble in water at a broad pH value [8]. Through emulsion-crosslinking, Peng *et al.* prepared hollow microspehres from N-methylated chitosan with diameters range from 2-5 um [9]. Liu *et al.* synthesized an amphiphilic carboxymethyl-hexanoyl chitosan [10] which formed hollow nanocapsules with 20-200 nm in diameter [11]. As a demanding drug-carrier in medical and pharmaceutical sciences, stable chitosan hollow microsphere is probably one of the most valuable candidates.

Presently, the hydrophobic groups of amphiphilic chitosan derivatives ever reported generally contain long alkyl [12,13], long acyl [10] and aryl [14], while the hydrophilic ones include carboxymethyl [10], sulfate [12], phosphate [15,16], N-trimethyl [17] and polyethylene glycol [14,18]. To prepare amphiphilic chitosan

hollow microspheres as drug carriers, the substituents, especially the hydrophilic groups, should be non-toxic and biocompatible. It's impossible to form stable core-hell structure through nothing but self-assembly of amphiphilic chitosan. Amino groups within the backbone of chitosan should be crosslinked chemically to form stable and hard shell thereafter self-assembly process. That's to say, adequate primary amino groups (-NH_2) existed in amphiphilic chitosan are necessary for preparing hollow microspheres. To the best of our knowledge, most reports ever reported about amphiphilic chitosan derivatives did not pay much attention to this problem.

In this work, we report a novel amphiphilic N-octyl O-methoxy polyethylene glycol (MPEG) chitosan possessing adequate primary amino groups. PEG chain has been proved to be non-toxic, very flexible and highly hydrated, soluble in water and majority organic solvents, and is the most widely used biocompatible polymer for chemical and biological applications [19]. Through the effective protection of -NH_2 groups within the backbone of chitosan during the modification process, the chitosan derivatives synthesized in this study preserve a certain amount of -NH_2 groups for latter chemical crosslinking to prepare eventually sizecontrollable hollow microspheres.

2. EXPERIMENTAL

2.1. Materials

Chitosan (Mr = 1 × 10^5, degree of deacetylation (DD) = 95%) was provided by Zhejiang Aoxing Biochemical Co. Ltd (China). Octylaldehyde was obtained from Guangzhou Damo Chemical Co. Ltd (China). Methoxy polyethylene glycol (MPEG, Mr = 1900) was purchased from Alfa Aesar. Methyl iodide was ordered from Shanghai Jingchun Chemical Reagent Factory (China). Dimethylformamide (DMF) was distilled under reduced pressure and stored over molecular sieves. Dialysis tube was achieved from SPECTRUM (Canada) with a molecular weight cut-off (MWCO) of 6000~8000. Ag_2O was freshly prepared from $AgNO_3$ and KOH in our laboratory. All other materials used in this study were of analytical grade and without further purification.

2.2. Synthetic Procedures

2.2.1. Synthesis of N-Octyl Chitosan (NOC)

N-octyl chitosan was prepared as reported previously (**Scheme 1**). Briefly, chitosan (5.0 g, 31 mmol) was suspended in 60 ml methanol with active stirring at room temperature before the addition of octaldehyde (5.0 ml, 31 mmol). Then, KBH_4 (2.5 g) dissolved in 10 ml water was added dropwise to the mixture after 24 h. The reaction solution was neutralized with hydrochloric acid and

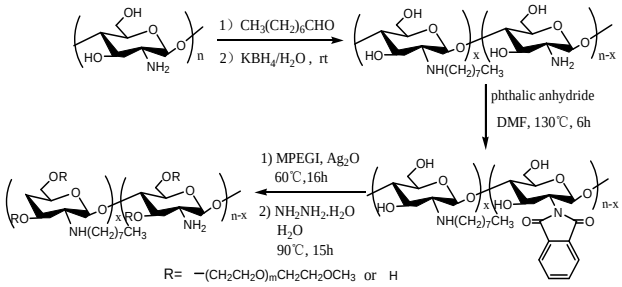

Scheme 1. Synthetic procedure of N-octyl-O-MPEG chitosan.

the product was precipitated with methanol after a further 24 h continuous stirring. The precipitate was filtered, washed repeatedly with methanol and water and then dried under vacuum at 60℃ overnight to give 7.0 g N-octyl chitosan. Degree of N-substitution of octyl was 54.3% from element analysis.

2.2.2. Synthesis of N-Octyl-N-Phthaloyl Chitosan (NONPC)

The synthesis of N-octyl-N-phthaloyl chitosan (NONPC) is described briefly as follows. A mixture of N-octyl chitosan (3.0 g, 13.8 mmol) and phthalic anhydride (PHA) (2.8 g, 3 mol equiv to amino) in 30 ml DMF was heated to 130℃ under nitrogen with magnetic stirring. After 6 h, the brown precipitate obtained by pouring the solution into ice-water was collected by filtration, extracted with ethanol in Soxhlet's apparatus for 48 h, and dried under vacuum at 50℃ to give 3.6 g NONPC products.

2.2.3. Synthesis of Methoxy Polyethylene Glycol Lodide (MPEGI)

Methoxy polyethylene glycol iodide (MPEGI) was synthesized according to the reports by Gorochovceva and Makuska [19]. Briefly, MPEG-1900 (19 g, 10 mmol), triphenylphosphite (8.0 ml, 30 mmol) and methyl iodide (4.3 ml, 30 mmol) were mixed and stirred in a three-neck flask at 120℃ for 6 h. Then, the reaction mixture was cooled, dissolved in toluene, precipitated in 500 ml diethyl ether, and then filtered, washed several times with diethyl ether and dried in air to give pale yellow product. The yield of the product was 92%.

2.2.4. Synthesis of N-Octyl-O-MPEG Chitosan (NOOMC)

The synthetic procedure of N-octyl-O-MPEG chitosan (NOOMC) is carried out by using NONPC, MPEGI and Ag_2O with different grams or molar ratios as the starting materials (**Table 1**). Firstly, NONPC, MPEGI and Ag_2O were mixed and heated at 60℃ for 16 h with magnetic stirring. Then, hydrazine monohydrate (80%, 40 ml or 20 ml) and distilled water (80 ml or 40 ml) were poured

into the mixture and the temperature was raised to 90℃ and maintained for 15 h before the mixture was filtered to remove solid impurity. The filtrate solution was dialyzed against water for 72 h and then concentrated before the solid residue was dried in vacuum at 50℃ to give final products of N-octyl-O-MPEG chitosan (NOOMC). Depending on different amount of hydrazine monohydrate and distilled water used during the synthesis, the products of NOOMC with two different degree of substitutions (DS) of MPEG were labeled as NOOMC (I) and NOOMC (II), respectively.

2.3. Characterization

^{1}H NMR spectra were recorded at 400MHz using a Bruker DRX-400 spectrometer. CF_3COOD and D_2O were used as the solvents for chitosan and its derivatives, respectively. Elemental analysis was determined using an Elementar Vario EL III analyzer. FTIR spectra were obtained from Fourier transformation infrared spectrometer (Analect RFX-65A) in KBr discs. Molecular weight of the amphiphilic chitosan was determined using Waters 515-410 gel permeation chromatography (GPC).

3. RESULTS AND DISCUSSION

3.1. Synthesis of the Chitosan Derivatives

Generally, amphiphilic chitosan could be prepared through introducing the hydrophilic moiety first and the hydrophobic one later [12,13], or in the reverse order [11,20]. The latter procedure was adopted in this investigation. As shown in **Scheme 1**, the amphiphilic chitosan derivatives were synthesized through the following three steps. At the first step, hydrophobic octyl groups were introduced by Schiff reaction prior to MPEG. Octylaldhyde residue was found very easy to be removed with heterogeneous reaction, and rather difficult to be excluded when Schiff reaction is carried out at the last step. Meanwhile, if MPEG was introduced onto hydroxyl firstly, the molecule weight of the resultant O-MPEG chitosan would be much higher than chitosan, and the mole ratio of octylaldehyde and O-MPEG chitosan is difficult to calculate and control in Schiff reaction.

Table 1. Amounts of reactants in synthesizing NOOMC with different degree of substitutions.

No.	NONPC/g	MPEGI/g	Ag_2O/g	m(NONPC): m(MPEGI): m(Ag_2O) *	product
(I)	1.5	10.2	1.2	1:1:1	NOOMC(Ⅰ)
(II)	0.8	10.8	1.3	1:2:2	NOOMC(Ⅱ)

NONPC, N-octyl-N-phthaloyl chitosan; MPEGI, methoxy polyethylene glycol iodide; NOOMC, N-octyl-O-MPEG chitosan. ***** m represents mole ratio.

It has been estimated that amino groups at C-2 show higher nucleophilic activity than hydroxyl groups (either C-3 or C-6) in the main backbone of chitosan [21]. Thereby, to avoid the grafting of MPEG onto amino groups which retained in N-octyl chitosan, it is necessary to protect amino groups in advance by the use of phthalic anhydride. This protection method was reported earlier in 1991 by Nishimura *et al.* [22], which has been applied to various region-selective modifications of chitosan [21,23]. A key point for this pathway is the fact that chitosan is insoluble in several organic solvents, such as DMF, while N-phthaloyl derivative of chitosan is soluble [18,22]. N-octyl chitosan, just like chitosan, has also a bad solubility in organic solvent. It was found in our experiment that N-octyl-N-phthaloyl chitosan is soluble in DMF, which is of great significance for further reaction with MPEG iodide. Accordingly, N-phthaloyl group is the prerequisite for both protection of active amino in chitosan and solubilization of the product in DMF.

As mentioned above, a certain amount of primary amino is indispensable for the preparing of amphiphilic chitosan hollow microspheres. It is identified from **Scheme 1** that the content of primary amino of the final product is determined by the first step reaction. Hence, primary amino cannot be modified and replaced completely with octyl groups. In our study, to assure an incomplete substitution reaction on amino groups, we adopted an appropriate molar ratio of chitosan to octylaldehyde in Schiff reaction. It is expected that we could get amphiphilic chitosan possessing different amount of active amino groups. That is, a certain extent of primary amino content could be preserved through controlling the molar ratio of the starting materials. Further investigations are currently under way in our laboratory.

Compared with Schiff reaction at the first step, the amino groups retained in N-octyl chitosan should be modified completely with phthalimide groups to avoid their participation in further reaction. Threefold excess of phthalic anhydride was used in our experiment to protect amino as complete as possible. The course of the etherification of N-octyl-N-phthaloyl with MPEGI was similar to that described by Natalijia Gorochovceva *et al.* [18] where Ag_2O is a suitable and effective catalyzer for etherification. The reaction between chitosan hydroxyl groups and MPEGI is irreversible and proceeds till the consumption of active functional groups. In our study, the degree of substitution (DS) of MPEG is represented from the molar ratio of MPEGI to N-octyl-N-phthaloyl chitosan. N-octyl-O-MPEG chitosan with different DS of MPEG is illustrated from the molar ratio of the above two reagents.

3.2. Characterization of Chitosan Derivatives

The degree of substitution (DS) of chitosan derivatives was calculated by comparing C and N molar ratio ob-

tained from the elemental analysis data (**Table 1**). The DS (54.3%) of N-octyl chitosan (NOC) confirms the incomplete modification by octylaldehyde with 54.3% of amino groups substituted and about 45% of them retained in NOC. According to the variation in m(C)/m(N) of NOC and N-octyl-N-phthaloyl chitosan (NONPC), it can be calculated that the DS of phthlimide groups is 66.3%, which exceeds the amino content (about 45%) of NOC. This indicates that the retained amino groups were entirely protected and only a few hydroxyl groups were modified simultaneously, which is identical with the report [23] that treatment of chitosan with phthalic anhydride generally results in partial O-phthaloylation in addition to N-substitution. The DS of MPEG grafts on the final product was obtained by comparing C/N of NOC and N-octyl-O-MPEG chitosan. As can be seen from **Table 2**, the DS of NOOMC (I) was only 41.8% as the molar ratio m (NONPC)/m(MPEGI) equals to 1:1. When the same molar ratio was increased up to 2:1, the DS of NOOMC (II) reached 88.4%, more than twice as much as the DS of NOOMC (I).

Structure changes of chitosan and its derivatives were confirmed by FTIR spectra (**Figure 1**). The N-octyl-N-phthaloyl chitosan (NONPC) shows new or intensified absorptions at 2927, 2858, 1464 cm^{-1} which attributed to octyl chains and 1776, 1716, 721 cm^{-1} which assigned to the phthalimide groups. On the contrary, the peak at about 1600 cm^{-1}, which belongs to $-NH_2$ in chitosan, disappeared in the IR spectra of NONPC. The above information from IR spectra indicates that octyl groups were successfully introduced to chitosan and the retained amino groups were protected completely by phthalimide groups. The IR spectra (c, d in **Figure 1**) of N-octyl-O-MPEG chitosan (NOOMC) also reveal the absorption bands characteristic of chitosan and two modified groups. Distinctive absorption bands at 2889 cm^{-1} (C-H stretching) and 1110 cm^{-1} around belong to MPEG grafts while those at 1676, 1646 cm^{-1} attribute to the primary amino which retained in chitosan derivative.

Table 2. Elemental analysis (%) and the degree of substitution (DS) of chitosan derivatives.

Sample	C	N	H	m (C)/ m (N)*	DS (%)
Chitosan	39.68	7.59	7.85	6.10	—
NOC	53.50	5.98	9.19	10.44	54.3[a]
NONPC	55.74	4.13	6.75	15.75	66.3[b]
NOOMC (I)	52.01	1.17	8.89	51.86	41.8[c]
NOOMC (II)	52.62	0.71	9.47	86.46	88.4[d]

NOC, N-octyl chitosan; NONPC, N-octyl-N-phthaloyl chitosan; NOOMC, N-octyl-O-MPEG chitosan. * m represents mole ratio. [a] DS of N-octyl groups; [b] DS of N-phthalimide groups; [c,d] DS of O-MPEG grafts.

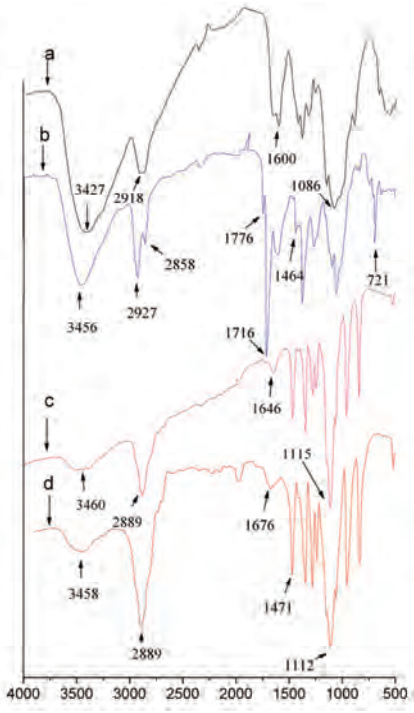

Figure 1. FTIR spectra of chitosan and its derivatives. a-chitosan, b-NONPC, c-NOOMC (I), d-NOOMC (II). NONPC, N-octyl-N-phthaloyl chitosan; NOOMC, N-octyl -O-MPEG chitosan.

It should be noted that the absorptions of octyl groups (2927, 2858, 1464 cm^{-1}) were overlapped by the much stronger absorptions of MPEG grafts (2889 cm^{-1}, 1471 cm^{-1}). The peak at 3458 cm^{-1} which attributed to $-NH_2$ and -OH declined and that at 1776 cm^{-1} and 1716 cm^{-1} characteristic of phthalimide groups disappeared in the FTIR spectra of the final product. It is thus concluded that MPEG groups were introduced to hydroxyl and the protecting groups were removed successfully.

More information about chitosan and its derivatives can be obtained from ^1H NMR analysis (**Figures 2-3**). In comparison with the spectra of chitosan itself (**Figure 2**), ^1H NMR spectra of NOOMC (II) (**Figure 3**) differ greatly in that the signals at 3.50-3.60 and 3.25 which assigned to the ethoxyl hydrogen ($C\mathbf{H}_2$-$C\mathbf{H}_2$-O) and methoxyl hydrogen (-$OC\mathbf{H}_3$) of MPEG grafts, respectively, and that the small peaks at 3.10, 2.80, 1.15 which attributed to the methylene hydrogen around nitrogen (N-$C\mathbf{H}_2$-$(CH_2)_6$-CH_3), other six methylene hydrogens (N-CH_2-$(C\mathbf{H}_2)_6$-CH_3) and the methyl hydrogen (N-CH_2-$(CH_2)_6$-$C\mathbf{H}_3$), respectively. The signals of hydrogen within chitosan backbone (3.60-3.80, H3 H4 H5 H6) were covered partially by that of ethoxyl hydrogen. As illustrated in **Figure 3**, the peaks of hydrogen in octyl groups and chitosan backbone were not so obvious as those of MPEG with a high DS of MPEG grafts and a

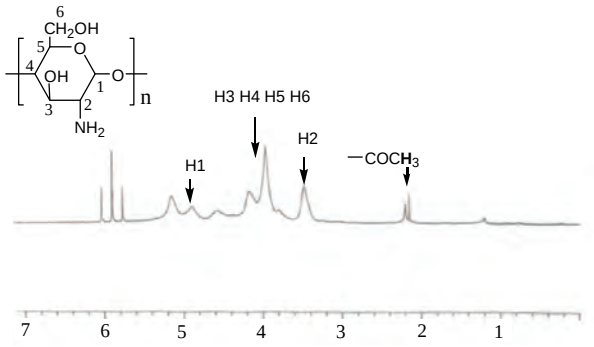

Figure 2. ^{1}H NMR spectra of chitosan.

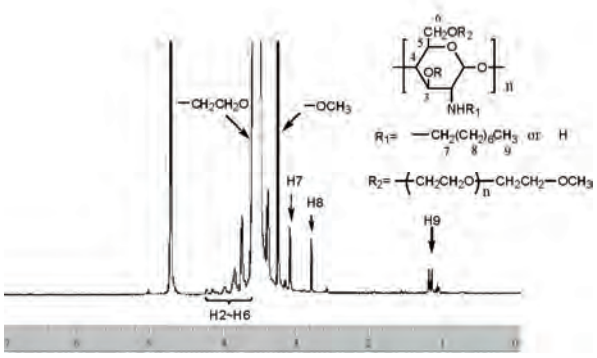

Figure 3. ^{1}H NMR spectra of N-octyl-O-MPEG chitosan (NOOMC Ⅱ).

much large number of hydrogen it contained.

Molecular weight of the amphiphilic chitosan (NOOMC (I)) was measured by gel permeation chromatography (GPC). The results showed that Mw of NOOMC (I) is near 1×10^5 and Mz is about 1.6×10^5, which is a little bit smaller than that calculated by Element Analysis (2×10^5). It might be caused by the existence of trace amount of unreacted MPEGI after dialysis or cleavage of chitosan chains during modifications.

4. CONCLUSIONS

N-octyl-O-MPEG chitosan (NOOMC), was synthesized for the first time with fair production yield and high degree of substitution of amphiphilic groups. The degree of substitution of octyl groups reached 54.3% while that of MPEG grafts amounted to 41.8%-88.4% depending on the variation of N-octyl-N-phthaloyl chitosan to methoxy polyethylene glycol iodide molar ratio. With the introduction of the amphiphilic groups, the chitosan derivatives were endowed with good solubility in water and potential self-assembly properties. Significantly, the effective protection of amino groups was successfully adopted to retain a certain amount of -NH_2 in the derivatives, which is indispensable for preparing hollow microspheres.

5. ACKNOWLEDGEMENTS

The authors express their gratitude to National Natural Science Foundations of China and Natural Science Foundation of Guangdong Province, China, for financial support.

REFERENCES

[1] Peng, X.H., Zhang, L.N. and Kennedy, J.F. (2006) Release behavior of microspheres from cross-linked N-methylated chitosan encapsulated ofloxacin. *Carbohydrate Polymers*, **65(3)**, 288-295.

[2] Ye, Y.Q., Yang, F.L., Hu, F.Q., Du, Y.Z., Yuan, H. and Yu, H.Y. (2008) Core-modified chitosan-based polymeric micelles for controlled release of doxorubicin. *International Journal of Pharmaceutics*, **352(1-2)**, 294-301.

[3] van Nostrum, C.F. (2004) Polymeric micelles to deliver photosensitizers for photodynamic therapy. *Advanced Drug Delivery Reviews*, **56(1)**, 9-16.

[4] Maeda, H., Wu, J., Sawa, T., Matsumura, Y. and Hori, K. (2000) Tumor vascular permeability and the EPR effect in macromolecular therapeutics: A review. *Journal of Controlled Release*, **65(1-2)**, 271-284.

[5] Liu, X.M., Wang, L.S., Wang, L., Huang, J.C. and He, C.B. (2004) The effect of salt and pH on the phase-transition behaviors of temperature-sensitive copolymers based on N-isopropylacrylamide. *Biomaterials*, **25(25)**, 5659-5666.

[6] Mourya, V.K. and Inamdar, N.N. (2008) Chitosan-modifications and applications: Opportunities galore. *Reactive & Functional Polymers*, **68(6)**, 1013-1051.

[7] Chandy, T. and Sharma, C.P. (1990) Chitosan - as a Biomaterial. *Biomaterials Artificial Cells and Artificial Organs*, **18(1)**, 1-24.

[8] Sieval, A.B., Thanou, M., Kotze, A.F., Verhoef, J.E., Brussee, J. and Junginger, H.E. (1998) Preparation and NMR characterization of highly substituted N-trimethyl chitosan chloride. *Carbohydrate Polymers*, **36(2-3)**, 157-165.

[9] Peng, X.H. and Zhang, L. (2005) Surface fabrication of hollow microspheres from N-methylated chitosan cross-linked with gultaraldehyde. *Langmuir*, **21(3)**, 1091-1095.

[10] Liu, T.Y., Chen, S.Y., Lin, Y.L. and Liu, D.M. (2006) Synthesis and characterization of amphiphatic carboxymethyl-hexanoyl chitosan hydrogel: Water-retention ability and drug encapsulation. *Langmuir*, **22(23)**, 9740-9745.

[11] Liu, K.H., Chen, S.Y., Liu, D.M. and Liu, T.Y. (2008) Self-assembled hollow nanocapsule from amphiphatic carboxymethyl-hexanoyl chitosan as drug carrier. *Macromolecules*, **41(17)**, 6511-6516.

[12] Zhang, C., Ping, Q.N., Zhang, H.J. and Jian, S. (2003) Preparation of N-alkyl-O-sulfate chitosan derivatives and micellar solubilization of taxol. *Carbohydrate Polymers*, **54(2)**, 137-141.

[13] Zhang, C., Ding, Y., Yu, L.L. and Ping, Q.N. (2007) Polymeric micelle systems of hydroxycamptothecin based on amphiphilic N-alkyl-N-trimethyl chitosan derivatives. *Colloids and Surfaces B-Biointerfaces*, **55(2)**, 192-199.

[14] Yoksan, R. and Chirachanchai, S. (2008) Amphiphilic

chitosan nanosphere: Studies on formation, toxicity, and guest molecule incorporation. *Bioorganic & Medicinal Chemistry*, **16(5)**, 2687-2696.

[15] Jayakumar, R., Nagahama, H., Furuike, T. and Tamura, H. (2008) Synthesis of phosphorylated chitosan by novel method and its characterization. *International Journal of Biological Macromolecules*, **42(4)**, 335-339.

[16] Jayakumar, R., Egawa, T., Furuike, T., Nair, S.V. and Tamura, H. (2009) Synthesis, characterization, and thermal properties of phosphorylated chitin for biomedical applications. *Polymer Engineering and Science*, **49(5)**, 844-849.

[17] Zhang, C., Ding, Y., Ping, Q.E. and Yu, L.L. (2006) Novel chitosan-derived nanomaterials and their micelle-forming properties. *Journal of Agricultural and Food Chemistry*, **54(22)**, 8409-8416.

[18] Gorochovceva, N. and Makuska, R. (2004) Synthesis and study of water-soluble chitosan-O-poly (ethylene glycol) graft copolymers. *European Polymer Journal*, **40(4)**, 685-691.

[19] Kulbokaite, R., Ciuta, G., Netopilik, M. and Makuska, R. (2009) N-PEG'ylation of chitosan via "click chemistry" reactions. *Reactive & Functional Polymers*, **69(10)**, 771-778.

[20] Ngawhirunpat, T., Wonglertnirant, N., Opanasopit, P., Ruktanonchai, U., Yoksan, R., Wasanasuk, K. and Chirachanchai, S. (2009) Incorporation methods for cholic acid chitosan-g-mPEG self-assembly micellar sys- tem containing camptothecin. *Colloids and Surfaces B-Biointerfaces*, **74(1)**, 253-259.

[21] Makuska, R. and Gorochovceva, N. (2006) Regioselective grafting of poly(ethylene glycol) onto chitosan through C-6 position of glucosamine units. *Carbohydrate Polymers*, **64(2)**, 319-327.

[22] Nishimura, S.I., Kohgo, O., Kurita, K. and Kuzuhara, H. (1991) Chemospecific manipulations of a rigid polysaccharide-syntheses of novel chitosan derivatives with excellent solubility in common organic-solvents by regioselective chemical modifications. *Macromolecules*, **24(17)**, 4745-4748.

[23] Hu, Y.Q., Jiang, H.L., Xu, C.N., Wang, Y.J. and Zhu, K.J. (2005) Preparation and charac terization of poly (ethylene glycol)-g-chitosan with water- and organo-solubility. *Carbohydrate Polymers*, **61(4)**, 472-479.

Vol.2, No.7, 713-717 (2010)
doi:10.4236/ns.2010.27088

A sensitive, rapid and validated liquid chromatography – tandem mass spectrometry (LC-MS-MS) method for determination of Mimosine in *Mimosa pudica* Linn

Parikshit A. Champanerkar[1]*, Vikas V. Vaidya[1], Sunita Shailajan[1], Sasikumar N. Menon[2]

[1]Department of Chemistry, Ramnarain Ruia College, Mumbai University, Mumbai, India;
*Corresponding Author: parikshit_ac@indiatimes.com
[2]Therapeutic Drug Monitoring Laboratory, Sion Koliwada, Mumbai, India

Received 28 March 2010; revised 24 May 2010; accepted 2 June 2010.

ABSTRACT

A rapid, sensitive and accurate liquid chromatographic tandem mass spectrometric method is described for the determination of Mimosine in *Mimosa pudica* Linn. whole plant powder. Mimosine was extracted from the plant using 1.0% HCl in water. The chromatographic separation was achieved using a Thermo Hypurity C18 (50 x 4.6 mm) 5.0 µ column interfaced with a triple quadrapole mass spectrometer. The mobile phase consisted of a mixture of Methanol: 10 mM ammonium formate buffer whose pH was adjusted to 3.00 ± 0.05 with formic acid (80:20, v/v) and was delivered at a flow rate of 1.0 mL min^{-1}. Electrospray ionization (ESI) source operated in the negative ion mode was used for the quantitation. Detection was performed using an Applied Biosystems Sciex API 3200 Mass spectrometer. The method was found to be simple, precise, accurate, fast, specific and sensitive and can be used for routine quality control analysis of Mimosine in *Mimosa pudica* Linn.

Keywords: LC-MS-MS; Mimosine; *Mimosa pudica* Linn

1. INTRODUCTION

Mimosa pudica Linn. (Fam. -Leguminosae) is commonly known as Sensitive plant in English and Lajvanti or Chuimui in Hindi language. The plant is distributed through out India especially in moist places. *Mimosa pudica* Linn. is also said to have larvicidal property [1]. It is used to treat menorrhagia and leucorrhoea [2-4]. In Ayurvedic system of medicine, *Mimosa pudica* Linn. has been described as an indispensable drug for blood pressure [5]. Phytochemical screening has revealed that the plant contains Mimosine (alkaloid), stigmasterol, leucoanthocyanidin, D-xylose and D-glucuronic acid, norepinephrine, D-pinitol, linoleic acid, oleic acid, palmitic acid, stearic acid, β-sitosterol and crocetin dimethyl ester. Of all these, the major compound present in *Mimosa pudica* Linn. is Mimosine [4]. Mimosine is used for treating the cutaneous effects of psoriasis and related skin disorders [6]. It is less soluble in methanol and ethanol, insoluble in other organic solvents, but sparingly soluble in water. It is soluble in dilute acid and base. Structure of Mimosine is shown in **Figure 1** [7].

The quality of herbal medicine that is the profile of the constituents in the final product has implication in efficacy and safety. Due to the complex nature and inherent variability of the chemical constituents of the plant based drugs, it is difficult to establish quality control parameters and modern analytical techniques are accepted to help in circumventing this problem [8]. Recently, the concept of marker-based standardization of herbal drugs is gaining momentum. Identification of major and unique compounds in herbs as markers and development of analytical methodologies for monitoring them are the key steps involved in marker-based standardization [9].

Quantitation of Mimosine from *Mimosa pudica* L. using RP-HPTLC has been reported [10]. A method using HPLC and spectrophotometric determination of Mimosine has also been reported [11,12]. Literature survey, hence, revealed that there is no method available in the

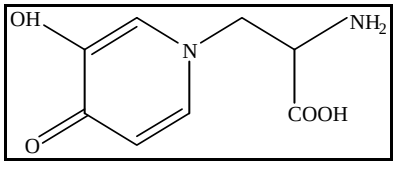

Figure 1. Structure of Mimosine.

public domain for quantitation of Mimosine from *Mimosa pudica* Linn. using an LC-MS-MS system. So, the aim of the present work was to develop a simple, fast, sensitive, precise, and accurate LC-MS-MS method for determination of Mimosine from *Mimosa pudica* L. The developed method was further validated as per ICH guidelines to indicate its suitability [13,14].

2. Experimental

2.1. Chemicals and Preparation of Standard Solutions

HPLC grade Methanol and acetonitrile were purchased from J.T. Baker, Mumbai, India. Extra pure Formic acid (99.9%) and ammonium formate was purchased from Fluka, Steinheim, Germany. High purity deionised water was prepared in-house using a Milli-Q water purification system obtained from Millipore, Bangalore, India. Mimosine standard (Purity 98%) was procured from Sigma-Aldrich (Aldrich Division; Steinheim, Federal Republic of Germany).

The stock solution A of Mimosine (1,000 µg mL^{-1}) was prepared by dissolving 25 mg of accurately weighed Mimosine in minimum quantity of 1.0% HCl in water and diluting with same solution up to the mark in a 25 mL standard volumetric flask. Further solution B of Mimosine (10 µg mL^{-1}) was prepared by transferring 0.25 mL of stock solution A and diluting with mobile phase up to the mark in a 25 mL volumetric flask. Different volumes in the range of 0.4-1.0 mL of stock solution B were transferred to 10 mL standard volumetric flasks and diluted up to the mark with the mobile phase, to provide a concentration range of 400-1000 ng mL^{-1}.

2.2. Plant Material and Preparation of Sample Solution

The plant *Mimosa pudica* L. was collected from Mumbai, Maharashtra, India and was authenticated by National Institute for Science Communication and Information Resources (NISCAIR), New Delhi, India. The collected plant material was dried at room temperature, under shade and then ground in a mixer to a fine powder. This was then passed through an ASTM BSS mesh (size 85) and stored in an airtight container at room temperature. 25 mg of the dried powder was accurately weighed, placed in a stoppered tube and 10 mL of Methanol was added. The sample was vortexed for 1-2 minutes and then mixed on a shaker for 60 minutes. The contents of the tube were then centrifuged at 4600 rpm and filtered through Whatmann No. 41 filter paper (E. Merck, Mumbai, India) and residue was collected in a 10 mL standard volumetric flask and 1.0% HCl in water was added up to the mark, the sample was vortexed for 1-2 minutes and left to stand overnight at room temperature. The content was filtered through Whatmann No. 41 filter paper and the clear supernatant was collected in a dry tube (solution C). Further solution D was prepared by transferring 1.0 mL of solution C and diluting with mobile phase up to the mark in a 10 mL volumetric flask. Solution D was used for further experiments.

2.3. Instrumentation and Chromatographic Conditions

A Hypurity C_{18}, (50 × 4.6 mm), 5 µ obtained from Thermo Electron, Mumbai, India was used for the compound retention. The mobile phase consisted of mixture of Methanol: 10mM ammonium formate buffer pH adjusted to 3.00 ± 0.05 with formic acid (80:20, v/v) and was delivered at a flow rate of 1.0 mL min^{-1} by employing a Shimadzu Prominence series (Kyoto, Japan) binary pump, at ambient temperature. Detection was achieved using an Applied Biosystems API 3200 MS-MS apparatus (Applied Biosystems, Ontario, Canada) fitted with a Turbo Ion Spray source. The instrument was interfaced with a computer running Applied Biosystems Analyst version 1.4.2 software. Electrospray ionization (ESI) was performed in the negative ion mode. The spray voltage and source temperature were −4500 V and 550°C respectively. Nitrogen was used as the collision gas. The Declustering Potential (DP), Collision Energy (CE), Entrance potential (EP), Cell Exit Potential (CXP) were optimized during tuning as −20, −24, −10, −4 eV for Mimosine. The collision activated dissociation (CAD) gas was set at 3 psi, while the curtain gas was set at 12 psi. The Applied Biosystems API 3200 LC-MS-MS apparatus was operated at unit resolution in the multiple reaction monitoring (MRM) mode, monitoring the transition of the molecular ion m/z 197.7 to the product ion m/z 162.8 for Mimosine. The instrument response was optimized for Mimosine by infusing a constant flow of a standard solution (1000 ng mL^{-1}) via a T-piece into the stream of mobile phase eluting from the column. **Figure 2** shows the product ion mass spectra obtained from collision-induced dissociation of the deprotonated molecular ions of Mimosine.

3. METHOD VALIDATION

3.1. System Suitability

System suitability tests are used to ensure reproducibility of the equipment. The test was carried out by injecting 10 µL of standard solution of Mimosine (600 ng mL^{-1}) six times. The % RSD was found to be 1.27% for Mimosine, which was acceptable as it is less than 2%.

3.2. Linearity

In order to establish linearity, standard solutions of Mi-

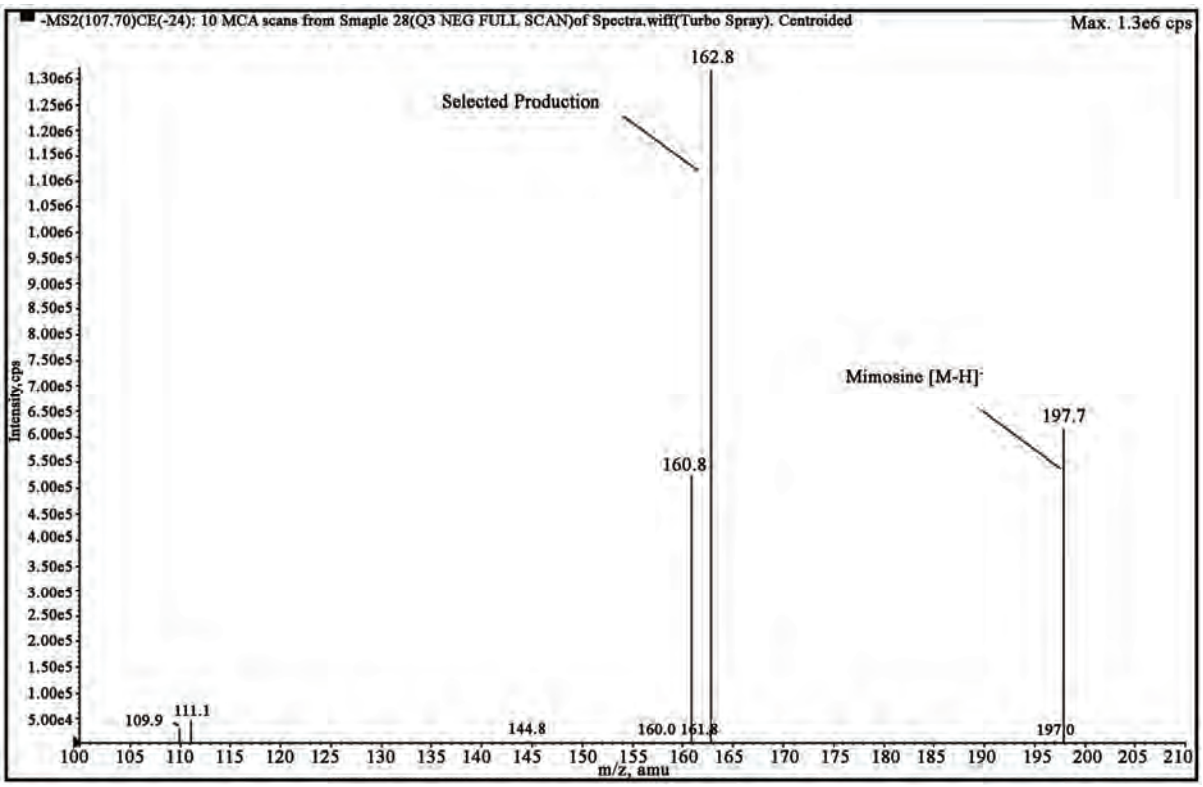

Figure 2. Representative Spectra of product ion of Mimosine.

mosine at six different concentrations (400.0, 5‰00.0, 600.0, 700.0, 800.0 and 1000.0 ng mL^{-1}) were prepared in mobile phase. Each of these solutions (10 µL) was injected and the detector response for the different concentrations was measured. A graph was plotted of drug peak area against concentration. The plot was linear in the range 400.0 ng mL^{-1} to 1000.0 ng mL^{-1} for Mimosine. The experiment was performed five times and the mean was used for the calculations. The equation of linear regression curve obtained was y = 94.4x − 1923.3, where y = (peak area), x = (concentration of Mimosine in ng mL^{-1}) with a correlation coefficient 0.9951. A typical chromatogram of standard and plant is shown in **Figure 3** and **Figure 4** respectively.

3.3. Limit of Detection and Limits of Quantitation

The signal-to-noise ratio of 3:1 and 10:1 was used to establish LOD and LOQ, respectively. The LOD and LOQ of Mimosine were 100 ng mL^{-1} and 400.0 ng mL^{-1}, respectively.

3.4. Assay

The developed LC-MS-MS method was used for determination of Mimosine from whole plant powder of *Mimosa pudica L.* The sample working solution D (10 µL) was injected and the area of Mimosine peak was measured. From the calibration curve, the amount of Mimosine in dry powder of *Mimosa pudica* L. was calculated. The retention time of Mimosine in sample solution and in the standard solution was found to be 0.67 min. The mean assay value of Mimosine was found to be 1.938 mg/g of plant powder with % RSD as 1.55%.

3.5. Precision and Accuracy

The intra-day and inter-day precision was used to study the variability of the method. The % RSD for intra-day and inter-day precision for Mimosine were 0.66 and 1.06%, respectively. Accuracy of the method was studied using the method of standard addition. Standard Mimosine solution were added to the extract of the whole plant powder of *Mimosa pudica* L. and the percent recovery was determined at two different levels 50% and 100%. Mimosine content was determined and the percent recovery was calculated. The results of recovery analysis are shown in **Table 1**.

4. RESULTS AND DISCUSSION

The high selectivity of MS-MS detection allowed the development of a very specific and rapid method for the determination of Mimosine in *Mimosa pudica* L. whole

Table 1. Results of recovery experiment.

Standard	Level	Pre analysed sample in (ng mL^{-1})	Amount of std added to pre analysed sample in (ng mL^{-1})	Total amount of std found in (ng mL^{-1})	SD	RSD (%) (n = 7)	Recovery (%)
	0	484.59	0	479.13	6.72	1.40	98.87
Mimosine	50%	484.59	250	730.79	7.40	1.01	99.48
	100%	484.59	500	979.39	10.96	1.12	99.47
						Mean	99.28

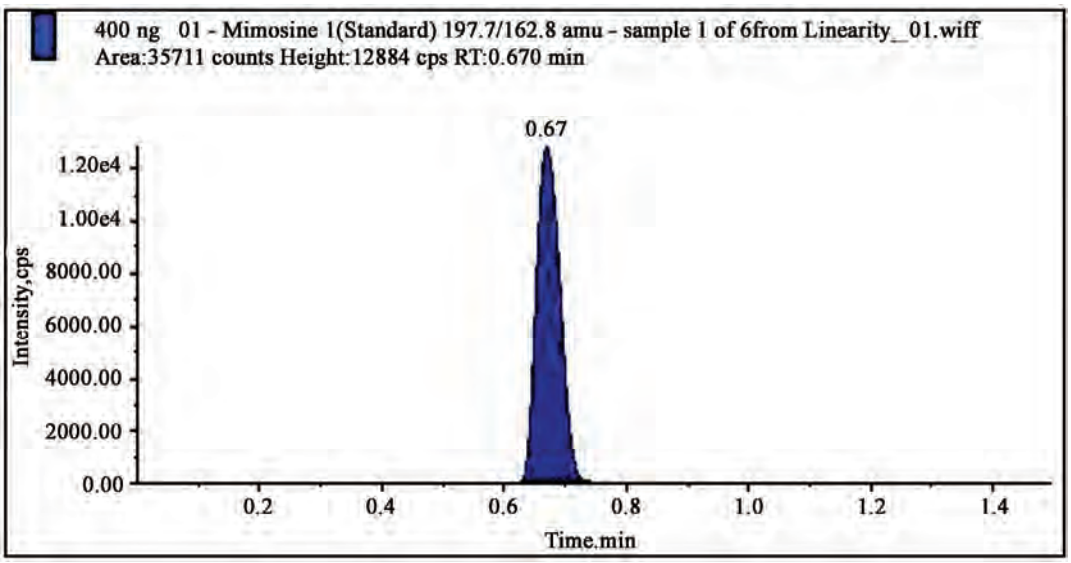

Figure 3. Representative chromatogram of standard Mimosine at LLOQ level (400 ng mL^{-1}).

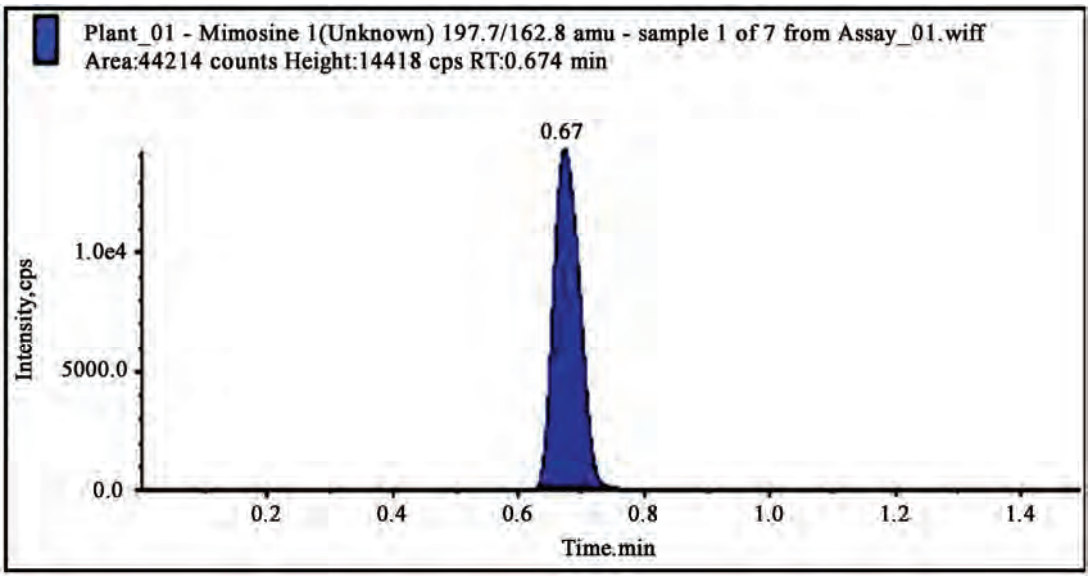

Figure 4. Representative chromatogram of plant *Mimosa pudica* L.

plant powder. During method development different options were evaluated to optimize, detection parameters and chromatography. Electrospray ionization (ESI) was evaluated to get better response of analytes as compared to atmospheric pressure chemical ionization (APCI) mode. It was found that the best signal was achieved

with the ESI negative ion mode. A mobile phase containing formic acid solution and Methanol in varying combinations was tried during the initial development stages. But the best signal for Mimosine was achieved using a mobile phase containing 10mM ammonium formate buffer pH adjusted to 3.00 ± 0.05 with formic acid in combination with Methanol (20:80 v/v). Use of a short Hypurity C_{18}, (50 mm × 4.6 mm), 5 µ column resulted in reduced run time of 1.5 min. Regression analysis of calibration data showed that the linearity of Mimosine was observer over a concentration range of 400 ng mL^{-1} to 1000 ng mL^{-1} with regression coefficient of 0.9951. The concentration of Mimosine in 1.0 g of whole plant powder of *Mimosa pudica* L. was found to be 1.938 mg.

When the method was validated in terms of instrumental precision, intra-assay precision and intermediate precision, the percent RSD values were found to be less then 2, indicating that the proposed method is precise and reproducible. The accuracy of the method was established by means of recovery experiments. The mean recovery was close to 100%, which indicates that method is accurate. The low values of %COV for replicate analyses are indicative of precision of the method. The method is specific because it resolved the standard Mimosine (Retention time = 0.67) well in presence of other phytochemicals of whole plant powder of *Mimosa pudica* L.

5. CONCLUSIONS

A new LC-MS-MS method has been developed for quantification of Mimosine from whole plant powder of *Mimosa pudica* L. The method developed with careful validation was found to be fast, simple, precise, sensitive and accurate. The linearity, precision, accuracy of the method prove that the method is easily reproducible in any quality control set-up provided all the parameters are followed accurately.

REFERENCES

[1] Sharma, S.K. and Wattal, B.L. (1979) Efficacy of some mucilaginous seeds as biological control agents against mosquito larvae. *Journal of the Entomological Research*, **3(2)**, 172-176.

[2] Vaidya, G.H. and Sheth, U.K. (1986) *Mimosa pudica* Linn., its medicinal value and pilot clinical use in patients with menorrhagia. *Ancient Science of Life*, **5(3)**, 156-160.

[3] Hemadri, K. and Rao, S.S. (1983) Leucorrhoea and Menorrhagia. *Tribal Medicine and Ancient Science of Life*, **3(1)**, 40-41.

[4] Sharma, P.C., Yelna, M.B. and Dennis, T.J. (2001) Database on medicinal plants used in Ayurveda. *Central Council for Research in Ayurveda & Siddha, India*, **2**, 369-379.

[5] Aalok, P.K. (1997) Lajjalu-an indispensable drug for blood pressure. *Sachitra Ayurved*, **50(1)**, 21-22.

[6] Zeitune, M.G. and Laguens, R.M., Inventors, Xl global corporation, assignee, use of mimosine or a derivative thereof for treating the cutaneous effects of psoriasis and related skin disorders, and cosmetic or pharmaceutical composition containing same. US patent 424725.

[7] (2006) The Mreck index. *Mimosine*, **14(6199)**, 1069.

[8] Bagul, M.S. and Rajani, M. (2005) Phytochemical evaluation of classical formulation: A case study. *Indian Drugs*, **42(11)**, 15-19.

[9] Debey, N., Debey, N., Mehta, R. and Saluja, A. (2009) Determination of psoralen and plumbagin from its polyherbal oil formulation by an HPTLC. *Journal of AOAC International*, **92(3)**, 779-784.

[10] Nair, L.S., Menon, S.N., Shailajan, S., Baing, M.M. and Sane, R.T. (2007) Reverse phase high performance thin layer chromatographic quantification of Mimosine from whole plant of *Mimosa pudica* Linn. *Journal of Planer Chromatography-Modern TLC*, **20(1)**, 49-51.

[11] Puchala, R., Davis, J.J. and Sahlu, T. (1996) Determination of mimosine and 3,4-dihydroxypyridine in milk and plasma of goats. *Journal of Chromatography B*: *Biomedical Sciences and Applications*, **685(2)**, 375-378.

[12] Lalitha, K., Vargheese, C.M. and Balasubramanian, N., (1993) Spectrophotometric determination of Mimosine and e-hydroxy-4-(1H)-pyridone-the toxic principles of Leucaena leucocephala. *Analytical Biochemistry*, **213(1)**, 57-62.

[13] ICH-Q2A, (1994) Text on validation of analytical procedures. *Proceedings of the International Conference on Harmonization of Technical Requirements for Registration of Pharmaceuticals for Human Use*, Geneva.

[14] ICH-Q2B, (1996) Validation of analytical procedure: Methodology. *Proceedings of the International Conference on Harmonization of Technical Requirements for Registration of Pharmaceuticals for Human Use*, Geneva.

Vol.2, No.7, 718-725 (2010)
doi:10.4236/ns.2010.27089

Natural Science

Residues of 862, 921 of VP3 are associated with virulence in infectious bursal disease virus strain Harbin-1

Renmao Li[1,2], Haiying Wang[1,3], Guangming Huang[1], Manfu Zhang[1*]

[1]Lab for Animal Molecular Virology, College of Biological Sciences, China Agricultural University, Beijing, China; *Corresponding Author: Manfuzhang@yahoo.com
[2]Life Sciences and Technology School, Zhanjiang Normal University, Zhanjiang, China
[3]Department of Biochemistry and Molecular Biology, Peking University Health Center, Beijing, China

Received 25 February 2010; revised 28 April 2010; accepted 6 May 2010.

ABSTRACT

Reverse genetics was used to study the effect of particular amino acids of infectious bursal disease virus (IBDV) on virulence. Using site-directed mutagenesis, altering of two amino acids in VP2 (Q253H, A284T) and VP3 (H783Q, V862M, I921V) in the segment A of a Chinese very virulent IBDV field strain Harbin-1, 4 virus mutants including $H_{253/284}$, $H_{783/862}$, $H_{862/921}$, $H_{921/783}$ were rescued. To evaluate the characteristics of the recovered viruses in vivo, we inoculated 4-week-old chickens with virus mutants and rescued Harbin-1 (rHarbin-1), analyzed their bursae for pathological lesions 4 days postinfection. rHarbin-1 and $H_{783/862}$, $H_{253/284}$ caused severe bursal lesion, milder lesion for $H_{862/921}$, mildest for $H_{921/783}$. However, $H_{253/284}$ caused the lowest mortality. The results showed that residue at position Q253, A284 of VP2 and V862, I921 of VP3 gene are involved with virulence, but there is difference between VP2 and VP3's role in virulence. The ability of 862 and 921 to control virulence in VP3 is stronger than 253 and 284.

Keywords: IBDV; VP3; Mutagenesis; Reverse Genetics; Virulence

1. INTRODUCTION

Infectious bursal disease (IBD) is a highly contagious disease among young chickens and characterized by the destruction of the bursa of Fabricius. IBD was first described by Cosgrove [1], but in China the first case was reported in 1979 [2]. Nowadays IBD has spread worldwide and continues to threat the poultry industry. Infectious bursal disease virus (IBDV) is the causative agent of the disease, belonging to *Avibirnavirus* genus of the *Birnaviridae* family [3]. Europe had experienced the emergence of very virulent infectious bursal disease virus (vvIBDV) which can cause up to 70% flock mortality [4,5]. Meanwhile, vvIBDV infections also have been observed in Asia and in South America [6].

The genome of IBDV consists of two segments of double-stranded RNA (dsRNA), approximately 3.4 kb (segment A) and 2.7 kb (segment B) in length [7]. Segment A contains two partially overlapping open reading frames (ORFs). The larger ORF encodes a polyprotein (1,012 amino acids, 110 kDa) that is autocatalytically cleaved to yield the viral proteins pVP2 (VPX) (48 kDa), VP4 (29 kDa) and VP3 (33 kDa). During virus maturation, pVP2 is processed into matured VP2 (41 to 38 kDa), probably resulting from site-specific cleavage of pVP2 by a host cell-encoded protease [8]. The smaller ORF encodes the nonstructural protein VP5 (145 to 149 amino acids, 17 kDa). Segment B encodes VP1 (970 kDa) having putative RNA-dependent RNA polymerase activity [9,10]. This protein is covalently linked to the 5' ends of the genomic RNA segments or present at a free form [11,12]. VP2 and VP3 are the major structural protein of the virion. The VP2 is the major host-protective antigen of IBDV and contains the determinants responsible for causing antigenic variation [13-15]. Position 279 and 284 amino acids in the VP2 variable region possibly contribute to virulence of IBDV [16]. Residues 253 and 284 of the VP2 protein of the variant virus are necessary for tissue culture infectivity [17]. The virulence and pathogenic-phenotype markers of IBDV reside in VP2 and residues at position 253 (Gln), 279 (Asp) and 284 (Ala) of VP2 are involved in the virulence and

*Part of the contents in this article was presented in Shanghai University in June of 2009.

pathogenic phenotype of virulent IBDV [18-20]. However, recent study demonstrated VP2 is not the sole determinant of the very virulent phenotype [21]. C-terminal part of VP3 may play a decisive role in controlling the virulence [22]. VP3 could play an important role in receptor-mediated virus-cell attachment, which implied that VP3 has relation with virulence [23].

In order to verify if VP3 have molecular determinant of virulence for Chinese vvIBDV strain Harbin-1, amino acids in VP3 among Harbin-1, D78 (vaccine strain), TY89 (IBDV serotype II) were aligned, the different amino acids among them were listed in **Table 1**. TY89 could not infect B lymphocytes, having no virulence to B lymphocytes, and D78 has mild virulence to B lymphocytes. Based on the result of alignment the amino acids in VP3 that maybe involved in virulence could be found. Position 783 and 862 in Harbin-1 have different amino acids from D78, however, position 921 is different from TY89. To prove their role in virulence, position 783, 862 and 921 in VP3 were mutated subsequently to obtain the combination of two points mutation. As a control, position 253 and 284 in VP2 hypervarible region was mutated at the same time. By use of cRNA-based reverse-genetics system for IBDV [20], four virus mutants were recovered. Furthermore, the characteristics of recovered virus in vitro and in vivo were described and the amino acids responsible for virulence. In this paper we report the discovery that residues of 783, 862, 921 of VP3 are associated with virulence of IBDV.

2. MATERIALS AND METHODS

2.1. Virus and Cells

The very virulent strain Harbin-1 was kindly given by Harbin Veterinary Research Institute of the Chinese Academy of Agricultural Sciences. Harbin-1 causes 100% morbidity and mortality of specific-pathogen-free (SPF) chickens, the mean infection lethal dose (ILD_{50}) for SPF embryo is 10^{-4}/0.2 ml. Primary bursal cells were derived from 18-day-old embryonated SPF eggs (Merial, Beijing, China) and were grown in Dulbecco's minimal essential medium (DMEM, Sigma Aldrich, St. Louis, MO, USA) supplemented with 10% fetal calf serum (FCS) and maintained with DMEM with 5% FBS [22]. Transfection experiments were performed on primary bursal cells. All virus mutants including $H_{253/284}$, $H_{783/862}$, $H_{862/921}$, $H_{921/783}$ and rHarbin-1, Harbin-1 were used as the viruses for challenge at a dose of 1200 pfu per animal via eye and nose drop.

2.2. Construction of Full-Length CDNA Clones

Several clones for segment A and segment B of Harbin-1 were constructed, pGEM-T-HA (coding sequence of segment A clone), pGEM-T-H5′-A (5′ non-coding sequence of segment A clone), and pGEM-T-H3′A (3′ non-coding sequence of segment A clone), pGEM-T-HB (coding sequence of segment B clone), pGEM-T-H5′B (5′ non-coding sequence of segment B clone), pG EM-T-H3′B (3′ non-coding sequence of segment B clone). All recombinant plasmids were based on pGEM-T (Promega, Madison, WI, USA). There is partly overlapped area between CR (coding region) clone and NCR (non-coding region) clone for segment A and B. But the overlapped area lack appropriate restriction site, thus fusion PCR was used to ligate the NCR and CR to obtain the full length cDNA clone for segment A and B. Oligonucleotides HACR1, HACR2, HANCR1, HAN CR2, HBCR1, HBCR2, HBNCR1, HBNCR2 (**Table 2**) were adopted for segment A and B. For transcription in vitro, EcoRI site and T7 promoter was introduced into 5′ end of oligonucleotides; XbaI site at 3′ end in segment A and XhoI site at 3′ end in segment B. The fusion PCR product of segment A and B was ligated into the T-vector (Takara Bio, Dalian, China) to obtain full-length cDNA clone named as pRHA and pRHB respectively. The sequence of final products was determined by Takara Bio Ltd.

2.3. Site-Directed Mutagenesis

Mutations were introduced into the cDNA of segment A of Harbin-1 according to the manufacture's instruction of QuickChange site-directed mutagenesis kit (Stratagene, La Jolla, CA, USA) with minor modification. Amino acid residues 253, 284, 783, 862, 921 were located in large open reading frame of segment A and their

Table 1. Different AA in VP3 for Harbin-1 and vaccine strain, serotype II strain.

AA site	767	773	783	787	815	862	899	905	921	947	981	990	992	1005	AA site
strain															strain
Harbin-1	S	E	H	S	R	V	D	L	I	K	P	V	T	A	Harbin-1
D78	S	E	Q	S	R	M	D	L	I	K	L	A	T	A	D78
TY89	D	D	R	Q	K	M	E	P	V	R	P	A	S	T	TY89

Table 2. Oligonucleotides used for amplification of Harbin-1 sequence*.

Oligonucleotides	Qrientation	Position	Name
CTCCTCCTTCTACAACGCTATCAT	sense	71-94	HACR1
GAATCTAGAGGGGACCCGCGAACG XbaI	antisense	3246-3260	HACR2
GGAATTCTAATACGACTCACTATAGGGGGGATACGATCGGTCTG	sense	1-20	HANCR1
EcoRI			
GATCTTGCAGGTTCGTCATCGC	antisense	128-149	HANCR2
TGGCTACTAGGGGCGATGC	sense	42-6	HBCR
CTTCTTGAGTGGTTCCCATC	antisense	2756-2775	HBCR2
GGAATTCTAATACGACTCACTATAGGATACGATGGGTCTGACCCT	sense	1-21	HBNCR1
EcoRI			
GTCACTCATGGTGGCAGAATCAT	antisense	98-120	HBNCR2
AAACAAGCGTCCAtGGCCTTATACTGGGTGCTA	sense	876-908	253mut1
TAGCACCCAGTATAAGGCCATgGACGCTTGTTT	antisense	876-908	253mut2
GACAATGGGCTAACGACcGGCACTGACA	sense	965-992	284mut1
TGTCAGTGCCgGTCGTTAGCCCATTGTC	antisense	965-992	284mut2
GACCCACTGTTCCAaTCTGCGCTCAG	sense	2465-2490	783mut1
CTGAGCGCAGAtTGGAACAGTGGGTC	antisense	2465-2490	783mut2
CTCAAAGAAGaTGGAGACTATGGG	sense	2704-2727	862mut1
CCCATAGTCTCCAtCTTCTTTGAG	antisense	2704-2727	862mut2
CATCAGAAGAACAAgTCCTAAGGGCAG	sense	2877-2903	921mut1
CTGCCCTTAGGAcTTGTTCTTCTGATG	antisense	2625-2652	921mut2
TAACCGTCCTCAGCTTACCC	sense	625-644	outside1
TCAGGATTTGGGATCAGCTC	antisense	1246-1265	outside2
CCAACCAGCGAGATAACC	sense	1019-1036	inside 1
GGCGACCGTAACGACAG	antisense	1212-1228	inside 2
TTCTCAGCTAATATCGATGC	sense	842-861	53,84 inupper
GATGTGATTGGCTGGGTT	antisense	1057-1074	53,84 inlower
GTCCAACTGGGCGACGTT	sense	2296-2313	vp3 outupper
CTGGGATTGCGATGCTTCA	antisense	3069-3087	vp3 outlower
CTTCCACCCAATGCAGGAC	sense	2378-2396	783 inupper
CTTTGGCGACTTCGTCTATGA	antisense	2976-2996	62,21 inlower

*Sequence and location of the oligonucleotide used in the study. Underlined nucleotides are virus-specific. Altered nucleotides for mutagenesis are in lowercase, the altered coding nucleotide triplets are highlighted in boldface. Used restriction sites are highlighted in boldface and appropriate restriction enzymes are named. The positions where the primers bind (nucleotide number) are in accordance with the sequence of strain P2 (Mundt *et al.*, 1995).

base sites were in position 893(A→T), 984(G→A), 2483(T→A), 2718(G→A), 2895(A→G) respectively in segment of Harbin-1. First, single site-directed mutagenesis was introduced into the segment A of Harbin-1 with oligonucleotides 253 mut, 783 mut, 862 mut, 921 mut (**Table 2**); the mutants were sequenced to verify the

resultant mutation; after then the second site-directed mutagenesis was introduced into the first mutation product with oligonucleotides 284 mut, 862 mut, 921 mut, 783 mut (**Table 2**) to obtain two point mutagenesis clone named p253/284 m, p783/862 m, p862/921 m, p921/783 m respectively. The second mutation products were sequenced by the company (Takara). The obtained muta-genized plasmids with the alteration of two amino acids, Q253H-A284T, H783Q-V862M, V862M-I921V, H783 Q-I921V were used for subsequent transcription *in vitro* and transfection experiments.

2.4. Transcription and Transfection of Synthetic RNAs

The experiment was performed by the protocol described by Mundt with minor alterations [24]. For transcription *in vitro*, non-mutation and mutated plasmids of segment A and intact segment B were linearized by cleavage with XbaI and XholI respectively. After restrictive digestion, the products were adjusted to 0.5% SDS and incubated with proteinase K (0.5 mg/ml) for 1 hr at 37℃. The linearized DNA templates were recovered by ethanol precipitation, and 1 μg linearized DNA was used for transcription. Segment A and segment B was transcribed respectively. Transcription reaction mixture (30 μl) containing 40 mM Tris-HCl (pH 7.9), 10 mM NaCl, 6 mM $MgCl_2$, 2 mM spermidine, 0.5 mM ATP, 0.5 mM CTP, 0.5 mM UTP, 0.1 mM GTP, 0.25 mM cap analog [m7G(5′)ppp(5′)G] (Promega), 20 units RNasin, 130 units T7 RNA polymerase (Promega), and incubated at 37℃ for 1 hr. As controls, the transcription products were treated with either DNase or RNase (Promega).

After primary bursal cells were grown to 80% confluency in 35-mm dishes, the cells were washed with DMEM (free serum) and incubated at 37℃ for 10 minutes in a CO_2 incubator. The process was repeated again. Simultaneously, 60 μl DMEM (free serum) was incubated with 6 μl of Lipofectin reagent (Invitrogen, Carlsbad, CA, USA) for 60 min in a polystyrene tube at room temperature to form Lipofectin-DMEM mixture. Synthetic RNA transcripts of both segments resuspended in 30 μl of DEPC treated water were mixed and added to the DMEM-Lipofectin mixture, mixed gently and incubated on ice for 5 min. After removing the DMEM from the monolayers in the 35-mm dishes and replacing it with fresh 800 μl of DMEM, the nucleic acid-containing mixture was added drop-wise to the cells and swirled gently. After 2 hours of incubation at 37℃, the mixture was replaced with DMEM containing 5% FCS (without rinsing the cells), and further incubated at 37℃ for desired time intervals.

2.5. Virus Recovery from cRNA and Detect the Presence of Virus by AC-ELISA, RT-PCR and Plaque Assay

Two days after transfection, cells were frozen -thawed and centrifuged at 700 g to remove cellular debris. The supernatant was passaged for 4 times in the primary bursal cells, harvesting the cells for ELISA. In order to screen the recombinant virus from many samples AC-ELISA was performed. Each well of 96-wells polystyrene ELISA plates (Costar, Cambridge, MA, USA) were coated with 100 μl of chicken polyclonal IBDV antiserum, diluted in PBS at a ratio of 1:4000. After incubation at 37℃ for 1 hour, the plate was washed three times with washing buffer (1% Tween 80 in PBS) and each well was blocked by 100 μl of blocking buffer (0.5% gelatin in PBS) at 37℃ for 0.5 h. After three washes of the plate with washing buffer, 100 μl sample including positive and negative control was added in duplicate. The plate was then incubated at room temperature for 1 h and washed with washing buffer before 50 μl of MAbs M6 or B29 [25,26]., diluted 1:2500 and 1:1000 in antibody diluent (5% NaCl and 4% BSA in washing buffer) respectively, were added to the wells in duplicate. After incubation for 1 h at room temperature, the plate was washed three times with washing buffer. Subsequently, 50 μl of goat anti-mouse IgG-horseradish peroxidase (Sigma) diluted 1:1000 with antibody diluent was added. One hour later at room temperature, the plate was washed three times with washing buffer. After addition 100 μl TMB peroxidase substrate (Kirkegaard and Perry Laboratories Inc., Gaithersburg, MD, USA) and incubated at 37℃ for 15 min, the reaction was stopped by adding 100 μl 1 M H_3PO_4. The result was read by an ELISA reader at the optical density at 450 nm (OD450). If OD value of sample is greater than mean OD value plus 3 times standard deviation of negative control sample, then the sample is considered as positive and was stocked at −86℃ for future use.

The titre of virus mutants was determined using plaque assay [27] and prepared for future animal experiment. The titre is represented as PFU/ml.

IBDV mutants were reversely transcribed using outside 1 and nested PCR was amplified using outside 1, outside 2, inside 1 and inside 2 primer (**Table 2**).

2.6. Genetic Stability Analysis

If changes in the amino acid sequence occurred during passaging viral RNA of IBDV before challenge, the identity of virus have to be confirmed. The virus mutants were subjected to RT-PCR using oligonucleotides outside 1 and outside 2 for IBDV with VP2 mutation, VP3 outupper and VP3 outlower for IBDV with VP3 muatation before challenge (**Table 2**). Nested PCR was ampli-

fied with 783 inupper and 62, 21 inlower to identify virus with VP3 alteration (**Table 2**). Cloned PCR fragments of IBDV mutants were sequenced and obtained sequences were analyzed with DNAStar.

2.7. Virulence of IBDV Mutants in Young SPF Chickens

Forty eight 4-week-old SPF White Leghorn chickens were divided randomly into six groups including positive control group. Chickens were infected via eye and nose drop with total 1200 PFU. Non-inoculated hatchmates were used as negative controls. During the course of the experiment animals were observed daily for clinical signs and mortality. At 4 days p.i., all alive chickens from each group were bled and euthanized. The bursa of each chicken (include alive and dead) was removed, weighed and subdivided into two parts. One part was used for detecting the presence of IBD viral antigen by means of an AC-ELISA and RT-PCR. The second part was fixed in 10% neutral-buffered formalin for histology. Formalin-fixed bursal samples were embedded in paraffin, sectioned and stained with haematoxylin and eosin (H&E). Microscopic bursal lesion score (BLS) was determined by histopathological analysis of the bursa. BLS was evaluated on a scale of 0 to 5 as follows: 0, no abnormalities; 1, 1-20%; 2, 21-40%; 3, 41-60%; 4, 61-80%; and 5, 81-100% lymphocyte depletion [28].

2.8. Detection of Viral Antigen in Bursae after Challenge

Bursae were homogenized with homogenizer. The presence of virus in the bursal homogenate was detected with AC-ELISA which incorporated Mab 6 recognizing VP2-located epitopes [25].

3. RESULTS

3.1. Determination of Nucleotide Sequence of Harbin-1 Mutant

To establish a reverse genetics system the complete genomic sequence of Harbin-1 mutants was determined. The mutagenized plasmids were obtained with the alteration of two amino acids, Q253H-A284T, H783Q-V862M, V862M-I921V, H783Q-I921V.

3.2. Rescue of Recombinant Virus from cDNA

Primary bursal cells were transfected with synthesized cRNA of mutated segment A and intact segment B by means of lipofectin (Invitrogen). After every transfection, the resultant supernatant was used for RT-PCR and AC-ELISA to detect the presence of viruses. The samples were performed to RT-PCR after IBDV antigen was detectable using AC-ELISA. Electrophoresis result showed that there is one 209 bp band, whose sequence located in VP2 hypervarible region, on 1.2% agarose gel. The result of RT-PCR and AC-ELISA demonstrated that virus mutants were successfully recovered. From 10 transfection samples we obtained four mutant viruses designated as $H_{253/284}$, $H_{783/862}$, $H_{862/921}$, $H_{921/783}$ and rescued Harbin-1 named rHarbin-1.

3.3. Genetic Stability Analysis

Sequence analysis of the RT-PCR products confirmed the identity of the IBDV used. No amino acid substitutions compared to the sequence of the used plasmids (p253/284 m, p783/862 m, p861/921 m, p921/783 m) were found within the region flanked by primers used for RT-PCR, proving the genetic stability of the virus during virus pass aging.

3.4. Virulence Determinants for VP2 and VP3 in Chinese vvIBDV Strain

To evaluate the virulence of all virus mutants animal experiments were performed. Animals infected with vvIBDV (rHarbin-1) and $H_{783/862}$ showed severe clinical signs of IBD. The mortality rates were 7/8 for rHarbin-1, 5/8 for $H_{783/862}$, 1/8 for $H_{253/284}$ and $H_{862/921}$. In contrast, none of the animals infected with $H_{921/783}$ died or showed clinical signs of IBD. Bursae of chickens infected with the different virus mutants showed depletion of bursal cells in lymph nodule with remarkable differences (**Figure 1**). rHarbin-1 and $H_{253/284}$, $H_{783/862}$ induced severe bursal lesion (BLS of 5, 1.6, 3.1 respectively); $H_{862/921}$ induced mild lesion (BLS 1.5); $H_{921/783}$ hardly induce lesion (BLS 0). As to the ration of bursal weight and body weight, rHarbin-1 and $H_{783/862}$ showed severe bursal atrophy (3.39, 3.94 respectively). There was no remarkable difference among $H_{253/284}$, $H_{862/921}$, $H_{921/783}$ and negative control (4.0, 4.8, 4.94, 4.71 respectively) (**Table 3**). The above-mentioned results demonstrated that V862 and I921 in VP3 are probably the major virulence determinants, furthermore, 862 and 921 in VP3 has the stronger ability to manage virulence than 253 and 284 in VP2.

4. DISCUSSION

In recent years, many investigators have shown that mutations in the viral genome often lead to changes in the virulence, pathogenesis of animal viruses. A single amino acid substitution in the West Nile Virus Nonstructural protein NS2A disables its ability to inhibit Alpha/Beta interferon induction and attenuates virus in mice [18]; point mutations in an infectious bovine viral diarrhoea virus type2 cDNA transcript yields an attenu-

Table 3. Results of chicken challenged by four recombinant viruses.

Virus	Number of Chickens*	Mortality	Avg bursa/body wt, Ratio (SD), 10^3	Avg BLS** (SD)	Pathological Lesions
$H_{253/284}$	8	1/8	4.0 (2.0)^{ab}	1.6 (1.1)^{b}	individual lymphatic nodule necrosis and atrophy in dead chicken
$H_{783/862}$	8	5/8	3.9 (1.5)^{ab}	3.1 (2.6)^{c}	lymphatic nodule severe necrosis and atrophy in dead chickens
$H_{862/921}$	8	1/8	4.8 (1.4)^{b}	1.5 (1.4)^{b}	lymphatic nodule partly necrosis and slightly atrophy in dead chicken
$H_{921/783}$	8	0/8	4.9 (0.9)^{b}	0 (0.0)^{a}	lymphatic nodule slightly atrophy and widen interstice close to normal
rHarbin-1	8	7/8	3.4 (0.9)^{a}	5 (0.0)^{d}	lymphatic nodule appear necrosis, congest and hemorrhage
Native Harbin-1	8	7/8	3.1 (0.4)^{a}	5 (0.0)^{d}	lymphatic nodule appear necrosis, congest and severe hemorrhage, atrophy
Negative control	8	0/8	4.7 (0.3)^{b}	0 (0.0)^{a}	normal

*The indicated number of 4-week-old SPF chickens were infected via the eye and nose drop; **BLS of BF of each chicken investigated. Values within the same row with the same superscript letters are not significant ($P < 0.05$).

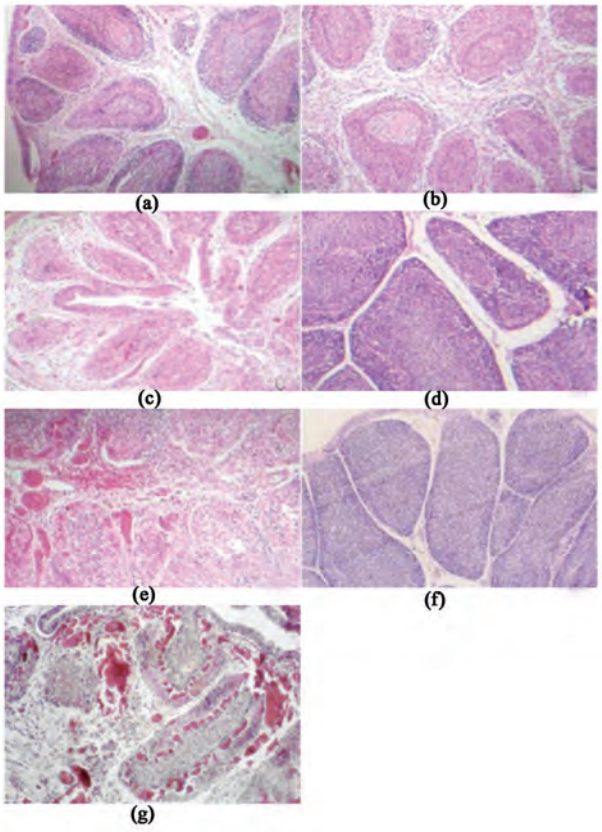

Figure 1. Microscopic pathological effect in bursae challenged by virus mutants (10 × 20) (a) $H_{253/284}$ single lymph nodule necrosis, atrophy, BLS 4; (b) $H_{783/862}$ lymph nodule severe necrosis, atrophy, BLS 4.5; (c) $H_{862/921}$ lymph nodule partly necrotize, BLS 2.3; (d) $H_{921/783}$ close to normal, BLS 0; (e) rHarbin-1 lymph nodule necrosis, congest and hemorrhage BLS 5; (f) CK (negative); (g) Harbin-1 (positive control) lymph nodule necrosis, congest and severe hemorrhage, atrophy BLS 5.

ated and protective viral progeny. Virulence of swine vesicular disease virus is determined at two amino acids in capsid protein VP1 and 2A protease [14]. Above mentioned phenomena elicit researchers on IBDV and they dedicated to study the virulence mechanism. A number of researchers such as Brandt, Yamaguchi, Lim, Mundt and so forth assumed position 253, 279, 284 amino acids in VP2 hypervarible region control phenotype, and could bind with B lymphocyte [3,17,21,29]. Lots of evidence showed that hypervarible region in VP2 involved in conformation dependent epitope and stimulate the chicken to produce protective neutralizing antibody [10, 29].

The result of chickens challenged with viruses showed that $H_{253/284}$ could induced slighter lesion than parental virus vvIBDV (Harbin-1), but in $H_{783/862}$ group, there are two kinds of appearance ,the bursa in alive chickens had not showed pathological sign, which could be due to the individual difference, but the bursae of dead chickens showed severe necrosis and atrophy, B lymphocyte depletion was up to the same 80-90% as Harbin-1; in $H_{862/921}$ group, a bursa of dead chicken had the same pathological lesion as Harbin-1, lymphocyte depletion up to above 90%, in other bursae of alive chickens depletion is only 10-20%, and appear partly necrosis and atrophy; in $H_{921/783}$ group bursae had very slightly pathological lesion except minor widening interstice, suggesting bursa was slight swollen. Therefore, $H_{921/783}$ virus appeared the slightest pathological lesion among all virus mutants. Compared with mDT-VP3C and mDCT-VP3C rescued by Boot who substituted the C-terminal part of VP3 of serotype 1 vvIBDV (isolate D6948) for the corresponding part of serotype 2 IBDV [22], $H_{921/783}$ induced slighter pathological lesion than

mDT-VP3C and mDCT-VP3C. mDT-VP3C and mDCT-VP3C could induced same bursa lesion as wild type D6948 and rD6948, suggesting mDT-VP3C and mDCT-VP3C had stronger residential virulence, but $H_{921/783}$ virus hardly has no residential virulence.

Our experiment demonstrated that VP3 and VP2 contain the determinant for virulence too besides VP2 in one strain. However, up to now most researches assume VP2 play an important role in virulence. The reason for this paradox about virulence controlling mechanism is unknown. Molecular determinant of virulence may depend the strains used. In addition we used two alterations of amino acid in this paper. Single alterations of aa 783, 862 and 921 were not tested, further study may be necessary to identify if single amino acid function or both of them function in virulence at the same time.

5. CONCLUSIONS

V862, I921 in VP3 is obvious virulence marker however I921 has more potential ability to control virulence than V862 and H783. Through animal challenge test we make clear the site in VP2 and VP3 involved in virulence, furthermore, the ability of 862 and 921 to control virulence in VP3 is more powerful than 253 and 284 in VP2.

6. ACKNOWLEDGEMENTS

We thank Professor Zhizhong Cui in Shandong Agricultural University for his assistance in animal experiment. Professor Zhao Deming in National Animal TSE Lab in China Agricultural University is gratefully acknowledged for his assistance in Quantitative realtime PCR experiment. This study was supported by Chinese NSFC grant No. 9893290 and INCO-China grant ERBIC18CT98-0330.

REFERENCES

[1] Cosgrove, A.S. (1962) An apparently new disease of chickens: Avian nephrosis. *Avian Diseases*, **6(3)**, 385-389.

[2] Wei, Y.W., Yu, X.P., Zheng, J.T., Chu, W.Y., Xu, H., Yu, X.M. and Yu, L. (2008) Reassortant infectious bursal disease virus isolated in China. *Virus Research*, **131(2)**, 279-282.

[3] Delmas, B. (2005) Birnaviridae. In: *Virus Taxonomy*, 8*th Report of the International Committee on Tax- onomy of Viruses*, Fauquet, C.M., Mayo, M.A., Maniloff, J., Desselberger, U. and Ball, L.A., Eds, Elsevier Academic, London, 561-569.

[4] Müller, H. (2003) Research on infectious bursal disease-the past, the present and the future. *Veterinary Microbiology*, **97(1-2)**, 153-165.

[5] Yamaguchi, T., Ogawa, M., Miyoshi, M., Inoshima, Y., Fukushi, H. and Hirai, K. (1997) Sequence and phylogenetic analyses of highly virulent infectious bursal disease virus. *Archives of Virology*, **142(7)**, 1441-1458.

[6] Ikuta, N., El-Attrache, J., Villegas, P., Garcia, E.M., Lunge, V.R., Fonseca, A.S., Oliveira, C. and Marques, E.K. (2001) Molecular characterization of Brazilian infectious bursal disease viruses. *Avian Diseases*, **45(2)**, 297-306.

[7] Dobos, P., Hill, B.J., Hallett, R., Kells, D.T.C., Becht, H. and Teninges, D. (1979) Biophysical and biochemical characterization of five animal viruses with bisegmented double-stranded RNA genomes. *Journal of Virology*, **32(2)**, 593-605.

[8] Kibenge, F.S., Qian, B., Cleghorn, J.R. and Martin, C.K. (1997) Infectious bursal disease virus polyprotein processing does not involve cellular proteases. *Archives of Virology*, **142(12)**, 2401-2419.

[9] Spies, U., Müller, H. and Becht, H. (1987) Properties of RNA polymerase activity associated with infectious bursal disease virus and characterization of its reaction products. *Virus Research*, **8(2)**, 127-140.

[10] Von Einem, U.I., Gorbalenya, A.E., Schirrmeier, H., Behrens, S.E., Letzel, T. and Mundt, E. (2004) VP1 of infectious bursal disease virus is an RNA-dependent RNA polymerase. *Journal of General Virology*, **85(8)**, 2221-2229.

[11] Dobos, P. (1993) *In vitro* guanylylation of infectious pancreatic necrosis virus polypeptide VP1. *Virology*, **193(1)**, 403-413.

[12] Spies, U. and Müller, H. (1990) Demonstration of enzyme activities requiredfor cap structure formation in infectious bursal disease virus, a member of the birnavirus group. *Journal of General Virology*, **71(Pt4)**, 977-981.

[13] Brown, M.D., Green, P. and Skinner, M.A. (1994) VP2 sequences of recent European 'very virulent' isolates of infectious bursal disease virus are closely related to each other but are distinct from those of 'classical' strains. *Journal of General Virology*, **75(Pt3)**, 675-680.

[14] Fahey, K.J., Erny, K. and Crooks, J. (1989) A conformational immunogen on VP2 of infectious bursal disease virus that induces virus-neutralizing antibodies that passively protect chickens. *Journal of General Virology*, **70(Pt6)**, 1473-1481.

[15] Letzel, T., Coulibaly, F., Rey, F.A., Delmas, B., Jagt, E.W., van Loon, A.A.M. and Mundt, E. (2007) Molecular and structural bases for the antigenicity of VP2 of infectious bursal disease virus. *Journal of Virology*, **81(23)**, 12827-12835.

[16] Yamaguchi, T., Ogawa, M., Inoshima, Y., Miyoshi, M., Fukushi, H. and Hirai, K. (1996) Identification of sequence changes responsible for the attenuation of highly virulent infectious bursal disease virus. *Virology*, **223(1)**, 219-223.

[17] Mundt, E. (1999) Tissue culture infectivity of different strains of infectious bursal disease virus is determined by

distinct amino acids in VP2. *Journal of General Virology*, **80(8)**, 2067-2076.

[18] Jackwood, D.J., Sreedevi, B., Lefever, L.J. and Sommer-Wagner, S.E. (2008) Studies on naturally occurring infectious bursal disease viruses suggest that a single amino acid substitution at position 253 in VP2 increases pathogenicity. *Virology*, **377(1)**, 110-116.

[19] Brandt, M., Yao, K., Liu, M., Heckert, R.A. and Vakharia, V.N. (2001) Molecular determinants of virulence, cell tropism, and pathogenic phenotype of infectious bursal disease virus. *Journal of Virology*, **75(24)**, 11974-11982.

[20] Van Loon, A.A.W.M., de Haas, N., Zeyda, I. and Mundt, E. (2002) Alteration of amino acids in VP2 of very virulent infectious bursal disease virus results in tissue culture adaptation and attenuation in chickens. *Journal of General Virology*, **83(1)**, 121-129.

[21] Boot, H.J., ter Huurne, A.A., Hoekman, A.J., Peeters, B.P. and Gielkens, A.L. (2000) Rescue of very virulent and mosaic infectious bursal disease virus from cloned cDNA: VP2 is not the sole determinant of the very virulent phenotype. *Journal of Virology*, **74(15)**, 6701-6711.

[22] Boot, H.J., ter Huurne, A.A., Hoekman, A.J., Pol, J.M, Gielkens, A.L. and Peeters, B.P. (2002) Exchange of the C-terminal part of VP3 from very virulent infectious bursal disease virus results in an attenuated virus with a unique antigenic structure. *Journal of Virology*, **76(20)**, 10346-10355.

[23] Yamaguchi, T., Kondo, T., Inoshima, Y., Ogawa, M., Miyoshi, M., Yanai, T., Masegi, T., Fukushi, H. and Hirai, K. (1996) *In vitro* attenuation of highly virulent infectious bursal disease virus: Some characteristics of attenuated strains. *Avian Diseases*, **40(3)**, 501-509.

[24] Mundt, E. and Vakharia, V.N. (1996) Synthetic transcripts of double-stranded Birnavirus genome are infectious. *Proceedings of National Academy of Sciences of USA*, **93(11-12)**, 11131-11136.

[25] Nunoya, T., Tajima, M. and Itakura, C. (1991) Primary culture of chicken bursal plical epithelium. *Research in Veterinary Science*, **50(3)**, 352-354.

[26] Eterradossi, N., Toquin, D., Rivallan, G. and Guittet, M. (1997) Modified activity of a VP2-located neutralizing epitope on various vaccine, pathogenic and hypervirulent strains of infectious bursal disease virus. *Archives of Virology*, **142(2)**, 255-270.

[27] Synder, D.B., Lana, D.P., Cho, B.R. and Marquardt, W.W. (1988) Group and strain-specific neutralization sites of infectious bursal disease virus defined with monoclonal antibodies. *Avian Diseases*, **32(5)**, 527-534.

[28] Hierholzer, J.C. and Killington, R.A. (1996) Suspension assay method. *Virology Methods Manual*, Academic, San Diego, 39-40.

[29] Schröder, A., van Loon, A.A.W.M., Goovaerts, D. and Mundt, E. (2000) Chimeras in noncoding regions between serotypes I and II of segment A of infectious bursal disease virus are viable and show pathogenic phenotype in chickens. *Journal of General Virology*, **81(23)**, 533-540.

Vol.2, No.7, 726-731 (2010)
doi:10.4236/ns.2010.27090

Natural Science

Review on dermatomycosis: pathogenesis and treatment

Deepika T. Lakshmipathy, Krishnan Kannabiran*

Division of Biomolecules and Genetics,School of Biosciences and Technology, VIT University, Vellore, India;
*Corresponding Author: kkb@vit.ac.in

Received 24 February 2010; revised 25 March 2010; accepted 3 April 2010.

ABSTRACT

Dermatophytes, a group of keratinophilic fungi thriving on the keratin substrate are the etiological agents responsible for causing cutaneous infections. Dermatophytosis is currently treated with the commercially available topical and oral antifungal agents in spite of the existing side effects. Treatment of these cutaneous infections with secondary metabolites produced by marine microorganisms is considered as a novel approach. For many years these organisms have been explored with the view of developing antibacterial, antifungal, antiviral, anticancer and antiparasitic drugs. Exploring the unexplored aspect of actinobacteria for developing antidermatophytic drugs is a novel attempt which needs further investigation.

Keywords: *Trichophyton*; *Microsporum*; *Epidermophyton*; *Tinea Infections*; Novel Approach; Actinobacteria

1. INTRODUCTION

1.1. Dermatophytes

Infections pertaining to mankind particularly those affecting the keratinized tissues are of serious concerns worldwide and are increasing on a global scale. Dermatomycoses are infections of the skin, hair and nail caused as a result of colonization of the keratinized layers of the body. This colonization is brought about by the organisms belonging to the three genera namely *Trichophyton*, *Microsporum* and *Epidermophyton* [1,2]. Infection may also be caused rarely by the members of the genus *Candida* and by non-dermatophytic moulds belonging to the genera *Fusarium*, *Scopulariopsis* and *Aspergillus* [3,4]. Interestingly dermatophytic infections are predominant in the tropical and subtropical countries; especially in the developing countries like India where the hot climate and humid weather is favourable to the acquisition and maintenance of the disease [5,6] and currently no race is totally free from dermatophytoses.

2. ECOLOGICAL CLASSIFICATION

In the course of evolution these pathogens have developed host specificity. This host specificity is ascribed to the difference in the composition of keratin [7]. Based on their host specificity dermatophytes are classified into three ecological groups namely *geophiles* (soil), *anthropophiles* (man) and *zoophiles* (animals) [8]. The geophilic dermatophytes are generally saprophytic and derive nutrients from keratinous substrates. Rarely these pathogens cause infection in animals and man. Examples include *Trichophyton ajelloi*, *Trichophyton terrestre*, *Microsporum fulvum*, *Micropsorum gypseum*, *Microsporum cookie* and *Epidermophyton stockdaleae* [9-11].

Zoophiles are pathogens with only one animal host and grow as saprophytes on animal materials. Zoophiles are also reported to infect human beings. Human beings acquire the infection from infected animals. Examples include *Trichophyton simii* (monkeys), *Trichophyton mentagrophytes* (rodents), *Trichophyton equinum* (horses), *Microsporum canis* (cats) and *Micropsorum nannum* (pigs) [12,13].

The primary hosts of anthropophilic species are human beings but they may also cause infection in animals. Transmission of infection is from man to man. Examples include *Trichophyton rubrum*, *Trichophyton kanei*, *Trichophyton schoenleini*, *Trichophyton concentricum*, *Trichophyton tonsurans*, *Micropsorum gypseum*, *audouinii*, *Microsporum ferrugineum* and *Epidermophyton floccosum* [14,15].

2.1. *Trichophyton*

The genus *Trichophyton* includes 24 species. The colonies on agar media are powdery, velvety or waxy. The predominant spore type is micro conidia with sparse

macro conidia [16]. Reverse side pigmentation is characteristic of the species and is used for the identification of the species within the genus [17,18]. The macro conidia are thin walled with smooth surface and variable shape [19]. Some of the *Trichophyton* species are fastidious in their requirement for amino acid as nitrogen source. *Trichophyton tonsurans* requires ornithine, citrul-line and Arginine whereas *Trichophyton mentagrophytes* requires methionine. This nutritional specificity has been used by many authors in the identification of the *Trichophyton* species [19].

2.2. *Microsporum*

The genus *Microsporum* includes 16 species. The colony *morphology* of Microsporum species on agar surface is either velvety or powdery with white to brown pigmentation [16]. Both macro and micro conidia are produced but the predominant conidial structures are macro conidia. Micro conidia are less abundant. The macro conidia are multi septate with thick wall and rough surface [20]. Rarely some species produce neither micro nor macro conidia [21]. They do not have any special nutritional requirements.

2.3. *Epidermophyton*

The genus *Epidermophyton* includes only 2 species. The colonies are slow-growing, powdery and unique brownish yellow in colour. This genus is devoid of micro conidia. Macro conidia are abundant and produced in clusters [16]. These macro conidia are thin walled with smooth surface [20].

3. DISTRIBUTION FREQUENCY OF DERMATOPHYTES AND DERMATOPHYTOSIS

All the three genera of dermatophytes namely *Trichophyton*, *Microsporum* and *Epidermophyton* are worldwide in geographical distribution. The predominant cause of dermatophytic infections is *Trichophyton* followed by *Epidermophyton* and *Microsporum*. Within the genus *Trichophyton*, *Trichophyton rubrum* is the predominant etiological agent accounting for 69.5% followed by *Trichophyton mentagrophytes*, *Trichophyton verrucosum* and *Trichophyton tonsurans* [22-24].

According to the World Health Organization (WHO) survey on the incidence of dermatophytic infection, about 20% the people world wide present with cutaneous infections [25]. The disease does not spare people of any age [26]. Among the tinea infections the most predominant type of infection is *tinea corporis* or *tinea circinata* followed by *tinea cruris*, *tinea pedis* and *Onychomycosis*. *Tinea corporis* accounts for about 70% of the dermatophytic infection [26].

4. PATHOGENESIS AND CLINICAL PRESENTATION

The possible route of entry for the dermatophytes into the host body is injured skin, scars and burns. Infection is caused by arthrospores or conidia. Resting hairs lack the essential nutrient required for the growth of the organism. Hence these hairs are not invaded during the process of infection [27]. The pathogen invades the uppermost, non-living, keratinized layer of the skin namely the stratum corneum, produces exo-enzyme keratinase and induces inflammatory reaction at the site of infection [28-31]. The customary signs of inflammatory reactions such as redness (ruber), swelling (induration), heat and alopecia (loss of hair) are seen at the infection site. Inflammation causes the pathogen to move away from the site of infection and take residence at a new site. This movement of the organism away from the infection site produces the classical ringed lesion [32] (**Figure 1**).

The infections caused by dermatophytes are commonly referred to as "*tinea*" or "ring-worm" infections due to the characteristic ringed lesions [33]. Based on the site of infection the tinea infections are referred to as *tinea capitis* (scalp), *tinea corporis* or *tinea circinata* (non-hairy, glaborous region of the body), *tinea pedis* ("Athletes' foot"; foot), *tinea ungium* ("*Onychomycosis*"; nail), *tinea mannum* (hands), *tinea barbae* ("Barbers' itch"; bearded region of face and neck), *tinea incognito* (steroid modified), *tinea imbricata* (modified form of

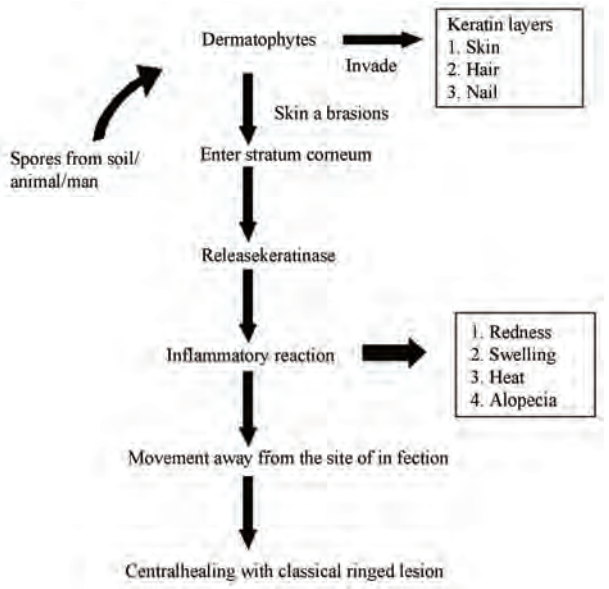

Figure 1. The schematic route of entry of dermatophytes into the host system and onset of immune response in the host in response to the pathogen entry.

tinea corporis), *tinea gladiatorium* (common among wrestlers') and *tinea cruris* ("Jocks' itch"; groin) [34].

5. IMMUNITY BEHIND DERMATOPHYTIC INFECTION

Host immune response to the invading pathogen is responsible for the clinical manifestations. The fungal pathogens induce both immediate hypersensitivity as well as cell mediated or delayed type hypersensitivity. Acquired resistance to the infection may also result from dermatophytic infection. The fungal growth is restricted by the inflammatory reactions produced as a result of infection with dermatophytes [35].

6. TREATMENT

Despite the advancements of science and technology, surprisingly the development of novel and efficient antifungal drugs is still lagging behind due to the very fact that fungi are also eukaryotic and have mechanisms similar to human beings [36]. Hence it becomes very difficult to develop an antifungal agent that is more specific in targeting the fungi alone without any damage to human beings. For successful treatment of the disease, proper diagnosis of the disease is always essential.

The treatment is chosen based on the infection site, etiological agent and penetration ability of the drug. The penetration ability and retention in the site of infection of the agent determines its efficacy and frequency of utility. Since the dermatophytes reside in the stratum corneum especially within the keratinocytes, the antifungal agents should have a good penetrating ability. The duration of treatment mainly depends on the type of infection and symptom. Generally a two-three week treatment is required for skin lesions whereas four-six week for feet inflammation [37].

Earlier, dermatomycosis was treated with the traditional topical antifungal agent *Whitfield's ointment*, a combination of 3% salicylic acid and 6% benzoic acid in a Vaseline base [38]. Next came into existence, *Castellani's paint*, a deep red coloured liquid, specifically effective against tinea ungium. Another topical preparation of importance was a combination of *silver nitrate* and *tincture iodine*. This preparation was effective against multiple lesions [39]. In general the dosage depends on the severity of infection, location and the efficacy of the drug. These topical preparations were applied twice a day for 2-3 weeks to prevent relapse condition. In addition to the above mentioned topical agents, tolnaftate, undecylenic acid, haloprogin, triacetin were in use for the treatment of dermatophytosis [39]. The year 1970 saw the release of Miconazole, the first in the line of azoles group. Since then many more were subsequently synthesized and added to this list during the same period. These antimycotic drugs belonged to the Azoles class of antifungal drugs. The major target of the azoles unlike the other antifungal agents is the cytochrome P_{450} enzyme [40] (**Figure 2**). Based on the number of nitrogen atoms the azoles derivatives are classified into 2 groups as imidazoles and triazoles [16].

Imidazoles include miconazole (1970), clotrimazole, ketaconazole (1978), econazole, bifonazole, tioconazole and oxiconazole [41]. The chronological order of the imidazoles to get FDA approval in United States is as follows miconazole (1974), econazole (1982), ketaconazole (1985), oxiconazole (1988) and clotrimazole (1993) [42]. The most recent drug to clear the FDA trials (2003) is Sertaconazole, a novel imidazole with broad spectrum antifungal activity [43]. In general the imidazoles exhibit side effects such as anorexia, constipation, headache, hepatitis, pruritis, exanthema and inhibition of synthesis of steroid hormone [44]. Triazoles include fluconazole, voriconazole, itraconazole (1980), posaconazole, teraconazole and ravuconazole. In comparison to the imidazoles, the triazoles exhibit lesser degree of side effects which includes nausea, dizziness and gastrointestinal upset [45]. Allylamines and benzyl amines were synthesized in the 1980s'. Allylamines include naftifine and terbinafine. Naftifine, terbinafine and benzylamine obtained FDA approval in United States in the year 1988, 1992 and 2001, respectively. The mode of action of these drugs is inhibition of the key enzyme squalene epoxidase, an essential enzyme involved in the synthesis of squalene epoxide from squalene [46] (**Figure 2**).

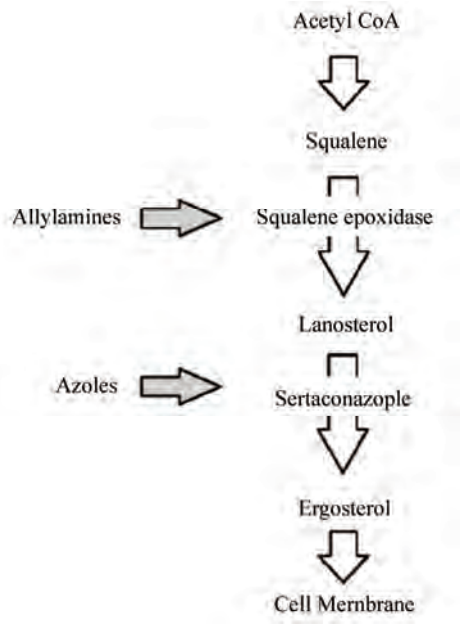

Figure 2. Schematic representation of the site of action of azoles, allylamines and benzyl amines.

Amorolfine, a morpholine drug targets the ergosterol synthesis similar to the azoles but at a site different from that of the azoles [47]. A new class of antifungal drug called hydroxypyridones became available since the year 2000. Ciclopiroxolamine, the representative drug of this class targets the cell membrane and affects the cell permeability. Apart from the above mentioned synthetic drugs many drugs such as Pyrrolo [1,2-a] [1,4] benzodiazepine with less side effects are being synthesized and experimented for treating dermatophytosis [48]. Griseofulvin, from *Penicillium chrysogenum* was isolated in 1930. Its antibacterial and antifungal potential was not fully understood until late 1950s'. It is the first antimycotic drug with a microbial origin [49]. Griseofulvin is a narrow spectrum antimycotic drug with fungistatic activity. It is very effective against all the dermatomycoses. The side effects include headache, nausea, bad taste, skin rash, systemic lupus erythematosus (SLE), porphyria and arthralgia. With all its side effects, griseofulvin still remains to be the gold-standard for treating dermatophytic infections [50]. Treatment of cutaneous infection using natural sources is the ongoing research work of many research groups across the globe. Compounds from the plants *Psorolea corylifolia* [51], *Azadirachta indica* [52], *Melaleuca alternifolia*, *Melaleuca dissitiflora*, *Melaleuca linariifolia* [53], *Nandina domestica* [54], *Didiscus oxeata* [55] have been reported to exhibit potential anti-dermatophytic activity. Further confirmation on the activity of these compounds is under investigation.

7. A NOVEL APPROACH TO SOLVE THE PROBLEM

More recently the scientific community has turned its attention to secondary metabolites from actinobacteria and its exploitation for various purposes which include therapeutic, environmental and industrial applications. With developing microbial resistance and need for safe and cost-effective antidermatophytic drugs, screening of actinobacteria for potential bioactive secondary metabolites becomes indispensible [56]. About 75-80% of the antibiotics that are available in the market are derived from *Streptomyces* [57]. To the best of our knowledge antidermatophytic secondary metabolite from *Streptomyces rochei* AK39 is the first report on antidermatophytic activity of actinobacteria [58]. Our investigation on the antidermatophytic activity of *Streptomyces* spp isolated from the saltpan region yielded three potential strains. The morphological, physiological and biochemical properties of these three potential isolates namely VITDDK1, VITDDK2 and VITDDK3 have been studied and reported [56,57]. The 16 S rRNA sequence of three strains *Streptomyces* spp. VITDDK1, *Streptomyces* spp. VITDDK2 and *Streptomyces* spp. VITDDK3 was submitted to the GenBank, NCBI under the accession numbers, GU223091, GU223092 and GU223093 respectively. The antidermatophytic activity of these three strains is anticipated to be due to high salt concentration of the environment. Under stress conditions microorganisms inhabiting the particular environment is said to produce complex chemicals that can be exploited medicinally.

8. CONCLUSIONS

The management of dermatophytic infections needs personal hygiene, awareness of infection, proper diagnosis and medication. At present there are a large number of antidermatophytic drugs available commercially. With increasing incidence of fungal infection, microbial resistance to the existing drugs, cost and side effects, there is a need for an antifungal drug that can overcome all these limitations. *Streptomyces* remains to be an unexhausted source of bioactive compounds and a boon to the medical field. Screening of Streptomyces from stressed environment can be a novel approach for obtaining potential lead molecules for clinical trials and later treatment of dermatomycosis.

9. ACKNOWLEDGEMENTS

The authors wish to thank the management of VIT University for providing the facilities to carry out this study and the International Foundation for Science (IFS, F 4185-1), Sweden and the Organization for the Prohibition of Chemical Weapons (OPCW), The Hague to one of the author (KK) for providing financial support.

REFERENCES

[1] Emmons, C.W., Bindford, C.H., Utz, J.P. and Kwon-Chung, K.L. (1977) Dermatophytoses. *Medical Mycology*, 3rd Edition, Lea and Febiger, Philadelphia, 117-167.

[2] Luilma, A.G., Sidrimb, J.J.C., Domingos, T.M., Cechinel, V.F. and Vietla, S.R. (2005) *In vitro* antifungal activity of dragon's blood from Croton urucurana against dermatophytes. *Journal of Ethnopharmacology*, **97(2)**, 409-412.

[3] Pinto, E., Pina-Vaz, C., Salgueiro, L., Goncalves, M.J., Costa-de-Oliveira, S., Carlos, C., Palmeira, A., Rodrigues, A. and Martinez-de-Oliveira, J. (2006) Antifungal activity of the essential oil of Thymus pulegioides on Candida, Aspergillus and dermatophyte species. *Journal of Medical Microbiology*, **55(10)**, 1367-1373.

[4] Naveed, A.M., Naeem, R. and Nasiruddin (2009) Non-dermatophyte moulds and yeasts as causative agents in Onychomycosis. *Journal of Pakistan Association of Dermatologists*, **19(2)**, 74-78.

[5] Rippon, J.W. (1988) *The Pathogenic Fungi and Pathogenic Actionmycetes*, 3rd Edition. WB Saunders, Phila-

delphia, 1988.
[6] Rao, A. (1959) Mycotic diseases in India - a critical review. *Bulletin of School of Tropical Medicine Calcutta*, 13-22.
[7] Georg, L.K. (1959) Animals ringworm in public health. *Diagnosis and Nature*, Bulletin, **57**.
[8] Rippon, J.W. (1982) Host specificity in dermatophytoses. *Proceedings of the Eight Congress of the International Society for Human and Animal Mycology*, 28-33.
[9] De Vroey, C. (1984) Ecological and epidemiological aspects in dermatophytoses. *Zbl Bakt Hyg.*, **257(2)**, 234-239.
[10] Baxter, M. and Pearson, R.D. (1969) The occurence of Microsporum nanumas a human pathogen and animal pathogen in New Zealand. *New Zealand Journal of Medical Laboratory Technology*, **23**, 87-90.
[11] Connole, M.D. (1990) Review of animal mycoses in Australia. *Mycopathologia*, **111(3)**, 133-164.
[12] English, M.P. (1972) The epidemiology of animal ringworm in man. *British Journal of Dermatology*, **86(3)**, 78-87.
[13] Marples, M.J. (1956) The ecology of Microsporum canis bodin in New Zealand. *Journal of Hygiene*, **54(3)**, 378-387.
[14] Georg, L.K. (1960) Epidemiology of dermatophytes sources of infection, modes of transmission and epidemicity. *Annals of the New York Academy of Sciences*, **89(2-3)**, 69-77.
[15] Kaplan, W. and Gump, R.H. (1958) Ringworm in the dog caused by Trichophyton rubrum. *Veterinary Medicine*, **53(1)**, 139-142.
[16] Jagdish, C. (1995) Dermatophytoses. *Medical Mycology*, 1st Etdition, 106-107.
[17] Wagner, D.K. and Sohnle, P.G. (1995) Cutaneous defenses against dermatophytes and yeasts. *Clinical Microbiology Reviews*, **8(3)**, 317-335.
[18] Larone, D.H. (1995) Medically important fungi: A guide to identification, 3rd Edition, American Society for Microbiology.
[19] Philpot, C.M. (1977) Use of nutritional tests for the differentiation of dermatophytes. *Sabouraudia*, **15(2)**, 141-150.
[20] Emmons, C.W. (1934) Dermatophytes-natural grouping based on the form of the spores and accessory organs. *Arch Dermatol Syphil*, **30(3)**, 337-362.
[21] St-Getmain, G. and Summerbell, R. (1996) Identifying filamentous fungi: A clinical laboratory handbook. Star Publishing, Belmont.
[22] Chen, B.K. and Friedlander, S.F. (2001) Tinea capitis update: A continuing conflict with an old adversary. *Current Opinion in Pediatrics*, **13(4)**, 331-335.
[23] Ciavaglia, M.C., de Carvalho, T.U. and de Souza, W. (1993) Interaction of trypanosoma cruzi with cells with altered glycosylation patterns. *Biochemical and Biophysical Research Communication*, **193(2)**, 718-721.
[24] Coloe, S.V. and Baird, R.W. (1999) Dermatophyte infections in Melbourne: Trends from 1961/64 to 1995/96. *Pathology*, **31(4)**, 395-397.
[25] Marques, S.A., Robles, A.M., Tortorano, A.M., Tuculet, M.A., Negroni, R. and Mendes, R.P. (2000) Mycoses associated with AIDS in the Third World. *Medical Mycology*, **38(Suppl. 1)**, 269-279.
[26] Vander Straten, M.R., Hossain, M.A. and Ghannoum, M.A. (2003) Cutaneous Infections dermatophytosis, onychomycosis, and tinea versicolor. *Infectious Disease Clinics of North America*, **17(1)**, 87-112.
[27] Weirzman, I. and Summerbell, R.C. (1995) The dermatophytes. *Clinical Microbiology Reviews*, **8(2)**, 240-259.
[28] Wawrzkiewicz, K., Wolski, T. and Lobarzewski, J. (1991) Screening the keratinolytic activity of dermatophytes in vitro. *Mycopathologia*, **114(3)**, 1-8.
[29] Lopez-Martinez, R., Manzano-Gayosso, P., Mier, T., Mendez-Tovar, L.J. and Hernandez-Hernandez, F. (1994) Exoenzymes of dermatophytes isolated from acute and chronic tinea. *Revista Latinoamericana de Microbiología*, **36(1)**, 17-20.
[30] Siesenop, U. and Bohm, H. (1995) Comperative studies on keratinase production of Trichophyton mentagrophytes strains of animal origin. *Mycoses*, **38(5-6)**, 205-209.
[31] Muhsin, T.M., Aubaid, A.H. and Al-Duboon, A.H. (1997) Extracellular enzyme activities of dermatophytes and yeast isolates on solid media. *Mycoses*, **40(11-12)**, 465-469.
[32] Dahl, M.V. (1994) Dermatophytosis and immune response. *Journal of the American Academy of Dermatology*, **31(3)**, S34-S41.
[33] Theodore, C.W., Brian, G.O., Yvonne, G. and Matthew, R.H. (2008) Generating and testing molecular hypotheses in the dermatophytes. *Eukaryotic Cell*, **7(8)**, 1238-1245.
[34] Judith, A.W. (2005) Allergy and dermatophytes. *Clinical Microbiology Reviews*, 30-43.
[35] Grappel, S.F., Bishop, C.T. and Blank, F. (1974) Immunology of dermatophytes and dermatophytosis. *Bacteriology Reviews*, **38(3)**, 222-250.
[36] Berdy, J. (1989) The discovery of new bioactive microbial metabolites: Screening and identification. In: *Bioactive Metabolites from Microorganisms*, Bushell, M.E., Grafe, U., Eds., Elsevier, Amsterdam, 3-25.
[37] Elewski, B.E. and Hazen, P.G. (1989) The superficial mycoses and the dermatophytes. *Journal of the American Academy of Dermatology*, **21(4)**, 655-673.
[38] Pavithran, K. (1985) Fungal infections of the skin. *Dermato-Venero-Leprology*, 77.
[39] Pasricha, J.S. (1981) Infections and infestations. *Treatment of Skin Diseases*, **82(1)**, 73-74.
[40] Elewski, B.E. (1993) Mechanisms of action of systemic antifungal agents. *Journal of the American Academy of Dermatology*, **28(3)**, 28-34.
[41] Michael, A.P. and Deanna, A.S. (2006) Review of *in vitro* activity of sertaconazole nitrate in the treatment of superficial fungal infections. *Diagnostic Microbiology Infectious Disease*, **56(4)**, 147-152.
[42] Van Cutsem, J.M. and Thienpont, D. (1972) Miconazole, a broad-spectrum antimycotic agent with antibacterial activity. *Chemotherapy*, **17(1)**, 392-404.
[43] Agut, J., Palacı´n, C., Salgado, J., Casas, E., Sacrista´n, A. and Ortiz, J.A. (1992) Direct membrane-damaging effect of sertaconazole on Candida albicans as a mechanism of its fungicidal activity. *Arzneimittelforschung*, **42(5A)**, 721-724.
[44] Katsambas, A., Antoniou, C.H., Frangouli, E., Avgerinou, G., Michailidis, D. and Stratigos, J. (1989) A double-

blind trial of treatment of seborrhoic dermatitis with 2% ketaconazole cream compared with 1% hydrocortisone cream. *British Journal of Dermatology*, **12(Suppl 14)**, 353-357.

[45] Grant, S.M. and Clissold, S.P. (1989) Itraconazole: A review of its pharmacodynamic and pharmacokinetic properties and therapeutic use in superficial and systemic mycosis. *Drugs*, **37(3)**, 310-344.

[46] Wolverton, S.E. (2001) Systemic antifungal drugs. *Comprehensive Dermatologic Drug Therapy*, 2nd Edition, Saunders.

[47] Andriole, V.T. (2000) Current and future antifungal therapy: New targets for antifungal therapy. *International Journal of Antimicrobial Agents*, **16(3)**, 317-322.

[48] Lieven, M., Jef, V.G., Frans, V.G., Filip, W., Patrick, M., Vic, S., Gilkerson, T., Roger, N., David, C. and Richardsc, R.D. (2005) Pyrrolo[1,2-a][1,4]benzodiazepine: A novel class of non-azole anti-dermatophyte anti-fungal agents. *Bioorganic & Medicinal Chemistry Letters*, **15(14)**, 3453-3458.

[49] Oxford, A.E., Raistruck, H. and Simonarat, P. (1939) Studies in the biochemistry of microorganisms, Griseofulvin CHOCI, a metabolic product of Penicillium griseofulvin dierck. *Biochemistry*, **33(2)**, 248-252.

[50] Gentles, J.C. (1958) Experimental ringworm of guinea pigs: Oral treatment with griseofulvin. *Nature*, **182(4633)**, 476-477.

[51] Rajendra, P.N., Anandi, C., Balasubramanian, S. and Pugalendi, K.V. (2004) Antidermatophytic activity of extracts from Psoralea corylifolia (Fabaceae) correlated with the presence of a flavonoid compound. *Journal of Ethnopharmacology*, **91(1)**, 21-24.

[52] Natarajan, V., Venugopal, P.V. and Menon, T. (2003) Effect of Azadirachta indica (Neem) on the growth pattern of dermatophytes. *Indian Journal of Medical Microbiology*, **21(2)**, 98-101.

[53] Nenoff, P., Haustein, U.F. and Brandt, W. (1996) Antifungal activity of essential oil of Melaleuca alternifolia against pathogenic fungi *in vitro*. *Skin Pharmacology*, **9(6)**, 388-394.

[54] Vivek, K.B., Jung, I.Y. and Sun, C.K. (2009) Antifungal potential of essential oil and various Organic extracts of Nandina domestica Thunb against skin infectious fungal pathogens. *Applied Microbiology and Biotechnology*, **83(6)**, 1127-1133.

[55] Helena, G., Sonia, S.F., Ana, I.R. and Rob, V.S. (2004) Antifungal activity of (+) -curcuphenol, a metabolite from the marine sponge didiscus oxeata. *Marine Drugs*, **2(1)**, 8-13.

[56] Deepika, T.L. and Kannabiran, K. (2009) A morphological, biochemical and biological studies of halophilic Streptomyces sp isolated from saltpan environment. *American Journal of Infectious Diseases*, **5(3)**, 207-213.

[57] Deepika, T.L. and Kannabiran, K. (2009) A report on antidermatophytic activity of actinomycetes isolated from Ennore coast of Chennai, Tamil Nadu, India. *International Journal of Integrative Biology*, **6(3)**, 132-136.

[58] Vijayakumar, R., Muthukumar, C., Thajuddin, N., Panneerselvam, A. and Saravanamuthu, R. (2007) Studies on the diversity of actinomycetes in the Palk Strait region of Bay of Bengal, India. *Actinomycetologica*, **21(2)**, 59-65.

Vol.2, No.7, 732-736 (2010)
doi:10.4236/ns.2010.27091

Natural Science

Familial aggregation and heritability for cardiovascular risk factors: a family based study in Punjab, India

Raman Kumar, Badaruddoza*

Department of Human Genetics, Guru Nanak Dev University, Amritsar, India; *Corresponding Author: doza13@yahoo.co.in

Received 19 March 2010; revised 15 April 2010; accepted 20 April 2010.

ABSTRACT

Background: It is well established that the people with elevated SBP, DBP, BMI and WHR are more prone to cardiovascular disease. However, very few studies have focused on the amount of familial aggregation and heritability of these cardiovascular risk factors in Indian population. Therefore, purpose of this study was to investigate the familial aggregation of blood pressures with respect to certain anthropometric traits and to determine the relative roles of heredity in the etiology of SBP and DBP in a sample of families with three generations. Methods: The study has been conducted through house to house family study among three generations such as offspring, parent and grandparent in a scheduled caste community (Ramdasia) in Punjab. A total of 1400 individuals, constituting 380 families were surveyed for blood pressure, pulse rate, pulse pressure and anthropometric measurements to study familial aggregation and heritability for cardiovascular risk factors. The analysis represents a multivariate model which includes the each individual family data for estimation of familial correlation and heritability. Results: All risk factors showed positive familial correlation but magnitudes are different in various pairs of combination. Correlations generally are higher among genetically close relatives such as brother-sisters or parent-offspring and are lower among spouses. The estimated heritabilities were 22% for systolic and 27% for diastolic blood pressure, 19% for BMI and 17% for WHR. Conclusions: These results indicate a strong familial aggregation of cardiovascular risk factors such as SBP and DBP in this population and also showed that this familial influence can be detected from anthropometric measurements and genetic closeness. Almost all anthropometric variables were found to be significant with blood pressures among three generations.

Keywords: Familial Aggregation; Heritability; Risk Factors; Ramdasia Population; Punjab

1. INTRODUCTION

There is much epidemiological evidence that environmental cofactors and anthropometric characteristics are directly and consistently correlated with cardiovascular diseases in developing countries [1-7]. It has been reported that almost 30% of risk factors for cardiovascular diseases are accounted by genetic heritability and at least approximately 70% of risk factors are of familial in nature [8-13]. However, many authors have contradicted that what extent to which that observed familial aggregation on both systolic and diastolic is due to genetic or environmental reason. Some authors have argued that familial aggregation on diastolic blood pressure is more than systolic blood pressure or vice versa [14]. However, in India the pattern of risk factors for cardiovascular diseases are different to cut across the cultural patterns and geographic regions. Therefore, in Indian context the paucity of family based information and complex etiology of this disease made it difficult for understanding how these factors contribute to the cardiovascular diseases. Hence, the major purpose of this study was to investigate the familial aggregation of blood pressures with respect to certain anthropometric traits and to determine the relative roles of heredity in the etiology of SBP and DBP in a sample of families with three generations such as offspring, parent and grandparent in Punjab, a north Indian state. Our working hypotheses were that there is familial aggregation of blood pressure in the studied families and the association of blood pressure in first degree relatives is more than spouse pairs.

2. MATERIALS AND METHODS

For the present study the population included 1400 indi-

viduals constituting 380 families with three generations. Individuals in the parental generation (N = 780) range in age from 30.5 to 60.7 years. The age of offspring (N = 456) range from 9.5 to 26.7 years. The age of the grandparent generation (N = 164) range from 52.8 to 85.6 years. All families were recruited from Ramdasia community (Ramdasia community is socially and educationally backward from the rest of the population in Punjab) to reduce the confounding effect ethnically determined genetic differences. For recruitment of the subjects family history of heart disease was not the criteria, however, randomly selected families exhibiting a broad cross selection of cardiovascular risk factor levels.

2.1. Phenotypes Measurements

This study was approved by the Ethics Review Committee of Guru Nanak Dev University, Amritsar, India and written consent was obtained from all the participants. Comprehensive and elaborated questionnaires related health, life style, demographic features, socio-economic status and family history were completed by the participants before physical measurement. Blood pressure was measure on the right arm of the subjects in a sitting position after 10 minutes of rest using a mercury sphygmomanometer and a stethoscope with an accuracy of 2 mm Hg by following the recommendations of American Heart Association [15]. On the basis of circumference of the participants arm, a regular adult or large or medium cuff has been chosen. Systolic and diastolic blood pressures were defined at the first and fifth phases of Korotkoff sounds respectively. The pulse rate was measured for 60 seconds. The average of two measurements was used as the estimates of SBP and DBP in the present analysis. Mean arterial blood pressure (MBP) was calculated as DBP + (SBP-DBP)/3 [16]. The pulse pressure was calculated as SBP-DBP.

The other anthropometric measurements were taken from each individual include height, weight, five circumferences (chest, waist, hip, arm and calf) and biceps and triceps skinfolds. All measurements were taken with standard anthropometric techniques [17-18]. Body mass index (BMI) and waist to hip ratio were defined as weight/height^2 (kg/m^2) and waist circumference divided by hip circumferences respectively.

2.2. Statistical Methods

All statistical analyses were performed using SPSS software. The $p < 0.05$ level was selected as the criterion of statistical significance. Heritability estimation was done from regression of offspring on parents.

3. RESULTS

Table 1 shows the summary of data for offspring, parent and grandparent generations with both sexes. The mean ages and standard deviations for different generations are: 18.00 ± 5.12 (male offspring), 17.63 ± 4.95 (female offspring), 41.19 ± 9.12 (male parents), 38.05 ± 9.16 (female parents), 67.52 ± 9.10 (male grandparents) and 62.46 ± 8.72 (female grandparents). In general, maximum mean values of anthropometric measurements such as height, weight and calf circumference for male parent generation; BMI, chest, hip and arm circumferences, biceps and triceps skinfolds for female parent generation; waist circumference, WHR for female grandparent generation have been observed in the present analysis. The maximum SBP, DBP, MBP, pulse rate and pressure have been found in female grandparent generation. On average, offspring generations have lower mean values of almost all measured phenotypes. As shown in the **Table 2** all the means of the measured variables have significant differences ($p < 0.001$) between different intra-generations for all measured variables. However, age, DBP, calf and hip circumferences, and WHR have found maximum intra-generational differences.

Estimates of familial correlations among household members and estimated sample size are presented in **Table 3**. All correlations are positive and maximum familial correlations for almost all the traits were found in close genetically related brother-sister combination. The lowest familial correlations for all the traits were found in spouses. The familial correlations for SBP and DBP are also significantly higher between father-male offspring combination. However, the stronger correlations were found in various traits among different combinations such as for biceps skinfold, chest circumference, pulse pressure between father-male offspring; for arm circumference between father-female offspring; for BMI, WHR and pulse rate between mother-female offspring. Therefore, these risk factors showed the patterns of familial correlation which were stronger among more genetic control relationship and lower in spouse.

Table 4 shows estimated genetic component of variance and heritability for cardiovascular risk factors in this population. The genetic variance included only the additive genetic variance and these are significantly greater than zero for all the risk factors. The genetic effect of these risk factors may be assumed from the square root of these variances. For SBP the genetic effect is 10.56 mm Hg and it contributes 22% (heritability) of the variation in systolic blood pressure. For diastolic blood pressure the genetic effects is 7.28 mmHg and it contributes 27% of the variation in this population. However, the contributions of genetic effects of other variables such as pulse rate, pulse pressure, body mass index (BMI), waist to hip ratio (WHR), biceps and triceps skinfolds, arm and calf circumferences are 10.03 minutes (heritability 10%), 8.75 mm (heritability 30%),

Table 1. Descriptive statistics of measured phenotypes between among different generations.

Variables	Male Offspring		Female Offspring		Male Parent		Female Parent		Male Grandparent		Female Grandparent	
	Mean ± SD	Inter-quartile **range**	**Mean ± SD**	Inter-qua-rtile **range**	**Mean ± SD**	Inter-quartile **range**	**Mean ± SD**	Inter-quartile **range**	**Mean ± SD**	Inter-quartile **range**	**Mean ± SD**	Inter-quartile **range**
Age (yrs)	18.00 ± 5.12	7.00-35.00	17.63 ± 4.95	7.00-30.00	41.19 ± 9.12	21.00-67.00	38.05 ± 9.16	20.00-65.00	67.52 ± 9.10	46.00-96.00	62.46 ± 8.72	40.00-85.00
Height (cm)	157.79 ± 10.6	101.50 − 183.0	150.21 ± 9.98	105.00 − 172.00	167.71 ± 6.44	148.70 − 186.1	154.12 ± 5.5	136.20 − 172.3	164.96 ± 7.1	142.7 − 183.3	152.13 ± 6.23	131.00 − 168.0
Weight (kg)	47.43 ± 11.42	14.00 − 92.00	42.87 ± 10.56	15.00 − 89.00	65.19 ± 10.82	37.00 − 98	59.25 ± 11.9	32.00 − 105.00	55.68 ± 10.2	40.00 − 93.30	56.49 ± 10.58	30.00 − 90.00
BMI (kg/m^2)	18.42 ± 3.56	11.26 − 35.57	18.77 ± 3.82	10.41 − 36.85	23.10 ± 3.75	13.54 − 34.51	24.87 ± 4.70	14.67 − 45.37	20.29 ± 4.05	13.71 − 31.66	24.33 ± 4.67	14.07 − 37.94
Chest circum(cm)	80.19 ± 9.12	52.50 − 116.40	77.32 ± 8.99	52.70 − 112.00	94.31 ± 8.52	73.00 − 120.20	94.81 ± 8.45	70.00 − 130.00	90.23 ± 8.49	77.6 − 113.00	94.65 ± 8.20	71.00 − 119.00
Waist circum(cm)	75.17 ± 10.35	47.80 − 115.00	72.43 ± 9.68	46.5 − 113.00	94.36 ± 8.46	61.60 − 129.90	96.81 ± 9.99	61.00 − 136.00	89.24 ± 10.3	65.40 − 121.0	97.98 ± 9.99	65.00 − 127.00
Hip circum. (cm)	82.16 ± 9.42	52.00 − 112.00	81.78 ± 8.48	47.00 − 121.50	94.12 ± 7.88	73.33 − 122.40	94.66 ± 9.01	72.50 − 130.00	87.89 ± 8.11	76.30 − 106.4	93.94 ± 9.84	72.00 − 121.30
WHR	0.91 ± 0.06	0.71 − 1.10	0.86 ± 0.070	0.69 − 1.09	1.00 ± 0.07	1.253 − 0.759	1.00 ± 0.11	0.07 − 1.88	1.01 ± 0.09	0.804 − 1.269	1.04 ± 0.143	0.10 − 1.294
Arm circum. (cm)	22.87 ± 4.39	13.90 − 37.80	21.97 ± 3.51	13.80 − 33.80	27.11 ± 3.28	18.40 − 37.00	26.78 ± 3.48	18.50 − 38.50	24.00 ± 3.56	17.30 − 33.40	26.08 ± 3.82	17.20 − 35.50
Calf circum (cm)	28.32 ± 4.13	18.00 − 42.00	27.13 ± 3.64	17.40 − 41.50	31.87 ± 3.39	21.00 − 41.80	30.63 ± 3.64	17.80 − 42.50	28.85 ± 3.64	16.40 − 37.60	28.96 ± 3.69	22.20 − 37.30
Biceps skinfold (mm)	6.30 ± 2.57	3.00 − 17.00	7.66 ± 3.42	3.00 − 32.00	7.84 ± 2.91	2.00 − 20.00	10.58 ± 4.05	3.00 − 31.00	5.89 ± 3.04	2.00 − 17.00	9.56 ± 4.38	3.00 − 29.00
Triceps skinfold (mm)	9.94 ± 4.34	4.00 − 17.00	13.50 ± 4.31	4.00 − 42.00	12.49 ± 4.48	3.00 − 32.00	20.10 ± 6.73	3.00 − 31.00	9.72 ± 5.07	3.00 − 28.00	18.37 ± 7.84	4.00 − 4.00
SBP (mm/Hg)	116.47 ± 10.5	90.00 − 150	111.59 ± 9.22	80.00 − 140.00	128.09 ± 9.20	90.00 − 210.00	122.98 ± 9.4	80.00 − 190.00	136.96 ± 9.7	100.0 − 220.0	144.57 ± 10.1	90.00 − 240.00
DBP (mm/Hg)	76.50 ± 7.29	55.00 − 110.00	73.95 ± 6.70	50.00−90.00	82.11 ± 7.80	60.00 − 120.00	78.73 ± 8.15	60.00 − 120.00	82.42 ± 8.08	50.00 − 120.0	85.17 ± 9.97	50.00 − 120.00
MBP (mm/Hg)	89.80 ± 7.68	66.00 − 120.00	86.41 ± 6.79	63.33 − 106.66	97.39 ± 9.19	70.00 − 150	93.45 ± 9.18	66.66 − 140.00	100.26 ± 9.6	66.66 − 153.3	104.76 ± 10.0	63.33 − 160.00
Pulse rate	81.96 ± 8.02	20.00 − 90.00	85.37 ± 8.67	60.00 − 121.00	82.91 ± 9.78	60.00 − 120.00	85.58 ± 10.8	60.00 − 90.00	84.48 ± 8.99	65.00 − 140.0	85.79 ± 8.25	60.00 − 113.00
Pulse pressure	40.49 ± 8.76	54.00 − 132.00	37.87 ± 7.43	20.00 − 60.00	46.13 ± 10.77	10.00 − 90.00	44.29 ± 10.8	20.00 − 95.00	55.16 ± 9.37	10.00 − 20.00	59.14 ± 9.61	20.00 − 130.00

Table 2. T-values with 95% confidence level between intra-generational differences of mean values for all measured phenotypes.

Variables	t	P	95% confidence level of the difference
Age (yrs)	4.715	< 0.005	18.55-63.05
Height (cm)	54.37	< 0.000	150.36-165.28
Weight (kg)	16.49	< 0.000	45.99-62.97
BMI (kg/m^2)	18.67	< 0.000	18.65-24.61
Chest circumference (cm)	27.62	< 0.000	80.34-96.82
Waist circumference (cm)	19.19	< 0.000	75.92-99.40
Hip circumference (cm)	36.09	< 0.000	82.74-95.43
WHR	34.29	< 0.000	0.89-1.04
Arm circumference (cm)	28.16	< 0.000	22.53-27.06
Calf circumference (cm)	42.33	< 0.000	22.53-27.06
Biceps skinfold (mm)	10.72	< 0.000	6.06-9.88
Triceps skinfold (mm)	7.93	< 0.001	9.48-18.56
SBP (mm/Hg)	25.12	< 0.000	113.86-139.82
DBP (mm/Hg)	46.78	< 0.000	75.83-84.19
MBP (mm/Hg)	34.43	< 0.000	88.24-102.48
Pulse rate	160.52	< 0.000	83.35-86.29
Pulse pressure	12.65	< 0.000	37.87-59.16

Table 3. Estimates of familial correlation for cardiovascular risk factors.

Variables	BMI	WHR	BISF	TRISF	AC	CC	PR	PP	SBP	DBP	MBP
Spouse (n = 312)	0.09	0.08	0.05	0.05	0.12	0.07	0.08	0.07	0.04	0.05	0.06
Father-male offspring (n = 270)	0.21	0.12	0.16	0.02	0.11	0.18	0.07	0.13	0.31	0.30	0.25
Father-female offspring (n = 186)	0.15	0.12	0.12	0.05	0.19	0.12	0.07	0.08	0.21	0.20	0.20
Mother-male offspring (n = 270)	0.23	0.14	0.01	0.04	0.18	0.10	0.07	0.04	0.17	0.15	0.14
Mother-female offspring (n = 186)	0.29	0.12	0.03	0.06	0.12	0.13	0.18	0.04	0.20	0.18	0.16
Brother-sister (n = 186)	0.38	0.31	0.15	0.15	0.15	0.12	.21	0.14	0.34	0.31	0.30
Grandfather-male 0ffspring (n = 66)	0.12	0.07	0.07	0.08	0.03	0.14	0.05	0.11	0.16	0.19	0.19
Grandfather-female (n = 66) offspring	0.12	0.13	0.12	0.02	0.18	0.12	0.10	0.02	0.13	0.14	0.14
Grandmother-male offspring (n = 99)	0.10	0.10	0.08	0.06	0.14	0.02	0.0	0.06	0.13	0.17	0.16
Grandmother-female offspring (n = 99)	0.12	0.11	0.13	0.03	0.14	0.09	0.02	0.12	0.14	0.15	0.13

BMI = Body mass index; WHR = Waist-Hip ratio; AC = Arm circumference; CC = Calf circumference; BISF = Biceps skinfold; TRISF = Triceps skinfold; SBP = Systolic blood pressure; DBP = Diastolic blood pressure; MBP = Mean arterial blood pressure; PR = Pulse rate; PP = Pulse pressure.

Table 4. Estimated genetic component of variance and heritability for cardiovascular risk factors.

Risk Factors	Genetic Variance	Heritability
SBP (mm/Hg)	111.72	22%
DBP (mm/Hg)	53.14	27%
MBP (mm/Hg)	58.94	35%
Pulse rate	100.61	10%
Pulse pressure	76.56%	30%
BMI (kg/m^2)	12.67	19%
WHR	0.05	17%
Biceps skinfold (mm)	6.60	21%
Triceps skinfold (mm)	18.83	14%
Arm circumference (cm)	19.36	12%
Chest circumference (cm)	17.05	35%

3.54 kg/m^2 (heritability 19%), 0.22 (heritability 17%), 2.56 mm (heritability 21%), 4.33 mm (heritability 14%), 4.4 cm (heritability 12%) and 4.13 cm (heritability 35%) respectively in this population.

4. DISCUSSION

The analysis from the present studies of three generations families in Punjab, a north Indian state have demonstrated strong familial aggregation of BMI, WHR, SBP and DBP for cardiovascular risk factors. The close genetic relationship such as parent-offspring, brother-sister correlations were significantly higher ($p < 0.05$) than non-genetic or distant genetic relationship such as spouses and grandparents. Overall, heritabilities were estimated to be 22% for SBP, 27% for DBP, 19% for BMI, 17% for WHR and 21% biceps skinfold. Therefore, the present observation suggested that genetically more close relatives have greater chance to aggregate cardiovascular risk factors than non-genetical and distant relatives. Many previous studies have also supported this hypothesis [4,7,10-12,19-21]. The present heritability analysis represents the additive effects of genes. The greater range of heritability for different cardiovascular risk factors have suggested a greater genetic influences in the familial aggregation of SBP, DBP, pulse pressure, BMI, chest circumference and biceps skinfold. However the sample size of three generations strengthens the statistical power to identify the association of cardiovascular risk factors with different relationships.

In this context, the present population due to its homogeneous nature provides a good opportunity to assess the familial determinants of cardiovascular risk factors. Families in this population are sufficiently large and joint in addition to that physical environment and diet contrast are also almost similar. In conclusion, our data suggest a significant familial aggregation of cardiovascular risk factors for SBP, DBP, BMI and WHR.

5. ACKNOWLEDGEMENTS

First author (RK) is thankful to the University Grants Commission, Government of India, for providing Rajiv Gandhi National Fellowship (No. F.16-31/2006 /SA-II) in the Department of Human Genetics, Guru Nanak Dev University, Amritsar, Punjab, India.

REFERENCES

[1] Yu, Z., Nissinen, A., Vartianen, E., Song, G., Guo, Z. and Tians, H. (2000) Changes cardiovascular risk factors in different socio-economic groups: Seven years trends in Chinese Urban population. *Journal of Epidemiology and Community Health*, **54(9)**, 692-696.

[2] Badaruddoza and Afzal, M. (1999) Age specific difference in blood pressure among inbred and noninbred North Indian Children. *Journal of Biosocial Science*, **24(2)**, 177-184.

[3] Badaruddoza and Afzal, M. (2000) Trend of blood pressure in North Indian children. *Indian Journal of Physiology and Pharmacology*, **44(3)**, 304-310.

[4] Wang, X., Wang, B., Chen, C., Yang, J., Fang, Z., Zuckerman, B. and Xu, X. (1999) Familial aggregation of blood pressure in a rural Chinese community. *American Journal of Epidemiology*, **149(5)**, 412-420.

[5] Lasser, U. and Breckenkamp, J. (2005) Trends in risk factors control in Germany 1984-1998: High blood pressure and total cholesterol. *European Journal of Public Health*, **16(2)**, 217-222.

[6] Tomson, J. and Lip, G.Y.H. (2005) Blood pressure demographics, nature on nurture, gene or environment. *BMC Medicine*, **3(8)**, 3-8.

[7] Badaruddoza and Kumar, R. (2009) Cardiovascular risk factor and familial aggregation of blood pressure with respect to anthropometric variables in a schedule caste population of Punjab. *Anthropologischer Anzeiger*, **67(2)**, 111-119.

[8] Brand, F.N., Kiely, D.K., Kanel, W.B., *et al*. (1992) Family patterns of coronary heart disease mortality: The Framingham longevity study. *Journal of Clinical Epidemiology*, **45(2)**, 169-174.

[9] Hopper, J.L. and Carlin, J.B. (1992) Familial aggregation of a disease consequent upon correlation between relatives in risk factors measured in continuous scale. *American Journal of Epidemiology*, **136(9)**, 1138-1147.

[10] Knuiman, M.W., Divitini, M.L., Bartholomew, H.C. and Welborn, T.A. (1996) Spouse correlations in Cardiovacsular risk factors and the effect of marriage duration. *American Journal of Epidemiology*, **143(1)**, 48-53.

[11] Knuiman, M.W., Divitini, M.L., Welborn, T.A. and Bartholomew, H.C (1996) Familial correlations, cohabitation effects, and heritability for cardiovascular risk factors. *Annals of Epidemiology*, **6(3)**, 188-194.

[12] Fuentes, R.M., Notkola, I.L., Shemeikka, S., Tuomilehto, J. and Nissinen, A. (2000) Familial pressure: A population based family study in eastern Finland. *Journal of Human Hypertension*, **14(7)**, 441-445.

[13] Harrap, S.B., Stebbing, M., Hopper, J.L., Hoang, H.N. and Giles, G.G. (2000) Familial patterns of covariation

for cardiovascular risk factors in adults: The Victorian family heart study. *American Journal of Epidemiology*, **152(8)**, 704-715.

[14] Knuiman, M.W., Jamrozik, K., Welborn, T.A., Divitini, M.L. and Whittal, D.E. (1995) Age and secular trends in risk factors for cardiovascular disease in Busselton. *Australian Journal of Public Health*, **19(4)**, 375-385.

[15] American Heart Association, (1981) Report of subcommittee of postgraduate education committee recommendations for human blood pressure determination of sphygmomanometer. *Circulation*, **64**, 510A-599B.

[16] Pérusse, L., Rice, T., Bouchard, C., Vogler, G.P. and Roa, D.C. (1989) Cardiovascular risk factors in the French Canadian population. Resolution of genetic and familial environmental effects on blood pressure by using extensive information on environmental correlates. *American Journal of Human Genetics*, **45(2)**, 240-251.

[17] Singh, I.P. and Bhasin, M.K. (1968) *Anthropometry*, Kamla Raj Enterprises, Delhi.

[18] Weiner, J.S. and Lourie, J.A. (1981) *Practical Human Biology*, Academic Press, London.

[19] Tambs, K., Moum, T., Holmen, J., Eaves, J.L., Neale, M.C., Lund-Larsen, P.J. and Næss, S. (1992) Genetic and environmental effects on blood pressure in a Norwegian sample. *Genetic Epidemiology*, **9(1)**, 11-26.

[20] Rice, T., Rao, R., Pérusse, L., Bouchard, C. and Rao, D.C. (2000) Tracking of familial resemblance for resting blood pressure over time in the Quebec family study. *Human Biology*, **72(3)**, 415-431.

[21] Jee, S.H., Suh, I., Won, S.Y. and Kim, M. (2002) Familial correlation and heritability for cardiovascular risk factors. Y*onsei Medical Journal*, **43(2)**, 160-164.

Vol.2, No.7, 737-740 (2010)
doi:10.4236/ns.2010.27092

Characterization of seed storage protein patterns of four Iranian Pistachios using SDS-PAGE

Ali Akbar Ehsanpour*, Behrokh Shojaie, Fatemeh Rostami

Department of Biology, Faculty of Science, University of Isfahan, Isfahan, Iran; *Corresponding Author: ehsanpou@yahoo.com

Received 6 March 2010; revised 10 April 2010; accepted 15 April 2010.

ABSTRACT

We used SDS-PAGE to evaluate and characterize the protein patterns of seed storage proteins in four pistachios cultivars (Akbari, Ahmad Aghaei, Fandoghi, and Kaleghouchi). Total protein content of pistachio seeds in all cultivars did not show any significant difference. Results of SDS PAGE pattern of a few protein bands were up regulated whereas some other bands showed down regulation. The identified protein patterns may be used protein marker for pistachio cultivars.

Keywords: Pistachio; Protein Marker; SDS PAGE

1. INTRODUCTION

Pistacia vera L. (pistachio) (2n = 32) is belong to Anacardiaceae family. Iran is one of the largest producer and exporter of pistachio (300,000 tones per year) in the world [1]. Pistachio seed is a very high source of protein, lipid, and vitamins such as vitamin A, B1, B2C, and Niacin. It has also a high percentage of potassium, calcium and phosphorous. Iranian pistachios are different in sizes and shape and they are divided into four major groups including round (Fandoghi), jumbo (Kaleghouchi) and long (Akbari, Ahmad Aghaei) (http://en.wikipedia.org/wiki/Pistachio and http://www.sahravi.com/pistachio/iranian-pistachio.htm).

Plant storage proteins can be classified into two classes; seed storage proteins (SSPs) and vegetative storage proteins (VSPs). SSPs are a set of proteins that accumulate at high levels in seeds during the late stages of seed development, whereas VSPs are proteins that accumulate in vegetative tissues such as leaves, stems and tubers, depending on the plant species. SSP genes were classic targets for work on plant molecular biology. Their abundant expression in seeds allowed for easy detection of the gene transcripts and cDNA cloning during research on plant molecular biology in late 70's to early 80's. Characterization of germplasm using biochemical fingerprinting has got special attention due to its increased used in crop improvement and the selection of desirable genotypes for breeding crops. The use of genetic markers and protein profiling has also been successfully used to resolve the taxonomic and evolutionary problems of several crop plants [2-6]. The seed storage protein analyses helps in identification and characterization of diversity in crop varieties, cultivars and their wild varieties and also provides information on phylogenetic relationship of the accessions. It is also known that variation in protein bands provide information on the relationship among the used seeds collected from various geographical regions [6-8]. There are different amounts of storage proteins in all plant seeds. They play two main roles including nitrogen and energy source and defense against insects and pathogens such as bacteria and fungi.

Since, seed storage protein analysis can be a useful tool for identification of species, varieties and cultivars, in this study we investigate the protein pattern in four Iranian pistachios seeds (Akbari, Ahmad Aghaei, Fandoghi, Kaleghouchi) in order to find protein bands as markers for cultivar characterization.

2. MATERIALS AND METHODS

2.1. Plant Material

Fresh mature seeds of Pistachio cultivars including Akbari, Ahmad Aghaei, Fandoghi, and Kaleghouchi were harvested from pistachio garden in Ardestan, Isfahan, Iran.

2.2. Extraction of Seed Proteins

Seed coats from fresh ten seeds from each cultivar were removed and kernels were then grounded in liquid nitrogen with a mortar and pestle. The seed storage proteins from each cultivar was extracted with cold acetone

by stirring the mixture at 50 rpm at 4˚C for 48 h, and subsequently the defatted powder of each cultivar of pistachio was air dried at room temperature for 8 h. Next, the dry powder was suspended in 1:20 (w/v) of 1 ml of 50 mM Tris-HCl buffer containing 1 mM DTT, 2 mM EDTA, 2 mM 2-Mercaptoethanol, pH 7.5. The suspension was stirred at 50 rpm at 4˚C overnight and was centrifuged for 25 min at 14000 rpm at 4˚C. The precipitate was discarded and the supernatant was used for total soluble protein (mg g1-dp or defatted powder) assay according to modified Bradford method [9] described by Olson and Markwell [10] using bovine serum albumin as standard protein and SDS-PAGE analysis. SDS-PAGE was performed using 12% separating and 5% stacking gels [11]. After electrophoresis at 120 V, protein bands were stained using silver nitrate and finally the relative density of protein bands were analyzed by ImageJ (http://rsb.info.nih.gov/ij/). The intensity of protein bands in different samples were analyzed by NTSYSPc2 program. In order to augment accuracy, all experiments including exaction and SDS-PAGE were repeated at least four times. Data were subjected to ANOVA and the mean differences were compared by Duncan test at $P < 0.05$.

3. RESULTS

To investigate variations among four Iranian pistachio cultivars, seed storage proteins from cultivar Akbari (A), Ahmad Aghaei (AA), Fandoghi (F) and Kaleghouchi (K) were analyzed. As shown in **Figure 1**, no significant difference in total protein content was observed in four pistachio cultivars.

The SDS-PAGE protein patterns of four pistachio cultivars showed changes in seven protein bands (**Figure 2**). Subsequently, the relative levels of protein concentration of these seven protein bands were analyzed by Image J program (**Figure 3**). Five protein bands (1, 2, 3, 4 and 5) with approximate MW 45, 33, 32, 27 and 20 kDa respectively, showed maximum expression level in cultivar AA. Protein bands of 6 and 7 with approximate MW 16 and 15 kDa showed maximum expression level in cultivar A, respectively. However, bands 3 and 4 were not detectable in cultivars K and A, while they were detected in the other cultivars. Protein bands 2, 5 and 6 had lower expression level in cultivar F. The minimum level of protein band 1 was observed in cultivar A and protein band 7 in cultivar K.

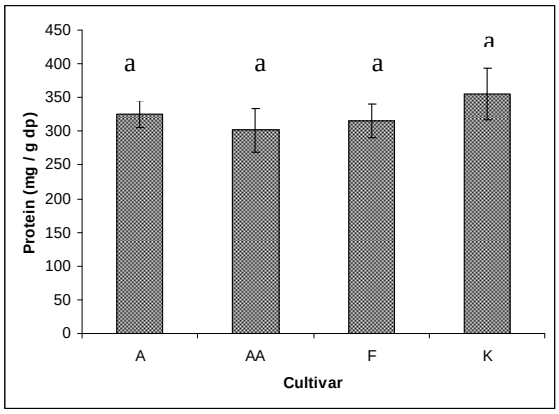

Figure 1. Total soluble protein in four pistachio cultivars Akbari (A), Ahmad Aghaei (AA), Fandoghi (F) and Kaleghouchi (K), defatted powder (dp). Values are the means ± SE. Similar letters (a) indicate no significant difference ($P < 0.05$) based on Duncan test in four pistachio cultivars.

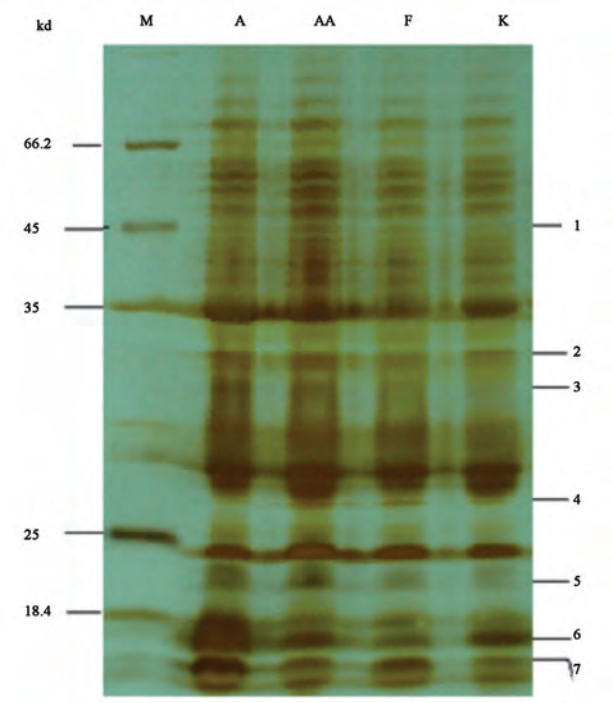

Figure 2. SDS-PAGE pattern of four pistachio cultivars Akbari (A), Ahmad Aghaei (AA), Fandoghi (F) and Kaleghouchi (K) protein marker (M).

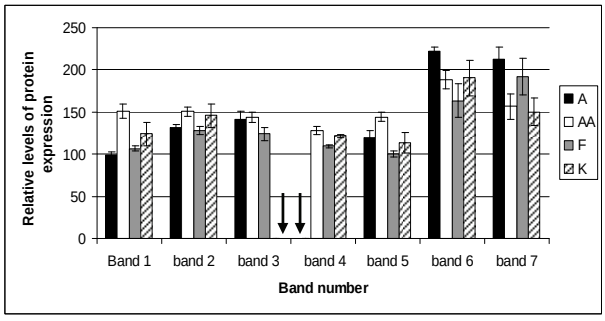

Figure 3. Relative levels of protein expression of pistachio cultivars Akbari (A), Ahmad Aghaei (AA), Fandoghi (F) and Kaleghouchi (K). Values are the means ± SE of proteins bands from three independent experiments.

4. DISCUSSION

Electrophoresis of proteins is a powerful tool for identification of genetic diversity and the SDS-PAGE is particularly considered as a reliable technology because seed storage proteins are highly independent of environmental fluctuations [12,13]. Seed protein patterns can also be used as a promising tool for distinguishing cultivars of particular crop species [14,15]. However, only a few studies indicated that cultivar identification was not possible with the SDS-PAGE method [16]. The SDS-PAGE is considered to be a practical and reliable method for species identification [17].

According to the results of the SDS-PAGE, the overall pattern of seed storage-proteins showed the diversity of pistachio cultivars. The diversity in seed storage proteins has also been reported by Khan *et al.* for wheat varieties [18]. Moreover, identification of three wheat genotypes including ILC-195, CM-2000 and CM-98/99 has also been reported by protein markers [19].

Since in mature seeds, type and amount of proteins are more constant than other plant tissues [20] therefore, the SDS-PAGE pattern of seed storage proteins of pistachio showed polymorphism on the basis of difference in protein intensity among genotypes. The presence or absence of protein bands has also been applied for detection of polymorphism of Brassica cultivars [21].

The present investigation revealed variation in different cultivars of pistachio seeds with regard to their total seed protein profiles. Regarding interspecific variation among cultivars this investigation revealed some variations. The genetic affinities within cultivars of the same species generally corroborated the morphological analysis. Similar to our finding the result of differentiation of yellow sarson and brown seeded types of Brassica clearly separated the yellow seeded and brown seeded varieties by SDS PAGE [22]. However, we can conclude that, SDS-PAGE can reveal the differences among seed storage proteins of pistacia cultivars.

5. ACKNOWLEDGEMENTS

Authors wish to thank University of Isfahan for their support.

REFERENCES

[1] Ehsanpour, A.A., Tavasoli, M. and Arab, L. (2008) Sex determination of *Pistacia vera* L. using ISSR markers. *Malaysian Applied Biology*, **37(2)**, 25-28.

[2] Ladizinsky, G. and Hymowitz, T. (1979) Seed protein electrophoresis in taxonomic and evolutionary studies. *TAG Theoretical and Applied Genetics*, **54(4)**, 145-151.

[3] Khan, M.K. (1990) Production and utility of chickpea (*Cicer arietinum* L.) in Pakistan. *Progressive Farming*, **10(6)**, 28-33.

[4] Murphy, R.W., Sites, J.W., Buth, D.G. and Haufler, C.H. (1990) Protein isozymes electrophoresis. In: *Molecular Systematic*. Hillis, D.H. and Moritz, C., Eds., *Sinnauer Association, Sunderland*, Massachusetts, 45-126.

[5] Nakajima, K. (1994) Biotechnology for crop improvement in Japan. In: *Biotechnology Application in Agriculture in Asia and Pacific*, Published by Asian Productivity Organization, 87-107.

[6] Ghafoor, A., Gulbaaz, F.N., Afzal, M., Ashraf, M. and Arshad, M. (2003) Inter-relationship between SDS-PAGE markers and agronomic traits in chickpea (*Cicer arietinum* L.). *Pakistan Journal of Botany*, **35(4)**, 613-624.

[7] Satija, D.R., Adrash, B., Gupta, S.K. and Bala, A. (2002) Genetic diversity in relation to protein and protein fractions in chickpea (*Cicer arietinum* L.). *Crop-Improvement*, **29(2)**, 122-135.

[8] Asghar, R., Siddique, T. and Afzal, M. (2003) Inter and intra-specific variation in SDS-PAGE electrophoregrams of total seed protein in chickpea (*Cicer arietinum* L.) germplasm. *Pakistan Journal of Biological Sciences*, **6(24)**, 1991-1995.

[9] Bradford, M. (1976) A rapid and sensitive method for the quantitayion of microgram quantities of protein utilizing the principle of protein-dye binding. *Analytical Biochemistry*, **72(1-2)**, 248-254.

[10] Olson, B.J.S.C. and Markwell, J. (2007) Assays for determination of protein concentration. *Current Protocols in Protein Science*, **3(4)**, 3.4.1-3.4.29.

[11] Hames, B.D. (1990) One-dimensional polyacrylamide gel electrophoresis. In: Hames, B.D. and Rickwood, D., Eds., *Gel Electrophoresis of Proteins*, 2nd Edition, Oxford University Press, New York, 382.

[12] Javid, A., Ghafoor, A. and Anwar, R. (2004) Seed storage protein electrophoresis in groundnut for evaluating genetic diversity. *Pakistan Journal of Botany*, **36(1)**, 25-29.

[13] Iqbal, S.H., Ghafoor, A. and Ayub, N. (2005) Relationship between SDS-PAGE markers and *Ascochyta blight* in chickpea, *Pakistan Journal of Botany*, **37(1)**, 87-96.

[14] Jha, S.S. and Ohri, D. (1996) Phylogenetic relationships of *Cajanus cajan* (L.) Millsp. (pigeonpea) and its wild relatives based on seed protein profiles. *Genetic Resources and Crop Evolution*, **43(3)**, 275-281.

[15] Seferoglua, S., Seferoglua, H.G., Tekintasa, F.E. and Baltab, F. (2006) Biochemical composition influenced by different locations in Uzun pistachio cv. (*Pistacia vera* L.) grown in Turkey. *Journal of Food Composition and Analysis*, **19(5)**, 461-465.

[16] De Vries, I.M. (1996) Characterisation and identification of *Lactuca sativa* cultivars and wild relatives with SDS-electrophoresis (*Lactuca* sect. *Lactuca*, *Compositae*), *Genetic Resources and Crop Evolution*, **43(3)**, 193-202.

[17] Gepts, P. (1989) Genetic diversity of seed storage proteins in plants. In: Brown, A.H.D., Clegg, M.T., Kahler, A.L. and Weir, B.S., Eds., *Plant Population Genetics, Breeding and Genetic Resources*, Sinauer Associates Inc., Sunderland, Massachusetts, 64-82.

[18] Khan, M.F., Schumann, E. and Weber, W.E. (2002) Characterization of Pakistani wheat varieties for general cultivation in the mountainous regions of Azad Kashmir. *Asian Journal of Plant Sciences*, **1(6)**, 699-702.

[19] Zeb, A., Zahir, A., Ahmad, T. and Abdumanon, A. (2006) Physiochemical characteristics of wheat varieties growing in the same and different ecological regions of Pakistan. *Pakistan Journal of Biological Sciences*, **9(9)**, 1823-1828.

[20] Magni, C., Scarafoni, A., Herndl, A., Sessa, F., Prinsi, B., Espen, L. and Duranti, M. (2007) Combined 2D electrophoretic approaches for the study of white lupin mature seed storage proteome. *Phytochemistry*, **68(7)**, 997-1007.

[21] Sadia, M., Salman, A.M., Rabbani, M.A. and Pearce, S.R. (2009) Electrophoretic characterization and the relationship between some *Brassica* species. *Electronic Journal of Biology*, **5(1)**, 1-4.

[22] Das, S. and Mukherjee, K.K. (1995) Comparative study on seed proteins of Ipomoea. *Seed Science and Technology*, **23(2)**, 501-509.

Vol.2, No.7, 741-747 (2010)
doi:10.4236/ns.2010.27093

Natural Science

Comparison of factor loadings for anthropometric and physiometric measures among type 2 diabetic males, pre- and post-menopausal females in North Indian Punjabi population

Badaruddoza*, Basanti Barna, Amarjit Singh Bhanwer

Department of Human Genetics, Guru Nanak Dev University, Amritsar, India; *Corresponding Author: doza13@yahoo.co.in

Received 10 April 2010; revised 18 May 2010; accepted 23 May 2010.

ABSTRACT

Background: The objective of the present study was to compare the relationship of anthropometric and physiometric characteristics using principal component factor analysis among three groups of type 2 diabetic subjects such as males, pre- and post-menopausal females in North Indian Punjabi population. Method: A total of 349 type 2 diabetic subjects (males 157; females 192; 88 pre- and 104 post-menopausal) were ascertained for the present study. Different anthropometric and physiometric measurements were taken. Principal component factor analysis (PCFA) was applied to identify the components which are more close to type 2 diabetes among the three groups. Results: PCFA revealed five uncorrelated components which explained 79% of the total variance among diabetic males and six unrelated components which explained 78% of the total variance among pre- and post-menopausal females. The important two factors could be identified as central obesity (factor 1) and blood pressure (factor 2) among these three groups. Conclusion: Higher clustering of obesity and blood pressures were found in diabetic males as compared to pre- and post-menopausal diabetic females in North Indian Punjabi population whereas, waist to hip ratio (WHR) has maximum loading in post-menopausal females as compared to others.

Keywords: Factor Analysis; Blood Pressure; Type 2 Diabetes; Anthropometry; Punjabi Population

1. INTRODUCTION

The relationships between type 2 diabetes mellitus (T2DM), anthropometric variables and blood pressures are statistically complex [1,2]. Strong inter-correlation between anthropometric and physiometric variables creates complexities in the analysis and interpretation of independent associations of these variables with the development of type 2 diabetes. Principal Component Factor Analysis (PCFA) is the technique to reduce a large number of variables to a smaller number of factors which are more closely associated with antecedent [2-4]. The objective of the present study using principal component factor analysis is to compare the relationship between anthropometric and physiometric components with diabetic males, pre- and post-meno-pausal females in North Indian Punjabi population. The attention has also been given to find out which factors can be used as significant predictors of T2DM.

2. MATERIALS AND METHODS

Present study was conducted at the different clinical centres such as Heart Station and Diabetic Clinic, A.P. Hospital and Heart Care Centre, Diabetic Clinic and Research Institute in Amritsar district in the state of Punjab among Punjabi population. Punjabi population may be defined as similar genotype groupings and aggregate of similar cultural practices, life style pattern, social influence and similar ethnic characteristics with Punjabi language speaking and at least reside in Punjab for the last 20 years. A total of 349 type 2 diabetic individuals participated in the baseline examination for the present study which occurred from October 2008 to September 2009. Among total individuals 157 and 192 are males and females respectively whereas, among females 88 and 104 are pre- and post-menopausal. All participants provided written informed consent.

2.1. Anthropometric Measurements

Actual age and age on the onset of the disease were recorded from the subject's health card provided by the

clinical centres. Height, weight, circumferences of waist (WC), hip (HC), arm (AC) and Calf (CC) and four skin fold thickness (biceps, triceps, sub-scapular and supra-iliac) were taken by female author on each individual using standard anthropometric techniques and tools [5,6]. Height and weight were measured to the nearest 0.5 cm and 0.1 kg respectively. Body mass index (BMI) was calculated for an estimate of overall adiposity using the formula: BMI = weight (kg)/height (m^2). Waist and Hip circumference (WC and HC) for an estimate of central obesity [7] were measured to the nearest 0.5 cm with a steel tape. Waist to hip ratio (WHR) was calculated using the standard formula: WHR = WC (cm)/HC (cm). A Lange skinfold calliper was used to measure the skinfolds to the nearest 0.2 mm. Two subsequent measurements were taken and averages were used in the analysis.

2.2. Physiometric Measurements

Left arm blood pressures (first phase systolic and fifth phase diastolic) were taken from each participant with standard mercury sphygmomanometer after a 5 min rest. The average of the two subsequent measurements was used for analysis. All efforts were made to minimize the factors which affect the blood pressure like anxiety, fear, stress, laughing and recent activity [8]. Mean arterial blood pressure (MBP) was calculated for each of the two readings taken for SBP and DBP by using the formula: MBP = SBP + (SBP-DBP)/3 [9]. The radial artery at the wrist was used to count the pulse. It was counted over one minute. The difference of SBP and DBP was used as pulse pressure.

3. STATISTICAL ANALYSIS

Descriptive statistics such as means, standard deviations and coefficient of skewness were calculated for all variables. All statistical analysis including factor analyses were conducted by SPSS (Statistical Package for Social Sciences, version 17.0, SPSS Inc. USA). Each of the anthropometric and physiometric variables is highly inter-correlated with each others and creates a methodological problem for analysis the data. PCFA is used when variables are highly correlated and this multivariate statistical tool able to reduce a large number of inter-correlated variables to a smaller number of principal components which account for most of the variance in the data [10,11]. Factor analysis has done on the basis of correlation matrix which helps to understand the amount of association between the variables, factor extraction and orthogonal rotation to make factors easily interpretable. Hence, PCFA was used to extract uncorrelated factors and varimax rotation, which is an orthogonal rotation in which the factors are assumed to act independently, was used in the present study. Factor loadings were equivalent to the correlation coefficients between the variables (rows) and factors (columns). The final factors pattern was interpreted using factor loadings of ≥ 0.4. Extracted factors or number of factors to be retained was based on eigenvalue criteria ≥ 1.0. Eigenvalues indicate the amount of variance explained by each factor. A factor with low eigenvalue has a little contribution to explain the variances in the variables and may be ignored. The first and second principal components were identified through largest and second largest amount of variance in the data and so on. Communality is the squared multiple correlation for the variable (as dependent) using as predictors. Hence, the communality estimates is the measure the percent of variance in a given variable explained by all factors. A communality of 0.75 and 0.25 considered large and low respectively. Low communality indicates variables are negligibly related to each other. The probability values less than or equal to 0.05 (two-tailed) were considered to be significant.

4. RESULTS

Table 1 presents the mean, standard deviation (SD) and skewness of anthropometric and physiometric variables. All right skewed distributions have converted to a normal distribution by square root transformation whereas; reciprocal transformation is used for left skewed distribution among type 2 diabetic males, pre- and post-menopausal females. The highest mean age for onset of T2DM was found among post-menopausal females (52.46 ± 6.22years) and the lowest mean age for the onset of disease was found among pre-menopausal females (36.97 ± 5.96 years) as compared to males (45.19 ± 7.79 years). The other highest mean values of important anthropometric indicator such as BMI, hip circumference, biceps skinfold, triceps skinfold and arm circumference were found among diabetic post-menopausal females as compared to males and pre-menopausal females. The diabetic males have higher mean values for WHR and waist circumference. The physiometric variables such as SBP, DBP, pulse rate and pulse pressure have not shown any specific trend among three groups of diabetic subjects. Bivariate correlations of the traits were examined among type 2 diabetic males, pre- and post-menopausal females and are presented in **Tables 2** to **4**. Waist circumference, hip circumference, biceps skinfold, triceps skinfold, arm circumference and calf circumference with Weight and BMI; hip circumference, biceps skinfold, triceps skinfold, arm circumference and calf circumference with waist circumference have been found signifi-

Table 1. Descriptive Statistics of Anthropometric and Physiometric variables among type 2 diabetic male, pre- and post-menopausal females in the present study population (n = 349).

VARIABLES	MALE (N = 157)			FEMALE (N = 192)					
				PRE-MENOPAUSAL (N = 88)			POST-MENOPAUSAL (N = 104)		
	MEAN	SD	SKEW-NESS	MEAN	SD	SKEWNESS	MEAN	SD	SKEW-NESS
Age (yrs)	53.994	8.093	0.466	46.89	7.85	−0.009	58.39	7.49	0.45
Onset age (yrs)	45.197	7.792	0.836	36.97	5.96	−0.28	52.46	6.22	1.02
Height (cm)	169.131	8.582	−5.437	154.95	5.599	0.19	155.80	6.95	1.57
Weight (Kg)	76.697	6.976	0.533	63.52	7.55	0.36	67.70	8.20	0.43
BMI(kg/m^2)	26.555	3.870	0.370	26.25	3.34	0.21	28.00	5.60	0.62
WHR	0.941	0.0732	0.586	0.88	0.07	0.75	0.87	0.07	−0.17
Waist circumference(cm)	96.014	8.512	0.267	87.23	9.90	0.597	90.26	9.32	0.49
Hip circumference (cm)	101.94	9.056	0.242	99.18	9.59	0.68	103.07	10.97	0.52
Biceps skinfold (mm)	10.806	5.968	1.745	13.11	5.05	0.395	13.26	5.58	1.03
Triceps Skinfold (mm)	14.005	5.053	3.201	17.12	5.19	0.299	17.54	6.76	0.58
Subscapular skinfold (mm)	-------	-------	--------	24.94	4.88	−0.39	26.66	5.399	0.04
Supra-iliac skinfold (mm)	-------	--------	--------	21.37	3.82	−0.14	24.37	4.43	0.10
Arm Circumference (cm)	27.838	3.192	0.282	27.27	3.39	0.18	28.20	3.90	0.87
Calf circumference (cm)	33.548	3.868	0.502	31.97	3.62	0.24	32.34	3.67	0.04
Systolic blood pressure (mmHg)	124.656	9.266	1.802	121.72	8.82	0.86	124.95	9.49	0.798
Diastolic blood pressure (mmHg)	80.083	10.475	1.090	79.55	9.93	−0.12	79.70	9.81	1.04
Mean Blood Pressure (mmHg)	95.924	9.384	2.081	93.56	9.67	0.57	96.14	8.27	2.695
Pulse Rate	83.229	8.471	0.251	85.10	8.85	0.12	83.98	8.24	0.15
Pulse Pressure	44.790	7.232	1.660	42.27	7.58	0.77	46.41	7.08	1.296

Significant at least at $p \leq 0.05$
SD = Standard Deviation

cantly associated at least 5% level ($p < 0.05$) among all diabetic males, pre- and post-menopausal females. SBP and DBP were found to be significantly associated with weight, BMI, waist circumference, hip circumference, biceps skinfold and triceps skinfold at least 5% level ($p < 0.05$) among diabetic pre- and post-menopausal females. Whereas, WHR was found significantly associated ($p < 0.05$) with other anthropometric variables among only type 2 diabetic males.

The comparison of factor loading pattern of six factors (components) is presented in **Table 5** among diabetic males, pre- and post-menopausal females. Only variables with factor loading greater than or equal to 0.4 were considered for present interpretation among three groups. After Varimax rotation, weight, BMI, waist circumference, hip circumference, arm and calf circumferences are relatively large and positively loaded (> 0.7) on factor 1 among males, pre- and post-menopausal females. However, on factor 1 highest loading was found in weight (0.944) for males, hip circumference (0.883) for pre-menopausal females and BMI (0.940) for post-menopausal females. The physiometric variables such as SBP, DBP and pulse pressure are grouped together and loaded positively on factor 2 among three groups. Maximum loading has found for SBP (> 0.90) on factor 2 for all three groups, whereas loading of DBP for this factor is just above the cut-off value (0.4) for post-menopausal females. Both mean age (actual age and onset age of type 2 diabetes) have found maximum loading (0.952 and 0.940) on factor 3 among males, whereas, skinfold thickness (biceps, triceps, sub-scapular and supra-iliac) grouped together and loaded significantly among pre- and post-menopausal females. Only triceps skinfold and biceps skinfold among males have positive loading on factor 4, whereas, actual mean age and the mean age of onset of the disease have grouped for higher positive loading among pre- and post-menopausal females. Only WHR has positive loading on factor 5 among males, whereas, WHR and waist circumference for pre-menopausal females and WHR, height and waist circumference for post-menopausal females have positive loading on this factor. However WHR has maximum positive loading (≥ 0.80) among pre- and post-menopausal females but for males it is just above cut-off value (0.55). Only Height and pulse rate have positive loading on factor 6 among pre- and post-menopausal female whereas, all variables are extracted on this factor among males. The five factors explained 79% of the total variance among males in which the first two factors cumulatively explained 54% of the total variance. Whereas, the six factors explained 78% of the total variance among pre- and post-menopausal females in which first two factors cumulatively explained 48% and 49% of the total variance respectively. The eigenvalue of the first two factors have also been seen maximum among males, pre- and post-menopausal females. The

Table 2. Inter-correlation matrix of selected anthropometric variables among males of Type 2 Diabetes Mellitus (T2DM).

VARIABLES	Age (yrs)	OA (yrs)	Ht (cm)	Wt (Kg)	BMI (kg/m^2)	WHR	WC (cm)	HC (cm)	BSkn (mm)	T Skn (mm)	AC (cm)	CC (cm)	SBP (mmHg)	DBP (mmHg)	MBP (mmHg)	PR	PP
Age (yrs)		.81*	−.05	−.06	−.007	.03	.05	.03	−.003	−.08	−.04	−.09	−.05	−.05	−.10	−.12	.02
Onset age (yrs)			−.03	.09	.16	.09	.17	.16	.09	.01	.10	.04	−.08	−.005	−0.12	−.13	−.06
Height (cm)				.09	−.15	−.12	−.06	−.007	−.17	−.27	−.02	−.03	−.007	−.07	−0.04	−.04	.03
Weight (Kg)					.91*	.48*	.87*	.84*	.58*	.40*	.73*	.73*	.08	.18	0.11	−.11	.05
BMI(kg/m^2)						.50*	.85*	.80*	.57*	.46*	.73*	.73*	.07	.18	0.11	−.12	.03
WHR							.68*	.20*	.33*	.40*	.42*	.34*	.03	.12	0.04	−.19	−.001
Waist circumference (cm)								.82*	.62*	.45*	.75*	.70*	.01	.13	0.05	−.20*	−.004
Hip circumference (cm)									.60*	.32*	.70*	.70*	−.006	.09	0.05	−.09	−.009
Biceps skinfold (mm)										.72*	.64*	.50*	.003	.07	−0.02	−.13	.011
Triceps Skinfold (mm)											.46*	.32*	−.04	.04	−0.04	−.13	−.03
Arm Circumference (cm)												.68*	.03	.13	0.06	−.13	−.005
Calf circumference (cm)													.001	.04	0.01	−.10	−.001
Systolic blood pressure (mmHg)														.73	0.86*	.08	.90*
Diastolic blood pressure (mmHg)															0.80*	−.004	.40*
Mean Blood Pressure (mmHg)																.053	.67*
Pulse Rate																	.09*
Pulse Pressure																	

Significant at least at $p \leq 0.05$; OA = Onset age, yrs = years, Ht = Height, Wt = Weight, BMI = Body Mass Index, WHR = Waist Hip Ratio, WC = Waist Circumference, HC = Hip Circumference, BS = Biceps skinfold, TS = Triceps skinfold, SS = Sub-scapular skinfold, SiS = Supra-iliac skinfold, AC = Arm Circumference, CC = Calf Circumference, SBP = Systolic Blood Pressure, DBP = Diastollic Blood Pressure, MBP = Mean Blood Pressure, PR = Pulse Rate, PP = Pulse Pressure.

common greater communality estimates (> 0.70) have found on age, onset age of disease, weight, BMI, waist circumference, hip circumference, triceps skinfold, SBP among three groups. WHR has maximum communality estimates among pre- and post-menopausal females.

5. DISCUSSION

The present quantitative analysis have shown that which of the anthropometric and physiometric traits (BMI, WHR, weight, waist circumference, hip circumference, skinfolds, SBP, DBP, and pulse pressure) are more closely associated and act as a good predictors for further risk among three groups of T2DM individuals such as males, pre- and post-menopausal females in North Indian Punjabi population. The present study also provides through PCFA among three groups that which of the traits would require more attention to clinicians for raised risk of T2DM.

The many previous studies suggested that obesity, overweight, glucose intolerance, hypertension and elevated blood pressures are closely associated with T2DM [12-18].The present analysis showed a common association of BMI, WHR, waist circumference, hip circumference and subcutaneous fat with T2DM incidence among males, pre-and post-menopausal females.

Table 3. Inter-correlation matrix of selected variables among pre-menopausal females of Type 2 Diabetes Mellitus (T2DM).

VARIABLES	Age (yrs)	OA (yrs)	Ht (cm)	Wt (Kg)	BMI (kg/m^2)	WHR	WC (cm)	HC (cm)	BSkn (mm)	T Skn (mm)	SS (mm)	SiS (mm)	AC (cm)	CC (cm)	SBP (mmHg)	DBP (mmHg)	MBP (mmHg)	PR	PP
Age (yrs)		.54*	−.08	−.05	−.14	.10	.08	.03	.05	.07	.06	.04	−.09	−.14	.13	−.04	.02	−.06	.22
OA (yrs)			−.03	−.03	−.06	−.05	−.03	.02	−.02	.08	−.006	.19	−.04	.06	.17	.10	.10	.05	.19
Ht (cm)				.30	−.08	.10	.06	.0097	.013	.04	.16	.06	.15	.09	.02	.03	.03	.22	.006
Wt (Kg)					.83*	.15	.80*	.82*	.53*	.42	.36*	.50*	.70*	.51*	.17	.11	.19	−.06	.13
BMI(kg/m^2)						.08	.68*	.73*	.58*	.45	.34*	.43*	.68*	.61*	.16	.09	.18	−.13	.15
WHR							.51*	−.16	.009	−.12	.10	.14	−.03	−.02	−.05	−.02	.007	.04	−.08
WC(cm)								.75*	.48*	.30*	.22*	.42*	.58*	.46*	.18	.20*	.24*	−.08	.08
HC (cm)									.56*	.45*	.21*	.40*	.69*	.53*	.24*	.24*	.28*	−.14	.14
BS (mm)										.80*	.45*	.46*	.66*	.49*	.15	.03	.099	−.30*	.19
T S (mm)											.38*	.36*	.54*	.38*	.13	−.07	.04	−.25*	.25
SS (mm)												.66*	.24*	.16	−.05	−.05	−.06	−.19	−.03
SiS (mm)													.35*	.31*	.12	.09	.10	−.05	.10
AC (cm)														.66*	.008	−.03	.03	−.13	.02
CC (cm)															.008	.04	.05	−.14	−.008
SBP (mmHg)																.71*	.91*	−.09	.87*
DBP (mmHg)																	.85*	.09	.29*
MBP (mmHg)																		−.009	.65*
P R																			−.17
P P																			

Significant at least at $p \leq 0.05$; OA = Onset age, yrs = years, Ht = Height, Wt = Weight, BMI = Body Mass Index, WHR = Waist Hip Ratio, WC = Waist Circumference, HC = Hip Circumference, BS = Biceps skinfold, TS = Triceps skinfold, SS = Sub-scapular skinfold, SiS = Supra-iliac skinfold, AC = Arm Circumference, CC = Calf Circumference, SBP = Systolic Blood Pressure, DBP = Diastolic Blood Pressure, MBP = Mean Blood Pressure, PR = Pulse Rate, PP = Pulse Pressure.

Table 4. Inter-correlation matrix of variables among post-menopausal females of Type 2 Diabetes Mellitus (T2DM).

VARIABLES	Age (yrs)	OA (yrs)	Ht (cm)	Wt (Kg)	BMI (kg/m^2)	WHR	WC (cm)	HC (cm)	BSkn (mm)	T Skn (mm)	SS (mm)	SiS (mm)	AC (cm)	CC (cm)	SBP (mmHg)	DBP (mmHg)	MBP (mmHg)	PR	PP
Age (yrs)		.73*	−.12	.007	.06	−.01	.17	.15	−.08	−.02	−.20*	−.07	−.04	.03	.06	−.07	.14	.15	.09
OA (yrs)			−.08	−.03	.006	.04	.07	.03	−.04	.04	−.09	−.05	−.08	−.02	.06	.099	.16	.15	.005
Ht (cm)				.19	−.23*	.17	.06	−.05	.04	.10	.03	−.08	−.09	−.02	−.15	−.07	−.11	−.03	−.19
Wt (Kg)					.90*	.18	.80*	.83*	.53*	.40*	.54*	.52*	.76*	.74*	.13	.18	.10	.05	−.005
BMI(kg/m^2)						.07	.77*	.85*	.50*	.35*	.52*	.55*	.80*	.74*	.20	.20*	.16	.08	.09
WHR							.47*	−.08	.10	.10	.10	.03	.01	−.02	.002	−.09	.10	−.03	.05
WC(cm)								.796*	.53*	.42*	.495*	.46*	.65*	.62*	.19	.083	.20	.10	.15
HC (cm)									.50*	1.0	.55*	.53*	.77*	.75*	.16	.12	.14	.05	.09
BS (mm)										.78*	.50*	.47*	.44*	.44*	.06	.05	.009	.013	.06
T S (mm)											.44*	.37*	.33*	.33*	.03	−.05	.01	.013	.10
SS (mm)												.60*	.49*	.43*	−.09	−.02	−.15	−.002	−.12
SiS (mm)													.48*	.49*	.18	.12	.03	−.03	.12
AC (cm)														.69*	.12	.21*	.12	.05	.007
CC (cm)															.20*	.16	.12	.06	.14
SBP (mmHg)																.59*	.72*	.13	.86*
DBP (mmHg)																	.56*	.13	.16
MBP (mmHg)																		.003	.53*
PR																			.06
PP																			

Significant at least at $p \leq 0.05$; OA = Onset age, yrs = years, Ht = Height, Wt = Weight, BMI = Body Mass Index, WHR = Waist Hip Ratio, WC = Waist Circumference, HC = Hip Circumference, BS = Biceps skinfold, TS = Triceps skinfold, SS = Sub-scapular skinfold, SiS = Supra-iliac skinfold, AC = Arm Circumference, CC = Calf Circumference, SBP = Systolic Blood Pressure, DBP = Diastolic Blood Pressure, MBP = Mean Blood Pressure, PR = Pulse Rate, PP = Pulse Pressure.

Table 5. Comparison of factor loadings by principal component analysis with Varimax rotation and communalities of the risk factors among type 2 diabetic male, pre-menopausal and post-menopausal females (n = 349).

VARIABLES	FACTOR 1			FACTOR 2			FACTOR 3			FACTOR 4			FACTOR 5			FACTOR 6			COMMU-NALITY ESTIMATES		
	M	PRF	POF	M	PRF	POF	M	PRF	POF	M	PRF	POF	M	PRF	POF	M	PRF	POF	M	PRF	POF
Age (yrs)	−.046	−.083	.042	−.025	.038	.041	.952	.057	−.072	.008	.860	.930	.053	.136	−.021	----	−.134	.010	.912	.787	.874
Onset age (yrs)	.114	.013	−.035	−.054	.105	.048	.940	.021	.021	.015	.868	.873	.054	−.097	.006	----	.111	.168	.902	.787	.794
Height (cm)	.056	.041	−.099	−.035	.030	−.217	−.080	.303	.104	−.827	−.084	−.196	.118	.007	.652	----	.726	.404	.709	.629	.695
Weight (Kg)	.944	.833	.903	.091	.117	.017	−.147	.260	.160	−.043	−.042	−.029	.102	.255	.241	----	.173	.129	.912	.872	.917
BMI(kg/m^2)	.905	.841	.940	.088	.101	.112	.054	.171	.111	.154	−.108	.054	.083	.154	−.057	----	−.118	−.026	.861	.796	.916
WHR	.432	−.029	.072	.061	−.060	.092	.007	.107	.034	.278	.025	.080	.550	.913	.831	----	.006	−.296	.569	.849	.799
Waist circumference(cm)	.900	.735	.796	.033	.133	.139	.078	.087	.215	.117	.039	.182	.253	.620	.412	----	−.030	−.072	.894	.953	.908
Hip circumference (cm)	.911	.883	.903	.002	.202	.048	.088	.060	.184	−.031	.039	.103	−.088	.019	−.064	----	−.037	.027	.846	.827	.867
Biceps skinfold (mm)	.663	.633	.419	−.020	.067	.025	−.002	.527	.794	.473	.043	−.046	.106	−.125	.064	----	−.271	.045	.675	.775	.814
Triceps Skinfold (mm)	.429	.511	.245	−.051	.033	.021	−.110	.540	.880	.680	.114	.045	.245	−.267	.103	----	−.257	.036	.722	.704	.848
Subscapular skinfold (mm)	--	.137	.571	--	−.071	−.197	--	.871	.469	---	−.030	−.179	--	.103	.005	----	.032	−.037	----	.795	.619
Supra-iliac skinfold (mm)	--	.346	.577	--	.079	.091	--	.684	.413	---	.125	−.104	--	.202	−.143	----	.105	−.107	-----	.661	.554
Arm Circumference (cm)	.838	.863	.871	.030	−.071	.037	−.006	.175	.077	.115	−.041	−.078	.113	−.096	−.053	----	.014	.070	.729	.792	.780
Calf circumference (cm)	.837	.763	.811	−.025	−.046	.103	−.062	.048	.141	−.011	−.021	−.006	.002	−.135	−.053	----	.031	.057	.705	.606	.694
Systolic blood pressure (mmHg)	.006	.056	.102	.970	.975	.957	−.028	.050	.031	−.013	.103	−.002	.036	−.034	−.057	----	−.066	.101	.944	.972	.941
Diastolic blood pressure (mmHg)	.097	.076	.190	.823	.817	.579	−.009	−.117	−.163	.061	−.063	−.135	.086	.082	−.084	----	.178	.539	.698	.729	.714
Mean Blood Pressure (mmHg)	.035	.104	.102	.934	.965	.833	−.082	−.043	−.115	−.007	−.014	.103	−.003	.046	.112	----	.046	.108	.880	.948	.752
Pulse Rate	−.049	−.084	.028	.060	−.032	.035	−.097	−.254	.062	.088	.065	.235	−.862	−.005	−.059	----	.752	.642	.769	.642	.477
Pulse Pressure	.007	.015	−.032	.814	.767	.846	.020	.165	.178	−.029	.207	.066	−.084	−040	−.060	----	−.209	−.215	.671	.721	.802
Eigenvalue	6.016	5.917	6.408	3.190	3.159	2.876	1.837	1.762	1.804	1.318	1.574	1.444	1.034	1.228	1.201	---	1.204	1.034	---	---	---
Variance Explained(%)	35.389	31.140	33.726	18.767	16.626	15.135	10.806	9.274	9.496	7.756	8.286	7.601	6.084	6.464	6.322	---	6.336	5.440	----	---	----
Cumulative Variance(%)	35.389	31.140	33.726	54.157	47.767	48.860	64.962	57.041	58.356	72.718	65.327	65.957	78.801	71.791	72.28	---	78.127	77.719	---	---	---

Factor Loadings ≥ 0.4; M = Males, PMF = Pre-menopausal females, POF = Post-menopausal females.

PCFA is applied to identify the significant association with T2DM among three groups. As far as concern in the North Indian Punjabi population, very little information [15,19-21] to identify the underlying factors/components of the T2DM are available. In this consideration the present work has been undertaken among the males and females (pre- and post-menopausal). PCFA have identified five factors with 79% explained variance among male diabetic subjects and six factors with 78% explained variance among pre- and post-menopausal diabetic female subjects.

It is important to note that neither of the anthropometric and physiometric variables equally loaded on all five or six components. Factor 1 is the most diverse among three groups. It could be identified as weight, BMI, waist circumference for males; hip circumference, BMI, weight for pre-menopausal females and BMI, weight, hip circumference for post-menopausal females. However weight for males, hip circumference for pre-menopausal and BMI for post- menopausal females are heavily loaded. The second factor could be identified as SBP and DBP for males and pre-menopausal females and DBP for post-menopausal females. This component is most clearly and heavily loaded. Therefore, among diabetic individuals, males and pre-menopausal females were very closely associated with SBP and DBP whereas, post-menopausal diabetic females were more concerned with DBP only. Among male diabetic subjects factor three was grouped with actual age and age of onset of the disease, whereas, subcutaneous fat was identified as factor three. Factor four could be identified as subcutaneous fat for males, whereas actual age and age of onset of the disease were grouped together for factor four.

Factor five could be identified as WHR for the three groups. However, WHR is heavily loaded for pre- and post-menopausal females. Pulse rate could be identified as factor six for both pre- and post-menopausal females, whereas, no sixth factor is identified for males.

The present factor analysis confirmed that cluster of at least three variables such as, weight, BMI, waist circumference which have identified as factor one explained 35%, 31% and 34% of the total variance among diabetic males, pre- and post-menopausal females respectively. Therefore, the cluster of weight, BMI and waist circumference could be classified as central obesity and this cluster is equally associated with diabetic males and post-menopausal females. Furthermore, in the present study, the second factor, that is blood pressures explained 19%, 17% and 15% of the total variance among diabetic males, pre- and post-menopausal females. The blood pressures (SBP and DBP) were positively and significantly associated with diabetic males. Therefore the above two types factors such as, central obesity and blood pressures are more predispose among diabetic males as compared to females. PCFA also confirmed that WHR and pulse pressure are significantly

associated with diabetic pre- and post-menopausal females as compared to diabetic males. Therefore, it is very difficult to single out of the particular variable which is more associated with male or pre- and post-menopausal females due to the fact that many overlapping variables have found as more than one factor among all the three groups. Further, research with PCFA is required on other Indian ethnic groups to compare the present trend of the study.

6. ACKNOWLEDGEMENTS

The authors are greatful to Dr Rohit Kapoor; Dr. A. P. Singh and Dr. Puneet Arora for their co-operation during the data collection. This work is financially supported by University Grants Commission, New Delhi [DRS I (UGC-SAP)].

REFERENCES

[1] Meigs, J.B. (2000) Invited commentary: Insulin resistance syndrome? Syndrome X? Multiple metabolic syndrome? A syndrome at all? Factor analysis reveals patterns in the fabric of correlated metabolic risk factors. *American Journal of Epidemiology*, **152(10)**, 908-911.

[2] Hanley, A.J., Karter, A.J. and Festa, A. (2002) Factor analysis of metabolic syndrome using directly measured insulin sensitivity: The insulin resistance atherosclerosis study. *Diabetes*, **51(8)**, 2642-2647.

[3] Ghose, A., Bose, K. and Das Chaudhari, A.B. (2003) Association of food pattern, central obesity measures and metabolic risk factors for coronary heart disease (CHD) in middle aged Bengalee Hindu men, Calcutta, India. *Asia Pacific Journal of Clinical Nutrition*, **12(2)**, 166-171.

[4] Ghose, A. (2005) Factor analysis of metabolic syndrome among the middle-aged Bengalee Hindu men of Calcutta, India. *Diabetes/Metabolism Research and Reviews*, **21(1)**, 58-64.

[5] Singh, I.P. and Bhasin, M.K. (1968) *Anthropometry*, Kamla Raj Enterprises, Delhi.

[6] Weiner, J.S. and Lourie, J.A. (1981) *Practical Human Biology*, Academic Press, London.

[7] Lemieux, S., Prud'homme, D., Bouchard, C., Tremblay, A. and Despres, J.P. (1996) A single threshold value of waist girth identifies normal weight and overweight subjects with excess visceral adipose tissue. *American Journal of Clinical Nutrition*, **64(5)**, 685-693.

[8] Badaruddoza and Afzal, M. (1999) Age specific differences in blood pressure among inbred and non-inbred North Indian children. *Journal of Biosciences*, **24(2)**, 177-184.

[9] Perusse, L., Rice, T., Bouchard, C., Vogler, G.P. and Rao, D.C. (1989) Cardiovascular risk factors in the French Canadian population: Resolution of genetic and familial environmental effects on blood pressure by using extensive information on environmental correlates. *American Journal of Human Genetics*, **45(2)**, 240-251.

[10] Truxillo, C. (2003) Multivariate statistical methods: Practical research applications course notes. SAS Institute, USA.

[11] Wu, C.Z., Lin, J.D., Li, J.C., Hsiao, F.C., Hsich, C.H., Kuo, S.W., Hung, Y.J., Lu, C.H., He, C.T. and Pei, D. (2008) Factor analysis of metabolic syndrome using direct measurement of insulin resistance in Chinese with different degrees of glucose tolerance. *Indian Journal of Medical Research*, **127(1)**, 336-343.

[12] Singh, R., Shaw, J. and Zimmet, P. (2004) Epidemiology of childhood type 2 diabetes in the developing world. *Pediatric Diabetes*, **5(3)**, 154-168.

[13] Li, J.K., Ng, M.C., So, W.Y., Chiu, C.K., Ozaki, R., Tong, P.C., Cockram, C.S. and Chan, J.C. (2006) Phenotypic and genetic clustering of diabetes and metabolic syndrome in Chinese families with type 2 diabetes mellitus. *Diabetes/Metabolism Research and Reviews*, **22(6)**, 46-52.

[14] Comuzzie, A.G., Tejero, M.E., Funahash, T., Martin, L.J., Kisseban, A., Takahashi, S., Tanaka, S., Rainwater, D.L., Matsuzawa, Y., MacCluer, J.W. and Blangero, J. (2007) The genes influencing adiponectin levels also influence risk factors for metabolic syndrome and type 2 diabetes. *Human Biology*, **79(2)**, 191-200.

[15] Rai, E., Sharma, S., Koul, A., Bhat, A.K., Bhanwer, A.J. and Bamezai, R.N. (2007) Interaction between the UCP2-866G/A, mtDNA 10398G/A and PGC1alpha p.Thr394Thr and p.Gly482Ser polymorphisms in type 2 diabetes in North Indian population. *Human Genetics*, **122(5)**, 535-540.

[16] Franceschini, N., Almasy, L., MacCluer, J.W., Goring, H.H., Cole, S.A., Diego, V.P., Laston, S., Howard, B.V., Lee, E.T., Best, L.G., Fabsitz, R.R. and North, K.E. (2008) Diabetes-specific genetic effects on obesity traits in American Indian populations: The strong heart family study. *BMC Medical Genetics*, **9(1)**, 90-96.

[17] van't Riet, E., Alsseme, M., Nijpels, G. and Dekker, J.M. (2008) Estimating the individual risk of diabetes: Not on the grounds of overweight only. *Nederlands Tijdschr Geneeskd*, **152(44)**, 2385-2388.

[18] Dunkley, A.J., Taub, N.A., Davis, M.J., Stone, M.A. and Khunti, K.C. (2009) Is having a family history of type 2 diabetes or cardiovascular disease a predictive factor for metabolic syndrome? *Primary Care Diabetes*, **3(1)**, 49-56.

[19] Matharoo, K., Kumar, A., Randhawa, N.K., Arora, P. and Bhanwer, A.J.S. (2006) Angiotensin converting enzyme gene insertion/deletion polymorphism in type 2 diabetes (T2DM) patients from Punjab. *Journal of Punjab Academy of Sciences*, **3(3)**, 7-12.

[20] Sanghera, D.K., Bhatti, J.S., Bhatti, G.K., Ralhan, S.K., Wander, G.S., Singh, J.R., Bunker, C.H., Weeks, D.E., Kamboh, M.I. and Ferrell, R.E. (2006) The Khatri Sikh Diabetes Study (SDS): Study design, methodology, sample collection, and initial results. *Human Biology*, **78(1)**, 43-63.

[21] Sanghera, D.K., Ortega, L., Han, S., Singh, J., Ralhan, S.K., Wander, G.S., Mehra, N.K., Mulvihill, J.J., Ferrell R.E., Nath, S.K. and Kamboh, M.I. (2008) Impact of nine common type 2 diabetes risk polymorphisms in Asian Indian Sikhs: PPARG2 (Pro12Ala), IGF2BP2, TCF7L2 and FTO variants confer a significant risk. *BMC Medical Genetics*, **9(1)**, 59-67.

Vol.2, No.7, 748-759 (2010)
doi:10.4236/ns.2010.27094

Natural Science

Environmental stress upon hepatopancreatic cells of freshwater prawns (Decapoda: Caridea) from the floodplain of Paraná River

Pablo Collins

Instituto Nacional de Limnología (CONICET-UNL) Ciudad Universitaria, Pje El Pozo s/n, 3000 Santa Fe Santa Fe Argentina TE 0054-0342-4511645 int 113, Fac. de Bioq. y Cs. Biol. UNL, Fac. de Tecnología y Ciencias, UADER; pcollins@arnet.com.ar

Received 10 March 2010; revised 11 April 2010; accepted 17 April 2010.

ABSTRACT

In order to evaluate the influence of stressed environments on hepatopancreatic cells of freshwater prawns, *Macrobachium borellii* Nobili, 1896 and *Palaemonetes argentinus* Nobili 1901, (Crustacea, Decapoda, Palaemonidae) were collected at three different aquatic environments with different relationship to urban development in Argentina. Furthermore the effects of several cypermethryn concentration on hepatopancreatic cell of *M. borellii* and *P. argentinus* were evaluated in a laboratory assays. The "N° 1" lake (Santa Fe Argentina) which is more affected by the anthropogenic pressure and "Don Felipe" lake which is still not strongly by human activities were the studied sites from the floodplain of Paraná river. While Alejandra lake was the intermedia effects sites. Different damaged ultrastructures were found in F- and R-cells of prawns in the stressed lake. The predominant features were: disrupted the microvillous border, swelled mitochondria, reduction of endoplasmic reticulum, dyctiosomes, glycoproteins, desnaturalization of vacuole membrane and premature autolysis. Moreover the F-cell number was higher in the environment near to city than in the others sites. Similar effects were observed in the cypermethryn assays. The observations clearly indicate that the ultrastructure of midgut gland in the both palaemonids varies depending on the site from which animals are collected and the biocid presence. So, in this case it can be stated that the hepatopancreas histology of freshwater prawns is a good tool to monitor the impact of a stressed environment upon freshwater prawns.

Keywords: Palaemonidae; Midgut Gland; Shrimp; Hepatopancreas; Environmental Stress

1. INTRODUCTION

Freshwater prawns are an important and abundant group in the floodplain of the Paraná River, mainly the species *Macrobrachium borellii* Nobili, 1896 and *Palaemonetes argentinus* Nobili, 1901. Both prawns have as habit the lotic and lentic environment from La Pampa region, Argentina [1]. This area is characterized by intensive farming, and urban-industries development. Thus the aquatic environment gathers several elements which affect the quality of the rivers and lakes, mainly at the rain events [2]. The nutrient increase, toxins presence and others xenobiotic input, such as biocid and heavy metals, provoke changes in the normal conditions that according to inflow regime (sewage of various degree of treatment, thermal regime, weather conditions and land use) affects the quality conditions of the receptors [3,4].

In the last decades there have been many studies about the influences of exogenous factors upon crustaceans, being the majority of these researches made as laboratory tests. Such works revealed important basic data, and it can be refered to in case of evaluating the environmental influences upon hepatopancreas. There exists a close correlation with different kind of stresses and the ultrastructure of hepatopancreas [5-17]. Some products and/or household waste, such as industrial discharges, pesticides or sewage are transformed and degraded through various reactions with other biotic and abiotic components, when they get into the river. These elements may alter the hepatopancreatic cells and it could be used as biological markers so as to assess the toxic properties of the environmental contaminants [18-20].

The aim of the present work is to compare the ultrastructure of the hepatopancreatic cells of *M. borellii* and

P. argentinus freshwater prawns at three natural environments with different quality water, in relationship with the biocid use, human activities or land use.

2. MATERIALS AND METHODS

2.1. Sampling Prawns

Juveniles, males and females of *M. borellii* and *P. argentinus* (Crustacea, Decapoda, Palaemonidae) were sampled in the lakes "Don Felipe" (31° 39' S, 60° 41' W), "Alejandra" (31° 45' S, 60°31' W) and "N° 1" (31° 40' S, 60°30' W) (Santa Fe, Argentina) during a time of low and high water phases of the flooding cycle (winter and summer, respectively) (**Figure 1**), and they samples were immediately taken to laboratory.

2.2. Sites of Study

The three lakes are placed in the Paraná River floodplain, and they have different relations with human activities and land use. In this river, the water level declined from summer to winter, with a new flooding pulse in spring. They have an average annual discharge of 18,000 m³/s and a peak of 60,000 m³/s [21]. The flooding water of the lentic bodies in the alluvial valley dilutes the biotic densities of the communities, and during the isolation or low water phase these concentrations recover rapidly. The animal densities show important oscillations among the lakes depending on its volume, distance to the river, amplitude-longitude of flooding pulse and time of water residence [22-24].

"Don Felipe" is an oxbow lake close to the Colastiné River which is a secondary branch directly connected to the main channel (**Figure 1**). This fact changes its volume depending on the input of water flow from the Colastiné River. In the isolated phase, its maximum and mean depth is 2 m and 0.66 m respectively [25]. The main industrialized cities occur about 400 km away from studied site. Most of the wasted material (e.g. from food industries) are rapidly dissolved when it reaches the flood valley.

"Alejandra lake" is an overflow lake with a direct connection to the Coronda River with a total length of 900 m, 1.8 m depth and it has an area of 75,000 m^2 approximately (**Figure 1**). The land use near this lake is low with a scarce impact on the environment. It is a weekend residential area but it is near to Santa Fe and Santo Tome cities.

"N° 1" is an abandoned meander scroll lake (**Figure 1**) with a 0.55 m depth average during the isolated phase (Collins, unpublished) located close to the Salado river (a river with high dissolved contents salt), and its volume changes depending on the input of water flow from the Salado and Santa Fe rivers. During the high water period, the water Salado River is retained by the Paraná system. The Salado River passes through a series of industries and farmlands in which biocides and fertilizers are applied upon them. Moreover industrial discharges and waste-water emitted from the cities (Santa Fe and Santo Tomé) are poured into the last sections of the river.

2.3. Measurement of Water Parameters

The target variables to analyze in each sampling event were taken in the top layer and three meters from the coast line. These were water temperature; conductivity; pH; transparency; nitrate; ammonia; orthophosphate; dissolved oxygen; demand biological of oxygen 5 (DBO5); glyphosate; lead and copper. The samples were collected in polyethylene bottles and preserved at 2-4ºC to posterior analysis in some cases. Temperature, conductivity, pH and dissolved oxygen were taken in situ with digital sensors (Hanna HI9143, HI991003, HI9033). Transparency was measured with Secchi disc. All the analytical methods, conformed to EPA methods [26] or Standard Methods [27], were determined by a spetrophotometer Metrolab330 (nitrate; ammonia; orthophosphate), a spetrophotometer Perkin Elmer (limit 4 ug/L) (heavy metals) and with a high precision liquid cromatography (limit 0.2 ug/L) (biocid). The parameters were sampled weekly in a month during summer and winter.

2.4. Hepatopancreatic Cells Evaluation with TEM

Dissections of the midgut glands were done for three juveniles, males and females of both prawns (*M. borellii* and *P. argentinus*) in intermolt stage according to Drach and Tchernigovtzeff [28] from the three lakes. Adults without gonadal maturation evidence were used. Dissections were conducted under a binocular microscope and placed in 2% cold glutaraldehyde solution at pH 7.4 for 2 hr at 1-4°C. The tissues were then washed in several changes of Sörensen buffer followed by postfixation in 2% osmium tetroxide solution for 2 hr at 1-4°C. After dehydration in graded ethilic alcohol the material was embedded in (ERL) araldite resin. Sections with gold interference colours were obtained using a Reichert-Jung Ultramicrotome with a glass and a diamond knife and then mounted on coated copper slot grids. The hepatopancreas sections in the grids were then double stained in uranyl acetate (saturated solution in 70% methanol, 4 h) followed by lead citrate (5 min) and viewed in a Siemens Electron Microscope 101. The cell types were identified and quantified in each observed section (5 for each specimen).

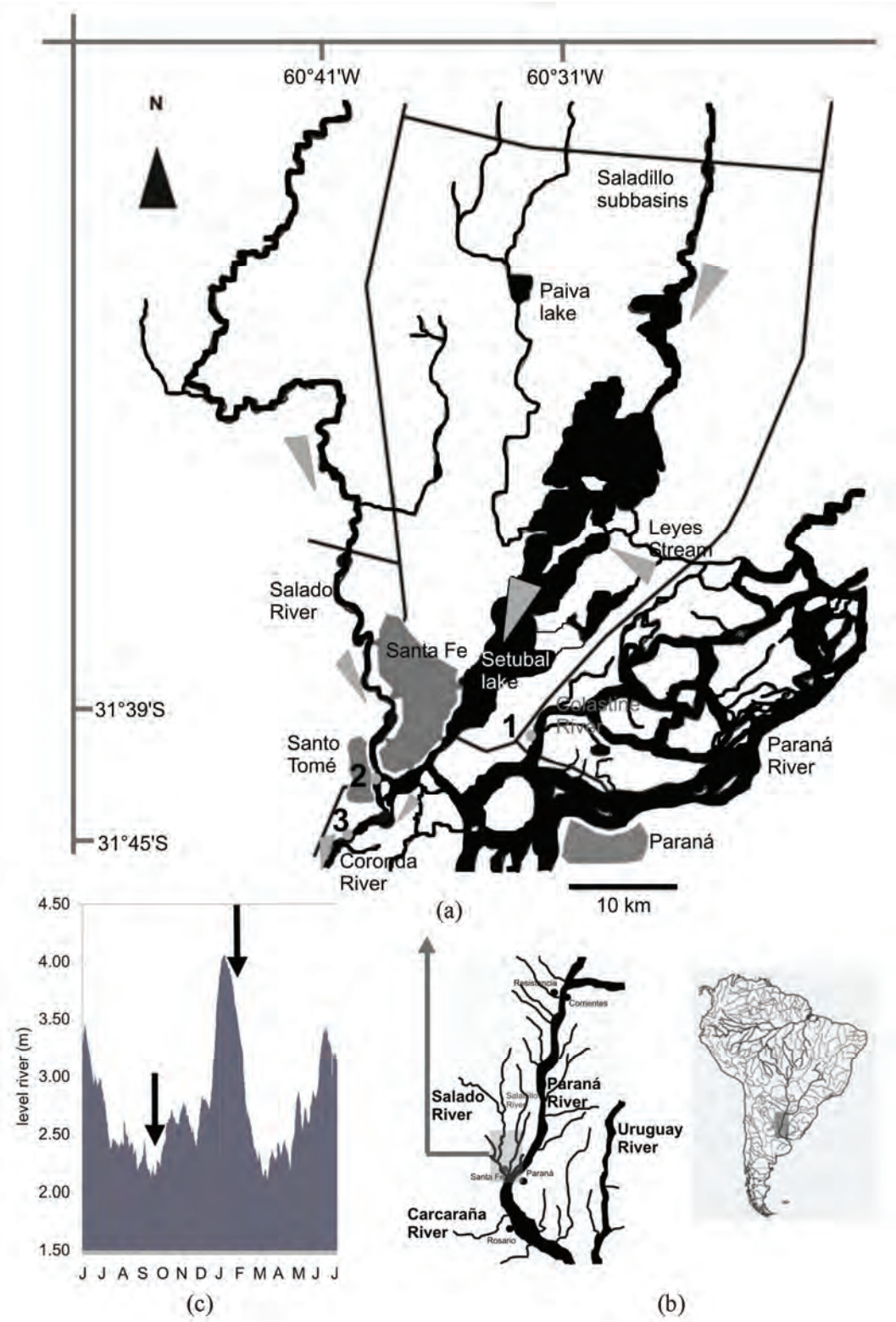

Figure 1. Study sites in the floodplain of Paraná Medio River (Santa Fe, Argentina). A) Main rivers and cities indicating the three sampling environments (1: Don Felipe, 2: N° 1, 3: Alejandra). B) Main rivers in the de la Plata Systems. C) Seasonal variation of water level in the Paraná Rriver (Santa Fe port limnigraph) (arrows indicated the sampling time).

2.5. Laboratory Assays

In order to evaluate on the hepatopancreatic cell of the prawns the effects of cypermethrin, an extensively biocid used in the farms and urban region, was done a laboratory assays. The biocid was used in its commercial form (Sherpa®: cypermethrin). Prawns (*M. borellii* and *P. argentinus*) were kept in plastic containers of 0.9 m^2 and 40 l with a density of 55 ind/m. The nominal sublethal concentrations (cypermethrin (CY): 0.01; 0.001 and 0.0001 µg CY/l) [29] were applied only once. The protocol was: first a continuous flow of water without biocid of 1 ml/s during 15 days in all containers. After that, the solutions with biocid were applied in the same flow rate (1 ml/s) during one day. Later on the flow returned to water without cypermethrin. The control group was treated the similar forms in order to flow rate and experience time. The prawns were daily fed with fish muscle "ad libitum" and the mortality was registered in all containers. The experience lasted 45 days. Each seven day, the prawn hepatopancreas in intermolt phase were dissected, and they were processed by a routine histological method (dehydrated in alcohol series and embedded in paraffin wax). They were cut into thin sections of 6 µm thickness by a rotative microtome. The hystological cuts of these organs were stained with haematoxylin and eosin to observe of the biocide effects in the light microscope (5 cut for each prawns). The hepatopancreatic cells were identificated and quantificated.

2.6. Data Analysis

Water quality parameters of each environment were compared with ANOVA and Tukey post-test. In the same way, differences in hepatopancreatic cell number were evaluated with ANOVA. In the assays, survival and hepatopancreatic cell data from control and experimental groups were analysed with ANOVA in conjunction with Tukey post-test too. All data were previously evaluated to normality and homoscedasticity [30].

3. RESULTS

3.1. Environment Quality

In all the lakes, significant differences (ANOVA $p < 0.05$) were registered for some parameters and sampling time (**Table 1**), being the conductivity in "N° 1" lake (near the Salado River) the highest unlike. Furthermore, these differences were high for both sampling periods, with a decrease values in summer during flooding period (**Table 1**). The pH was not similar among all the sites, but differences between floods and drought phases occur only in the environment near to the Coronda River. Dissolved oxygen did not differ in the three lakes, being the values lower during winter. Nutrients, such as orthophosphorous, were different between Don Felipe and the other lakes, corresponding high values in summer (**Table 1**). Nitrate values got the highest level in the Coronda River (Alejandra lake). The unlike data of winter and summer were not relevant ($p > 0.05$). Ammonia concentration oscillated from 0.006 (Don Felipe summer) to 0.069 (N° 1 winter), showing difference between sampling time. The unlike values among sites was not significantly (**Table 1**). DBO5 was bigger in the environment near the Coronda River, receiving its water from the Salado and Santa Fe Rivers (**Figure 1**). In summer, all lakes have a distinct DBO5 but without statistically significance, except in Don Felipe lake. In low water phase (**Table 1**), glyphosate, residues of glyphosate, and lead were registered in the N° 1 lake near the Santa Fe and Santo Tomé cities.

Table 1. Mean and standard deviations of environmental parameters measured in the three lakes (Don Felipe, N° 1 and Alejandra lakes) and two sampling times.

	Don Felipe lake		N° 1 lake		Alejandra lake	
	winter	summer	winter	summer	winter	summer
Temperature °C	14.8 ± 1.63 ^{b}	23.7 ± 1.11 ^{b}	13.6 ± 1.56 ^{b}	23.8 ± 0.97 ^{b}	14.7 ± 1.12 ^{b}	23.9 ± 1.12 ^{b}
Conductivity µS cm^{-1}	150 ± 30.3 $^{a\,b}$	104 ±19.3 $^{a\,b}$	5580 ± 1337.9 $^{a\,b}$	994 ± 29.8 $^{a\,b}$	261 ± 55.2 $^{a\,b}$	128 ± 17.3 $^{a\,b}$
Transparency cm	27.5 ± 2.38 ^{b}	16.7 ± 3.79 ^{b}	29.5 ± 3.00 ^{b}	16.7 ± 3.79 ^{b}	31.8 ± 7.89 ^{b}	13.0 ± 5.29 ^{b}
pH	6.9 ± 0.29 ^{a}	6.7 ± 0.05 ^{a}	7.7 ± 0.20 ^{a}	7.5 ± 0.14 ^{a}	7.3 ± 0.12 $^{a\,b}$	6.8 ± 0.08 $^{a\,b}$
Dissolved oxygen ml l^{-1}	8.8 ± 1.20 ^{b}	6.4 ± 1.09 ^{b}	9.2 ± 0.60 ^{b}	5.9 ± 2.69 ^{b}	9.6 ± 1.23 ^{b}	7.9 ± 0.29 ^{b}
DBO_5 ml l^{-1}	3.1 ± 1.68 ^{ab}	1.8 ± 0.69 ^{ab}	3.3 ± 2.25 ^{a}	3.7 ± 0.52 ^{a}	4.5 ± 4.96 ^{a}	4.2 ± 0.87 ^{a}
nitrate mg l^{-1}	1.5 ± 0.28	1.8 ± 0.25	1.5 ± 0.61	1.5 ± 0.31	2.3 ± 1.20	2.8 ± 1.31
ammonia mg l^{-1}	0.026 ± 0.018 ^{b}	0.009 ± 0.006 ^{b}	0.037 ± 0.028 ^{b}	0.013 ± 0.015 ^{b}	0.023 ± 0.017 ^{b}	0.012 ± 0.002 ^{b}
orthophosphate mg l^{-1}	1.6 ± 1.06 ^{a}	1.1 ± 0.62 ^{a}	0.7 ± 0.27 $^{a\,b}$	2.1 ± 0.20 $^{a\,b}$	0.6 ± 0.64 $^{a\,b}$	2.6 ± 0.33 $^{a\,b}$
glyphosate* µg l^{-1}	< 0.2	< 0.2	3.2	< 0.2	< 0.2	< 0.2
Pb µg l^{-1}	< 4	< 4	49	< 4	< 4	< 4
Cu µg l^{-1}	< 5	< 5	55	7.2	< 5	< 5

Significant differences according to ANOVA and Tukey post test ($p < 0.05$) a) among environment; b) between sampling times; *glyphosate and their metabolite (AMPA).

3.2. Hepatopancreatic Cells

There have been alterations in the midgut glands of juveniles, males and females of both prawns species from "N° 1" lake of Los Sapos island near Santo Tomé and Santa Fe cities and Alejandra lake. The variability of the damage degree was important. This depended on the prawn origen, and the seasons (low and high water level and temperature). The major alterations for both prawn species were observed in the F- and R-cells, and the percentage of the cell type was differed from those prawns in Don Felipe lake (mainly F-cell) (**Table 2**). Some prawns from Alejandra lake show similar alterations than those from N° 1 lake. The difference was observed in the affected cell number, and/or in the intensity of the alteration. Both prawn species showed similar hepatopancreatic cell frequency in all lakes and seasons (**Table 2**).

In apical zone of the alterated F-cells showed a damaged microvilli border. The endoplasmic reticulum (**Figure 2(f)**) and the mitochondria were more abundant and swelled, and the cristae of the last was damaged and increased in number compared with the mitochondria of those prawns from Don Felipe lake. Endoplasmic reticulum was either broken up into vesicles and/or exhibits dilated profiles (**Figures 2(a)**, **(c)**, **(f)**, **(h)** and **(i)**). The glycoproteins granules and others organelles were increased too, e.g. in the basal region. Amorphous corpuscles with high electron density were found in the cytoplasm (**Figures 2(a)**, **(b)**, **(f)** and **(g)**). In the most affected F-cells (mainly in N° 1 lake) organelles lysis, including cell nucleus were observed without breaking the wall cell (**Figures 2(b)**, **(d)** and **(g)**). The normal F-cells (*M. borellii* and *P. argentinus*) belonging to "Don Felipe" lake showed abundant rER without dilated profiles in the apical zone. The organelles have a homogeneous distribution, e.g. the cytoplasm contains glycoprotein (or free ribosomes), peroxisomas, vesicles and few and small mitochondria. In the basal region, it is more frequently found the presence of Golgy systems with distended cisterns, and surrounded by small and dense vesicles.

The R-cells of prawns from N° 1 and Alejandra lakes were affected in similar ways. The main alterations were: in the apical zone of R-cells, the microvilli border was somewhat shortened and sometimes it lacked the microvillar core filaments (**Figures 3(a)**, **(b)** and **(e)**). The endoplasmic reticulum was disrupted and the number of residual bodies increased. The mitochondria were swelled and sometimes its walls became deteriorated (**Figures 3(b)**, **(e)**, **(f)** and **(g)**). The lipid vacuole had an abrading multilayered membrane (**Figures 3(b)** and **(e)**). Material with high electron density was observed near this vacuole in the apical zone (**Figure 3(a)**). R-cells with premature autolizing appearance were frequent (**Figures 3(d)**, **(f)** and **(g)**). In the basal region, there were few glycoprotein granules, and only the mitochondria was increased and swelled, and its cristae was damaged (**Figures 3(c)**, **(d)** and **(g)**). The normal R-cells of prawns from Don Felipe Lake have in apical zone a large number of mitochondria, vesicles and glycoprotein, which are prolonged in concentrated below the apical plasma membrane. The undamaged microvillous border was regular in all the extensions. In the basal region endoplasmic reticulum (rER and sER), glycoprotein granules and many mitochondria were observed. The B-cells did not show alterations that differ from the normal of hepatopancreatic cell cycles (**Figures 4(a)** and **(b)**) except affections in some B-cells, main in N° 1 lake, where autolising of organelles were registered (**Figures 4(c)** and **(d)**).

Other changes, such as basophyles vacuole groups and differents residuals bodies, were observed in apical zone of the F-cells in both species. Moreover, evident autolising of the organelles (**Figures 5(a)**, **(b)** and **(e)**) and indefinable elements associated with residuals bodies in R-cells with abundant and distended cisterns of endoplasmic reticulum were frequent in the studied species from N° 1 lake (**Figures 5(c)** and **(d)**).

3.3. Low and high water Level and Temperature

The alterations were detected for both seasons and in the same studied sites. The highest number of damaged cell was registered in winter with low water level and tem-

Table 2. Hepatopancreatic cell frequency of two prawns and three lakes (Don Felipe, N° 1 and Alejandra lakes) during two sampling times (winter and summer) (540 total observed sections).

	Don Felipe lake		N° 1 lake		Alejandra lake	
M. borellii	winter	summer	winter	summer	winter	summer
F-cell	29 ± 1.6^{a}	32 ± 1.1^{a}	49 ± 6.6^{ab}	43 ± 5.7^{ab}	38 ± 2.2^{a}	39 ± 6.1^{a}
R-cell	35 ± 3.3^{a}	39 ± 4.3^{a}	25 ± 5.9^{a}	23 ± 6.8^{a}	32 ± 5.2^{a}	37 ± 4.6^{a}
B-cell	36 ± 2.8^{ab}	29 ± 1.9^{ab}	26 ± 3.4^{ab}	34 ± 7.9^{ab}	30 ± 8.9^{ab}	24 ± 2.0^{ab}
P. argentinus						
F-cell	32 ± 6.3^{ab}	25 ± 3.1^{ab}	54 ± 5.6^{ab}	46 ± 4.7^{ab}	36 ± 3.2^{a}	33 ± 1.2^{a}
R-cell	37 ± 5.3^{a}	43 ± 4.3^{a}	23 ± 3.9^{ab}	31 ± 4.8^{ab}	32 ± 5.5^{a}	37 ± 4.6^{a}
B-cell	31 ± 2.3^{a}	32 ± 3.7^{a}	23 ± 3.0^{a}	23 ± 6.3^{a}	32 ± 4.7^{a}	30 ± 1.2^{a}

Significant differences according to ANOVA and Tukey post test ($p < 0.05$). [a] among environment; [b] between sampling times.

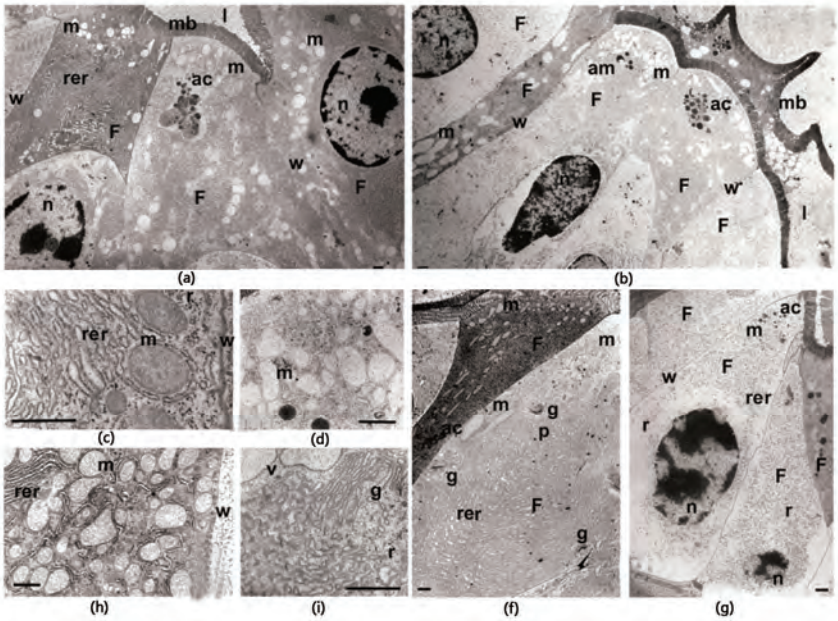

Figure 2. F-cell of *Macrobrachium borellii* and *Palaemonetes argentinus* from Alejandra (a and f respectively) and N°1 lakes (b and g resepctively). Apical cell zone of *M. borellii* in N° 1 lake with lysis appearence of mitchondria, endoplasmic reticulum and glycoprotein granules (d). Basal zone of F-cell in *M. borellii* (c) sampled at Alejandra and *P. argentinus* cell (h and i) from both lakes with vesicles, golgi bodies and glycoprotein granules, endoplasmic reticulum forms cistern and vacuolizing dictyiosomes. Abbreviations: F-cell (F), rough endoplasmic reticulum (rer), golgi bodies (g), high electron density corpuscles (ac), lumen cell (l), microvillous border (mb), mitochondria (m), vesicles (v), ribosomes (r), peroxisomes (p), nucleus (n), wall cell (w). Bars: 0.1 μm approximately.

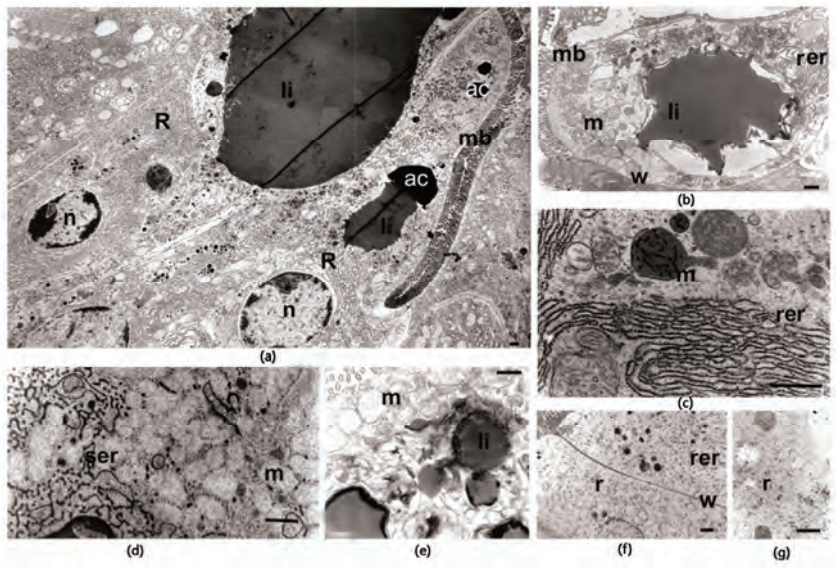

Figure 3. R-cell of *Macrobrachium borellii* and *Palaemonetes argentinus* affected in different levels from Alejandra and N° 1 lakes. Apical zone with microvillous border deteriorated, endoplasmic reticulum and shortened and mitochondria swelled, small vesicles, high electron density corpuscles and lipid vacuole with a multilayered membrane disrupted (a, b, e, f). Basal zone with endoplasmic reticulum vesiculated (rER and sER), glycoprotein granules and mitochondria swelled (in some R-cells were found a disrupted wall mitochondria) or with lysis appearance (c, d). Abbreviations: R-cell (R), rough endoplasmic reticulum (rer), smooth endoplasmic reticulum (ser), high electron density corpuscles (ac), lipid vacuole (li), microvillous border (mb), mitochondria (m), ribosomes (r), nucleus (n), wall cell (w). Bars: 0.1 μm approximately.

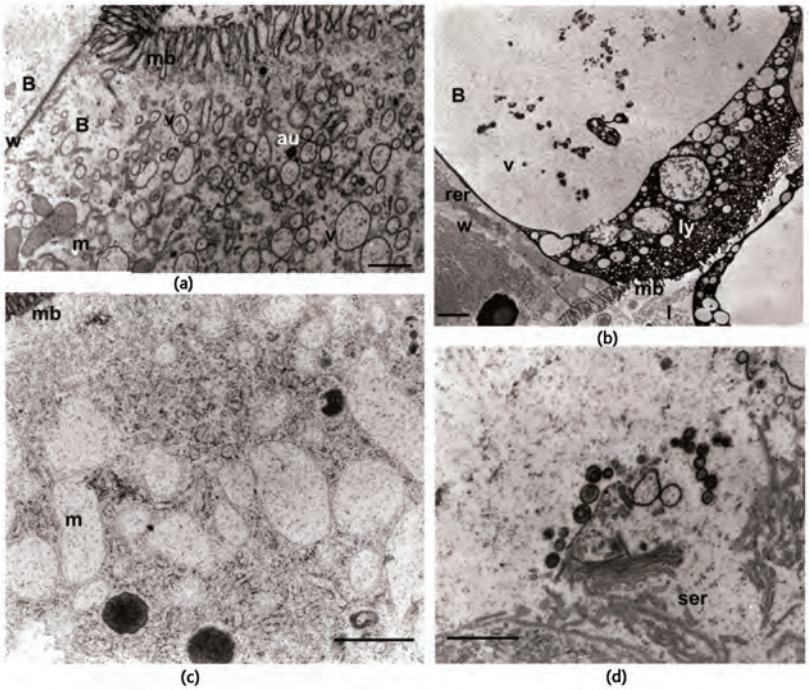

Figure 4. B-cell of *Macrobrachium borellii* and *Palaemonetes argentinus* from Alejandra and N° 1 lakes. Two moment of cell cycle without stress evidence (a, b) but in some cell was observed organelles autolysis in cytoplasm (c, d). Abbreviations: B-cell (B), rough endoplasmic reticulum (rer), smooth endoplasmic reticulum (ser), autosomes (au), lumen cell (l), microvillous border (mb), mitochondria (m), vesicles (v), lisosomes (ly), wall cell (w). Bars: 0.1 μm approximately.

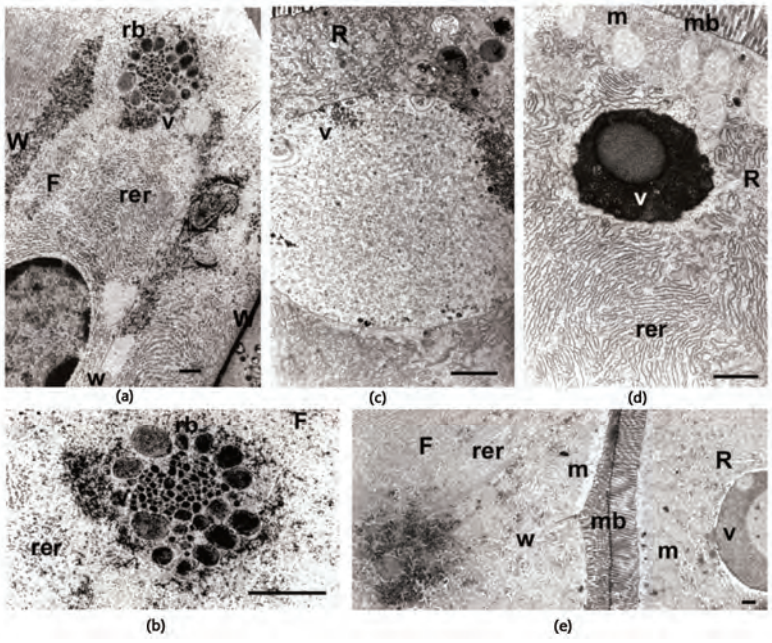

Figure 5. Others hepatopancreatic cell evidence of stress in *Macrobrachium borellii* and *Palaemonetes argentinus* from Alejandra and N° 1 lakes. Apical zone of F-cells with undefinible residual bodies and organelles autolysis. (a, b, e) In R-cells with differents vesicles without lipid content and swelled endoplasmc reticulum (c, d, e). Abbreviations: F-cell (F), R-cell (R), rough endoplasmic reticulum (rer), residual bodies (rb), microvillous border (mb), mitochondria (m), vesicles (v), wall cell (w). Bars: 0.1 μm approximately.

perature (**Table 2**). The percentage of affected prawns was not different (ANOVA $p > 0.005$) between the species M. borellii and P. argentinus. The "N° 1" lake had the highest percentage of alterated cells in prawns with 75%, 32% in Alejandra lake and only 9% in Don Felipe lake approximately. In this last one, the alterations coincided with the observations indicated as starvation effects (lipid dropplets with multilayered wall in R-cells). Moreover, the cell type frequency varied with the prawn origen (Don Felipe, N° 1 and Alejandra lakes), being the frequency of F-cells higher in prawns from N° 1 lake during samples of winter than other origin (**Table 2**).

In summer the number of affected cells disminished in all the lakes (45 % in "N° 1" lake, 26% in Alejandra lake and only 2% in Don Felipe lake approximately), and the cell type frequency was similar (**Table 2**).

3.4. Laboratory Assays

In both prawns, damaged hepatopancreatic cells by the pyretroid have had a relationship with the tested concentrations, being the cell frequency in each tested concentrations differents with the control at the end of the experience (ANOVA $F(0.05, 2, 22) = 11.31$; $p < 0.0021$). The F-cells were more abundant than all the others (**Figure 6**). The difference among C2, C3 and control, in the F-cell percentage, occurred during the second week whereas in the C1 it was in the third week (**Figure 6**). In the experience, the F-cell presence oscillated with changes significant among treated groups (Tukey's $p > 0.05$). The B-cell percentage in all cypermethrin concentrations were low, 12% (C1) and 19% (C3).

Prawn survivals in treated groups varied significantly during the 35 days of assays (ANOVA $F(0.05, 2, 22) = 350.64$; $p < 0.0001$, Tukey`s $p < 0.05$), and in the control group there had low mortality (**Figure 6**)

4. DISCUSSION

The hepatopancreas of both freshwater prawns (*M. borellii* and *P. argentinus*), which consists of four cell types, undergoes ultrastructural changes depending on the quality of the environment. This fact was observed in the F-, R- and B-cells in different intensities. In these cells, microvilli border, endoplasmic reticulum and mitochondria were the most affected ultrastructure together with and the increase of residual bodies number. Moreover premature autolysis development was observed.

On the one hand, three measured parameters have differed, being the conductivity the most variable. Transparency reflected a great density of algae in the "N° 1" lake before flooding period (November-April), which could be due to a nutrient rise. Also, this coincides with high DBO5 values. In the studied environments, different algae species can produce phytotoxins, exposing the prawns to this toxic stress. This situation could probably activate the antioxidant defences in the hepatopancreas leading to multiple oxidative processes and an effective detoxification [31]. The cytoskeleton could be destroyed by an increase in protein phosphorylation level, occurring cell necrosis [32]. The immune system responds with a melanization process which could act as a possible ROS scavenger [33]. Besides, the B-cell showed an intracell digestion what carried out, possibly, with posterior organelles degeneration in all cells, such as it was suggested in exposed crabs to microcystins [34]. Moreover the large vacuole of B-cells contains digestive enzimes, e.g. cathepsin L (MeCatL) [35]. It was recognized that in transicional cells F/B occurs P-glycoprotein (P-gp), suggesting a function in specialized cells for accumulation and elimination of toxic compounds [36].

On the other, many substances may be toxic taking into account their nature and amount, which are being released by industries and cities to fresh waters and/or the washing of farmlands during rains [37]. In these waste waters, the heavy metals could be important quantitatively, and these are toxic elements for decapods [38, 39]. Moreover, these xenobiotic elements were present in sites near to the cities, in other studies, several heavy

Table 3. Heavy metals measurements in sediment of several sites of Salado river close to the more affected sampling area (from a work [40]).

Loc.	Cu	Zn	Pb	Cd	Cr	Fe	Mn
1	19.54	21.29	19.47	n.d	55.18	107.1	793.05
2	0.78	0.05	1.9	n.d.	1.23	190.18	17.09
17	1.03	0.21	1.03	nd	0.64	nd	1.77
16	21.06	25.29	13.96	nd	9.71	560.92	182.26

values in µg/g; Localities: (1) Salado river in Motorway bridge (2 km up the river of "N° 1" lake approximately), (2) Salado river in Santo Tomé-Santa Fe bridge (200 m down the river of "N° 1" lake approximately), (17) Salado river in Recreo city (10 km up the river of "N° 1" lake, approximately), (16) Las Prusianas river in Grutly (50 km up the river of "N° 1" lake, approximately).

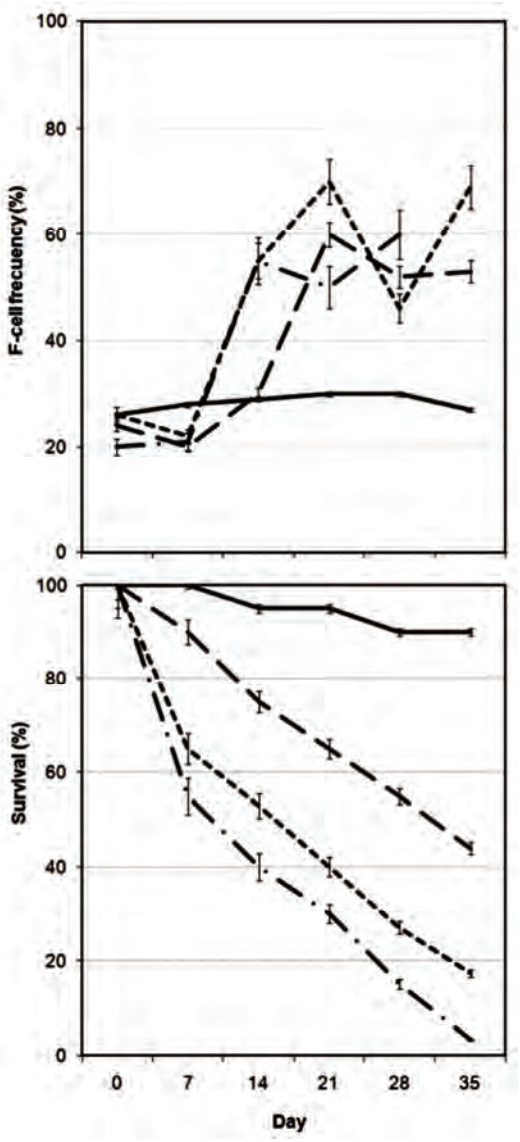

Figure 6. F-cell frequency and survival percentage of freshwater prawns (*Macrobrachium borellii* and *Palaemonetes argentinus*) in the 35 days laboratory assays with several cypermethryn concentrations. Solid line: control groups; dash and point line: 0.01 µg CY/l groups; point line: 0.001 µg CY/l groups; dashed line: 0.0001 µg CY/l groups).

metals were registered at different points of the Salado River sediments (**Table 3**), being a possible cause of potential stress effects. Another parameter that might provoke alterations in the prawns hepatopancreas is temperature but this do not suggest any alteration, due to the fact that lipid consumption for thermal stress occurs at 29°C in *M. borellii* [41], and the samplings were taken during spring (September-December) with lower temperatures.

Some of the observed changes in the hepatopancreatic cells were correlated with the starvation process and xenobiotics effects which were described for other decapods [5,6,8,9,18,42,43]. The affected prawns from N° 1 lake and the assay had similar evidence of stress in the hepatopancreas. The pyretroid is an biocid that it is used in non-urban and urban environments, and it could potentially get into the aquatic systems by different ways (e.g. perfution, rain drenage). This could induce to ROS production and to the formation of oxidative tissues in the hepatopancreas of prawns, while their cells have different biochemicals mechanisms to protect themselves from oxidative damage among which the glutathione plays an important role [44]. Different intrinsic factors such as specific capacity to stress tolerance, size, nutritional condition and extrinsic factors (e.g. temperature, conductivity, ph) are important to evaluate the populational effects in a natural environment. The high percentage of F-cells of exposed prawns to cypermethrin could indicate that some detoxification mechanisms is activated, including a more activity of the endoplasmic reticulum and ribosomes in this cell type than in others. The low number of B-cell could be interpreted as an increase of the exoxitation of the B-cells to hepatopancreas lumen. Moreover another efluents, e.g. oil product (PAH), provoked a size disminish in the hepatopancreas cells [43]. Furthermore, cell number varies significantly during the molt cycle (mainly, R-cell and F-cell) linked with a change in the enzimatic activity (ATPasas and Na /K ATPasas) [45], considering only the prawns in intermolt phase (c) by even.

The variation in the ultrastructure could have affected the absorption mechanisms and protein synthesis as observed by Papathanassiou and King [42]. However we could say that these prawns can tolerate some degree of environmental stress due to the fact that populations of these species were found in “Laguna N° 1” lake with similar sizes [46] to those taken from environment with low human interference (Don Felipe lake) [25]. Thus we can infer that there must be some detoxification mechanisms such as those described by several authors [18,38, 47-51], where the F-cells could have a main rol. In these works it was also included the capture of transuranic elements, the deactivation of insecticides by rER or removal of metals by granule formulation and its excretion as detoxification pathways. These routes, together with that of the complete renewal of the epithelium occurring after several mitotic pulses [52] and/or some other mechanisms which involve a increase mitochondrial activity, could have allowed the presence of *M. borellii* and *P. argentinus* in this environment.

However, the detoxification is only feasible when the intensities of stressors do not exceed a particular thresh-

old value, otherwise it produces cellular damage [13] and then the point-of-no return could be reached, such as it was observed in starved individuals of Penaeus monodon [9], and in this study according to the evidence in the cypermethrin assay.

5. CONCLUSIONS

The damage cell is irreversible to live of this prawn when the values achieved determined concentrations or stress level. The F-cell was increased with the intensities of the stressors such as mechanisms of detoxification. This involves a growth in numbers and size of rER, ribosomes, and mitochondria. Therefore, the reserves in the vacuole of R-cell are used to contribute to consume energy in the detoxification pathway. This justified the starvation conditions that is observed in some prawns.

The midgut glands of *M. borellii* and *P. argentinus* reacts to water quality variations, and the structural changes in cells and tissues represent the most sensitive level. It is showed the synergistic impact of an element, its metabolites and other exogenous and endogenous factors showing the hepatopancreas as a good tool in the determination of a stress areas of the natural environment.

6. ACKNOWLEDGEMENTS

The study was supported by a grant CONICET PIP 6275 (2006-2007).

REFERENCES

[1] Collins, P., Williner, V. and Giri, F. (2006) Trophic relationships in Crustacea Decapoda of a river with floodplain. In: Elewa, A.M.T., Ed., *Predation in Organisms*: *A Distinct Phenomenon*, Springer Verlag, Heidelberg, 59-86.

[2] Gardi, C. (2001) Land use, agronomic management and water quality in a small Northern Italian watershed. *Agriculture Ecosystems & Environment*, **87(3)**, 1-12.

[3] Turner, R.E., Dortch, Q., Justic, D. and Swenson, E. (2002) Nitrogen loading into an urban estuary: Lake Pontchartrain (Louisiana, U.S.A.). *Hydrobiologia*, **487(1)**, 137-152.

[4] Friedler, E., Juanico, M. and Shelef, G. (2003) Simulation model of wastewater stabilization reservoirs. *Ecological Engineering*, **20(2)**, 121-145.

[5] Storch, V., Janssen, H.H. and Cases, E. (1982) The effects of starvation on the hepatopancreas of the coconut crab, Birgus latro (L.) (Crustacea, Decapoda). *Zoologischer Anzeiger*, **208(3-4)**, 115-123.

[6] Storch, V. and Anger, K. (1983) Influence of starvation and feeding on the hepatopancreas of larval Hyas araneus (Decapoda, Majidae). *Helgoländer Meeresun*, **36(1)**, 67-75.

[7] Storch, V. and Burkhardt, P. (1984) Influence of nutritional stress on the hepatopancreas of Talitrus saltator (Peracarida, Amphipoda). *Helgoländer Meeresun*, **38(1)**, 65-73.

[8] Anger, K., Storch, V., Anger, V. and Capuzzo, J.M. (1985) Effects of starvation on moult cycle and hepatopancreas of stage I lobster (Homarus americanus) larvae. *Helgoländer Meeresun*, **39(2)**, 107-116.

[9] Vogt, G., Storch, V., Quinitio, E. and Pascual, F. (1985) Midgut gland as monitor organ for the nutritional value of diets in Penaeus monodon (Decapoda). *Aquaculture*, **48(1)**, 1-12.

[10] Hryniewiecka-Szyfter, Z. and Storch, V. (1986) The influence of starvation and different diets on the hindgut of Isopoda (Mesidotea entomon, Oniscus asellus, Porcellio scaber). *Protoplasma*, **134(1)**, 53-59.

[11] Vogt, G., Quinitio, E. and Pascual, F. (1986) Leucaena leucocephala leaves in formulated feed for Penaeus monodon: A concrete example of the application of histology in nutrition research. *Aquaculture*, **59(3-4)**, 209-234.

[12] Elendt, B.P. and Storch, V. (1990) Starvation-induced alterations of the ultrastructure of the midgut of Daphnia magna Straus, 1820 (Cladocera). *Journal of Crustacean Biology*, **10(1)**, 79-86.

[13] Triebskorn, R., Köhler, H.R., Zahn, T., Vogt, G., Ludwig, M., Rumpf, S., Kratzmann, M., Alberti, G. and Storch, V. (1991) Invertebrate cells as targets for hazardous substances. *Zeitschfirt fuer Angewandte Zoologie*, **78(3)**, 277-287.

[14] Vogt, G. (1992) Transformation of anterior midgut and hepatopancreas cells by Monodon Baculovirus (MBV) in Penaeus monodon postlarvae. *Aquaculture*, **107(2-3)**, 239-248.

[15] Vogt, G. (1996) Cytopathology of Bay of Piran Shrimp Virus (BPSV), a new Crustacean virus from Mediterranean Sea. *Journal of Invertebrate Pathology*, **68(3)**, 239-245.

[16] Vogt, G. (1997) Hepatopancreatic brush border lysis (HBL)-a new bacterial disease of the shrimp Palaemon elegans. *Diseases of Aquatic Organisms*, **29(2)**, 151-155.

[17] Bhavan, P. S. and Geraldine, P. (2000) Histopathology of the hepatopancreas and gills of the prawn Macrobrachium malcolmsonii exposure to endosulfan. *Aquatic Toxicology*, **50(4)**, 331-339.

[18] Vogt, G. (1987) Monitoring of environmental pollutants such as pesticides in prawn aquaculture by histological diagnosis. *Aquaculture*, **67(1)**, 157-164.

[19] Vogt, G. (1988) Anwendung der experimentellen Histologie zur Diagnostik in der Krebsaquakultur. In: Rosenthal, H., Saint-Paul, U. and Hilge, V., Eds., *Perspektiven der Deutschen Aquakultur*, Biologisches Anstalt Helgoland, Hamburg, 159-165.

[20] Shugart, L.R., Bickham, J., Jackim, G., McMahon, G., Ridley, W., Stein, J. and Sterinert, S. (1992) DNA alterations. In: Huggett, R.J., Kimerle, P.M., Mehrle, R.A. and Bergman, H.L., Eds., *Biomarkers: Biochemical, Physiological and Histological Markers of Anthropogenic Stress*,

Lewis Publishers, Chelsea, 125-153.
[21] Bonetto, A.A. and Wais, I.R. (1995) Southern South American streams and rivers. In: Cushing, C.E., Cummins, K.W. and Minshall, G.W., Eds., *Ecosystems of the World* 22 *River and Stream Ecosystems*, Elsevier, Amsterdam, 257-293.
[22] Garcia de Emiliani, M.O. (1980) Fitoplancton de una laguna del valle aluvial del Paraná medio ("Los Matadores", Santa Fe, Argentina). I. Estructura y distribución en relación a factores ambientales. *Ecología*, **4(1)**, 127-140.
[23] Paggi, J.C. and Jose de Paggi, S. (1990) Zooplankton of the lotic and lentic environments of the Middle Paraná River. *Acta Limnologica Brasiliensis*, **3**, 685-719.
[24] Devercelli, M. (2006) A morphological and functional approach to the phytoplankton of the Middle Paraná River during an anomalous hydrological period. *Hydrobiologia*, **563(1)**, 465-478.
[25] Collins, P. and Paggi, J.C. (1998) Feeding ecology of Macrobrachium borellii (Nobili) (Decapoda: Palaemonidae) in flood valley of the River Paraná, Argentina. *Hydrobiologia*, **362(1-3)**, 21-30.
[26] US EPA (1983) Chemical methods for the examination of water and wastes. EPA-600/4-79-020, United States Environmental Protection Agency, Environmental Monitoring and Support Laboratory, Cincinnati.
[27] APHA. (1998) Standard methods for the examination of water and wastewater. American Public Health Association, Philadelphia.
[28] Drach, P. and Tchernigovtzeff, C. (1967) Sur la methode de determination des stades d'intermue et son application general aux Crustaces. *Vie et Milieu. Serie A. Biologie Marine*, **18(A)**, 595-610.
[29] Collins, P. and Cappello, S. (2006) Cypermethrin toxicity to aquatic life: Bioassays for the freshwater prawn Palaemonetes argentinus. *Archives of Environmental Contamination and Toxicology*, **51(1)**, 79-85.
[30] Zar, J.H. (1996) Biostatistical analysis. 3rd Edition, Prentice Hall, New Jersey.
[31] Kankaanpä, H.T., Holliday, J., Schoreder, H., Goddard, T.J., Fister, R. and Carmichael, W.W. (2005) Cyanobacteria and prawn farming in northern New South Wales, Australia–a case study on cyanobacteria diversity and hepatotoxin bioaccumulation. *Toxicology and Applied Pharmacology*, **203(3)**, 243-256
[32] Dawson, R.M. (1998) The toxicology of microcystins. *Toxicon*, **36(7)**, 953-962.
[33] Nappi, A.J. and Vass, E. (1993) Melanogenesis and the generation of cytotoxic molecules during insect cellular immune-reactions. *Pigment Cell Research*, **6(3)**, 117-126.
[34] Pinho, G.L., Moura da Rosa, C., Yunes, J.S., Luquet, C.M., Bianchini, A. and Monserrat, J.M. (2003) Toxic effects of microsystins in the hepatopancreas of the estuarine crab Chasmagnathus granulatus (Decapoda, Grapsidae). *Comparative Biochemistry and Physiology Part C*, **135(4)**, 459-468.
[35] Hu, K.-J. and Leung, P.-C. (2004) Shrimp cathepsin L encoded by an introless gene has predominant expression in hepatopancreas, and occurs in the nucleus of oocyte. *Comparative Biochemistry and Physiology Part B*, **137(1)**, 21-33.
[36] Kölher, A., Lauritzen, B., Jansen, D., Bottcher, P., Teguliwa, L. and Krune, G. (1998) Detection of P-glycoprotein mediated MDR/MXR in Carcinus maenas hepatopancreas by immuno-gold-silver labeling. *Marine Environmental Research*, **46(1-5)**, 411-414.
[37] Montagna, M. and Collins, P.A. (2007) Survival and growth of Palaemonetes argentinus (Decapoda; Caridea) exposed to insecticides with chlorpyrifos and endosulfan as active element. *Archives of Environmental Contamination and Toxicology*, **53(3)**, 371-378.
[38] Vogt, G. and Quinitio, E.T. (1994) Accumulation and excretion of metal granules in the prawn, Penaeus monodon, exposed to water-borne copper, lead, iron and calcium. *Aquatic Toxicology*, **28(3-4)**, 223-241.
[39] Hook, S.E. and Lee, R.F. (2004) Genotoxicant induced DNA damage and repair in early and late developmental stages of the grass shrimp Paleomonetes pugio embryo as measured by the comet assay. *Aquatic Toxicology*, **66(1)**, 1-14.
[40] INALI, (1997) Conservación manejo de ecosistemas acuáticos continentales. Contaminación y acuicultura (PID-BID 0230), 1994-1997, Conicet, Santo Tomé.
[41] Pollero, R.J., Baró, G., delR, M. and Irazú, C.E. (1991) Lipid classes consumption related to fasting and thermal stress in the shrimp Macrobrachium borellii. *Comparative Biochemistry and Physiology*, **99B**, 243-249.
[42] Papathanassiou, E. and King, P.E. (1984) Effects of starvation on the fine structure of the hepatopancreas in the common prawn Palaemon serratus (Pennant). *Comparative Biochemistry and Physiology*, **77A**, 243-249.
[43] Yamuna, A., Kabila, V. and Geraldine, P. (1996) Biochemical and histological alterations in the prawn Macrobrachium lamerrei following exposure to automobile discharge. *GeoJournal*, **40(1-5)**, 233-237.
[44] Cairrao, E., Couderchet, M., Soares, A.M. and Guilhermino, L. (2004) Glutathione-S-transferase activity of Fucus spp. as a biomarker of environmental contamination. *Aquatic Toxicology*, **70(4)**, 277-286.
[45] Zilli, L., Schiavone, R., Scordella, G., Zonno, V., Verri, T., Storelli, C. and Vilella, S. (2003) Changes in cell type composition and enzymatic activities in the hepatopancreas of Marsupenaeus japonicus during the moulting cycle. *Journal of Comparative Physiology B*, **173(4)**, 355-363.
[46] Collins, P. (1997) Ritmo diario de alimentación en el camarón Macrobrachium borellii (Decapoda, Palaemonidae). *Iheringia Série Zoologia*, **82(1)**, 19-24.
[47] Guary, J.C. and Négrel, R. (1981) Calcium phosphate granules: A trap for transuranic and iron in crab hepatopancreas. *Comparative Biochemistry and Physiology*, **68A**, 423-427.
[48] Lyon, R. and Sinkiss, K. (1984) The ultrastructure and metal containing inclusions of mature cell types in the hepatopancreas of a crayfish. *Tissue Cell*, **16(5)**, 805-817.
[49] Nott, J.A. (1991) Cytology of pollutant metals in marine invertebrate: A review of microanalytical applications. *Scanning Microscopy*, **5(1)**, 133-142.
[50] Roldan, B.M. and Shivers, R.R. (1987) The uptake and storage of iron and lead in cells of the crayfish (Orconectes propinguus) hepatopancreas and antennal gland. *Comparative Biochemistry and Physiology*, **86C**, 201-214.
[51] Vogt, G. (1990) Pathology of midgut gland-cells of Pe-

naeus monodon postlarvae after Leucaena leucoce-phala feeding. *Disease of Aquatic Organisms*, **9(1)**, 45-61.

[52] Hopkin, S.P. and Nott, J.A. (1980) Studies on the digestive cycle of the shore crab Carcinus maenas (L.) with special reference to the B-cells in the hepatopancreas. *Journal of the Marine Biological Association of the United Kingdom*, **60(1)**, 891-907.

Vol.2, No.7, 760-763 (2010)
doi:10.4236/ns.2010.27095

Natural Science

Multidimensional electrostatic energy and classical renormalization

Sami M. AL-Jaber

College of Applied Sciences, Palestine Technical University-Kadoorie, Tulkarm, Palestine; Permanent Address: Department of Physics, An-Najah National University, Nablus, Palestine; jaber@najah.edu

Received 8 April 2010; revised 20 May 2010; accepted 26 May 2010.

ABSTRACT

Recent interest in problems in higher space dimensions is becoming increasingly important and attracted the attention of many investigators in variety of fields in physics. In this paper, the electrostatic energy of two geometries (a charged spherical shell and a non-conducting sphere) is calculated in higher space dimension, *N*. It is shown that as the space dimension increases, up to *N* = 9, the electrostatic energy of the two geometries decreases and beyond *N* = 9 it increases. Furthermore, we discuss a simple example which illustrates classical renormalization in electrostatics in higher dimensions.

Keywords: Electrostatic Energy; Higher Dimensions; Renormalization

1. INTRODUCTION

The space dimension N plays an important role in studying many physical problems. It has been used for the radial wave functions of the hydrogen like atoms in N dimensions [1,2]. Exactly solvable models have also been investigated [3,4]. In addition, a great deal of recent work in field theory [5], high energy physics [6], and in cosmology [7] has been conducted. Furthermore, problems of mathematical interest have been investigated in higher dimensions [8,9]. One of the fundamental quantities in physics is the electrostatic energy which is currently investigated by many workers in various areas [10-12]. Therefore, the present author is motivated to consider the effect of space dimension on the electrostatic energy of two simple, but illustrative, systems. A connected technique to electrostatic energy is the renormalization in classical field theory. Renormalization is needed to eliminate divergences which appear in the computation of Feyman graphs so that sensible physical results can be achieved [13-15]. Just recently, Corbò [16] considered renormalization technique in classical fields and Tort [17] discussed renormalization of electrostatic energy. So in the present paper, we will consider an example of classical renormalization of electrostatic energy in higher space dimensions. The organization of the present paper is as follows: In Section 2, we consider electrostatic energy in a hyper spherical shell. In Section 3, we calculate the electrostatic energy of a non conducting hyper sphere. In Section 4, we present an example of renormalization of electrostatic energy in higher space dimensions. Section 5 is devoted for conclusions.

2. ELECTROSTATIC ENERGY OF A HYPER SPHERICAL SHELL

We consider a charged hyper spherical shell of radius R and charge Q in N-dimensional space. Our purpose is to calculate the electrostatic energy of the shell by two methods. In the first method, we calculate the work done to bring the charge Q infinitesimally from infinity to the surface of the shell, while in the second method, we evaluate the volume integral over the squared of the electric filed, $\vec{E}$. The two methods require the electric field and the electric potential in space. Gauss's Law in N-dimensions is

$$\oint \vec{E}\cdot d\vec{A} = \oint E\, r^{N-1} d\Omega = \frac{q_{enc}}{\varepsilon_0} \tag{1}$$

The angular surface integral gives [18],

$$\oint d\Omega = \frac{2\pi^{N/2}}{\Gamma(N/2)}, \tag{2}$$

where $\Gamma(x)$ is the Gamma function. Since the charge is distributed on the surface, the above two equations yield

$$E = \frac{Q\,\Gamma(N/2)}{2\varepsilon_0 \pi^{N/2} r^{N-1}}, \quad r > R \tag{3}$$

and $E = 0$ for $r < R$. The electric potential is given by

$$V = -\int_{\infty}^{r} \vec{E} \cdot d\vec{r} = \frac{Q\,\Gamma(N/2)}{2\varepsilon_0 (N-2)\pi^{N/2} r^{N-2}}\,, \quad r \geq R \tag{4}$$

The first method yields the electrostatic energy, W as

$$W = \frac{1}{2}\int \sigma\, V\, dA = \frac{Q^2\Gamma(N/2)}{4\varepsilon_0 \pi^{N/2}(N-2)}\frac{1}{R^{N-2}}\,, \tag{5}$$

Which can be written as

$$W = \frac{Q^2}{2\varepsilon_0 S(N-2)R^{N-2}}, \tag{6}$$

where σ is the surface charge density and S is the surface area of a unit shell as given in **Eq.2**. The second method enables us to write

$$W = \frac{1}{2}\varepsilon_0 \int E^2 d\tau = \frac{1}{2\varepsilon_0}\left(\frac{\Gamma(N/2)}{2\pi^{N/2}}\right)^2 \int_R^{\infty} \frac{Q^2}{r^{2N-2}} r^{N-1} dr d\Omega$$

$$= \frac{Q^2\Gamma(N/2)}{4\varepsilon_0 \pi^{N/2}(N-2)}\frac{1}{R^{N-2}}\,, \tag{7}$$

Which is the same result given in **Eq.5**. It is interesting to note that our result yields the well-known result [19] for the three-dimensional case (N = 3), namely $W = \frac{Q^2}{8\pi\varepsilon_0 R}$. It is noticed that the electrostatic energy of the hyper shell depends on the space dimension N. It is illustrative to calculate the electrostatic energy (W_{shell}), with R = 1, for different values of N. This is calculated in units of $Q^2/8\pi\varepsilon_0$ and is shown in the second column of **Table 1**. Our calculated results clearly show that the electrostatic energy has a minimum at the space dimension N = 9. This can be explained as follows: In higher space dimensions, there are more orientations in space and thus more angles (N-1). This implies that it is relatively easy to assemble electric charges on the hyper surface of the shell which explains the decrease in the electrostatic energy as the space dimension increases up to N = 9. However, beyond this value of N, the surface area of the shell becomes smaller and smaller so that the decrease in the surface area, as N increases, dominates over the increase in the angular orientation. In mathematical terms, the surface area times (N-2) has a maximum at N = 9 and thus the electrostatic energy has a minimum at that value of N. It is tempting to investigate the behavior of the electrostatic energy for very large N. This can be checked by using Stirling's formula [20]

$$\Gamma(1+n) = n! \approx n^n \sqrt{2\pi n}\, e^{-n}, \tag{8}$$

and letting $n \to (N-2)/2$, one finds for very large N

$$W_{shell} \approx \frac{Q^2}{4\varepsilon_0}\left(\frac{1}{2\pi e}\right)^{(N-2)/2} (N-2)^{(N-3)/2}. \tag{9}$$

In the infinite dimensional space, the above equation gives an infinite electrostatic energy in the limit as $N \to \infty$. In this limiting case the surface area of the shell vanishes as can be seen from **Eq.2** and the use of Stirling's formula. Therefore, the shell behaves like a point charge in the infinite dimensional space and thus one expects the divergence of the electrostatic energy as an infinite self energy of a point particle.

3. ELECTROSTATIC ENERGY OF A CHARGED NON-CONDUCTING HPER SPHERE

Our main purpose here is to calculate the electrostatic energy of a uniformly charged non-conduction sphere in N-dimensional space. Following the second method of Section 2, we calculate the electric field inside and outside the sphere. The application of Gauss's Law given in **Eq.1** gives

$$\vec{E} = \frac{Q\Gamma(N/2)}{2\varepsilon_0 \pi^{N/2}} \begin{cases} \dfrac{1}{r^{N-1}}\hat{r} & r \geq R \\ \dfrac{r}{R^N}\hat{r} & r \leq R\,, \end{cases} \tag{10}$$

where Q is the charge in the sphere. The electrostatic energy of the hyper sphere is thus

$$W_{sphere} = \frac{1}{2}\varepsilon_0 \int E^2 d\tau$$

$$= \frac{1}{2}\varepsilon_0 \left(\frac{Q\Gamma(N/2)}{2\varepsilon_0 \pi^{N/2}}\right)^2 \left[\int_R^{\infty} \frac{r^{N-1}}{r^{2N-2}} dr + \int_0^R \frac{r^{N+1}}{R^{2N}} dr\right] \int d\Omega\,.$$

The integrals in the curly bracket yield $\frac{2N}{(N^2-4)}\frac{1}{R^{N-2}}$ and the integral over Ω is given by **Eq.2**, Therefore, the electrostatic energy is simplified to

$$W_{sphere} = \frac{N\,Q^2\,\Gamma(N/2)}{2\varepsilon_0 \pi^{N/2} R^{N-2}(N^2-4)}, \tag{11}$$

which can be written as

$$W_{sphere} = \frac{Q^2}{\varepsilon_0 V(N^2-4)R^{N-2}}, \tag{12}$$

where $V(=2\pi^{N/2}/N\Gamma(N/2))$ is the volume of the unit sphere in the N-dimensional space [18]. Clearly, the above electrostatic energy depends on the space dimension N, and it yields the well-known result [19] for N = 3, namely

$$W_{sphere}(N=3) = \frac{1}{4\pi\varepsilon_0}\frac{3Q^2}{5R}.$$

It is again constructive to calculate the electrostatic energy, in units of $Q^2/4\pi\varepsilon_0$, with R = 1 for different values of N. This is shown in the last column of **Table 1**. As before, the electrostatic energy has a minimum at the

space dimension N = 9. But here, the volume of the hyper sphere time (N^2–4) has a maximum at N = 9 and hence the electrostatic energy has a minimum at that value. As it was checked in the previous section, the electrostatic energy becomes infinite in the infinite dimensional space ($N \to \infty$). In this limiting case the volume of the hyper sphere vanishes and thus the sphere behaves as a point charge with an infinite self energy.

4. RENORMALIZATION OF ELECTROSTATIC ENERGY

Renormalization, as is widely believed, is required in quantum field theory [21-23]. The main task of renormalization is to handle and eliminate the divergences so that one can obtain sensible physical results. Recently, it has been reported that renormalization can be applied to classical fields: For example, Corbò [16] gave two examples for renormalization of electrostatic potential and Tort [17] presented an example for renormalization of electrostatic energy. Our purpose here is to generalize Tort's example to higher space dimension *N*. Beside its mathematical interest, we will show that the divergence (or so-called singularity) of the electrostatic energy persists in the infinite dimensional space. Following Tort's model for the classical atom, we consider a point electric charge of magnitude *Ze*, where *Z* is the atomic number and *e* is the electron charge, surrounded by a concentric thin hyper-spherical shell of radius R and electric charge equal to −*Ze*. Ionization (partial or total) of this atom amounts to the removal of part of or the entire negative charge from the shell. This can be achieved by letting $-Ze \to -Ze(1-\lambda)$, where $\lambda \in [0,1]$. We will show below that the renormalization of the electrostatic energy (ΔU) in N dimensions is given by

$$\Delta U = U_{final} - U_{initial} = \frac{(\lambda Ze)^2 \Gamma(N/2)}{4\varepsilon_0 \pi^{N/2}(N-2)R^{N-2}} \tag{13}$$

The electric field inside the shell is only due to the point charge, since there is no contribution comes from the shell. Thus, the application of Gauss's Law, given in **Eq.1**, yields

$$\vec{E} = \frac{Ze\Gamma(N/2)}{2\varepsilon_0 \pi^{N/2} r^{N-1}} \hat{r}, \qquad 0 < r < R \tag{14}$$

and $\vec{E} = 0$ for $r > R$. The initial electrostatic energy before ionization can be calculated as

$$\begin{aligned} U_{initial} &= \frac{1}{2}\varepsilon_0 \int E^2 d^N r \\ &= \frac{1}{2\varepsilon_0}\left(\frac{Ze\Gamma(N/2)}{2\pi^{N/2}}\right)^2 \int_0^R \frac{1}{r^{2N-2}} r^{N-1} dr d\Omega \\ &= \frac{Z^2 e^2 \Gamma(N/2)}{4\varepsilon_0 \pi^{N/2}(N-2)}\left(-\frac{1}{r^{N-2}}\right)_0^R \end{aligned} \tag{15}$$

Obviously, the function $1/(r^{N-1})$ diverges at the origin and thus we have a singular point at $r = 0$. As Tort suggested, we can avoid this problem by introducing a finite non-null radius δ for the point charge and thus

$$U_{initial} = \frac{Z^2 e^2 \Gamma(N/2)}{4\varepsilon_0 \pi^{N/2}(N-2)}\left(\frac{1}{\delta^{N-2}} - \frac{1}{R^{N-2}}\right). \tag{16}$$

Now, when the atom is ionized part of the charge $(-\lambda Ze)$ of the shell will move to infinity and thus the enclosed charge within a hyper-spherical Gaussian surface of radius $r > R$. Will be $q = Ze - Ze(1-\lambda) = \lambda Ze$. It is clear that the electric field, for $r > R$, remains the same as before ionization (see **Eq.14**) and for $r > R$ Gauss's Law immediately gives

$$\vec{E} = \frac{\lambda Ze\Gamma(N/2)}{2\varepsilon_0 \pi^{N/2} r^{N-1}} \hat{r}. \qquad r > R \tag{17}$$

Therefore the final electrostatic energy becomes

$$\begin{aligned} U_{final} &= \frac{Z^2 e^2 \Gamma(N/2)}{4\varepsilon_0 \pi^{N/2}(N-2)}\left(\frac{1}{\delta^{N-2}} - \frac{1}{R^{N-2}}\right) \\ &+ \frac{\varepsilon_0}{2}\int_R^\infty \left(\frac{\lambda Ze\Gamma(N/2)}{2\varepsilon_0 \pi^{N/2} r^{N-1}}\right)^2 r^{N-1} dr d\Omega \end{aligned} \tag{18}$$

The first term is just $U_{initial}$ and the integral in the second term has the same form as that of **Eq.7** and thus, one gets

$$U_{final} = U_{initial} + \frac{(\lambda Ze)^2 \Gamma(N/2)}{4\varepsilon_0 \pi^{N/2}(N-2)} \frac{1}{R^{(N-2)}} \tag{19}$$

Therefore, the change in the electrostatic energy is

$$\Delta U = U_{final} - U_{initial} = \frac{(\lambda Ze)^2 \Gamma(N/2)}{4_0 \pi^{N/2}(N-2)} \frac{1}{R^{N-2}}, \tag{20}$$

which is exactly the same as the electrostatic energy of a hyper-spherical shell that we found in Section 2. It is noticed that the variation of electrostatic energy is finite for all values of space dimension *N*, except for $N = \infty$ where ΔU becomes infinite. Therefore, the renormalization of the electrostatic energy works out for all space dimensions but failed in the infinite dimensional space. The persistent of the singularity in the infinite dimensional space is a result of the infinite electrostatic energy of the hyper-shell in that space, as we outlined in Section 2.

5. CONCLUSIONS

We have obtained the electrostatic energy of two systems (a charged spherical shell and a charged non-conducting sphere) in the *N*-dimensional space. Our calculated results show that the electrostatic energy decreases as the space dimension increases up to $N = 9$ and it increases without limit beyond that

Table 1. The electrostatic energy of the shell and the sphere as function of space dimension.

N	$W_{shell}(Q^2/8\pi\varepsilon_0)$	$W_{sphere}(Q^2/4\pi\varepsilon_0)$
3	1	0.6
4	0.318	0.2
5	0.159	0.11
6	0.101	0.07
7	0.076	0.06
8	0.065	0.051
9	0.060	0.049
10	0.062	0.051
11	0.067	0.057
12	0.078	0.067
13	0.097	0.08
14	0.125	0.11
15	0.169	0.15
16	0.238	0.21
17	0.349	0.31
18	0.531	0.47
19	0.835	0.75
20	1.353	1.23
30	6.8×10^3	640
40	2.3×10^6	2.18×10^6
50	3.0×10^{10}	2.9×10^{10}
100	5.4×10^{36}	5.3×10^{36}

value. This behavior is explained as follows: Each of the quantities $S(N-2)$ and $V(N^2-4)$ has a maximum at $N=9$ and thus the electrostatic energy of each system has a minimum at this value, as shown in **Eqs.6** and **12**. Our results also show that the electrostatic energy, for both systems, becomes infinite in the infinite dimensional space. Furthermore, we considered classical renormalization of electrostatic energy for a simplified model of a classical atom in higher space dimension. It was shown that the variation in electrostatic energy (the final minus the initial energy) is exactly the same as that of the hyper-shell, and thus the singularity persists in the infinite dimensional space.

REFERENCES

[1] Kalnins, E.G., Miller, W. and Pogosyan, G.S. (2002) The Coulomb oscillator relation on *n*-dimensional spheres and hyperboloids. *Physics of Atomic Nuclei*, **65(6)**, 1086-1094.

[2] AL-Jaber, S.M. (1998) Hydrogen atom in *N* dimensions. *International Journal of Theoretical Physics*, **37(4)**, 1289-1298.

[3] Halberg, A.S. (2001) The central symmetric screened Coulomb potential in *N* dimensions. *Hadronic Journal*, **24(5)**, 519-530.

[4] Brack, M. and Murthy, M.V. (2003) Harmonically trapped fermion gases: Exact and asymptotic results in arbitrary dimensions. *Journal of Physics A*: *Mathematical and General*, **36(4)**, 1111-1133.

[5] Weldon, H.A. (2003) Quantization of higher-derivative field theories. *Annals of Physics*, **305(2)**, 137-150.

[6] Griffiths, J.B. and Podolsky, J. (2010) The Linet-Tian solution with a positive cosmological constant in four and higher dimensions. *Physical Review D*, **81(6)**, 064015-064020.

[7] Wetterich, C. (2009) Dilation symmetry in higher dimensions and the vanishing of the cosmological constant. *Physical Review Letters*, **102(14)**, 141303-141306.

[8] Li, W. and Yang, F. (2003) N-dimensional space-time unit spheres and Lorentz transformation. *Advances in Applied Clifford Algebras*, **13(1)**, 57-64.

[9] Plyukhin, A.V. (2010) Stochastic process leading to wave equations in dimensions higher than one. *Physical Review E*, **81(2 Pt 1)**, 021113-021117.

[10] Kajimoto, N., Manaka, T. and Iwamoto, M. (2006) Electrostatic energies stored in dipolar films and analysis of decaying process of a large surface potential of ALq_3 films. *Chemical Physics Letters*, **430(4-6)**, 340-344.

[11] Ferreira, G.F. (2000) The electrostatic energy of thin charged straight threads and coils and the work to bend straight threads into coils. *Journal of Electrostatics*, **49(1-2)**, 23-30.

[12] Pask, J.E. and Sterne, A. (2005) Real-space formulation of the electrostatic potential and total energy of solids. *Physical Review B*, **71(11)**, 113101-113104.

[13] Ryder, L.H. (1996) Quantum filed theory. Cambridge University Press, Cambridge.

[14] Perskin, M.E. and Schroeder, D.V. (1995) An introduction to quantum field theory. Addison-Wesley, Reading, Massachusetts.

[15] Alexandre, J. (2005) Concepts of renormalization in physics. *Science Progress*, **88(1)**, 1-16.

[16] Corbò, G. (2010) Renormalization in classical field theory. *European Journal of Physics*, **31(1)**, L5-L8.

[17] Tort, A.C. (2010) Another example of classical renormalization in electrostatics. *European Journal of Physics*, **31(2)**, L49-L50.

[18] AL-Jaber, S.M. (1999) Fermi gas in D-dimensional space. *International Journal of Theoretical Physics*, **38(3)**, 919-923.

[19] Griffiths, D.J. (1999) Introduction to electrodynamics. Addison-Wesley, Reading, Massachusetts.

[20] Boas, M.L. (2006) Mathematical methods in the physical sciences. John Wiley, New York.

[21] Connes, A. and Kreimer, D. (1999) Renormalization in quantum field theory and the Riemann-Hilbert problem. *Journal of High Energy Physics*, **9**, 024.

[22] Falk, S., Häubling, R. and Scheck, F. (2010) Renormalization in quantum field theory: An improved rigorous method. *Journal of Physics A*: *Mathematical Theoretical*, **43(3)**, 035401.

[23] Borsányi, S. and Reinosa, U. (2009) Renormalized non-equilibrium quantum field theory: Scalar fields. *Physical Review D*, **80(12)**, 125029-125046.

Vol.2, No.7, 764-768 (2010)
doi:10.4236/ns.2010.27096

Natural Science

Pyrogenicity of hyaluronic acid hydrogel cross-linked by divinyl sulfone for soft tissue augmentation

Jin-Tae Kim[1], Jae-Ha Choi[1], Deuk-Yong Lee[2]*

[1]Department of Advanced Materials Engineering, Chungbuk National University, Cheongju, Korea
[2]Department of Materials Engineering, Daelim University College, Anyang, Korea; *Corresponding Author: dylee@daelim.ac.kr

Received 3 March 2010; revised 23 April 2010; accepted 29 April 2010.

ABSTRACT

Hyaluronic acid hydrogels (HAHs) were synthesized by immersing the micro-beads in phosphate buffered saline solution to assess short-term biocompatibility of the gels by means of the rabbit pyrogen test and the bacterial endotoxin test. The rise in body temperature of 3 male New Zealand white rabbits weighing about 2~3 kg (12~16 weeks old) following intravenous injection of the test article (10 mL/kg) was monitored at 30 min intervals in 3 h to examine the pyrogenicity. No rabbits showed an individual rise in temperature of 0.5°C or more above its respective control temperature. The temperature rises of the rabbits after injection were 0.12°C, 0.13°C, and 0.18°C, respectively, suggesting that HAH meets the requirements for the absence of pyrogens. The bacterial endotoxin test revealed that the concentration of endotoxins required to cause the lysate to clot under standard conditions was < 0.125 EU/mL. Comparing the HAHs that was synthesized in this experiment to the ones approved by FDA, the amount of < 0.125 EU/mL endotoxins is relatively safe and effective. The test solution did not contain any interfering factors under the experimental conditions used. It is conceivable that the HAHs are likely to be suitable injectable dermal filler for facial soft tissue augmentation due to the absence of pyrogens.

Keywords: Hyaluronic Acid Hydrogel; Injectable Dermal Filler; Pryogenicity; Endotoxin; Interfering Factor; Soft Tissue Augmentation

1. INTRODUCTION

Hydrogels as injection augmentation of facial soft tissue have attracted immediate attention due to their regeneration properties of various tissues, mechanical properties, softness, oxygen permeability, similarities the body's own highly hydrated composition and excellent biocompatibilities [1-8]. They demonstrated their efficacy in correcting aesthetic defects such as congenital or hypovolumetries, nasolabial furrows, forehead, glabella wrinkles, cheekbone, chin hypovolumetry and lip augmentation. They are known to be highly swollen and insoluble networks that can be used to entrap cells. It is noted that higher equilibrium swelling promotes nutrient diffusion into the gel and cellular waste removal out of the gel, while the insolubility provides the structural integrity necessary for tissue growth [1,2].

Among natural polymers, such as collagen, gelatin, fibrin, alginic acid, chitosan and hyaluronic acid (HA), crosslink-stabilized HA is highly acknowledged as a naturally derived injectable filler due to its longevity of correction, a reduced risk of immunogenicity and hypersensitivity, and its controllable mechanical and degradation properties [1,7]. HA is a linear polysaccharide formed from disaccharide units containing *N*-acetyl-*D*-glucosamine and glucuronic acid [2,8]. HA molecule is stabilized to produce cross-linked gel suitable for soft-tissue implantation, resulting in improving its resistance to enzymatic degradation within the dermis without compromising its biocompatibility.

HA hydrogels cross-linked by divinyl sulfone (HAHs) were prepared by immersing the micro-beads in phosphate buffered saline solution (NaH_2PO_4) [9]. HAHs for soft tissue augmentation are reported to be biologically inert and non-allergic and do not require allergy testing before implantation. Prior to the evaluation of long-term toxicity (genotoxicity) and carcinogenicity after the injection because they have been used within the dermis for several months, it is necessary to examine adverse and allergic reactions of the HAH, such as short-term pyrogenicity [5]. Although the rabbit pyrogen test has played a key role to control pyrogenicity of the drugs for long time, the test has limitations due to insufficient accuracy. The bacterial endotoxin test, which is based on

highly sensitive clotting of *Limulus Amoebocyte Lysate* (LAL) by endotoxin, has been applied in place of the pyrogen test. However, the LAL test has also limitations in detection of such *in vivo* synergistic effect of endotoxin and the drugs [10]. The pyrogenicity of the HAH is investigated to assess the short-term biocompatibility by means of the rabbit pyrogen test and the LAL test (gel-clot method) [10,11].

2. METHODS

2.1. Materials

HA solutions of 4.0 wt% concentration were prepared by dissolving a 3.2 g of sodium hyaluronate (Mw = 1 × 10^6 Da, Shiseido Co., Japan) in 8 mL of 0.05 mol/L NaOH at room temperature. A pH in the range of 12 to 14 was achieved by adding 0.4 mL of 10 mol/L NaOH to the HA solution. Then, the HA solution was placed in a solution hopper attached to the Masterflex L/S tubing pump (Cole Parmer, USA) and fed into a syringe equipped with a 14-gage metal needle at a flow rate of 0.2 mL/min. Micro-beads with diameters of 0.2 to 0.3 mm were fabricated by supplying compressed air with a pressure of 34.475 Pa along the HA solution nozzle. The nozzle was enclosed by a delivery tube with a diameter of 6 mm [9]. Micro-beads were collected into a solution mixture of 0.4 mL of divinyl sulfone (≥ 98%, Sigma and Aldrich, Germany) and 40 mL of 2-methyl-1-propanol (99%, Aldrich), followed by a stirring process (140~160 rpm) for 24 h at room temperature. Then, the cross-linked micro-beads were immersed in ethanol for 0.5 h to clean the beads by removing impurities such as divinyl sulfone and 2-methyl-1-propanol. After 3-time cleaning in ethanol, micro-beads were dried at 60°C in vacuum (20 torr). The as-dried micro-beads were immersed in 80 mL of phosphate buffered saline solution (NaH_2PO_4) for 2 h to obtain HAHs, as shown in **Figure 1**. The HAHs were then provided in a 1 mL sterilized syringe with luer-lok type capped.

2.2. Rabbit Pyrogen Test

Male New Zealand white rabbits weighing about 2~3 kg (12~16 weeks old) were employed for pyrogenicity. The material extract was prepared in the static conditions in sterile physiological saline solution (1 g in 50 mL) for 72 h at 37°C, followed by centrifuging for 10 min at 3000 rpm and filtering (Whatman, Grade 4, England). Not more than 30 min prior to the injection of the test dose, the control temperature of each rabbit was determined. The control temperature is the base for the determination of any temperature increase resulting from the injection of a test solution. Rabbits, whose control temperatures did vary by more than 1°C from each other, were excluded. In addition, any rabbits having a temperature exceeding 39.8°C were also excluded. The test involved measuring the rise in body temperature of rabbits following intravenous injection of the test article and was designed for products that can be tolerated by the test rabbit in a dose not exceed 10 mL/kg injected intravenously, within a period of not more than 10 min. Injection was performed after warming the test solution to a temperature of 37 ± 2°C.

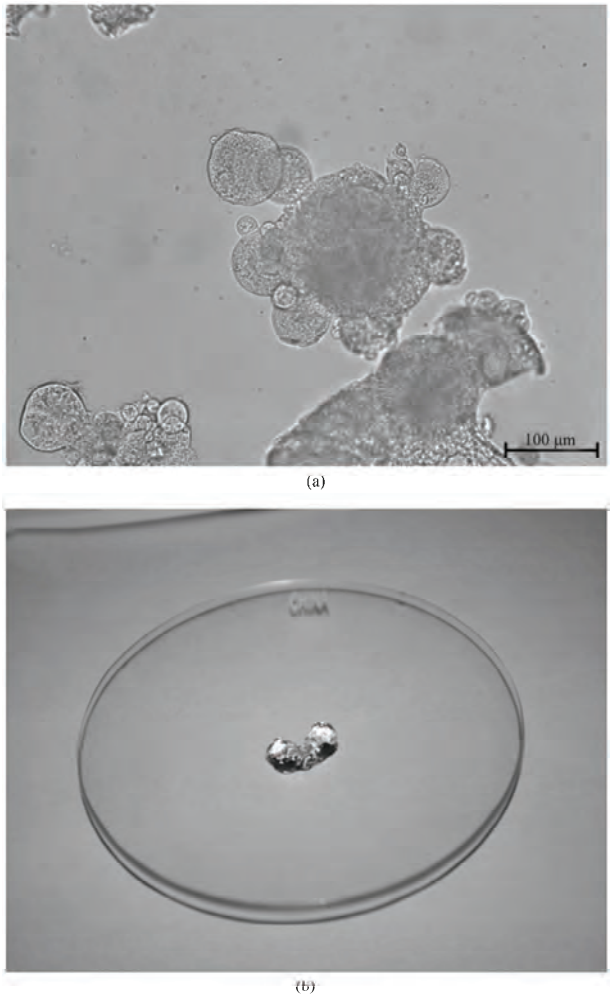

Figure 1. Photographs of (a) the micro-beads immersed in phosphate buffered saline solution and (b) hyaluronic acid hydrogels.

After the injection, the body temperature is monitored at 30 min intervals in 3 h. If no rabbit shows an individual rise in temperature of 0.5°C or more above its respective control temperature, the product meets the requirements for the absence of pyrogens. If any rabbit shows an individual temperature rise of 0.5°C or more, continue the test using 5 other rabbits. If not more than 3 of 8 rabbits show individual rises in temperature of 0.5°C or more and if the sum of 8 individual maximum

temperature rises does not exceed 3.3°C, the material under examination meets the requirements for the absence of pyrogens.

2.3. *In Vitro* Endotoxin Test

The pyrogens that almost invariably contaminate parenteral pharmaceuticals are bacterial endotoxins (lipopolysaccharides, LPS)-cell wall material from gram negative bacteria [10]. The LAL test detects only LPS, which caused extracellular coagulation of the blood of the horseshoe crab, *Limulus polyphemus*. The bacterial endotoxin test, which is based on highly sensitive clotting of LAL by endotoxin, has been applied in place of the pyrogen test for testing parenteral human drugs [10, 11]. The gel-clot testing was performed to detect bacterial endotoxin. The gel-clot method is based upon the reaction between bacterial endotoxin and a single test LAL (CAMBREX, Lot No. GL1403).

All glassware was depyrogenated for 4 h at 180°C and the test was carried out in clean-bench to avoid the endotoxin contamination. The material extract was prepared in the static conditions in LAL reagent water (BIO Whittaker, 1 g in 40 mL) for 1 h at 37°C. The concentration of endotoxins required to cause the lysate to clot under standard conditions is the labeled lysate sensitivity (λ), expressed IU/mL. Endotoxin is expressed in International Unit (IU). One IU of endotoxin is equal to one Endotoxin Unit (EU). Standard solutions of at least four concentrations equivalent to 2λ, 1λ, 0.5λ, and 0.25λ were prepared by diluting the standard endotoxin stock solution with LAL reagent water. A volume of the lysate solution was mixed with an equal volume of one of the standard solutions. The mixture was incubated for 60 ± 2 min at 37 ± 1°C. Following 1 h of incubation at 37°C, the test tube was examined by 180° inversion for the presence of a stable solid clot. A clotted incubation mixture is considered to be a positive result. A result is negative if an intact gel is not formed. The test is not valid unless the lowest concentration of the standard solutions shows a negative result in all replicate tests. The end-point is the last positive result in the series of decreasing concentrations of endotoxin. The mean value of the logarithms of the end-point concentrations and then the antilogarithm of the mean value is calculated. The geometric mean end-point concentration is the measured sensitivity of the lysate solution. If this is not less than 0.5 and not more than 2, the labeled sensitivity is confirmed and is used in the tests performed with this lysate. Solutions, as shown in **Table 1** (A, B, C, and D), are prepared to confirm the labeled lysate sensitivity. The test is not valid unless both replicates of two positive control solutions B and C are positive and those of the negative control solution D are negative.

3. RESULTS AND DISCUSSION

The rise in body temperature of 3 Male New Zealand white rabbits following intravenous injection of the test article (10 mL/kg) was monitored at 30 min intervals in 3 h to examine the pyrogenicity. It is found that the increase in body weight was normal, as summarized in **Table 2**. No mortality and abnormal clinical signs were detected. No rabbits showed an individual rise in temperature of 0.5°C or more above its respective control temperature, as shown in **Figure 2**. The temperature rises of the rabbits after injection were 0.12°C, 0.13°C, and 0.18°C, respectively, suggesting that the HAH meets the requirements for the absence of pyrogens.

The gel-clot technique allows detection or quantification of endotoxins and is based on clotting of the lysate in the presence of endotoxins [11]. The concentration of endotoxins required to cause the lysate to clot under standard conditions is the labeled lysate sensitivity. To ensure both the precision and validity of the test, the

Table 1. Solutions for the gel-clot test.

solution	endotoxin concentration/solution to which endotoxin is added	replicates
A	None/sample solution	2
B	2λ/sample solution	2
C	2λ/LAL reagent water	2
D	none/ LAL reagent water	2

Table 2. Body weight changes.

Rabbits	Receipt day (g)	Injection day (g)
1	2268.6	2377.8
2	2161.6	2276.0
3	1957.4	2091.1
Mean	2129.2	2248.3
SD	158.1	145.3

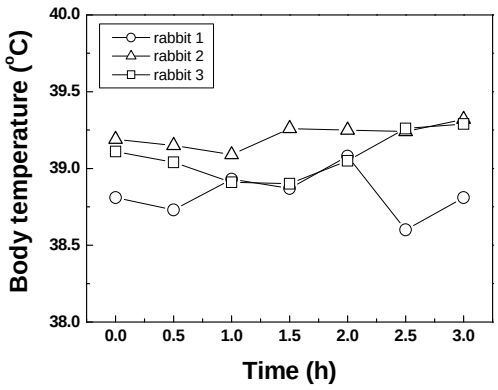

Figure 2. The variation in body temperature of 3 Male New Zealand white rabbits after intravenous injection of the test article. Note that the body temperature is monitored at 30 min intervals in 3 h.

labeled lysate sensitivity and the test for interfering factors were performed by using solutions for the gel-clot test as summarized in **Table 1**. The end-point is the last positive results in the series of decreasing concentrations of endotoxin. The geometric mean end-point concentration is the measured sensitivity of the lysate solution. The mean value of the logarithms of the end-point concentrations is equivalent to the antilogarithm of the mean value, (Antilog Mean = 0.12 EU/mL). The antilogarithm of the mean value is calculated to be −0.921. If the geometric mean end-point concentration of 0.12 EU/mL is not less than 0.5λ (0.06) and not more than 2λ (0.24), the labeled sensitivity is confirmed and is used in the tests performed with this lysate, as shown in **Table 3**. For the lysate to clot under standard conditions, < 0.125 EU/mL was found to be the required concentration of endotoxins. The material extract was prepared in the static conditions in LAL reagent water for 1 h at 37°C [11]. After considering the dilution factor, the final concentration of endotoxin was determined to be < 0.005 EU/mg. According to FDA's "Summary of Safety and Effectiveness Data," endotoxin concentrations are 0.5 EU/mL, 20 EU/syringe, 0.08 EU/mL for the three approved injectable dermal HAH fillers in market, respectively [12-14]. Comparing the HAHs that was synthesized in this experiment to the ones approved by FDA, the amount of < 0.125 EU/mL endotoxins is relatively safe and effective [12-14].

The test for interfering factors is repeated when any changes are made to the experimental conditions that are likely to influence the result of the test. The test is not valid unless all replicates of solutions A and D show no reaction and the result of solution C confirms the labeled lysate sensitivity. If the sensitivity of the lysate determined with solution B is not less than 0.5 and not greater than 2, the test solution does not contain interfering factors under the experimental conditions used. Otherwise, the solution interferes with the test. Test results, as listed in **Table 4**, implied free of interfering factors because solutions A and D showed reaction and the lysate sensitivity with solution B was within the experimental range (0.5~2) [11].

Table 3. Test for confirmation of the labeled lysate sensitivity.

No. of time	Endotoxin dilution (EU/mL)					End-point (EU/mL)
	0.24 (2λ)	0.12 (1λ)	0.06 (0.5λ)	0.03 (0.25λ)	LAL RW*	
1	+	+	-	-	-	0.12
2	+	+	-	-	-	0.12
3	+	+	-	-	-	0.12
4	+	+	-	-	-	0.12

+: positive, -: negative, RW: reagent water.

Table 4. Test for interfering factors.

Solution	No. of time	Endotoxin dilution (EU/mL)				End-point (EU/mL)
		0.24 (2λ)	0.12 (1λ)	0.06 (0.5λ)	0.03 (0.25λ)	
B	1	+	+	-	-	0.12
	2	+	+	-	-	0.12
	3	+	+	-	-	0.12
	4	+	+	-	-	0.12
C	1	+	+	-	-	0.12
	2	+	+	-	-	0.12

*solution A: all positive, solution D: all negative.

4. CONCLUSIONS

Short-term biocompatibility of the HAHs prepared by immersing the micro-beads in phosphate buffered saline solution was evaluated by examining the rabbit pyrogen test and the bacterial endotoxin test. No rabbits showed an individual rise in temperature of 0.5°C or more above its respective control temperature after intravenous injection of the test article (10 mL/kg) to 3 male New Zealand white rabbits. The temperature rises of the rabbits after injection were 0.12°C, 0.13°C, and 0.18°C, respectively, suggesting that the HAH meets the requirements for the absence of pyrogens. The concentration of endotoxins required to cause the lysate to clot under standard conditions was determined to be < 0.125 EU/mL. Comparing the HAHs that was synthesized in this study to the injectable dermal fillers approved by FDA (0.5 EU/mL), the amount of < 0.125 EU/mL endotoxins is relatively safe and effective. The test solution was free of interfering factors under the experimental conditions used. It is suggested that the HAHs are likely to be suitable filler for facial soft tissue augmentation due to the absence of pyrogens.

REFERENCES

[1] Jeon, O., Song, S.J., Lee, K., Park, M.H., Lee, S., Hahn, S.K., Kim, S. and Kim, B. (2007) Mechanical properties and degradation behaviors of hyaluronic acid hydrogels cross-linked at various cross-linking densities. *Carbohydrate Polymers*, **70(3)**, 251-257.

[2] Monheit, G.D. and Coleman, K.M. (2006) Hyaluronic acid fillers. *Dermatol Therapy*, **19(3)**, 141-150.

[3] Kim, J.T. and Choi, J.H. (2009) Production and evaluation of hyaluronic acid gel for soft tissue augmentation. *Biomaterials Research*, **13(9)**, 105-108.

[4] Maas, C.S., Papel, I.D., Creene, D. and Stoker, D.A. (1997) Complications of injectable synthetic polymers in facial augmentation. *Dermatologic Surgery*, **23(10)**, 871-877.

[5] Hoffmann, C., Schuller-Petrovic, S., Soyer, H.P. and Kerl, H. (1999) Adverse reactions after cosmetic lip augmentation with permanent biologically inert implant materials. *Journal of the American Academy of Dermatology*, **40(1)**,

100-102.

[6] Narins, R.S., Brandt, F., Leyden, J., Lorenc, Z.P., Rubin, M. and Smith, S. (2003) A randomized, double-blind, multicenter comparison of the efficacy and tolerability of restylane versus zyplast for the correction of nasolabial folds. *Dermatologic Surgery*, **29(6)**, 588-595.

[7] Ramires, P.A., Miccoli, M.A., Panzarini, E., Dini, L. and Protopapa, C. (2005) *In Vitro* and *In Vivo* biocompatibility evaluation of a polyalkylimide hydrogel for soft tissue augmentation. *Journal of Biomedical Materials Research Part B*: *Applied Biomaterials*, **72B(2)**, 230-238.

[8] Kogan, G., Soltes, L., Stern, R. and Gemeiner, P. (2007) Hyaluronic acid: A natural biopolymer with a broad range of biomedical and industrial applications. *Biotechnology Letters*, **29(1)**, 17-25.

[9] Kim, J.T., Kook, C.H. and Choi, J.H. (2009) Production equipment and method of polymer gel for bio-implanting. *Journal of Korean Society of Mechanical Technology*, **11(2)**, 89-94.

[10] Ochiai, M., Yamamoto, A., Kataoka, M., Toyoizumi, H., Arakawa, Y. and Horiuchi, Y. (2007) A quantitative *in vitro* assay to detect biological activity of endotoxin using rabbit peripheral blood. *Proceedings of the* 6*th World Congress on Alternative and Animal Use in the Life Science*, **14(3)**, 641-645.

[11] (2002) European Pharmacopoeia, 4th Edition, *Bacterial Endotoxins*, 140-147.

[12] http://www.accessdata.fda.gov/cdrh_docs/pdf2/P020023b.pdf

[13] http://www.accessdata.fda.gov/cdrh_docs/pdf5/P050033b.pdf

[14] http://www.accessdata.fda.gov/cdrh_docs/pdf5/P050047b.pdf

Vol.2, No.7, 769-779 (2010)
doi:10.4236/ns.2010.27097

Natural Science

The effect of cartilaginous rings on particle deposition by convection and Brownian diffusion

Hans O. Åkerstedt[1], Sofie M. Högberg[1], T. Staffan Lundström[1], Thomas Sandström[2]

[1]Division of Fluid Mechanics, Luleå University of Technology, Luleå, Sweden; Sofie.Hogberg@ltu.se; staffan.lundstrom@ltu.se; Corresponding Author: hake@ltu.se
[2]Department of Public Health and Clinical Medicine, Division of Respiratory Medicine & Allergy, Umeå University, Umeå, Sweden; thomas.sandstrom@lung.umu.se

Received 26 March 2010; revised 11 May 2010; accepted 18 May 2010.

ABSTRACT

The deposition of spherical nanoparticles by convection and Brownian diffusion in a pipe with a cartilaginous ring structure is studied. Analytical results for a fully developed flow are found for small amplitude rings using the interactive boundary layer theory. It is found that the local deposition rate is at maximum at a position approximately one twelfth of the spacing between the rings before the minimum cross section of the tube. For larger ring amplitudes the problem is solved numerically and separation then takes place in the depressions between the rings, and maximum deposition is found at the point of reattachment of the flow approximately at the same point as in the analytical theory. Cumulative deposition results are also provided with larger deposition rates with the inclusion of the cartilaginous rings. Deposition results for a developing flow are also provided. For the same volume flux as for fully developed flow the deposition is about 25% larger. In general conclusions about the position of maximum deposition rate from the analytic theory of fully developed flow also applies qualitatively to the case of developing flow.

Keywords: Nanoparticles; Convection; Brownian Motion; Deposition; Respiratory Airways; Cartilaginous Rings

1. INTRODUCTION

Usage of nanoparticles in material design enables the development of new superior products as well as improvement of existing ones, but these tiny particles are potentially toxic and pose substantial health risks [1]. There is an increasing literature that discusses the ability of nanoparticles to cause adverse effects in cellular functions [2]. Depending on the field of application, nanoparticles may enter the body via inhalation, dermal, oral or injection exposure routes. Carbon nanotubes, for instance, have a diameter of approximately 10 nm with a very much larger length of 1-10 μm, and if inhaled then, they may probably quite easily move through the airways down to the alveoli. Once in the alveoli, they can get stuck and initiate different diseases, in a similar manner as asbestos fibres. Thus, knowledge of transport and deposition properties of aerosol particles in lung flows is essential. Such knowledge is also useful in the optimization of drug delivery with pharmaceutical aerosols.

Of special interest is the effect of cartilaginous rings, located in the upper generations of the human airways, on nanoparticle deposition caused by convection and diffusion. These rings give the airway wall an uneven surface, with ring forms protruding into the airway lumen, and with depressions between the rings. These regular and symmetric structures are expected to influence turbulent as well as laminar airflow directly passing them, which could potentially affect deposition in this region. Measurements of a physical model with cartilaginous rings have been done by Zhang and Finlay [3] using particles of size about 5 μm. They find an increase in deposition of about 20% due to cartilaginous rings.

In the present study, we examine the diffusion of smaller spherical particles and their deposition on the walls of an airway with cartilaginous rings, while leaving the corresponding problem for fibres for future studies. The results provided by the present analysis for spherical particles can then be considered as an upper limit for the deposition of fibres.

One method to determine particle deposition in the diffusion limit is to solve the Langevin equation with a stochastic force on the particle in a given flow field cal-

culated from the Navier-Stokes equations. To find deposition statistics, however, a large number of particles need to be launched [4]. An alternative approach is to consider the equation describing the evolution of the probability density, the Fokker-Planck equation, which has the advantage of directly providing the statistical averages [5]. The disadvantage of this method is that for large Peclet-numbers (Pe), implying small diffusion, very thin boundary layers develop, and these are difficult to resolve numerically. The Fokker-Planck equation has the same form as the convective-diffusion equation, describing the evolution of the concentration of particles. In the present paper, the particle deposition is derived by combining the Navier-Stokes equations and the convective-diffusion equation. This methodology has previously been applied by Ingham [6-8] and Martonen *et al.* [9] for deposition in smooth-walled tubes.

A lot of research has been done using a similar set of equations describing in heat transfer and mass transfer with wavy walls that often occurs in engineering applications. In these applications however the Pe-number is often much smaller, of the same order as the Re-number. Here we consider Pe much larger than the Re-number. We also believe that these general results are not so well known in connection to the biological application considered in the present paper.

The paper is organized as follows. In Section 2, an approximate analytic solution of the Navier-Stokes equation is presented together with solutions of the convective-diffusion equation. To solve the problem for the flow with a weakly perturbed sinusoidal boundary, a linearized interactive boundary layer theory is employed [10]. To start with, and as a zero-order solution, a fully developed pipe flow is chosen. The analytic solution has the advantages that it provides a better understanding of the flow and that it introduces the relevant scaling of the problem. Furthermore, it can be used to verify the corresponding numerical results, to be presented in Subsection 3.1 Due to the previously mentioned numerical difficulties with very large Pe, we only consider light breathing conditions, which implies large but modest Pe. In Subsection 3.2, a developing flow is considered. For this case, it turns out to be handy to take a numerical approach, since an analytical treatment is difficult, even without rings. To validate the numerical work, the results are finally compared with approximate treatments of entry flow in smooth-walled tubes presented by Ingham [7-8] and Martonen *et al*. [9]. Here two rather different configurations of cartilaginous rings are considered.

In a real respiratory system neither fully developed nor developing axisymmetric tube occurs. It is rather a combination of the two since after an airway bifurcation approximately half the flow attaches a new wall creating a new developing thin velocity boundary layer. However we believe that the two extreme cases considered in this paper gives a first estimate of the number of deposited particles in the real case.

2. THEORY

2.1. The Interactive Boundary Layer Theory

The axisymmetric geometry in **Figure 1** is considered, for which the flow may be described by the dimensionless Navier-Stokes equations according to

$$\begin{aligned} u\frac{\partial u}{\partial x}+\mathrm{v}\frac{\partial u}{\partial r}&=-\frac{\partial p}{\partial x}+Re^{-1}\left(\frac{1}{r}\frac{\partial}{\partial r}\left(r\frac{\partial u}{\partial r}\right)+\frac{\partial^2 u}{\partial x^2}\right)\\ u\frac{\partial \mathrm{v}}{\partial x}+\mathrm{v}\frac{\partial \mathrm{v}}{\partial r}&=-\frac{\partial p}{\partial r}+Re^{-1}\left(\frac{1}{r}\frac{\partial}{\partial r}\left(r\frac{\partial \mathrm{v}}{\partial r}\right)+\frac{\partial^2 \mathrm{v}}{\partial x^2}-\frac{\mathrm{v}}{r^2}\right) \quad (1)\\ \frac{\partial u}{\partial x}+\frac{1}{r}\frac{\partial}{\partial r}(r\mathrm{v})&=0 \end{aligned}$$

Here u is the stream-wise velocity and v the radial velocity, and p is the pressure. In addition, the convective-diffusion equation is introduced in the form

$$u\frac{\partial c}{\partial x}+\mathrm{v}\frac{\partial c}{\partial r}=\mathrm{Pe}^{-1}\left(\frac{1}{r}\frac{\partial}{\partial r}\left(r\frac{\partial c}{\partial r}\right)+\frac{\partial^2 c}{\partial x^2}\right) \quad (2)$$

in order to study the diffusion of particles embedded in the fluid. In (2), c can be considered as concentration of particles, while in a Fokker-Planck context as a probability density function.

The Reynolds number Re and the Peclet number Pe are now defined as

$$\begin{aligned} \mathrm{Re}&=\frac{U_0 a}{\nu}=\frac{\bar{U}2a}{\nu}\\ \mathrm{Pe}&=\frac{U_0 a}{D}=\frac{\bar{U}2a}{D} \end{aligned} \quad (3)$$

where U_0 is the maximum velocity for the fully developed pipe flow, $\bar{U}$ is the mean velocity at the inlet for the developing flow, ν is the viscosity, D is the diffusion coefficient, and a is the inlet pipe radius.

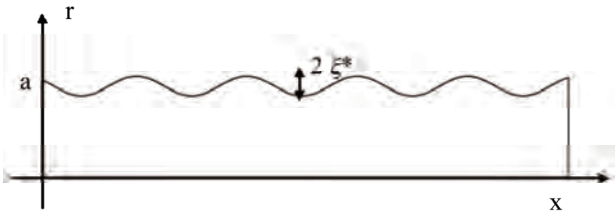

Figure 1. Axisymmetric geometry of a simple cartilaginous ring configuration.

The validity of Navier-Stokes depends on the Knudsen number, $\mathrm{Kn} = \lambda / L$, where λ is the mean free-path and L is a characteristic length scale of the problem. For small Kn the Navier-Stokes equations can be derived from an expansion in small Kn-numbers of the more fundamental gas kinetic theory (Chapman and Cowling, [11]). For the flow in a pipe the radius can be considered as a characteristic length and then the Knudsen number is very small in the present application. For the flow past a spherical particle with radius of the order of nano-meters, the Knudsen number is however not small and the Navier-Stokes equations are not valid. In a layer close to the particle, of the order of the mean-free path of the air-molecules, the more fundamental gas kinetic theory must be applied. The role of the Navier-Stokes equations is then to provide with "outer" local values of the velocity field for the free-molecular flow around the particle. The drag force and the drag coefficient of the spherical particle are only known theoretically for small Kn numbers (continuum limit) and large Kn numbers (free-molecule limit). For the continuum limit the drag coefficient is

$$k_d = 3\pi\rho\nu d_f \tag{4}$$

where d_f is the particle diameter.

For the intermediate range of Kn numbers an empirical correction, known as the Cunningham factor is introduced as

$$Cu = 1 + \frac{\lambda}{d_f}(2.34 + 1.05\exp(-0.39\frac{d_f}{\lambda})) . \tag{5}$$

The expression for the drag coefficient is then

$$k_d = \frac{3\pi\rho\nu d_f}{Cu} \tag{6}$$

which provides a value for the drag coefficient for all Knudsen numbers, $\mathrm{Kn} = \lambda / d_f$. For Brownian diffusion the diffusion coefficient D is then related to the drag as

$$D = \frac{\kappa T}{k_d} = \frac{\kappa T\, Cu}{3\pi\rho\nu d_f} \tag{7}$$

where κ is Boltzmanns constant and T is the temperature. The wavy boundary is described in terms of the dimensionless amplitude ζ, defined as

$$\zeta = \frac{\zeta^*}{a} .$$

In order to analyze the flow problem analytically, an interactive boundary layer theory is applied to the fluid flow problem. Following the presentation by Sobey [10], the solution of the Navier-Stokes equation is divided into two parts, the outer part describing the core flow and the inner one describing the flow in the neighbourhood of the boundary. The present formulation of the theory is applicable when the typical length scale of the wall perturbation is of the same order as the pipe radius. In this so called "fine indentation limit" a balancing of the order of magnitude of terms gives that the wave amplitude scales with the Reynolds number as

$$\varsigma = O(\mathrm{Re}^{-1/3}) . \tag{8}$$

The core flow is then described by the small ζ and large re-number expansions

$$\begin{aligned} u^c(r,x) &= 1 - r^2 + \varsigma^2 u_1(r,x) + \ldots \\ v^c(r,x) &= \varsigma^2 v_1(r,x) + \ldots \\ \psi^c(r,x) &= \frac{1}{2}r^2 + \frac{1}{4}r^4 + \varsigma^2\psi_1(r,x) + \ldots \end{aligned} \tag{9}$$

in which the leading order terms correspond to unperturbed pipe flow, and the second terms are corrections due to the finite amplitude of the wavy boundary. In the correction terms note the relationship between the amplitude ζ and the Reynolds number given in (8). For a description of the boundary layer, a coordinate R is introduced in the following manner:

$$R = (1 - r)\,\mathrm{Re}^{1/3} \tag{10}$$

within the present formulation, the velocities in the boundary layer are scaled as

$$\begin{aligned} u &= \mathrm{Re}^{-1/3}\,\bar{u} \quad , \bar{u} = O(1) \\ \mathrm{v} &= \mathrm{Re}^{-2/3}\,\bar{\mathrm{v}} \quad , \bar{\mathrm{v}} = O(1). \end{aligned} \tag{11}$$

The boundary layer equation for the axial velocity component can be defined as

$$\bar{u}\frac{\partial\bar{u}}{\partial x} - \bar{\mathrm{V}}\frac{\partial\bar{u}}{\partial R} = -\frac{d\hat{p}}{dx} + \frac{\partial^2\bar{u}}{\partial R^2} \tag{12}$$

where the pressure gradient is only a function of the stream-wise coordinate and the pressure scales as

$$p = \mathrm{Re}^{1/3}\,\hat{p} \quad , \hat{p} = O(1) . \tag{13}$$

It is convenient to rewrite (12) in terms of the stream-function Ψ of the boundary layer as

$$\begin{aligned} \bar{u} &= -\frac{\partial\Psi}{\partial R} \\ \bar{\mathrm{V}} &= -\frac{\partial\Psi}{\partial x} \end{aligned} \tag{14}$$

where

$$\psi = \mathrm{Re}^{-2/3}\,\Psi \quad , \Psi = O(1). \tag{15}$$

Another wall coordinate is introduced as

$$Y = R - \mu f(x) , \tag{16}$$

where $f(x) = O(1)$ is the shape of the wall and μ is a parameter controlling the amplitude of the wavy wall. The boundary layer (12) then becomes

$$\frac{\partial \Psi}{\partial Y}\frac{\partial^2 \Psi}{\partial x \partial Y} - \frac{\partial \Psi}{\partial x}\frac{\partial^2 \Psi}{\partial Y^2} = -\frac{d\hat{p}}{dx} + \frac{\partial^3 \Psi}{\partial Y^3} \tag{17}$$

where the asymptotic matching condition with the outer core solution is given by

$$\frac{\partial \Psi}{\partial Y} \to -2(Y + f(x)) + O(\mathrm{Re}^{-2/3}) \ as\ Y \to \infty \tag{18}$$

and the boundary condition at the wall $R = f(x)$ is the usual condition of no slip, such that

$$\Psi(x,0) = 0 \quad , \quad \frac{\partial \Psi}{\partial Y}(x,0) = 0. \tag{19}$$

To proceed analytically, the boundary layer (17) is solved for the case of a small perturbation of the cylindrical wall so that $\mu << 1$.

This means that solutions corresponding to flow separation cannot be strictly described, however increasing μ from small values give a first indication of where the flow may separate. For larger wall perturbations $\mu = O(1)$, (17) has to be solved numerically together with boundary conditions and matching with the core solution and the upstream solution. For small μ we assume that the solution of the boundary layer equation can be written as

$$\Psi = -Y^2 + \mu \Psi_\mu(x,Y). \tag{20}$$

The matching with the outer core solution is then expressed as

$$\frac{\partial \Psi_\mu}{\partial Y} \to -2 f(x) \ \ as Y \to \infty. \tag{21}$$

After linearization the boundary layer, (17) becomes

$$\frac{\partial^2}{\partial Y^2}\left(\frac{\partial^2 \Psi_\mu}{\partial Y^2}\right) + 2Y\frac{\partial}{\partial x}\left(\frac{\partial^2 \Psi_\mu}{\partial Y^2}\right) = 0\,, \tag{22}$$

which can be solved by introducing the Fourier transform

$$\hat{\Psi}_\mu = \int_{-\infty}^{\infty} \Psi_\mu \exp(ikx)dx\,. \tag{23}$$

A solution for the first derivative is of the form

$$\frac{\partial \hat{\Psi}_\mu}{\partial Y} = \hat{W}(k)\int_0^Y Ai((2ik)^{1/3}s)ds \tag{24}$$

where $\hat{W}(k)$ is a general function of k and Ai is the Airy-function. Matching with the core solution requires that

$$\frac{\partial \hat{\Psi}_\mu}{\partial Y} \to -2\hat{f}(k) as Y \to \infty \tag{25}$$

which determines the function $\hat{W}(k)$ and we find

$$\frac{\partial^2 \hat{\Psi}_\mu}{\partial Y^2} = -6(2ik)^{1/3}\hat{f}(k)Ai((2ik)^{1/3}Y)\,. \tag{26}$$

The boundary layer velocity close to the boundary, therefore, is given by the Taylor expansion

$$\begin{aligned}\hat{\bar{u}} &= 2Y - \mu\frac{\partial \Psi_\mu}{\partial Y} = 2Y - \mu\frac{\partial^2 \Psi_\mu}{\partial Y^2}\bigg|_{Y=0} Y + \ldots \\ &= 2Y - 6\mu(2ik)^{1/3}\hat{f}(k)Ai(0)Y + \ldots\end{aligned} \tag{27}$$

After inverting the Fourier transform, the velocity becomes

$$\begin{aligned}\bar{u}(x,Y) &= 2Y - \frac{\mu}{2\pi}\int_{-\infty}^{\infty} 6(2IK)^{1/3}\hat{f}(k)Ai(0)\exp(-ikx)dkY \\ &+ \ldots = 2Y + \mu g(x)Y\end{aligned} \tag{28}$$

For a specific form of the boundary $f(x)$, the function $g(x)$ in (28) can be calculated. An interpretation of this term is that it corresponds to the wall shear stress introduced by the wavy boundary. The minimum of this function is therefore given to the position of minimum wall shear stress. Thus, in a situation in which μ increases from zero to small but finite values, this minimum gives an indication of where the flow first separates. The corresponding wall normal velocity to (28) is

$$\bar{v}(x,Y) = -\frac{1}{2}\mu g'(x)Y^2 - f'(x)(2 + \mu g(x))Y + \ldots \tag{29}$$

The expanded results (28-29) are of importance for the large Pe solution of the convective-diffusion equation since, as will be shown below, only the velocity components close to the boundary are required.

2.2. The Convective-Diffusion Equation

Next, consider the convective-diffusion equation

$$u\frac{\partial c}{\partial x} + v\frac{\partial c}{\partial r} = \mathrm{Pe}^{-1}\left(\frac{1}{r}\frac{\partial}{\partial r}\left(r\frac{\partial c}{\partial r}\right) + \frac{\partial^2 c}{\partial x^2}\right). \tag{30}$$

Since we consider the limit of large Pe, the lowest order approximation to (30) is simply

$$u\frac{\partial c}{\partial x} + v\frac{\partial c}{\partial r} = 0\,. \tag{31}$$

This suggests that the concentration is preserved along streamlines. For absorption of particles reaching the boundary, however, the required boundary condition is $c = 0$, which cannot be fulfilled by solutions of (31), therefore, a boundary layer analysis of (30) is required. Using the boundary variables introduced in the previous section, the diffusion equation can be written in the form

$$\bar{u}(x,Y)\frac{\partial c}{\partial x} - f'(x)\bar{u}(x,Y)\frac{\partial c}{\partial Y} - \bar{v}(x,Y)\frac{\partial c}{\partial Y} = \varepsilon\frac{\partial^2 c}{\partial Y^2} \quad \text{where } \varepsilon = \frac{\mathrm{Re}}{\mathrm{Pe}} \tag{32}$$

where the second derivative of c with respect to x is neglected as is a common praxis in boundary layer analysis. For the application in focus, ε is usually very small, so we consider this to be the case for the rest of this paper. Introducing a boundary layer variable $\bar{\eta} = Y\varepsilon^{-\nu}$, (32) transforms to

$$\bar{u}(x,\varepsilon^{\nu}\bar{\eta})\frac{\partial c}{\partial x} - f'(x)\bar{u}(x,\varepsilon^{\nu}\bar{\eta})\varepsilon^{-\nu}\frac{\partial c}{\partial \bar{\eta}} - + \bar{v}(x,\varepsilon^{\nu}\bar{\eta})\varepsilon^{-\nu}\frac{\partial c}{\partial \bar{\eta}} = \varepsilon^{1-2\nu}\frac{\partial^2 c}{\partial \bar{\eta}^2} \tag{33}$$

By Taylor-expanding the arguments of the velocity components and balancing the order of magnitude of the terms it is found that $\nu = 1/3$ implying that only the approximate form of the velocities in (28-29) are required. A similarity solution exists with a similarity variable of the type $\eta = \frac{\bar{\eta}}{h(x)}$ and with a corresponding differential equation

$$c''(\eta) + \left\{(2-\mu g)h'h^2 - \frac{1}{2}\mu g'h^3\right\}\eta^2 c'(\eta) = 0. \tag{34}$$

Choosing the quantity inside the bracket to be 3, the equation for the concentration boundary layer thickness $h(x)$ is obtained as

$$(2-\mu g)h'h^2 - \frac{1}{2}\mu g'h^3 = 3. \tag{35}$$

A solution corresponding to zero concentration boundary layer thickness $h(x)$ at entry $x = 0$ is then given by

$$h(x) = \frac{9^{1/3}}{(2-\mu g(x))^{1/2}}\left(\int_0^x (2-\mu g(\xi))^{1/2} d\xi\right)^{1/3}. \tag{36}$$

For $\mu = 0$ we recover the result for convective-diffusion in ordinary pipes. The equation for the concentration, (34), then becomes

$$c''(\eta) + 3\eta^2 c'(\eta) = 0 \cdot \tag{37}$$

The solution can be written in terms of the incomplete gamma function with solution fulfilling the boundary condition $c = 0$ at $\eta = 0$ as

$$c(\eta) = 1 - \frac{\Gamma(\frac{1}{3},\eta^3)}{\Gamma(\frac{1}{3})} = 1 - \frac{1}{\Gamma(\frac{1}{3})}\int_{\eta^3}^{\infty} e^{-t}t^{-2/3}dt\,. \tag{38}$$

Of special interest is the particle deposition due to diffusion, which corresponds to the normal component of the particle diffusion flux at the wall. In non-dimensional form this is

$$j_n = -\frac{1}{pe}(\hat{n}\cdot\nabla)c\Big|_{Y=o}. \tag{39}$$

Neglecting terms of order $O(\mu^2)$ we find the following expression for the deposition:

$$j_n = \frac{3pe^{-2/3}}{\Gamma(\frac{1}{3})h(x)}. \tag{40}$$

As an example of a possible cartilaginous wall-shape, we consider the periodic function

$$f(x) = \begin{cases} \frac{1}{2}\sin(k_0 x)H(x) & 0 < k_0 x < \pi \\ 0 & \pi < k_0 x < 2\pi \end{cases}. \tag{41}$$

Here, the parameter k_0 is measure of the spacing between the rings. A convenient lowest order approximation for the analytical analysis is the first two Fourier components of (41), *i.e.*,

$$f(x) = (\frac{1}{\pi} + \frac{1}{2}\sin(k_0 x - \delta))\,H(x) \tag{42}$$

inspection of bronchoscopic videos shows that for the application of cartilaginous rings, these simple wall shapes are quite reasonable, at least in some parts of the tracheobronchial tree and the shape given by (41) is similar to that studied by Martonen *et al*. [12]. The differences between the shape (42) and the shape considered by Martonen will be discussed in Subsection 3.2.

For $x > 0$ the inversion of the Fourier transforms, needed for the calculation of the velocity components, can be found by deforming the complex k-integration contour into the complex plane around a branch-cut chosen along the positive imaginary k-axis. For $x < 0$ the integration contour can be closed in the lower half complex k-plane yielding that it is zero. This means that there is no perturbation of the boundary layer flow upstream of $x = 0$. For $x > 0$ the following result is obtained after inversion of the Fourier integrals

$$\bar{u}(x,Y) = 2Y + \mu Ai(0)6\ 2^{1/3}\Big(\frac{\sqrt{3}}{2\pi^2}x^{-1/3}\Gamma(\frac{1}{3}) + \frac{1}{2}k_0^{1/3}\sin(k_0 x + \pi/6 - \delta) + \frac{k_0}{\pi}\frac{\sqrt{3}}{4}\cos\delta\int_0^{\infty}\frac{k^{1/3}e^{-kx}}{k^2+k_0^2}dk - \frac{1}{\pi}\frac{\sqrt{3}}{4}\sin\delta\int_0^{\infty}\frac{k^{4/3}e^{-kx}}{k^2+k_0^2}dk\Big)Y + \ldots$$

or for brevity

$$\bar{u}(x,Y) = 2Y + \mu g(x)Y + \ldots, \tag{43}$$

where $g(x)$ is defined by

$$g(x) = Ai(0)\,6\,2^{1/3}\left(\frac{1}{2}k_0^{1/3}\sin(k_0x+\pi/6-\delta)+\right.$$
$$+\frac{\sqrt{3}}{2\pi^2}x^{-1/3}\Gamma\left(\frac{1}{3}\right)+\frac{3}{4}\frac{\cos\delta\,k_0x^{2/3}}{\Gamma\left(\frac{2}{3}\right)}\left(1-(k_0x)^{-1/6}S_{\frac{7}{6},\frac{1}{2}}(k_0x)\right)+$$
$$\left.+\frac{1}{2}\frac{\sin\delta\,(k_0x)^{5/6}x^{-1/3}}{\Gamma\left(\frac{2}{3}\right)}\left(S_{\frac{1}{6},\frac{1}{2}}(k_0x)-(k_0x)^{-5/6}\right).\right. \tag{44}$$

Here $S_{\mu,\nu}(z)$ is a Lommel function defined in Abramowitz and Stegun [12]. For large x the first term in $g(x)$ dominates and is represented by a simple sinusoidal form.

In **Figure 2** the function $g(x)$ is plotted and compared with the shape of the boundary $f(x)$. It is noted that both functions have the same period with $g(x)$ ahead of $f(x)$ with a phase that for large x becomes $\pi/6$. Since $g(x)$ is the correction of the wall shear stress due to the wavy wall, this result can be used to pinpoint the position where separation first occurs. This position is where $g(x)$ has a minimum, *i.e.*, $\pi/6$ before the minimum of $f(x)$.

The behaviour of $g(x)$ is also essential for the particle deposition rate since, as will be shown below, $g(x)$ is at its maximum where the concentration boundary layer thickness is at its minimum. Correspondingly, the concentration boundary layer thickness is at its maximum at the point of first separation. From (36) the general expression for the concentration boundary layer thickness can be derived as

$$h(x) = \left(\frac{9}{2}\right)^{1/3}\frac{1}{\left(1+\frac{1}{2}\mu g(x)\right)^{1/2}}\left\{\int_0^x\left(1+\frac{1}{2}\mu g(\xi)\right)^{1/2}d\xi\right\}^{1/3} \tag{45}$$

Expanding (45) results in

$$h(x) = \left(\frac{9}{2}\right)^{1/3}x^{1/3}\left(1-\frac{1}{4}\mu g(x)+\frac{1}{12x}\int_0^x\mu g(\xi)d\xi\right)+\ldots \tag{46}$$

where it can be noted that the expansion (46) is invalid for very small x. The local deposition of particles can be obtained from the normal diffusive flux at the wall, given by

$$j_n = -\frac{1}{\mathrm{Pe}}(\hat{n}\cdot\nabla)c\Big|_{Y=0}. \tag{47}$$

Now, by inserting (45) into (47) the local flux is given by

$$j_n = \frac{3}{\Gamma\left(\frac{1}{3}\right)}\left(\frac{2}{9}\right)^{1/3}\mathrm{Pe}^{-2/3}\theta(x), \tag{48}$$

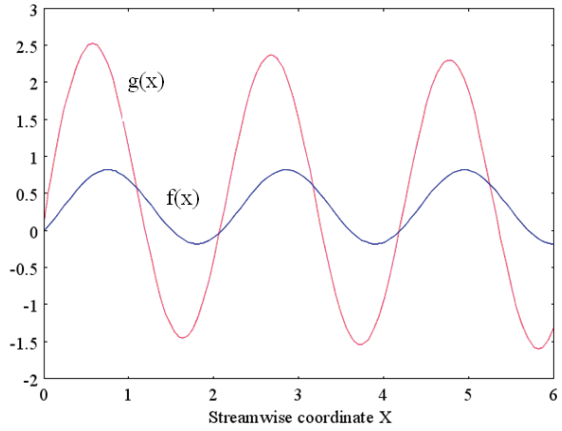

Figure 2. The functions $g(x)$ and $f(x)$.

or with numerical values

$$j_n = 0.6783\,\mathrm{Pe}^{-2/3}\theta(x)$$

where

$$\theta(x) = x^{-1/3}\left(1+\frac{1}{4}\mu g(x)-\frac{1}{12x}\int_0^x\mu g(\xi)d\xi\right)+. \tag{49}$$

Please observe that the scaling with Pe is the same as for ordinary pipe flow ($\mu = 0$).

Since the largest deposition occurs for the minimum thickness of $h(x)$, we note from (44-45) that the largest deposition is localized to the region just before the maximum of $f(x)$, which for the wall geometry defined in (42) is in fact approximately $\pi/6$ ahead of the maximum of $f(x)$. It follows that the minimum deposition occurs at the point of first separation.

Using expression (44), an analytic expression for the integral in (45) can be obtained as

$$\int_0^x g(\xi)\,d\xi = Ai(0)\,6\,2^{1/3}\left(\frac{1}{\Gamma\left(\frac{2}{3}\right)}x^{2/3}\left(\frac{3}{2\pi}-\frac{3}{10}\sin\delta\right)+\right.$$
$$+\frac{\cos\delta\,k_0^{-1/6}x^{1/2}}{2\Gamma\left(\frac{2}{3}\right)}S_{\frac{1}{6},\frac{1}{2}}(k_0x))+\frac{3}{10}\frac{\sin\delta\,k_0^{-1/6}x^{1/2}}{2\Gamma\left(\frac{2}{3}\right)}S_{\frac{7}{6},\frac{3}{2}}(k_0x))-$$
$$\left.+\frac{1}{2}\frac{\sin\delta\,k_0^{-7/6}x^{-1/2}}{\Gamma\left(\frac{2}{3}\right)}S_{\frac{1}{6},\frac{1}{2}}(k_0x)\right). \tag{50}$$

Combining this with (46) the local deposition rate given by (48) can be calculated. In **Figure 3**, the local deposition rate is plotted as a function of x for a finite and a zero value of μ. From this figure it is clearly seen that the maximum local deposition is slightly ahead of the minimum radius of the pipe.

It is also of interest to calculate the cumulative depo-

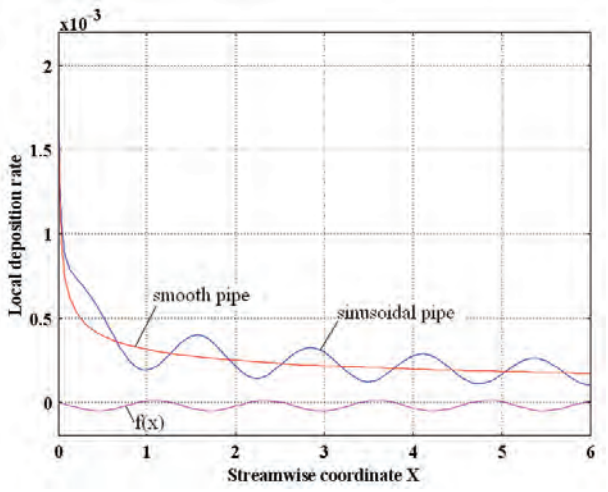

Figure 3. Local deposition rates for finite and zero value of μ. To connect the results with the ring structure, the shape of the rings $f(x)$ are also shown.

sition after a length X by performing the surface integral over the azimuth angle and the x-coordinate. This can be done analytically, but the expression is rather complicated and is omitted for brevity. The cumulative deposition after length X is instead written as

$$C(X)=\frac{6\pi}{\Gamma(\frac{1}{3})}(\frac{2}{9})^{-1/3}Pe^{-2/3}\Theta(\mu,X,k_0,\delta) \qquad (51)$$

where

$$\Theta(X)=\int_0^X x^{-1/3}(1+\frac{1}{4}\mu g(x)-\frac{1}{12x}\int_0^x \mu g(\xi)d\xi+...)dx\,. \qquad (52)$$

To get an expression for the probability of a particle to adhere to the boundary after a length X, (48) is divided by the inlet flux, which in dimensionless quantities is equal to $\pi/2$ so

$$P(X)=\frac{12}{\Gamma(\frac{1}{3})}(\frac{2}{9})^{-1/3}Pe^{-2/3}\Theta(\mu,X,k_0,\delta)\,. \qquad (53)$$

For cylinder tube flow $\mu=0$ a rather neat expression materializes

$$P_{cyl}(X)=\frac{18}{\Gamma(\frac{1}{3})}(\frac{2}{9})^{-1/3}Pe^{-2/3}X^{2/3}=4.0698Pe^{-2/3}X^{2/3}. \qquad (54)$$

This result is valid for a cylindrical smooth-walled tube, and is in agreement with the result given by Ingham [6] for a fully developed parabolic velocity profile. Analysis of (49) and (50) shows that the total deposition for finite μ is somewhat greater than for the case of an ordinary pipe, and effects from the waviness of the wall are clearly revealed, as exemplified in **Figure 4** where the cumulative deposition given by (50) is plotted for different amplitudes of the wall perturbation. The values of the dimensionless numbers are Re = 450 and Pe = 100000, corresponding approximately to light breathing conditions in generation 4 [12] with a particle diameter of 10 nm and pipe radius 2.25 mm. Results are shown for an ordinary smooth pipe, and for ring configurations with small ring-amplitudes $\zeta=0.025$ and $\zeta=0.05$, where we note the relation with μ as $\varsigma=1/2\ \mu\ \mathrm{Re}^{-1/3}$. The spacing of the rings is chosen such that there are five rings within a length of 6 radii, corresponding to the wavenumber $k_0=5$.

3. NUMERICAL RESULTS

3.1. Comparison of Theory with Numerical Solution for Parabolic Flow

The approximate theoretical analysis in Section 2 can only provide results for small ring-amplitudes without flow separation. For larger amplitudes it is necessary to solve the equations numerically. Hence, a numerical solution of (1-2) is considered. The commercial software Comsol Multiphysics 3.5 is used to serve this purpose, since this code enables the Navier-Stokes and convective-diffusion equations to be solved simultaneously. In Comsol, the finite element method is used, and an adaptive

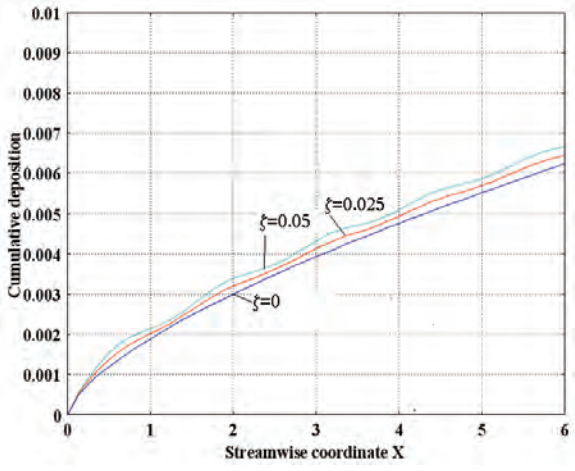

Figure 4. Cumulative deposition P along the wall as a function of position X as obtained from (50) for different ring-amplitudes.

mesh-refinement method is applied. For the implementation of the geometry and for post-processing, Comsol script or Matlab are used, both of which can be conveniently applied together with Comsol Multiphysics. To

start with, the equations for the wavy wall are solved (42) and then the theory presented in the previous section is used to validate the numerical results.

First, the theoretical (51) and numerical results for smooth-walled pipe flow are compared. The agreement is very good for Pe that equals to 100000 and with a Re of 450, despite the boundary layer approximation used in the theoretical analysis, see **Figure 5**. Next, the rings with a small amplitude of $\zeta = 0.025$ diameters is studied. The agreement between the local deposition rate as calculated from the numerical method and the analytic method presented in the former section is rather good, see **Figure 6**. The agreement between the methods for the corresponding cumulative deposition is also relatively good; where the deviation is most notable for small and large X, see **Figure 7**. It is therefore concluded that the numerical results are reliable and we proceed with considering larger values of the ring-amplitudes.

Consider a ring-amplitude of $\zeta = 0.1$, mimicking the size of amplitudes used in other studies of effects of the cartilaginous rings, e.g. (Martonen *et al*. 1994) [12]. There is a qualitative difference in the flow pattern between this case and that for small ζ. For $\zeta = 0.1$. The flow separates in the region between the rings, see the lower plot in **Figure 8**, while for $\zeta < 0.06$, there is no separation, see upper plot in **Figure 8**.

A rough criterion for separation can be obtained from the theory developed in Subsection 2.1. From the expression for the velocity profile at the wall $g(x)$ we find for large x that the wall shear stress becomes

$$\left.\frac{\partial \bar{u}}{\partial Y}\right|_{Y=0} = 2 + g(x)\mu \qquad (55)$$

at minimum $g(x)$ and for large x we have zero wall shear stress if

$$2\,\mathrm{Re}_{crit}^{-1/3} \approx Ai(0)\,6\,2^{1/3} k_0\, \varsigma_{crit}\,. \qquad (56)$$

Solving for critical amplitude we have

$$\varsigma_{crit} \approx 0.75\, k_0^{1/3}\, 2\,\mathrm{Re}_{crit}^{-1/3}\,. \qquad (57)$$

For the present case this gives the critical amplitude of about 0.06 which is quite close to the estimate from the numerical analysis.

In **Figure 8** the red area corresponds to high concentration c while the blue area corresponds to regions of lower concentration. Remarkably, but in accordance with the theory, the deposition is not larger in the separated regions, instead the maximum deposition occurs at the point of reattachment, *i.e.*, just before minimum contraction. This is also in agreement with the theory developed in Subsection 2.2 where the largest deposition is obtained at the maxima of the function $g(x)$ and the lowest deposition at the point of minimum $g(x)$, the latter corresponding to the position of first separation.

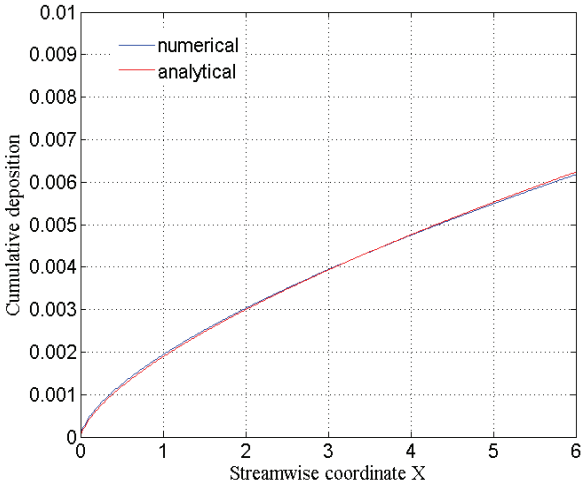

Figure 5. Comparison between numerical and analytical solutions for smooth pipe.

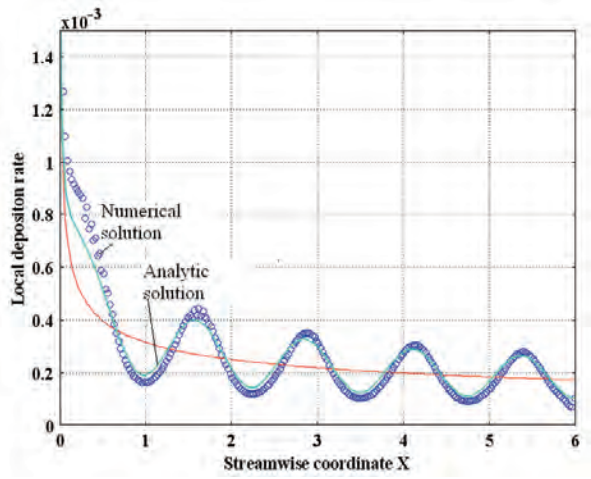

Figure 6. Comparison with numerical and analytical results for a ring amplitude $\zeta = 0.05$.

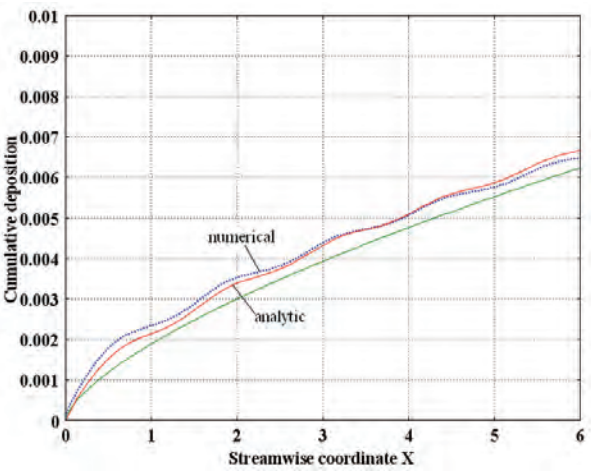

Figure 7. Cumulative deposition P along the wall as a function.

In **Figure 9** the cumulative deposition for amplitudes $\zeta = 0.1$ and $\zeta = 0.15$ are shown. It is noted that the largest increase in deposition compared to a smooth pipe is in the region before the first ring, where the deposition for the case $\zeta = 0.1$ is about 40% higher than for the smooth-walled tube.

3.2. Analytic and Numerical Results for Developing Flow

Since after an airway bifurcation approximately half the flow in each branch will have a developing character, we here consider a developing flow in an axisymmetric tube with cartilaginous rings. For this case an analytic approach is nontrivial, even without rings; hence, the case with cartilaginous rings is only treated numerically. Neglecting the rings, different approximate results have been presented in the literature. Ingham [7,8] applies an integral approach for the entry flow and solves the convective-diffusion equation numerically. An approximate expression for the deposition, similar to (51), is provided in the form

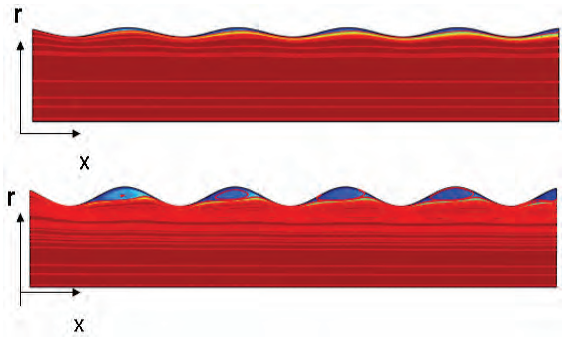

Figure 8 Concentration distribution and streamlines for $\zeta = 0.06$ (upper) and $\zeta = 0.1$ (lower).

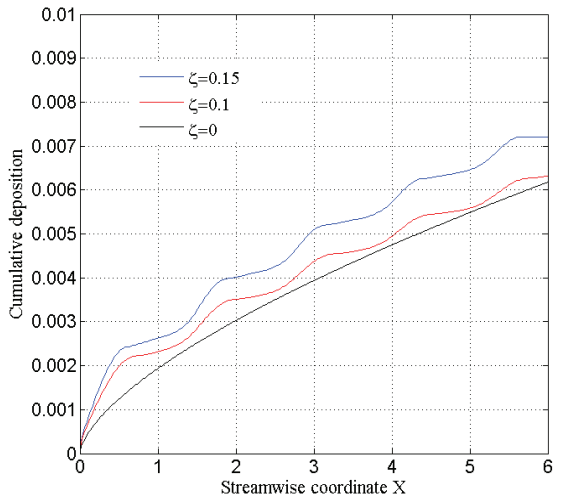

Figure 9. Cumulative deposition for different ring amplitudes.

$$P_{cyl}(X) = 3.023\left(\frac{X}{\mathrm{Re}}\right)^{5/9}\left(\frac{\mathrm{Pe}}{\mathrm{Re}}\right)^{-2/3} \quad (58)$$

which is valid for small $X/R < 0.02$. A similar approximate analytical result using a more heuristic method has been given by Martonen *et al.* [9] as

$$P_{cyl}(X) = 2.75\left(\frac{X}{\mathrm{Re}}\right)^{1/2}\left(\frac{\mathrm{Pe}}{\mathrm{Re}}\right)^{-2/3}. \quad (59)$$

We note the difference in the scaling for X/Re in (55) and (56). It is therefore of interest to consider this problem numerically where the applied conditions at the inlet correspond to uniform flow and the volume flux is the same as for the parabolic flow case with Re = 450 and Pe = 100000.

The numerical result obtained fits well in between the results of Ingham and Martonen as shown in **Figure 10**, where the solid red line corresponds to the numerical solution and the dash-dotted curve corresponds to the result (55) and the dashed line corresponds to the result (56). For comparison the analytical results for the fully developed case is also shown as dotted. It is seen that the deposition is about 25% larger for the developing flow as compared to the parabolic flow.

Since there is a disagreement in the power between (55) and (56), the power for the numerical solution is calculated to 0.5437 for large X, which is more close to the value $5/9 \approx 0.5556$ provided by Ingham [8] than the value 1/2 given by Martonen *et al.* [9]. On the other hand, the results by Martonen *et al.* [9], obtained from (56), have a good conformity near the entrance of the tube, which is as expected since the flow is of here of Blasius type, which has the power 1/2 (Schlichting *et al.* [13]).

Next we consider the total deposition for developing

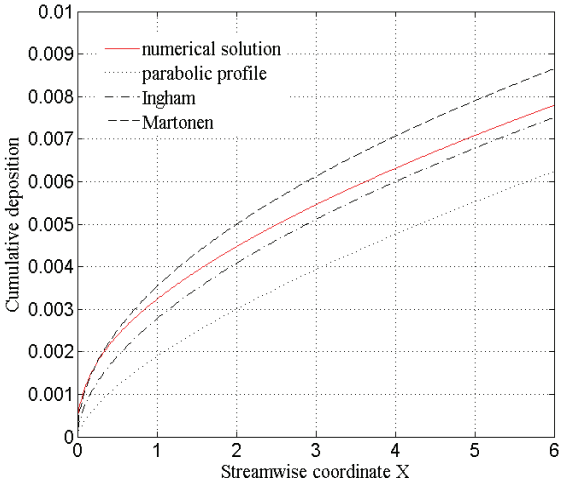

Figure 10. Comparison of different analytical results (55-56) with numerical solution for a smooth pipe with developing velocity profile.

flow for rings with amplitudes $z = 0.1$ and $\zeta = 0.15$. See **Figure 11**. The results show that the largest increase in deposition occurs before the first cartilage ring with an increase of the order of 25% for $\zeta = 0.1$ and 35% for $\zeta = 0.15$, when compared to the case of a smooth pipe. The total deposition is as for the fully developed case also increased considerably by increasing the amplitude from $\zeta = 0.1$ to $\zeta = 0.15$.

Considering other shapes of the cartilaginous rings is also of interest. The shape studied by Martonen *et al.* [12] is presented in **Figure 12**. To compare this case with the case studied above we consider the same number of rings. This means that the region between the rings is larger than for the case of the sinusoidal shape discussed above. Since these regions have lower deposition rates than in the region of smaller cross section the overall deposition is smaller than for the corresponding sinusoidal shapes see **Figure 13**.

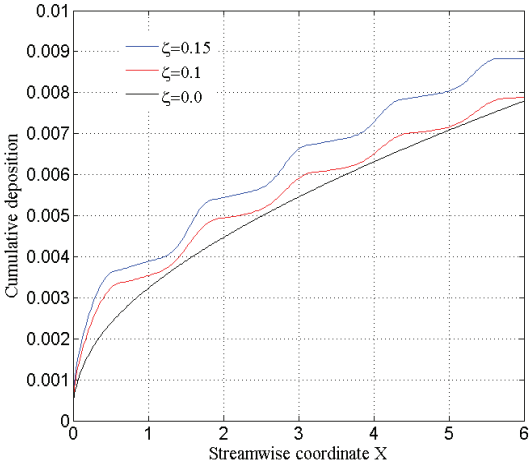

Figure 11. Cumulative deposition for different ring amplitudes for the case of developing flow.

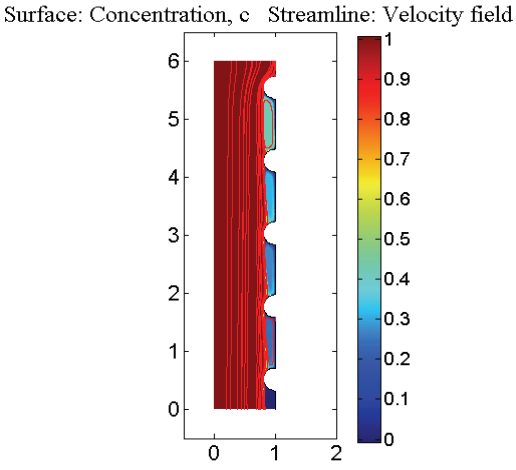

Figure 12 Cartilaginous ring configuration of Martonen type.

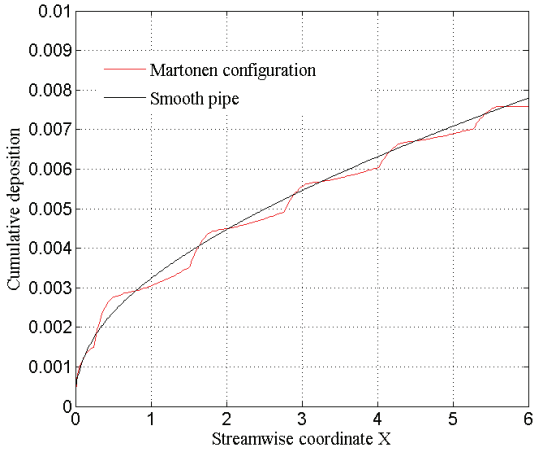

Figure 13. Cumulative deposition for the ring configuration by Martonen *et al* [12].

4. CONCLUSIONS AND DISCUSSION

The deposition of nano-sized spherical particles on thewalls of a cylindrical tube with periodically spaced cartilaginous rings has been explored. For fully developed flow and for small ring amplitudes analytic formulas are derived. It is found that the rings increase the deposition rate and it is shown analytically that the largest deposition occurs at a position approximately $\lambda/12$ before the minimum cross section where λ is the spacing between the rings. These results are validated with numerical computations. For larger amplitude of the rings $\zeta > 0.06$ corresponding to light breathing conditions, the flow separates and the largest local deposition is at the point of reattachment. Although it has a strong influence on the variation in deposition along the tube the total deposition is marginally effected by the amplitude of the rings for small amplitudes $\zeta < 0.10$. For slightly larger values of the amplitude $\zeta = 0.05$, the total deposition is however increased considerably.

For the case of a developing smooth-wall flow the deposition rates are 25% larger than for fully developed flow while the additional deposition effect caused by the cartilaginous rings is of the same order as for the fully-developed flow. The rate dependency can be of interest for flow in a tube downstream a bifurcation where approximately half of the flow attaches to a new wall. A comparison with the ring shapes considered by Martonen *et al.* [12] also illustrates another effect, the effect of the ratio of ring radius to the length between the rings. Considering the same number of rings as the sinusoidal shapes, the distance between the rings is larger and therefore from theory we know that these regions of separated

flow have lower deposition rates than in the regions close to the rings, and therefore the overall deposition is smaller.

Future work involves other breathing conditions especially heavy breathing conditions (large Pe) and non-spherical particles such as fibres. The effect of asymmetric flow after a bifurcation at inlet is also of great interest. Particle deposition due to cartilaginous rings in the trachea will also be considered. The flow in the trachea is in general turbulent and the present results which are valid for laminar flow can therefore then only be applied for very weak breathing conditions. Here it is of interest to investigate whether the separation due to the rings that occur for the laminar case will still be present in the turbulent case, since it is a well known phenomenon in fluid mechanics that turbulence resists the onset of separation.

In recent experiments (Åkerstedt *et al.* [15]) on carbon nanotubes it has been seen that the particles are electrically charged, therefore studies of deposition due to charged particles will also be considered.

5. ACKNOWLEDGEMENTS

The research is sponsored by the Swedish Research Council.

REFERENCES

[1] Poland, C.A., Duffin, R., Kinloch, I., Maynard, A., Wallace, W.A.H., Seaton, A., Stone, V., Brown, S., Macnee, W. and Donaldson, K. (2008) Carbon nanotubes introduced into the abdominal cavity of mice show asbestos-like pathogenicity in a pilot study. *Nature Nanotechnology*, **3(7)**, 423-428.

[2] Dobrovolskaia, M.A. and McNeil, S.E. (2007). Immunological properties of engineered nanomaterials. *Nature Nanotechnology*, **2(8)**, 469-478.

[3] Zhang, Y. and Finlay, W.H. (2005) Measurement of the effect of cartilaginous rings on particle deposition in a proximal lung bifurcation model. *Aerosol Science and Technology*, **39(5)**, 394-399.

[4] Högberg, S.M., Åkerstedt, H.O., Lundström, T.S. and Freund, J.B. (2008) Numerical model for fiber transport in the respiratory airways. *Proceedings of the* 19*th International Symposium on Transport Phenomena* (*ISTP*-19), Reyk-javik.

[5] Risken, H. (1996) The Fokker-Planck equation. Springer-Verlag, Berlin.

[6] Ingham, D.B. (1975) Diffusion of aerosols from a stream flowing through a cylindrical tube. *Journal of Aerosol Science*, **6(2)**, 125-132.

[7] Ingham, D.B. (1984) Diffusion of aerosols from a stream flowing through a short cylindrical tube. *Journal of Aerosol Science*, **15(5)**, 637-641.

[8] Ingham, D.B. (1991) Diffusion of aerosols in the entrance region of a smooth cylindrical pipe. *Journal of Aerosol Science*, **22(3)**, 253-257.

[9] Martonen, T., Zhang, Z. and Yang, Y. (1996) Particle diffusion with entrance effects in a smooth-walled cylinder. *Journal of Aerosol Science*, **27(1)**, 139-150.

[10] Sobey, I.J. (2000) Introduction to interactive boundary layer theory. *Oxford Applied Engineering and Mathematics*, Oxford University Press, Oxford.

[11] Chapman, S. and Cowling, T.G. (1952) The mathematical theory of non-uniform gases. Cambridge University Press, London.

[12] Martonen, T.B., Yang, Y. and Xue, Z.Q. (1994) Influence of cartilaginous rings on tracheobronchial fluid dynamics. *Inhalation Toxicology*, **6(3)**, 185-203.

[13] Abramowitz, M. and Stegun, I.A. (1972) *Handbook of Mathematical Functions*, Dover, New York.

[14] Schlichting, H. and Gersten, K. (2000) Boundary layer theory. 8th Edition, Springer-Verlag, Pope.

[15] Åkerstedt, H.O., Lundström, T.S. and Högberg, S.M. (2007) Electrostatic filtration of airborne nano-particles. *Journal of Nanostructured Poymers and Nanocomposites.* **3(4)**, 111-115.

Vol.2, No.7, 780-785 (2010)
doi:10.4236/ns.2010.27098

Natural Science

Flow behavior of UCM viscoelastic fluid in sudden contraction channel

Chunquan Fu[1], Hongliang Zhou[2], Hongjun Yin[1]*, Huiying Zhong[1], Haimei Jiang[3]

[1]Key Laboratory of Enhanced Oil and Gas Recovery Ministry of Educaion, Northeast Petroleum University, Daqing, China;
*Corresponding Author: yinhj7176@126.com
[2]Daqing Oilfield Company Ltd., Daqing, China; 13836758851@163.com
[3]China National Offshore Oil Company Research Center, Beijing, China; 3629461@163.com

Received 20 April 2010; revised 22 May 2010; accepted 26 May 2010.

ABSTRACT

A finite volume method for the numerical solution of viscoelastic flows is given. The flow of a differential upper-convected Maxwell (UCM) fluid through a contraction channel has been chosen as a prototype example. The conservation and constitutive equations are solved using the finite volume method (FVM) in a staggered grid with an upwind scheme for the viscoelastic stresses and a hybrid scheme for the velocities. An enhanced-in-speed pressure-correction algorithm is used and a method for handling the source term in the momentum equations is employed. Improved accuracy is achieved by a special discretization of the boundary conditions. Stable solutions are obtained for higher Weissenberg number (*We*), further extending the range of simulations with the FVM. Numerical results show the viscoelasticity of polymer solutions is the main factor influencing the sweep efficiency.

Keywords: Upper-Convected Maxwell (UCM) Model; Finite Volume Method; Viscoelasticity; Sweep Efficiency

1. INTRODUCTION

In the recent years, numerical simulation of viscoelastic flows has been a powerful tool for understanding the fluid behavior in a variety of processes of both industrial and scientific interest [1,2]. Polymeric fluids, owing to their viscoelastic characters, are of particular interest in the numerical simulation because of their wide applications in material processing and their different behavior from that of Newtonian fluids in ways which are often complex and striking. Although there have been many successful numerical predictions of elastic fluid flows [3-5], in which the Weissenberg number (*We*), standing for the elasticity, is low.

In the process of water flooding alone, the residual oil remaining within porous media is difficult to be displaced or recovered. In comparison, polymer flooding is more effective. Experimental results [2,5,6] indicated the viscoelasticity of polymer solutions can enhance the displacement efficiency, but there have been few theoretical studies on this subject.

In this work, with the upper-convected Maxwell (UCM) model, the fluid flow through a 4:1 sudden contraction channel is studied by using a stable finite volume scheme. An enhanced-in-speed pressure correction algorithm and a method for handling the source term in the momentum equations are employed. The simulation accuracy is improved by a special discretization of the boundary conditions. The presented method succeeds in providing accurate numerical solutions, and elasticity levels up to $We = 3.0$. Where with the finite difference method the *We*, standing for the elasticity, is less than 0.5 [7,8].

In the following sections, the description of the problem, the mathematical model of the flow and the solution method are described respectively. The discretization of the source term and the boundary conditions are separately examined. The contours of velocity, stream function and pressure are drawn. Finally, the simulation results are presented and conclusions are drawn regarding the use of the FVM for viscoelastic flow simulations.

Project supported by the 973 National Basic Research Program of China (Grant No: 2005cb221304), by Heilongjiang Provincial Science and Technology Plan Project (Grant No: GZ09A407) and by the Research Program of Innovation Team of Science and Technology in Enhanced Oil and Gas Recovery (Grant No: 2009td08)

2. MATHETICL MODEL

2.1. The Model of Sudden Contraction Channel

The micro-pores of an actual reservoir are in general complicated. These pores are often simplified in numerical simulation. The problem geometry is shown in **Figure 1**. It concerns the flow of a UCM fluid through a planar 4:1 sudden contraction channel. Then, flow behavior of viscoelastic polymer solutions is studied with this simplified physical model. Note that the dimension in the **Figure 1** are dimensionless.

2.2. Governing Equations

The isothermal flow through contraction for incompressible fluids, such as polymer solutions and melts, is governed by the equation of continuity and motion, which can be expressed as

$$\nabla \cdot v = 0 \tag{1}$$

$$\rho v \cdot \nabla v = -\nabla p + \nabla \cdot \tau \tag{2}$$

where v is the velocity vector, p the pressure, τ the extra stress tensor and ρ the density.

The constitutive equation that relates the stresses τ to the deformation history is predescribed by the UCM model, which in its differential form is written as

$$\tau + \lambda \overset{\nabla}{\tau} = \mu \dot{\gamma} \tag{3}$$

where λ is the relaxation time, μ a constant viscosity, $\dot{\gamma}$ the rate-of-strain tensor and $\overset{\nabla}{\tau}$ Oldroyd's upper convected derivative of the stress tensor τ.

The above equations are non dimensionalized by introducing the non-dimensional variables

$$x_D = \frac{x}{L}, y_D = \frac{y}{L}, \tau_D = \frac{L}{\eta U}\tau,$$

$$u_D = \frac{u}{U}, v_D = \frac{v}{U}, p_D = \frac{L}{\eta U}p.$$

where the characteristic velocity (U) and characteristic length (L) are taken as the average velocity in the downstream half channel and the width of the downstream half channel, respectively, η is the constant shear viscosity, u is the velocity component in the x direction, and v is the velocity component in the y direction.

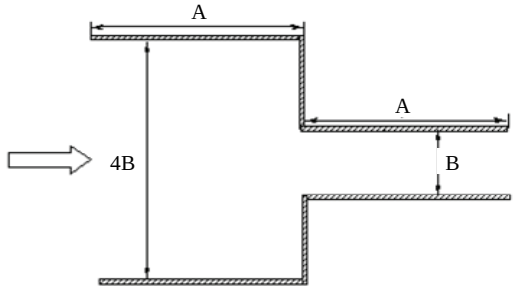

Figure 1. The model of sudden contraction channel.

Therefore, in the dimensionless form the governing equations are given in the following, where the subscript D is omitted for brevity.

For a two-dimensional system in a rectangular co-ordinates (x,y) with the velocity components (u,v), the continuity **Eq.1** can be written as

$$\frac{\partial u}{\partial x} + \frac{\partial v}{\partial y} = 0 \tag{4}$$

The momentum equation (**Eq.2**) is given by

$$Re[\frac{\partial}{\partial x}(uu) + \frac{\partial}{\partial y}(uv)] = -\frac{\partial p}{\partial x} + \frac{\partial \tau_{xx}}{\partial x} + \frac{\partial \tau_{xy}}{\partial y} \tag{5}$$

$$Re[\frac{\partial}{\partial x}(vv) + \frac{\partial}{\partial y}(vu)] = -\frac{\partial p}{\partial y} + \frac{\partial \tau_{xy}}{\partial x} + \frac{\partial \tau_{yy}}{\partial y} \tag{6}$$

and the constitutive equations for the UCM fluid can be written as

$$We[\frac{\partial}{\partial x}(u\tau_{xx}) + \frac{\partial}{\partial y}(v\tau_{xx})]$$
$$= 2\frac{\partial u}{\partial x} - (1 - 2We\frac{\partial u}{\partial x})\tau_{xx} + 2We\frac{\partial u}{\partial y}\tau_{xy} \tag{7}$$

$$We[\frac{\partial}{\partial x}(u\tau_{yy}) + \frac{\partial}{\partial y}(v\tau_{yy})]$$
$$= 2\frac{\partial v}{\partial y} - (1 - 2We\frac{\partial v}{\partial y})\tau_{yy} + 2We\frac{\partial v}{\partial x}\tau_{xy} \tag{8}$$

$$We[\frac{\partial}{\partial x}(u\tau_{xy}) + \frac{\partial}{\partial y}(v\tau_{xy})]$$
$$= (\frac{\partial v}{\partial x} + \frac{\partial u}{\partial y}) - \tau_{xy} + We(\frac{\partial v}{\partial x}\tau_{xx} + \frac{\partial u}{\partial y}\tau_{yy}) \tag{9}$$

where τ_{xx}, τ_{xy} and τ_{yy} are the stress components in usual sense.

The Weissenberg number (We) and Reynolds number (Re) in **Eq.9** are defined by

$$We = \lambda\frac{U}{L}, Re = \frac{\rho UL}{\eta}.$$

To solve **Eqs.4-9**, the boundary and initial conditions are given below.

For the full-developed steady Poiseuille flow, the inlet boundary condition is

$$u = 6(\frac{1}{4} - y^2), v = 0, \tau_{xx} = 2We(\frac{\partial u}{\partial y})^2,$$

$$\tau_{yy} = 0, \tau_{xy} = \frac{\partial u}{\partial y}.$$

No-slip conditions are imposed on solid boundaries

and symmetry conditions are specified on the symmetrical axis [9].

At the outlet a fully developed velocity profile is imposed with the homogeneous Neumann boundary conditions for the extra-stress, *i.e.*,

$$\frac{\partial \tau_{xx}}{\partial x} = \frac{\partial \tau_{xy}}{\partial x} = \frac{\partial \tau_{yy}}{\partial x} = 0$$

3. NUMERICAL ALGORITHM

The constitutive relation **Eq.3** is solved together with **Eqs.1** and **2** using the FVM. Here some details about our own implementation of the method are given.

3.1. Computational Grid

A grid is placed in the computational domain and a control volume is associated with each unknown on the grid. This grid, called the reference grid, remains fixed in space for all time. In this study, we assume that the sides of each control volume are aligned with the coordinate axes. Each component is integrated over an appropriate control volume [10]. The grid is shown in **Figure 2**.

The staggered grid is used in which the different dependent variables are approximated at different mesh points. Both meshes ensure that the solution is not polluted by spurious pressure modes. On a non-staggered mesh the familiar chequerboard mode is applied.

3.2. Discretization

A simple finite volume formulation is used for the discretization and the first-order Euler implicit formula is used for temporal differences because of its simplicity for implementation and unconditional stability in numerical computations.

In employing the FVM, the governing equations are written in the following general form [11]:

$$\nabla \cdot (mv\varphi) = \nabla \cdot (\Gamma \nabla \varphi) + S \qquad (10)$$

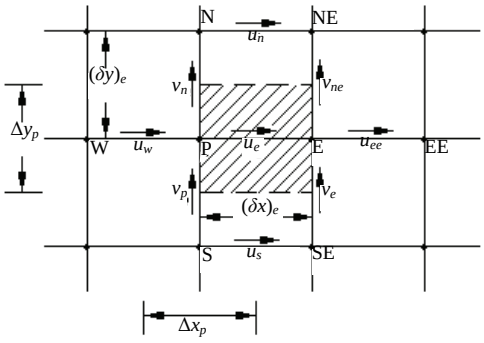

Figure 2. Staggered grid.

3.2.1. Discretization of Continuity Equations

The discretized continuity equation reflects the mass conservation for each cell:

$$F_e - F_w + F_n - F_s = 0 \qquad (11)$$

where

$$F_e = Reu_e\Delta y\,,\quad F_w = Reu_w\Delta y\,,$$

$$F_n = Reu_n\Delta x\,,\quad F_s = Reu_s\Delta x\,.$$

F_e is the outgoing mass flow rates at cell face e, u_e refers to the cell face velocity component, and the same for F_w, F_n, F_s and u_w, u_n, u_s.

3.2.2. Discretization of Momentum Equations

Eqs.5 and **6** can be written in the general form of **Eq.10** using the transformation

$$\tau'_{xx} = \tau_{xx} - 2\eta\frac{\partial u}{\partial x} \qquad (12)$$

$$\tau'_{yy} = \tau_{yy} - 2\eta\frac{\partial v}{\partial y} \qquad (13)$$

$$\tau'_{xy} = \tau_{xy} - \eta\left(\frac{\partial u}{\partial y} + \frac{\partial v}{\partial x}\right) \qquad (14)$$

where τ' is the elastic part of the stress tensor τ [12].

Substituting **Eqs.11-13** into the momentum equations and assuming a constant viscosity turn **Eqs.5** and **6** into

$$\frac{\partial}{\partial x}(\mathrm{Re}uu) + \frac{\partial}{\partial y}(\mathrm{Re}uv) = \frac{\partial}{\partial x}\left(\frac{\partial u}{\partial x}\right) + \frac{\partial}{\partial y}\left(\frac{\partial u}{\partial y}\right) + \frac{\partial \tau'_{xx}}{\partial x} + \frac{\partial \tau'_{xy}}{\partial y} + \frac{\partial}{\partial x}\left(\frac{\partial u}{\partial x} + \frac{\partial v}{\partial y}\right) - \frac{\partial p}{\partial x} \qquad (15)$$

$$\frac{\partial}{\partial x}(\mathrm{Re}vv) + \frac{\partial}{\partial y}(\mathrm{Re}vu) = \frac{\partial}{\partial x}\left(\frac{\partial v}{\partial x}\right) + \frac{\partial}{\partial y}\left(\frac{\partial v}{\partial y}\right) + \frac{\partial \tau'_{yy}}{\partial y} + \frac{\partial \tau'_{xy}}{\partial x} + \frac{\partial}{\partial x}\left(\frac{\partial u}{\partial x} + \frac{\partial v}{\partial y}\right) - \frac{\partial p}{\partial y} \qquad (16)$$

In **Eqs.15** and **16** the viscous parts are discretized as the diffusion terms of **Eq.10**, while the other terms on the right-hand side are treated as extra source terms.

Then the final discretized equations of momentum can be expressed symbolically in a general form:

$$a_P u_P = a_E u_E + a_W u_W + a_N u_N + a_S u_S + S_u \qquad (17)$$

where u_P refers to the cell velocity component, and the same for u_E, u_W, u_N and u_S.

$$a_E = \frac{\Delta y}{\delta x_e} + \max(-F_e, 0)\,,$$

$$a_W = \frac{\Delta y}{\delta x_w} + \max(F_w, 0)\,,$$

$$a_{\mathrm{N}} = \frac{\Delta x}{\delta y_{\mathrm{n}}} + \max(-F_{\mathrm{n}}, 0)$$

$$a_{\mathrm{S}} = \frac{\Delta x}{\delta y_{\mathrm{s}}} + \max(F_{\mathrm{s}}, 0)\,.$$

3.2.3. Discretization of Constitutive Equations

The adopted viscoelastic model also has the general transport equation from **Eq.10** without diffusion term ($\Gamma = 0$). To ensure numerical stability, generally, a first-order upwind difference (UD) is used for spatial discretization. Thus, the discretized constitutive equation can be written as

$$a_{ij\mathrm{P}}^{\tau}\tau_{ij\mathrm{P}} = a_{\mathrm{E}}^{\tau}\tau_{ij\mathrm{E}} + a_{\mathrm{W}}^{\tau}\tau_{ij\mathrm{W}} + a_{\mathrm{N}}^{\tau}\tau_{ij\mathrm{N}} + a_{\mathrm{S}}^{\tau}\tau_{ij\mathrm{S}} + S_{\tau ij} \qquad (18)$$

where $\tau_{ij\mathrm{P}}$ refers to the cell stress component, and the same for $\tau_{ij\mathrm{E}}$, $\tau_{ij\mathrm{W}}$, $\tau_{ij\mathrm{N}}$ and $\tau_{ij\mathrm{S}}$.

$$a_{\mathrm{E}}^{\tau} = We\max(-F_{\mathrm{e}}, 0)\,,\quad a_{\mathrm{W}}^{\tau} = We\max(F_{\mathrm{w}}, 0)\,,$$

$$a_{\mathrm{N}}^{\tau} = We\max(-F_{\mathrm{n}}, 0)\,,\quad a_{\mathrm{S}}^{\tau} = We\max(F_{\mathrm{s}}, 0)\,,$$

$$a_{\mathrm{P}}^{\tau} = \Delta x\Delta y + a_{\mathrm{E}}^{\tau} + a_{\mathrm{W}}^{\tau} + a_{\mathrm{N}}^{\tau} + a_{\mathrm{S}}^{\tau}$$

$$S_{\tau_{XX}} = (\frac{4}{3} + 2We\tau_{xx})(u_{\mathrm{e}} - u_{\mathrm{w}})\Delta y +$$

$$2We\tau_{xy}(u_{\mathrm{n}} - u_{\mathrm{s}})\Delta x - \frac{2}{3}(v_{\mathrm{n}} - v_{\mathrm{s}})$$

$$S_{\tau_{xy}} = (1 + We\tau_{yy})(u_{\mathrm{n}} - u_{\mathrm{s}}) + We\tau_{xy}(v_{\mathrm{n}} - v_{\mathrm{s}}) +$$

$$We\tau_{xy}(u_{\mathrm{e}} - u_{\mathrm{w}}) + (1 + We\tau_{xx})(v_{\mathrm{e}} - v_{\mathrm{w}})$$

$$S_{\tau_{yy}} = -\frac{2}{3}(u_{\mathrm{e}} - u_{\mathrm{w}}) + 2We\tau_{xy}(v_{\mathrm{e}} - v_{\mathrm{w}}) +$$

$$(\frac{4}{3} + 2We\tau_{yy})(v_{\mathrm{n}} - v_{\mathrm{s}})$$

where v_{e} refers to the cell face velocity component, and the same for v_{w}, v_{n}, v_{s}.

3.3. Solution of the Discretized Equations

In non-linear problems the equations are solved with iterative methods using an initial guess for the primitive variables and giving an approximate solution. The iterative methods have the advantage of less computer memory as they take advantage of zero elements in the coefficient matrix. In this work, the strongly implicit procedure (SIP) [13-15] is used, which involves the direct, simultaneous solution of the set of equations formed by modification of the original matrix equation. The modified matrix is constructed according to two criteria: 1) the equation set must remain more strongly implicit than in the alternating direction implicit (ADI) case; and 2) the elimination procedure for the modified set must be efficient.

4. RESULTS AND DISCUSSION

As discussed above, a numerical simulation method is used and the stream function contour, velocity contour and pressure contour with different *We* can be obtained. As an example, the stream function and velocity contours with *We* equates 0 to 3.0 are shown in **Figures 3-5**, respectively.

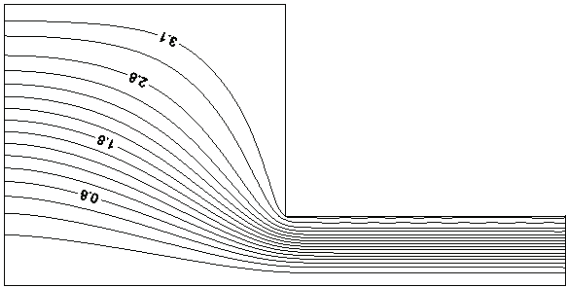

(a) *We* = 0, *Re* = 10^{-5}

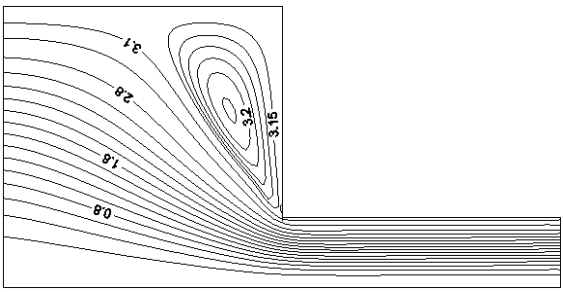

(b) *We* = 0.6, *Re* = 10^{-5}

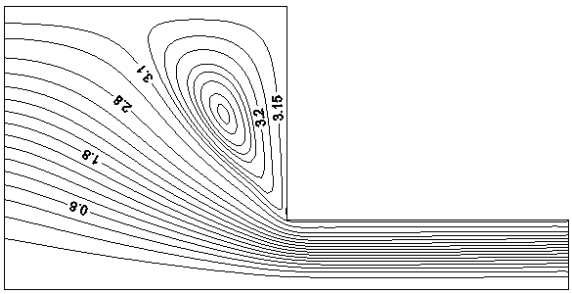

(c) *We* = 1.5, *Re* = 10^{-5}

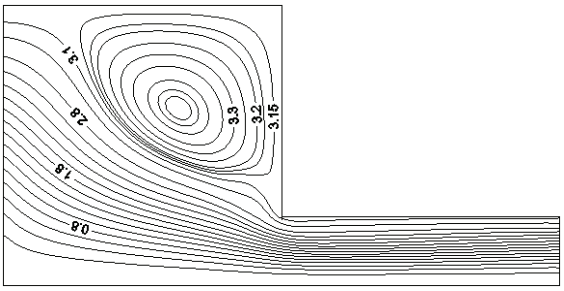

(d) *We* = 3.0, *Re* = 10^{-5}

Figure 3. Stream function contours.

Figure 3 shows the influence of the *We* on the stream function, we can see that when the Reynolds number is smaller, the vortex area is expanding as *We* increasing, and the corresponding vortex strength will be enhanced, thereby the fluid velocity and applied force in the convex corner will increase too. So, displacing the dead oil in convex corner, enhance vortex-convex is an important reason to raise the angle of displacement oil. This is because under the flowing conditions of reservoir (That is, Reynolds number is smaller), the viscoelastic of fluid plays a important role in fluid flow, the stronger the viscoelastic (That is, *We* is larger), the stronger the viscoelastic vortex is.

In **Figure 4**, from the area surrounded by the speed of $\boldsymbol{v}$ = 0.03125, it is seen that the micro sweep area and sweep efficiency increase as the *We* increases.

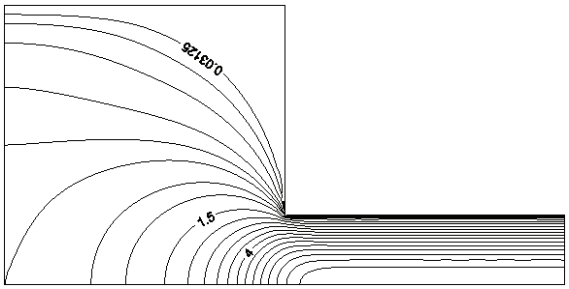

(a) *We* = 0, *Re* = 10^{-5}

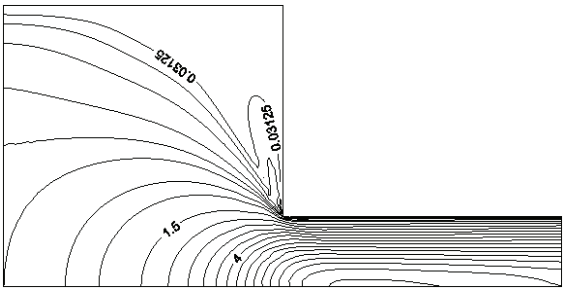

(b) *We* = 0.6, *Re* = 10^{-5}

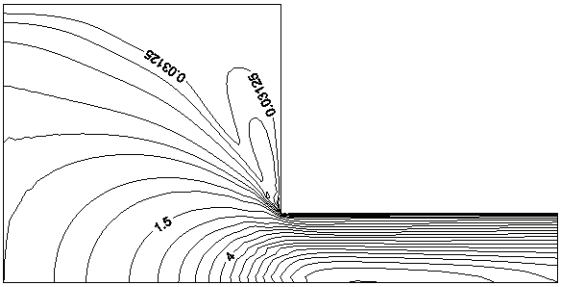

(c) *We* = 1.5, *Re* = 10^{-5}

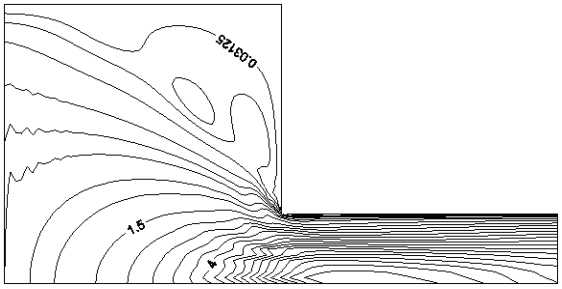

(d) *We* = 3.0, *Re* = 10^{-5}

Figure 4. Velocity contours.

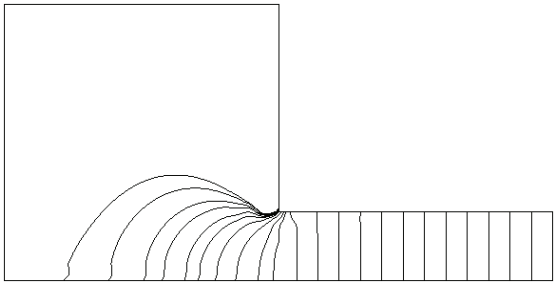

(a) *We* = 0, *Re* = 10^{-5}

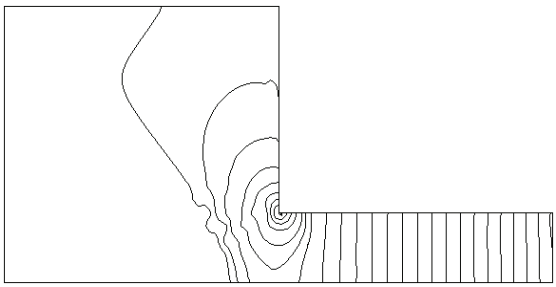

(b) *We* = 0.6, *Re* = 10^{-5}

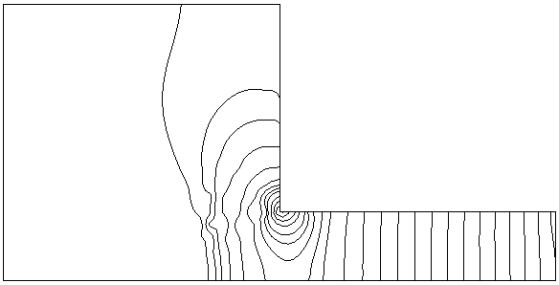

(c) *We* = 1.5, *Re* = 10^{-5}

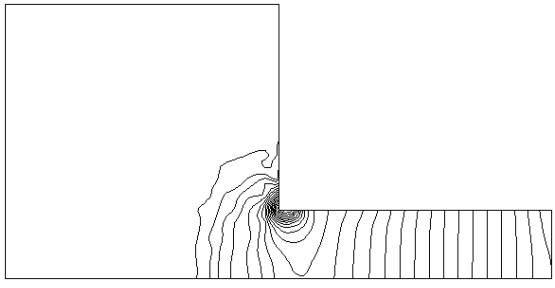

(d) *We* = 3.0, *Re* = 10^{-5}

Figure 5. Pressure contours.

In **Figure 5**, at the downstream of the contraction, the pressures change gently. In the convex area of contraction, pressures vary intensely and the difference grows larger with the increase of *We*. That is to say, the pressure loss mainly happens at corner. The the pressure drop is larger with a bigger *We*. The high pressure drop and high velocity of viscoelastic polymer solution at corner strengthen the displacement and wash action, and it will increase the microscopic sweep efficiency.

5. CONCLUSIONS

In this paper, the flow of a UCM model fluid through a 4:1 sudden contraction channel has been studied using a stable finite volume scheme. The solution method succeeds in obtaining accurate values for all variables at elasticity levels up to *We* = 3.0.

The present simulations reinforce the point that the FVM can be used as a viable alternative for the solution of viscoelastic problems. The results are accurate and offer an improvement over previous numerical solutions. Although the present study has been applied to a UCM fluid in a relatively simple geometry, it can be further extended to other more realistic constitutive equations, such as the Phan-Thien-Tanner or Giesekus-Leonov models, etc. and to other geometries encountered in polymer processing.

Numerical results show that the viscoelasticity of polymer solutions is the main factor influencing sweep efficiency. With increasing elasticity, the flowing area in the corner is enlarged significantly, thus the area with immobile zones becomes smaller. Flow velocity is larger than that for a Newtonian fluid, the sweep area and displacement efficiency increase as the elasticity increases. The pressure drop in the convex area is larger with a bigger elasticity, and it will strengthen the displacement and wash action at the corner. The viscoelastic behavior of the displacing polymer fluids can in general improve the displacement efficiency in pores compared to using Newtonian fluids. This conclusion should be useful in selecting polymer fluids and designing polymer flooding operations.

REFERENCES

[1] Zhang, L.J. and Yue, X.A. (2007) Mechanism for viscoelastic polymer solution percolating through porous media. *Journal of Hydrodynamics Series B*, **19(2)**, 241-248.

[2] Wang, D.M. and Lin, J.Z. (2008) Influence of the microforce produced by viscoelastic displacement of liquid on displacement efficiency. *Journal of Xi'an Shiyou University* (*Natural Science Edition*), **23(1)**, 43-55.

[3] Yin, H.J., Wang, D.M. and Zhong, H.Y. (2006) Study on flow behaviors of viscoelastic. polymer solution in micropore with dead end. *SPE* 101950, San Antonio, Texas, 786-795.

[4] Yin, H.J. and Zhong, H.Y. (2007) Numerical simulations of viscoelastic flows through one slot Channel. *Jour- nal of Hydrodynamics*, *Series B*, **19(2)**, 210-216.

[5] Wang, D.M., Cheng, J.C. and Yang, Q.Y. (2000) Viscouselastic polymer can increase in cores. *SPE* 63227, Dallas, Texas, 719-728.

[6] Huang, Y.Z., Yu, D.S. and Zhang, G.F. (1990) The study on micro polymer flooding mechanism. *Oilfield Chemistry*, **3**, 57-60.

[7] Yin, H.J. and Jiang, H.M. (2008) Bhavior of SPTT viscoelastic fluid in contraction channel. *Petroleum Geology & Oilfield Development in Daqing*, **27(2)**, 56-59.

[8] Zhang, L.J. (2001) Flow of voscoelastic fluid throught complex pores and its effect on microscopic displacement efficiency. *Daqing Peturelum Institute*, 37-37.

[9] Aboubacar, M., Matallah, H. and Webster, M.F. (2002) Highly elastic solutions for Oldroyd-B and Phan-Thien/ Tanner fluids with a finite volume/element method: Planar contraction flows. *Non-Newtonian Fluid Mech*, **103(1)**, 65-103.

[10] Jiang, H.M. (2009) The study on microscopic porous flow behavior of polymer solutions. *Daqing Peturelum Institute*, 10-26.

[11] Patankar, S.V. (1980) Numerical heat transfer and fluid flow [M]. New York, Hemisphere.

[12] Deng, J., Ren, A.L. and Zou, J.F. (2006) Three-dimensional flow around two tandem circular cylinders with various spacing at Re = 200. *Journal of Hydrodynamics*, *Series B*, **18(1)**, 48-54.

[13] Bao, F.B., Lin, J.Z. and Liu, Y.H. (2006) Research on the flow property in three dimensional cavity of microchannel. *Journal of Hydrodynamics*, *Series B*, **18(1)**, 20-25.

[14] Qu, J.P. and Xia, G.F. (1998) Reaserch on elastic behaviors of LDPE melt during capillary dynamic extrusion. *Journal of South China University of Technology* (*Natural Science*), **11**, 76-80.

[15] Fortin, A. and Zine, A. (1992) An improved GARES method for solving viscoelastic fluid flow problems. *Non-Newtonian Fluid Mechanics*, **42(1-2)**, 1-18.

Vol.2, No.1, 786-792 (2010)
doi:10.4236/ns.2010.27099

Natural Science

Great collapse (kepler's first law)

Mohammad Tayseer Kayed Al-Tamimi*

The National Center for Publishing, Irbid, Jordan; tamimi7551@yahoo.co.uk

Received 2 April 2010; revised 17 May 2010; accepted 22 May 2010.

ABSTRACT

When I put Kepler's first law under peer review, I note: 1) There is an isolation cordon between daytime and night = 13.88 m; 2) Earth's Rotation Axis loses its tendency to its mother (Polaris now) in winter; 3) Celestial's equator doesn't parallel Earth's equator; 4) Ice sheet in Antarctica equals ice sheet on arctic. But we find the field observation data contrary to that.

Keywords: Astronomy; Solar; Collapse; System; Coronal Model; Elliptical Orbit

1. INTRODUCTION

I think, it is not easy to call astrophysicists or astronomers to review Kepler's first law. But, when we take a look to the chart of celestial sphere, we strongly note that we could not put Earth's equator in parallel with celestial's equator, especially when we remember that the rotation axis of Earth is pointing (now) to Polaris; which is inclining about half degree to the North Celestial Pole (NCP) (See **Figure 1**).

Indeed, monkey does not set down there. But, when we try to take a deep looking in minutiae, we find our self in the circle of wondering, especially when we try to reread the data of **Figure 2**.

- How could the Earth's equator parallel the celestial's equator when (θz = θz´)?
- How could Earth's rotation axis tend to Polaris in winter when (θh = θh´≅θH)?
- Why we find some differences between daytime and night in times of Equinoxes when we use Kepler's first law?

But the hard question which stays with no good answer is (the penetration of Pluto in Neptune's orbit). How we can understand the events of 1989 - 1999, with the horizontal model of orbits (Kepler's theory)? Is there any relationship between this event and parallax, or ability of reflecting the light?

From these points, we can realize that we have to review the whole data of field observation concerning the celestial's sphere, which will be discussed in the following pages, where we can obtain the core of the REAL ASTRONOMY.

2. DEFINITIONS

Wherever these words or phrases are mentioned they have the following meanings:

- Earth's Orbit (EO): It is a closed and elliptical phantom line drawn by Earth when it is turning around the Sun.
- Major axis (MX): It is an image straight-line, its selvages touch of furthest points on elliptical orbit, and passes through its center.
- Ecliptic: It is closed phantom line drawn by the Sun during its apparent movement around the Earth (the Earth's orbit around the Sun). The extension of Ecliptic divides the wide strip of Zodiac into two equal halves (Its obliquity to celestial's equator at

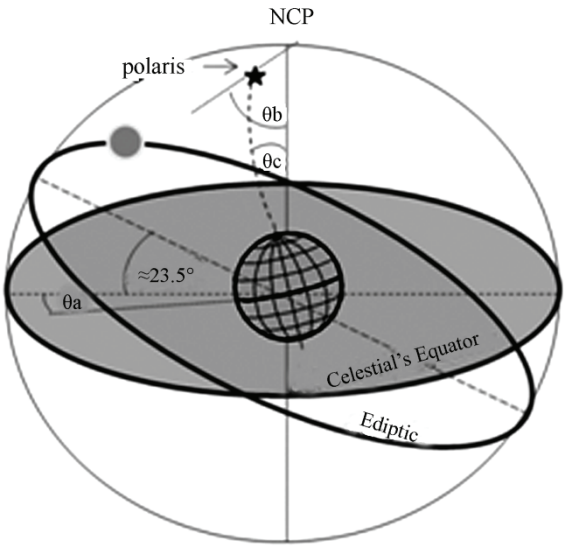

Figure 1. (ERA) is tending to polaris, which inclines to (NCP), about 0.5°, so we have an angle (θa) between earth's equator and celestial's equator.

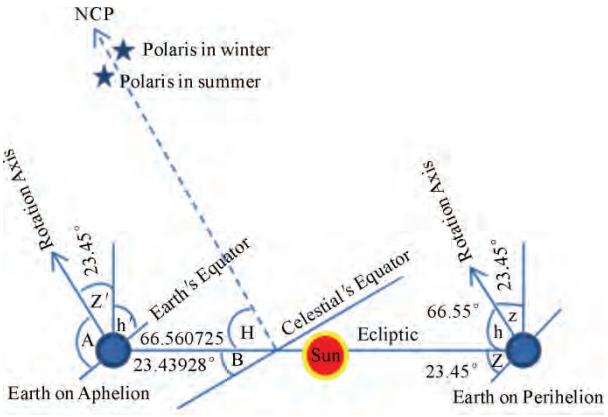

Figure 2. Two rotation axis are parallel; (with respect to; A = 90° = h + z) (h = h´), (Z = z = z´), (H + B = 90°).

J2000.0 = 23° 26´ 21.4119´´), which is moving in Zodiac 46.8″/1000 year [1].

- North Celestial Pole (NCP): It is a notional point located in the zenith of the center of the North Celestial Dome (NCD).
- Earth's Rotation Axis (ERA): It is a notional straight line passes (theoretically) through the center of the Earth's mass, and its two selvages touch of the center of the north and south poles of the earth's mass, and it stands vertically with the level of the Earth's equator.
- Earth's Poles Center (EPC): There are two opposite points on the surface of the Earth; the ERA is connecting between them in perpendicular with Earth's equator.
- Earth's Equator (EQ): It is a notional line surrounds the surface of Earth from its mid. EQ is the zero latitude on Earth. (Its inclination to Ecliptic = 23.45°).
- Zenith: It is a notional point in the Celestial Dome (CD) which is directly located above the observer who stands on Earth.
- Perihelion: It is a notional point on the EO, and a closest point on EO to the Sun.
- Celestial Equator (CQ): It is a phantom line which surrounds the great celestial sphere from its mid, (CQ) is the zero latitude of the sphere.
- Aphelion: It is a notional point on the (EO), and a furthest point on EO to the Sun.
- Polaris: It is a star which shines in the top of the NCD, and it inclines 0.44349° to the NCP.

3. SUPPOSITIONS OF THE RESEARCH

I assume the following points in this research:

- The inclination of (ERA) to falling column on ecliptic plane = 23° and 27´and 38.5881″ at Perihelion, but at Aphelion = 23° and 25´and 42.8238″.
- The distance between Sun and Earth (surface to surface), when Earth is located at Perihelion = 147.104×10^6 km.
- The distance between Sun and Earth (surface to surface), when Earth is located at Aphelion = 152.103×10^6 km.
- (MX) does not pass through the center of the Sun's mass.
- The inclination of tropic of Cancer to Ecliptic plane = 38.588″ (0.0107188 arc degree) to the south
- The inclination of tropic of Capricorn to Ecliptic plane = 1´ and 17.1761″ (0.0214376 arc degree) to the south. See **Figure 4**.

4. OBJECTIVES AND QUESTIONS OF THE RESEARCH

This research aims to explain the real astronomy, and then presents a new law in astronomy, which deals accurately with field observation data of (CD).

Also, this research poses the following questions:

- Does the center of the Sun locate in one of the two focuses of the Ecliptic?
- Does celestial's equator parallel Earth's equator?
- Why did we observe the penetration of Pluto in Neptune's orbit in 1989?
- Where is the location of Sun's center in Ecliptic?

5. DATA OF THE RESEARCH

I basically depend on the following facts:

- North selvage of (ERA) is pointing to Polaris, now.
- (ERA) is standing vertically on (EQ).
- Scientists are disagreed about the quantum of the inclination of the (ERA) to the falling column on Ecliptic plane [2].
- ea = a – (R´ + R + r), where (ea) is the distance between focus and orbit's center, (a) the radius of orbit, (R) the radius of Sun, (R´) the planet's radius, (r) the minimum distance between the Sun and the planet.
- $(a = \frac{1}{2}(2R' + 2R + r + r')$ *where*; *Astronomical Unit* (*AU*) = $\frac{1}{2}(300610772.272)$ *km*, (r´) the maximum distance between planet and Sun.
- Eccentricity $(e) = \frac{ea}{a} = \frac{r'-r}{r'+r}$.
- Equatorial diameter of Earth [3] = 12756.272 km.

- Sun's diameter = 1391016 kilometers ± 361.66 kilometers [4]
- Ice sheet on Arctic is more than the ice sheet in Antarctica [5].
- Obliquity of ecliptic to [4] (CQ) = 23° 26′ 21.4119″.
- Inclination [4] of (EQ) to orbit = 23° 27′.

6. PROBLEM OF RESEARCH

The problem of this research is summarized in:

1) (ERA) could not point to Polaris in winter.

2) Earth's equator does not parallel the celestial's equator.

3) Ice sheet on Arctic doesn't equal ice sheet in Antarctica.

4) Pluto could not penetrate in Neptune's orbit.

To explain this problem, I will try to imitate the first Law of Kepler, and put the data of this law on **Figure 3** as follows:

1) Side (a b) represents the major axis of Ecliptic.

2) Arrow (h) represents (ERA) when Earth stands at Perihelion. This arrow inclines 23.45º (23º and 27´) [4] to the Falling Column on Ecliptic (FCE).

3) Arrow (h´) represents (ERA) when Earth stands at Aphelion. This arrow inclines 23.45º (23º and 27´) to the (FCE).

4) Dashed arrow (n) is going from the center of (CD) toward the (NCP) and falls perpendicular on the celestial's equator.

5) Side (e a) represents the (FCE), also the side (e´ b).

6) Dashed line represents the celestial's equator. This line inclines 23.438281º (23º 26´ 21.4119″) [4] to ecliptic. See **Figure 3**.

Through these data which Kepler depended on it, in his first law; I can mark the following notes, and explain how and where the mistakes had been happened:

- ✓ $\theta_A = \theta_H = \theta_H' = \theta_A' = 23.45°$
- ✓ $\theta_k = 90°$
- ✓ $\theta_C = (90º - \theta_A) = 66º$ and 33´
- ✓ $\theta_D + \theta_C + \theta_B = 180º$. So; $\theta_D = 180º - (\theta_C + \theta_B) = 180º - 89º\ 59'\ 21.4119'' = 90º$ and 38.588″ (1)
- ✓ $\theta_E = (180º - \theta_D) = 89º\ 59'\ 21.4119''$ (2)
- ✓ $\theta_B = \theta_B'$ by reflection, so; $\theta_D' = 180º - (\theta_B' + \theta_C') = 90º$ and 38.588″ (3)

From this point we conclude that:

1) If arrow (h) could intersect with arrow (n), then this possibility is unavailable with arrow (h´). This defect lets us to review all estimations concerning the quantity of inclination of (ERA) to (FCE).

2) The results of two relationships (1) and (3) mean that the Earth's equator does not parallel the celestial's equator; please note: $\theta_E \neq (\theta_C + \theta_H)$ and $\theta_E \neq \theta_k$.

3) When we note that the $(\theta_D' > \theta_K > \theta_E)$, we realize that the (ERA) is losing its tendency to Polaris in winter.

4) These results indicate to (one or more) mistakes in the first law of Kepler.

7. DATA - PROCESSING

To process the problem of this research, we have to work with the real data, and let us imagine that we have two vertical and adjoined triangles at same level, and the rectangle (d, c, z, g) separates between them, as follows:

1) Side (a b) represents the ecliptic's plane (the major axis of ecliptic), and the column (e) stands perpendicular on it to the maximum right, and column (e´) to the maximum left.

2) Arrow (h) represents the (ERA) when Earth stands at Perihelion, which (in the same time) stands perpendicular on the (EQ).

3) Arrow (h´) represents the (ERA) when Earth stands at Aphelion, which (in the same time) stands perpendicular on the (EQ).

4) Side (a g) represents the sunlight which vertically falls on the tropic of cancer when Earth stands at Perihelion.

5) Side (b k) represents the sunlight which vertically falls on the tropic of Capricorn when Earth stands at Aphelion.

6) Side (g k) represents Sun's diameter.

7) Arrow (n) trends from the center of the (CD) towards the (NCP), and stands perpendicular on the (CQ).

8) Dashed line represents the (CQ) (See **Figure 4**).

Of course, this hypothesis will seem voiceless and blindness, but the trial of putting the smooth data of celestial's sphere on it, will make it enunciate by the whole truth; especially, when we try to handle the problem of research, as follows:

If the quantity of inclination of Earth's equator to ecliptic (in first law of Kepler) which equals 23.45º could not match the field observation data, we will take attention to the following issues:

1) The differences between two quantities (inclination of Earth's equator to orbit, and obliquity of the ecliptic), may be calculated as follows:

$$(23º\ 27') - (23º\ 26'\ 21.4119'') = 38.5881'' \quad (4)$$

2) Because the motion of Earth is taking double race when it is moving from south of Ecliptic to north of Ecliptic; first step when it moves from south of Ecliptic to Ecliptic plane, but the second step when it moves from Ecliptic plane to the north of Ecliptic. Then we find the inclination of Earth's equator to ecliptic takes place to south of the Ecliptic plane when Earth stands at Perihelion, but it takes place to north of Ecliptic plane when Earth stands at Aphelion. This rule requires adding the quantity of this difference (38.588″) to (23º27´)

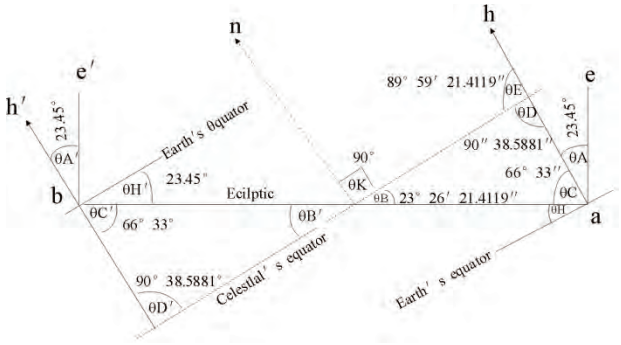

Figure 3. Data of kepler's first law.

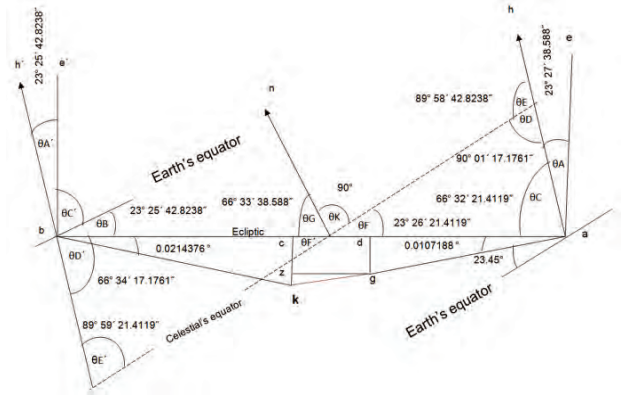

Figure 4. My theory.

when Earth stands at Perihelion, and deducting its double when Earth stands at Aphelion, as follows:

$$\theta_A = 23^o\ 27' + 38.588'' = 23^o\ 27'\ 38.588'' \quad (5)$$

$$\theta_A' = 23^o\ 27' - (38.588'' \times 2) = 23^o\ 25'\ 42.8238'' \quad (6)$$

Then: $\theta_C = 90^o - \theta_A = 66^o\ 32'\ 21.4119''$

where, $\theta_C' = 90^o - \theta_A' = 66^o\ 34'\ 17.1761''$

then: $\theta_D = 180^o - (\theta_C + \theta_F) = 90^o\ 1'\ 17.1761''$

$$\text{So: } \theta_E = 180^o - \theta_D = 89^o\ 58'\ 42.8238'' \quad (7)$$

3) These results concerning the angles on the Perihelion. But calculation of the angles on the Aphelion; need more complex than before:

$$(\theta_A' + \theta_C' + \theta_B) = 113°\ 25'\ 42.8238''$$

$\theta_D' = 180^o - (\theta_A' + \theta_C' + \theta_B) = 66^o\ 34'\ 17.1761''$.

So:

$$\theta_E' = 180^o - (\theta_D' + \theta_F') = 89^o\ 59'\ 21.4119'' \quad (8)$$

4) (23.45°) just equals the inclination of Earth's equator to Ecliptic at equinox.

5) The results in (5) and (6), mean that the inclination of tropic of cancer = 38.588″ to south of Ecliptic plane when Earth stand at Perihelion, and the inclination of tropic of Capricorn = 1′17.1761″ to south of Ecliptic plane when Earth stand at Aphelion.

6) The results in (7) and (8), indicate that the two arrows (h, h′) will intersect the arrow (n), but they will not intersect on the same point. The intersection point of arrow (h) with arrow (n) is closer to the center of (CD) than the intersection point of arrow (h′) with arrow (n), with attention that the location of Polaris is to the west of arrow (n) in summer solstice, where its location in winter solstice is to the east of arrow (n). To be certain of these results accuracy, we should do the following calculations:

a) If we consider that the side (a g) equals the length of sunlight which vertically falls on the tropic of cancer when Earth be on Perihelion + the radius of Earth (which equals 147110378.136 km), we can calculate the sides of the triangle (a g d) as follows:

In the triangle (a d g) we have a sharp angle (0.0107188°) in (a), so;

$$\text{Sine } 0.0107188° = \frac{gd}{ga}.$$

So; g d = Sine 0.0107188° ×147110378.136 km =

$$27521.1669 \text{ km}\ldots\ldots\ldots\ldots\ldots\ldots\ldots\ldots (9)$$

$$\text{if cosine } 0.0107188° = \frac{ad}{ga}$$

so the length of side (a d) = 147110375.5616 km (10)

if Cosine 0.0107188° = a c/a k, the length (a c) = 0.9999999825 × (1391016 + 147104000 + 6378.136) = 148501391.5373 km

so the length of side (c d) = (a c – a d) =

$$1391015.7517 \text{ km} \quad (11)$$

b) If we consider that the length of side (b k) = the length of sunlight which vertically falls on the tropic of Capricorn when Earth be on aphelion + the radius of Earth (which equals 152109378.136 km), we can calculate the length of the sides of triangle (b c k) as follows :

$$\text{Sine } (0.0214376°) = \frac{ck}{bk}. \text{ So;}$$

$$c\ k = 56912.7422 \text{ km} \quad (12)$$

$$\text{Cosine } (0.0214376°) = \frac{cb}{bk}. \text{ So;}$$

$$c\ b = 152109367.4888 \text{ km} \quad (13)$$

$$\text{Length of side (a b)} = (a\ d + c\ d + c\ b) = 300610758.8021 \text{ km} \quad (14)$$

So; the length of side (c d) ≠ the diameter of Sun, and the length of (a b) could not include the maximum and minimum distance between Sun and Earth (center to center); which equals 300610772.272 km.

When we review the relationships (11), (14) we realize that we could not put the diameter of Sun on side (c d), but we can do that on side (g k) (15)

From these points we can consider that the length of

the side (a b) is express the Major Axis of Earth's orbit, but it could not pass through the center of Sun (16)

When we note, $\theta_E \neq \theta_K$, we realize that; (CQ) does not parallel (EQ) (17)

After these results, we can say that:

1) The side (k g) exactly equals the Sun's diameter (1391016 km), which means; the side (k g) can (theoretically) pass through the center of Sun's mass, but the side (a b) could not do that; because the length of (a b) could not simulate the perceptible quantity of equation $(2a = (2R' + 2R + r + r')$ (. Also the length of side (c d) does not equal the Sun's diameter, which makes its passing through the center of Sun's mass, impossible.

2) The mid of (g k) represents the center of Sun's mass, which means that the center of Sun's mass is located far away from the focus (exactly 27534.18 km) (18)

3) The relationship (18) means that the orbits of planets (around the Sun) are built one over other (coronal model), and this model is the correct processing for confused calculations.

8. HARD EVIDENCES

With relationships (5) and (6) we noted that the angular width = 46.9214°, which means that the range of oblate of the shadow on Earth's surface reaches a maximum of 30.383 km when beam falls vertically on equator (0°), and reaches a minimum of (0 m) when beam falls vertically on latitude of 23.46071°. This movement enwraps 183.5 days. The result of this movement causes a longest night and a shortest night. (Note: If 46.9214° = 183.5 days, so 23.46071° = 91.75 days).

Depending on this result, we can know the speed of retrograding of splaying of the shadow (V_c) on Earth's surface at 23.46071° by the following equation;

$$V_C = \frac{\theta}{t} = \frac{23.46071^{\circ} \times 60' \times 60''}{91.75^{d} \times 86400^{s}} = 0.0106542733878292''/s$$

But to know the rate of oblateness (splaying), we can use the following equation;

$$C = \frac{(R_1 - R_2)}{R_1} = \frac{6387.136 - 6365.753}{6387.136} = 0.003347822$$

where (R_1) *is the equatorial radius of Earth and* (R_2) *is the polar radius.*

To know the maximum range of this oblateness;

$$C_{Max} = R_1 \times C = 30.383 \text{ km.}$$

To know the speed of retrograding of shadow's concavity on Earth's surface ($V_\supset$) when sunlight moves on arc from 0° to 23.46071°; we can use the following equation:

$$V_\supset = \frac{C_{Max}}{t} = \frac{30383m}{91.75^{d} \times 86400^{s}} = 0.00383275305278m/s$$

At last, we can derive the following equation to know the maximum range of concavity of Sun's beam on Earth's surface ($\supset_{Max}$);

$$\supset_{Max} = \frac{V_\supset \times \theta}{V_c}$$

$$= \frac{(0.00383275305278m/s)(23.46071^{\circ} \times 60' \times 60'')}{(0.010654273387829246139872842 87''/s)}$$

$$= 30383m$$

Which means that: there is no gap between daytime and night. But when we depend on 23.45° we note that the line of dark is staying away from line of light on surface of Earth, and this gap (isolation cordon) reaches in maximum to 13.88 meters, when we use the ($\supset_{Max}$) equation with 23.45°.

Another evidence; when we review the kepler's first law, we note that the dark and the light doesn't penetrate out of the North or South Polar circles (depending on 23.45°), I mean that the North or South Polar circles are receiving the same amount of dark or light at all time of the year, but in my theory (depending on 23.46071 in summer and 23.42856° in winter) we note that the dark (in winter) penetrates out of North Polar circle (C-zone) double the time of its penetration in the North Polar circle in summer. And we note that the light (in winter) penetrates out of South Polar circle (C´-zone) double the time of its penetration in South Polar circle in summer. This means that the ice on arctic is more than the ice in Antarctica. For this reason, the North Polar circle is receiving heat less than the South Polar circle, and for that we find the ice sheet on north is more than the ice sheet on south of Earth. See **Figure 5**.

Overall, I have a good evidence for this collapse, which comes from nature. When I left my first home in 2003 to a new apartment, after one month of my departure, the Local Electric Company came and cut the cable which was providing electricity to my first home, and left it hanging… the wind starts to move it east and west on the wall, and the cable starts to draw a line on the wall. After two years I noted that the cable has drown two lines on the wall, as seems in the following picture (see **Picture 1**). At first, I thought it is due to the contraction and expansion, but when I noted that the end of this cable was drawing the upper line in summer, and drawing the lower line in winter, I realized that there is another reason for that, (which means; there is no effectiveness of contraction and expanding on this result). Then I decided to return to Kepler's first law, and draw

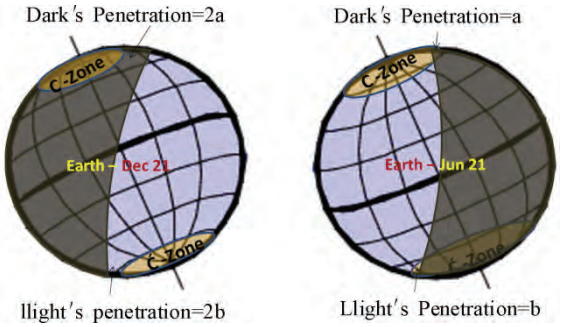

Figure 5. Wobbling of (dark and light) on polar circles.

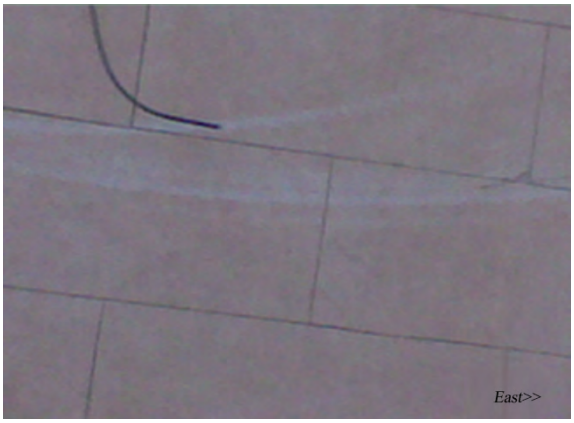

Picture 1. The cable appears when it was drawing two lines on the wall of my home.

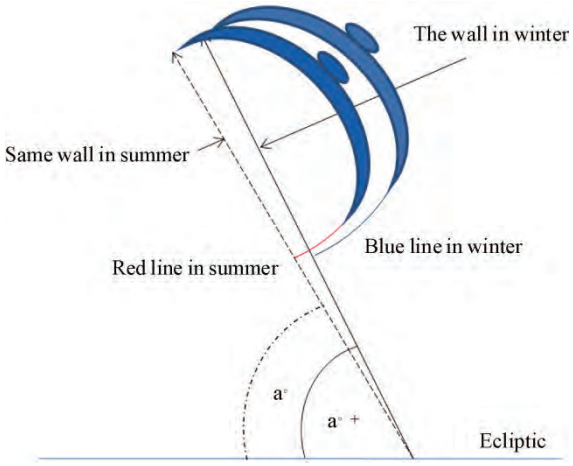

Figure 6. You can use the rule and the compass and protractor to prove that, you have to use different angles and same gap of compass and same length of wall.

these data on paper… at the end, I caught this fact:

If the angle between (EQ) and Ecliptic is steady all of the year (as seemed in **Figure 3**), the cable has to draw one line (one arc), but when we have two different angles (one in winter and another in summer, as seemed in **Figure 4**), the cable has to draw two lines (two different arcs) with two different directions (as seen in **Figure 6** and **Pictures 1**).

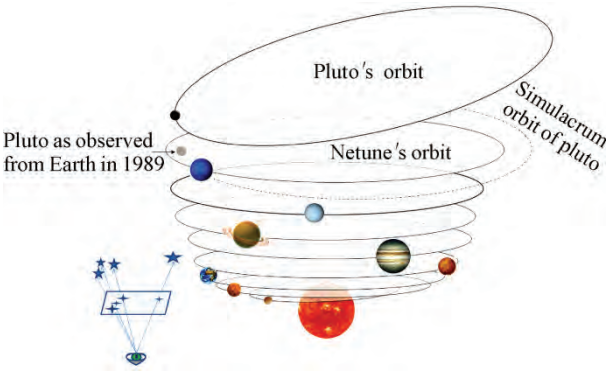

Figure 7. Coronal model and parallax.

Indeed, I got the same result when I had drawn these data on my paper (See **Figure 6**).

9. CONCLUSIONS

We can say that the research achieved its objectives, and gave an answer to its questions, and brought some evidences to this collapse, which are explained in **Figures 1-6** and **Picture 1**, been checked by many equations; which were pointed in relationships (1) to (18) respectively, and finally put a new law in astronomy which can be formulated as follows:

1) There is a distance between focus of Earth's orbit and center of Sun = 27534.18 km.

2) Celestial's equator does not parallel Earth's equator.

3) Orbits of planets are built around the Sun in an exact system, as a coronal model (see **Figure 7**).

This conclusion means:

- ✓ Center of sun's mass is far away from focus.
- ✓ Major axes of the orbits of outer planets don't touch the sun's mass.
- ✓ Major axis of the orbits of the inner planets and earth passe through sun's mass, but couldn't touch the center of sun's mass.

REFERENCES

[1] Allen's, (1999) *Astrophysical Quantities*, 4th Edition, Arthur N. Cox editor, Los Alamos, USA; *Obliquity Applet*, (2004) www.jgiesen.de; Hluk Akcam, Jan, (2004) *Precession and the Obliquity of the Ecliptic*, www.tenspheres.com

[2] Allen's, (1999) *Astrophysical Quantities*, 4th Edition, Arthur N. Cox., Ed., Los Alamos, USA; *The Nine Plants*, www.solarviews.com; Ali Abanda, (1998) *Elm Al-Falak wa Al-Anawa*, Amman; Dr. Jim Kaler, Quick guide to the celestial sphere. *Measuring the Sky*, www.Astro.illinois. edu; Dr. Zainab, (2001) Al-Mawsoa, Al-Falakia, Amman.

[3] Brandt, J.C. (1966) The physics and astronomy of the Sun and Stars. McGraw-Hill, New York.

[4] Allen's (1999) *Astrophysical Quantities*, 4th Edition, Cox, A.N., Ed., Los Alamos.

[5] Atarazi, A. (2010) Chief of Department of Geography, Yarmouk University (Private and Live Data).

Call for Papers

Natural Science

A Journal Published by Scientific Research Publishing, USA
www.scirp.org/journal/ns

Natural Science is an international journal dedicated to the latest advancement of natural sciences. The goal of this journal is to provide a platform for scientists and academicians all over the world to promote, share, and discuss various new issues and developments in different areas of natural sciences. All manuscripts must be prepared in English, and are subject to a rigorous and fair peer-review process. Accepted papers will immediately appear online followed by printed hard copy. The journal publishes original papers including but not limited to the following fields:

- **Astronomy & Space Sciences**
  - Astronomy
  - Astrophysics
  - Atmospheric Science
  - Space Physics
- **Earth Science**
  - Geography
  - Geology
  - Geophysics/Geochemistry
  - Oceanography
- **Chemistry**
  - Analytical Chemistry
  - Biochemistry
  - Computational Chemistry
  - Inorganic Chemistry
  - Organic Chemistry
  - Physical Chemistry
- **Life Science**
  - Cell Biology
  - Computational Biology
  - Genetics
  - Immunology
  - Medicine/Diseases
  - Microbiology
  - Molecular Biology
  - Neuroscience
  - Pharmacology/Toxicology
  - Physiology
  - Psychology
  - Virology
- **Physics**
  - Applied Physics
  - Atomic, Molecular, and Optical Physics
  - Biophysics
  - High Energy/Particle Physics
  - Material Science
  - Plasma Physics
- **Others**
  - Education
  - History of Science
  - Science and Innovations

We are also interested in: 1) Short Reports—2-5 page papers where an author can either present an idea with theoretical background but has not yet completed the research needed for a complete paper or preliminary data; 2) Book Reviews—Comments and critiques.

Notes for Intending Authors

Submitted papers should not be previously published nor be currently under consideration for publication elsewhere. Paper submission will be handled electronically through the website. For more details, please access the website.

Website and E-Mail

http://www.scirp.org/journal/ns ns@scirp.org

Natural Science, 2010, 2, 667-792
Published Online July 2010 in SciRes (http://www.scirp.org/journal/ns).

TABLE OF CONTENTS

Volume 2 Number 7 **July 2010**

ASTRONOMY & SPACE SCIENCES

CHEMISTRY

LIFE SCIENCE

PHYSICS

OTHERS

